Imaging heterogeneous glucose metabolism during tumour proliferation and migration

Hiroshi Kondo

Imperial College London

and

The Francis Crick Institute

PhD Supervisor: Erik Sahai and Kurt Anderson

A thesis submitted for the degree of

Doctor of Philosophy

Imperial College London

November 2019

Declaration

I Hiroshi Kondo confirm that the work presented in this thesis is my own. Where information has been derived from other sources, I confirm that this has been indicated in the thesis.

Copyright declaration

The copyright of this thesis rests with the author. Unless otherwise indicated, its contents are licensed under a Creative Commons Attribution-Non Commercial 4.0 International Licence (CC BY-NC).

Under this licence, you may copy and redistribute the material in any medium or format. You may also create and distribute modified versions of the work. This is on the condition that: you credit the author and do not use it, or any derivative works, for a commercial purpose.

When reusing or sharing this work, ensure you make the licence terms clear to others by naming the licence and linking to the licence text. Where a work has been adapted, you should indicate that the work has been changed and describe those changes.

Please seek permission from the copyright holder for uses of this work that are not included in this licence or permitted under UK Copyright Law.

Abstract

The tumour microenvironment plays an important role in tumour proliferation, invasion, and metastasis. In particular, cancer cells can exist in heterogeneous states within the complex tumour microenvironment including different nutrient accessibility, oxygen concentration, extracellular pH, and extracellular matrix (ECM) stiffness. Cancer cell characteristics vary among individual cells and metabolic reprogramming is a key feature of tumour microenvironmental adaptation. Cancer cells can switch nutrient source depending on the micro-environment with variation in the effect of aerobic glycolysis. Although heterogeneous metabolism in cancer cells is expected, experimental approaches to analyse cell metabolism at single cell resolution are limited.

In order to investigate heterogeneous cancer cell metabolism, I validated a fluorescence resonance energy transfer (FRET)-based glucose biosensor in breast cancer cell lines. Notably, I observed breast cancer cell lines have heterogeneous intracellular glucose levels and I analysed the functional significance of this metabolic heterogeneity. Multiplexed imaging clarified that high glucose cells take in and consume glucose faster than low glucose cells. Metabolomic analysis further revealed that high and low glucose cells mainly employ glycolysis and oxidative phosphorylation (OXPHOS), respectively. This inter-cellular heterogeneity is established by phosphoinositide 3-kinase (PI3K) signalling pathway and actin cytoskeletal dynamics. Migrating cells dramatically increase intracellular glucose levels by activating the PI3K/AKT signalling pathway and actin cytoskeletal remodelling. PI3K inhibitors can supress glycolysis and the proliferation of breast cancer cells. However, a subset of cells have a PI3K-independent mechanism to regulate glycolysis. Histone acetylation and its reader Bromodomain regulate cell metabolism. Combinatorial inhibition of PI3K and Bromodomain can effectively supress tumour growth.

Acknowledgement

I would like to express my heartfelt appreciation to my supervisors Erik Sahai and Kurt Anderson. Although I started my PhD programme at the The Beatson Institute, both of you gave me the opportunity to work on this great project in the Francis Crick Institute.

A special thanks to Erik for logical and shrewd supervision. I was able to find my research direction thanks to your support and advice with great vision.

A special thanks to Kurt for constant support, advice, and useful English lessons. Without your help, I couldn't have done my project.

Also, I would like to thank Chris Dunsby, Dimitrios Anastasiou, and Axel Behrens for their support. Committee meetings were very helpful to discuss and get ideas for my research project.

I would like to thank the Metabolomics, Flow cytometry, and Light microscopy facilities for technical support.

Finally, special thanks to all lab members of the Tumour Cell Biology Laboratory. I really enjoyed sharing experimental techniques, knowledge, and ideas.

Table of Contents

Abstract **3**
Acknowledgement **4**
Table of Contents **5**
Table of figures **8**
List of tables **12**
Abbreviations **13**
Chapter 1.Introduction **18**
1.1 Breast Cancer **18**
1.1.1 Heterogeneity of breast cancer 18
1.1.2 Breast cancer cell lines 19
1.1.3 PI3K signalling pathway in breast cancer 20
1.1.4 Hormone and targeted therapy 22
1.1.5 Therapeutic resistance of ER^+ breast cancer 22
1.2 Cancer cell metabolism **23**
1.2.1 Inter-cellular metabolic heterogeneity 23
1.2.2 Metabolic regulation 25
1.3 Tumour microenvironment **26**
1.3.1 Non-cellular tumour microenvironmental factors 26
1.3.2 Cancer Associated Fibroblasts (CAFs) 28
1.4 Epigenetic regulation of gene expression **29**
1.4.1 Epigenetic modifications 29
1.4.2 DNA methylation 31
1.4.3 Histone methylation 31
1.4.4 Histone acetylation 32
1.5 Fluorescence imaging **33**
1.5.1 Fluorescence microscopy 33
1.5.2 Fluorescence resonance energy transfer (FRET) 34
1.5.3 Fluorescence lifetime imaging microscopy (FLIM) 37
1.5.4 FRET and FLIM applications in tumour cell biology 38
Chapter 2.Materials & Methods **40**
2.1 Cell culture and transfection **40**
2.1.1 Cell culture 40
2.1.2 Lipofectamine 2000 transfection 41
2.1.3 X-tremeGENE™ HP DNA Transfection 41
2.2 Plasmids and DNA maps **41**
2.2.1 Plasmids 41
2.2.2 Gibson Assembly 43
2.2.3 DNA map of Glucose FRET biosensor (eCFP-Citrine) 45
2.2.4 DNA map of Glucose FRET biosensor (mTurquoise2 - sReACh) 46
2.2.5 DNA map of Pyruvate FRET biosensor 47
2.2.6 DNA map of Lactate FRET biosensor 48
2.2.7 DNA map of ATP FRET biosensor 49
2.3 Western Blot **50**
2.4 Inhibitors and siRNA **51**
2.4.1 Inhibitors 51
2.4.2 siRNA 52
2.5 Immunofluorescence analysis **53**

2.6 Immunohistochemistry 54
2.7 Viability tests 54
2.7.1 Crystal violet staining 54
2.7.2 IncuCyte S3 Live-Cell Analysis 54
2.8 Seahorse assay 55
2.9 Metabolomics 56
2.10 Migration Assays 57
2.10.1 Scratch assay 57
2.10.2 Wound healing assay 57
2.11 Confocal microscopy 57
2.12 Mouse xenograft model 58
2.13 Intravital imaging 59
2.14 Fluorescence lifetime imaging 59
2.15 Image analysis 60
2.15.1 Ratiometric FRET 60
2.15.2 Kymographs 60
2.15.3 Quantification of FRET ratio in xenograft tumours 61
2.15.4 Quantification of nuclei density in xenograft tumours 62
2.15.5 FLIM-FRET 63
2.15.6 NAD(P)H fluorescence lifetime 63
2.16 Statistics 64
Chapter 3.Imaging metabolic heterogeneity of breast cancer 65
3.1 Chapter summary 65
3.2 Metabolic Biosensors 65
3.2.1 Glucose FRET Biosensor 65
3.2.2 ATP FRET Biosensor 69
3.2.3 AMPK FRET Biosensor 70
3.2.4 Pyruvate FRET Biosensor 71
3.2.5 Lactate FRET Biosensor 72
3.2.6 NAD(P)H 73
3.2.7 2-NBDG 74
3.2.8 TMRE 75
3.2.9 CellRox 76
3.2.10 Summary of biosensor optimisation 77
3.3 Metabolic heterogeneity of breast cancer cell lines 78
3.3.1 Heterogeneity of intracellular glucose levels 78
3.3.2 Intracellular glucose levels discriminate glycolysis and OXPHOS 79
3.3.3 Intracellular glucose levels of breast cancer cell lines 83
3.3.4 OCR and ECAR measurements 94
3.3.5 Metabolomic analysis 95
3.4 Growth of high and low glucose cells 98
3.5 Chapter discussion 99
Chapter 4.Regulatory mechanism of heterogeneous glucose metabolism 100
4.1 Chapter summary 100
4.2 The effect of microenvironmental factors on cell metabolism 100
4.3 Intracellular glucose levels of different cell confluence 103
4.4 PI3K/AKT signalling regulates glucose metabolism 104
4.5 The effect of PI3K and PTEN inhibitor on cell metabolism 106
4.6 Actin cytoskeletal remodelling regulates glucose metabolism 108

4.7 Signalling pathway of regulating heterogeneous glucose metabolism 110
4.8 Signalling pathway in different cell confluences 112
4.9 Chapter discussion 113
Chapter 5.Migrating high glucose cells accelerate glycolysis 114
5.1 Chapter summary 114
5.2 Intravital imaging of intracellular glucose levels 114
5.2.1 Intravital imaging of intracellular glucose levels in MCF-7 cells 114
5.2.2 Intravital imaging of intracellular glucose levels in MDA-MB-231 cells 115
5.2.3 Histopathology analysis 117
5.3 Scratch-induced high glucose cells promote glycolytic cell metabolism 120
5.3.1 Scratch-induced migrating cells increase glucose levels 120
5.3.2 Scratch and wound healing assay in MCF-7 cells 122
5.3.3 Scratch-induced migrating cells decrease ATP levels 123
5.3.4 Nutrient requirement during cell migration 124
5.3.5 Imaging cell metabolism in scratch-induced migrating cells 126
5.3.6 Metabolomic analysis of migrating and non-migrating cells 128
5.3.7 Signalling pathway for regulating scratch-induced glycolysis 130
5.3.8 YAP localisation after scratch assay 131
5.4 Chapter discussion 133
Chapter 6.Epigenetic regulation of glucose metabolism and combinatorial approaches to therapy 134
6.1 Chapter summary 134
6.2 Epigenetic regulation of glucose metabolism 134
6.2.1 The effect of epigenetic inhibitors on Intracellular glucose levels 134
6.2.2 Lasting effect of epigenetic inhibitors 135
6.2.3 The effect of epigenetic inhibitors on high and low glucose cells 136
6.2.4 The effect of Acetyl-CoA on Intracellular glucose levels. 139
6.3 Combinatorial inhibition of PI3K and Bromodomain 140
6.3.1 Double treatment of PI3K and Bromodomain inhibitors 140
6.3.2 Combinatorial inhibition induced energetic stress 145
6.3.3 The effect of combinatorial inhibition on signalling pathways 146
6.3.4 Combinatorial inhibition in the scratch assay 147
6.4 Chapter discussion 149
Chapter 7.Discussion 150
7.1 Summary and reflection on the findings 150
7.1.1 Multiplexed imaging of cancer cell metabolism 150
7.1.2 Metabolic heterogeneity of breast cancer 152
7.1.3 The mechanism to reprogram glucose metabolism 155
7.1.4 Cell confluence remodels cell metabolism 157
7.1.5 Combinatorial inhibition of PI3K and Bromodomain for effective tumour suppression 158
7.2 Future perspective 159
7.2.1 Non-invasive live cell imaging 159
7.2.2 Imaging T cell maturation 160
7.2.3 Imaging metastatic disease 161
Chapter 8.Appendix 162
Reference List 163

Table of figures

Figure 1-1 Gene expression profile of breast cancer. 18
Figure 1-2 Structure of class IA PI3K. 20
Figure 1-3 PI3K/AKT signalling pathway in cancer. 21
Figure 1-4 Metabolic strategies of differentiated and cancer cells. 24
Figure 1-5 Oncogenic regulation of cancer cell metabolism. 26
Figure 1-6 Tumour microenvironmental factors. 27
Figure 1-7 Nutrient exchange among different types of cells. 29
Figure 1-8 Covalent modification of DNA and histones. 30
Figure 1-9 Kinetic microscopy techniques. 34
Figure 1-10 Mechanism of fluorescence excitation and emission. 34
Figure 1-11 FRET mechanism. 35
Figure 1-12 The mechanisms of FRET-based biosensors. 36
Figure 1-13 Principle of TCSPC-based fluorescence lifetime measurement. 38
Figure 2-1 Mechanism of PiggyBac transposon system. 42
Figure 2-2 Cloning of the glucose FRET biosensor 42
Figure 2-3 Overview of the Gibson Assembly 43
Figure 2-4 Experimental outline of immunofluorescence imaging. 53
Figure 2-5 Seahorse analysis of OCR and ECAR. 55
Figure 2-6 Experimental outline of metabolomic analysis. 56
Figure 2-7 Quantification of FRET ratio in xenograft tumours 61
Figure 2-8 Quantification of nuclei density in xenograft tumours 62
Figure 2-9 Fluorescence lifetime calculation using FLIMfit. 63
Figure 2-10 Fluorescence lifetime fitting curves of NAD(P)H. 64
Figure 3-1 Glucose FRET biosensor. 66
Figure 3-2 Proliferation of glucose FRET biosensor expressing MCF-7 cells. 66
Figure 3-3 Working range of the glucose FRET biosensor in MCF-7 cells. 67
Figure 3-4 Fluorescence lifetime of four different glucose FRET biosensors. 68
Figure 3-5 ATP FRET biosensor. 69
Figure 3-6 AMPK FRET biosensor. 70
Figure 3-7 Pyruvate FRET biosensor. 71
Figure 3-8 Lactate FRET biosensor. 72
Figure 3-9 Fluorescence lifetime imaging of NAD(P)H 73
Figure 3-10 Fluorescence imaging of 2-NBDG. 74

Figure 3-11 Fluorescence imaging of TMRE. 75
Figure 3-12 Fluorescence imaging of CellRox. 76
Figure 3-13 Heterogeneity of intracellular glucose levels. 78
Figure 3-14 Imaging glucose uptake and consumption. 80
Figure 3-15 Multiplexed imaging of glucose FRET biosensor and 2-NBDG. 81
Figure 3-16 Multiplexed imaging of intracellular glucose levels and energetic states. 82
Figure 3-17 Multiplexed imaging of glucose FRET biosensor, TMRE, and CellRox. 83
Figure 3-18 Intracellular glucose levels of breast cancer cell lines. 84
Figure 3-19 Imaging stability of intracellular glucose levels. 85
Figure 3-20 Stability of intracellular glucose level in breast cancer cell lines. 86
Figure 3-21 Long term stability of intracellular glucose levels. 88
Figure 3-22 Experimental outline of imaging FACS-isolated breast cancer cells... 89
Figure 3-23 FRET distribution of intracellular glucose levels in flow cytometry. 90
Figure 3-24 High and low glucose cell isolation in MCF-7 cells. 91
Figure 3-25 High and low glucose cell isolation in breast cancer cell lines. 92
Figure 3-26 Stability of FACS-isolated high and low glucose cells. 93
Figure 3-27 OCR and ECAR in FACS-isolated high and low glucose cells. 95
Figure 3-28 Experimental outline of metabolomics in high and low glucose cells.. 96
Figure 3-29 Metabolomic analysis of high and low glucose cells. 97
Figure 3-30 Proliferation of FACS-isolated high and low glucose cells. 99
Figure 4-1 Tumour microenvironmental factors regulate glucose metabolism..... 101
Figure 4-2 Cell metabolism of MCF-7 cells in normoxia and hypoxia. 102
Figure 4-3 Intracellular glucose levels with different cell confluences. 103
Figure 4-4 YAP localization with different cell confluence. 104
Figure 4-5 PI3K/AKT/mTOR signalling pathway regulates glucose metabolism.. 105
Figure 4-6 The effect of PI3K inhibitor on high and low glucose cells. 106
Figure 4-7 Cell metabolism of MCF-7 cells after inhibitor treatments. 107
Figure 4-8 PI3K/AKT signalling pathway regulates OCR and ECAR. 108
Figure 4-9 Actin cytoskeletal dynamics regulate glucose metabolism. 109
Figure 4-10 Actin cytoskeletal remodelling regulates OCR and ECAR. 109
Figure 4-11 Expression levels of metabolism regulator proteins in high and low glucose cells. 110
Figure 4-12 Western Blot of acetyl-lysine in high and low glucose cells. 111

Figure 4-13 Expression levels of metabolism regulator proteins in high and low cell confluence. 112
Figure 5-1 Intravital imaging of intracellular glucose levels in MCF-7 tumours. ... 115
Figure 5-2 Intravital imaging of intracellular glucose levels in MDA-MB-231 tumours. 116
Figure 5-3 Ratiometric FRET and FLIM-FRET of intracellular glucose levels. 117
Figure 5-4 IHC imaging of GLUT1 and pAKT in MCF-7 tumours. 118
Figure 5-5 Cell confluence of MCF-7 xenograft tumours. 119
Figure 5-6 Scratch assay of glucose FRET biosensor expressing MCF-7 cells. . 120
Figure 5-7 Outline of constructing kymograph..... 121
Figure 5-8 Scratch assay in breast cancer cell lines. 122
Figure 5-9 Comparison of scratch and wound healing assay. 123
Figure 5-10 Scratch assay of ATP biosensor expressing MCF-7 cells. 124
Figure 5-11 nutrient requirements of MCF-7 cells. 125
Figure 5-12 Imaging glucose uptake and consumption in scratch assay. 126
Figure 5-13 Multiplexed imaging of glucose levels and 2-NBDG in scratch assay. 127
Figure 5-14 Multiplexed imaging of glucose FRET biosensor and TMRE in scratch assay. 128
Figure 5-15 Metabolomic analysis of scratched and non-scratched MCF-7 cells. 129
Figure 5-16 Scratch assay of inhbitor-treated MCF-7 cells. 131
Figure 5-17 YAP localisation in scratch assay. 132
Figure 6-1 Epigenetic regulation of intracellular glucose levels. 135
Figure 6-2 Lasting effect of epigenetic inhibitors on intracellular glucose levels.. 136
Figure 6-3 The effect of epigenetic inhibitors on FACS-isolated high glucose cells. 137
Figure 6-4 The effect of epigenetic inhibitors on FACS-isolated low glucose cells. 138
Figure 6-5 The effect of Acetyl-CoA on intracellular glucose level. 139
Figure 6-6 Combinatorial inhibition of PI3K and Bromodomain. 140
Figure 6-7 The effect of combinatorial inhibition on metabolic stability. 141
Figure 6-8 The effect of combinatorial inhibitor on high and low glucose cells. ... 142
Figure 6-9 Viability analysis of combinatorial inhibition by crystal violet staining. 143
Figure 6-10 Viability analysis of combinatorial inhibition by IncuCyte. 143

Figure 6-11 Alternative drug treatment of PI3K and Bromodomain inhibitor. 144
Figure 6-12 The effect of combinatorial inhibition on energetic stress. 145
Figure 6-13 The effect of combinatorial inhibition on protein expression. 146
Figure 6-14 The effect of combinatorial inhibition on scratch-induced glucose increase. 147
Figure 6-15 The effect of combinatorial inhibition on scratch-induced ATP decrease. 148
Figure 7-1 Emission ranges of biosensors. 150
Figure 7-2 Multiplexed imaging of four biosensors. 151
Figure 7-3 Analysis of fluorophore pairs. 152
Figure 7-4 Metabolic stability and heterogeneity in breast cancer. 153
Figure 7-5 Mass spectrometry imaging (MSI) workflow. 154
Figure 7-6 Metabolic signalling pathways regulating glucose metabolism. 155
Figure 7-7 Genomic and transcriptional alterations during tumour progression... 156
Figure 7-8 Metabolic characteristics during cell migration. 157
Figure 7-9 Combinatorial inhibition of PI3K and Bromodomain 158
Figure 7-10 Metabolic reprogramming of T cells. 160
Figure 7-11 Imaging brain metastasis. 161

List of tables

Table 1-1 Subtypes and genetic mutations of breast cancer cell lines. 19
Table 1-2 Clinical trials of PI3K inhibitors in ER^+ breast cancer 23
Table 2-1 DMEM formulation 40
Table 2-2 FBS formulation 40
Table 2-3 Primers 44
Table 2-4 Primary antibodies 50
Table 2-5 Inhibitors 51
Table 2-6 siRNA 52
Table 2-7 Antibodies for Immunofluorescence imaging 54
Table 2-8 Mouse models 58
Table 3-1 Working range of biosensors 77
Table 8-1 Materials 162

Abbreviations

2-DG	2-Deoxy-D-glucose
2-NBDG	2-deoxy-2-[(7-nitro-2,1,3-benzoxadiazol-4-yl)amino]-D-glucose
aCGH	array-based comparative genomic hybridization
ACLY	ATP-citrate lyase
ADH	Atypical ductal hyperplasia
Ala	Alanine
AMPK	AMP-activated protein kinase
Arg	Arginine
ATP	Adenosine triphosphate
BCECF	2',7'-Bis-(2-Carboxyethyl)-5-(and-6)-Carboxyfluorescein
BD	Binding domain
BRD4	Bromodomain-containing protein 4
BSA	Bovine serum albumin
BSc	Basal cells
CAFs	Cancer associated fibroblasts
CD4	Cluster of differentiation 4
CD8	Cluster of differentiation 8
cDNA	complementary DNA
CFP	Cyan fluorescent protein
Cit	Citrulline
CM	Conditioned medium
CT	Computed Tomography
CtBP	C-terminal-binding protein
Cys	Cysteine
DAPI	4',6-diamidino-2-phenylindole
DME	DNA demethylases
DMEM	Dulbecco's modified Eagle medium
DMSO	Dimethyl sulfoxide
DNA	Deoxyribonucleic acid
DNMT	DNA methyltransferase
E2DH	17-β estradiol dehydrogenase
ECAR	Extracellular acidification rate

eCFP	enhanced cyan fluorescent protein
ECM	Extracellular matrix
EpCAM	Epithelial cell adhesion molecule
ER	Estrogen receptor
ERK	Extracellular signal-regulated kinase
eYFP	enhanced yellow fluorescent protein
Ezh2	Enhancer of zeste homolog 2
F1,6-BP	Fructose 1,6-bisphosphate
F6P	Fructose 6-phosphatate
FACS	Fluorescence-activated cell sorting
F-actin	Filamentous actin
FBP	Fructose 1,6-bisphosphate
FBS	Fetal bovine serum
FDG	Fluoro-2-deoxy-D-glucose
FFPE	Formalin-fixed paraffin-embedded
FHA1	Forkhead-associated domain 1
FLIM	Fluorescence lifetime imaging microscopy
FRET	Fluorescence resonance energy transfer
G6P	Glucose 6-phosphate
GA3P	Glyceraldehyde 3-phosphate
GaAsP	Gallium arsenide phosphide
G-actin	Globular actin
GC-MS	Gas chromatography-mass spectrometry
GFP	Green fluorescent protein
Gln	Glutamine
GLS1	Glutaminase 1
GLUT	Glucose transporter
GSH	Glutathione
GSK3β	Glycogen synthase kinase β
GTP	Guanosine triphosphate
hASCs	Human adipose tissue-driven stem cells
HAT	Histone acetyltransferase
HDAC	Histone deacetylase
HEK293	Human embryonic kidney cells 293
HEPES	4-(2-hydroxyethyl)-1-piperazineethanesulfonic acid

HER2	Human epidermal growth factor receptor 2
HIF-1	Hypoxia-inducible factor 1
HMT	Histone methyltransferase
HRP	Horseradish peroxidase
IGF	Insulin-like growth factor
IGF-1R	Insulin-like growth factor 1 receptor
IRF	Instrument response function
iSH2	inter Src homology 2
ITS	Insulin-transferrin-selenium
JmjC-KDM	Jumonji-domain containing lysine demethylase
KDM	Lysine demethylase
KMT	Lysine methyltransferase
LCs	Luminal cells
LICs	Leukaemia-initiating cells
LldR	L-lactate dehydrogenase regulator
LPs	Luminal progenitors
LSCM	Laser scanning confocal microscopes
MBD	Methyl-CpG-binding domain
MCF-7	Michigan Cancer Foundation-7
MCT	Monocarboxylate transporter
MDCK	Madin-Darby canine kidney
MEM	Modified eagle medium
MglB	Methyl-galactoside transporter subunit
MLC	Myosin light chain
MMP	Matrix metalloproteinase
MSCs	Mesenchymal stem cells
MSI	Mass spectrometry imaging
mTFP	monomeric Teal FP
mTOR	Mammalian target of rapamycin
N/C	Nuclear/cytoplasm
NADH	Nicotinamide adenine dinucleotide
NADPH	Nicotinamide adenine dinucleotide phosphate
NO	Nitric oxide
OCR	Oxygen consumption rate
OXPHOS	Oxidative phosphorylation

p85-BD	p85 binding domain
PAM50	Prediction analysis of microarray 50
PBS	Phosphate buffered saline
PDH	Pyruvate dehydrogenase
PdhR	Pyruvate dehydrogenase complex regulator
PDK1	Pyruvate dehydrogenase kinase isoform 1
PDK2	Pyruvate dehydrogenase kinase isoform 2
PDPK1	Phosphoinositide-dependent kinase-1
Pen Strep	Penicillin streptomycin
PET	Positron emission tomography
PFA	Paraformaldehyde
PFK1	Phosphofructokinase 1
PFKFB3	6-phosphfructo-2-kinase/fructose-2,6-bisphosphatase, isoform 3
PI3K	Phosphoinositide 3-kinase
PIP2	Phosphatidylinositol 4,5-bisphosphate
PIP3	Phosphatidylinositol 3,4,5-trisphosphate
PKM1	Pyruvate kinase isozymes M1
PKM2	Pyruvate kinase isozymes M2
PPP	Pentose phosphate pathway
PR	Progesterone receptor
PTEN	Phosphatase and tensin homolog deleted from chromosome 10
PVDF	Polyvinylidene difluoride
RFP	Red fluorescent protein
RNA	Ribonucleic acid
RNA-Seq	RNA sequencing
ROCK	Rho-associated protein kinase
ROS	Reactive oxygen species
RTKs	Receptor tyrosine kinases
SAM	S-adenosylmethionine
SDS	Sodium dodecyl sulfate
SH2	Src homology 2
SH3	Src homology 3
SHG	Second harmonic generation

TAMs	Tumour-associated macrophages
TBS	Tris-buffered saline
TCA	Tricarboxylic acid
TCSPC	Time correlated single photon counting
TDLU	Terminal ductal lobular unit
Teff	Effector T
TET	Ten-eleven translocation
TGF	Transforming growth factor
Wt	Wild type
YAP	Yes-associated protein
YFP	Yellow fluorescent protein

Chapter 1. Introduction

1.1 Breast Cancer

1.1.1 Heterogeneity of breast cancer

Breast cancer is the most common cancer affecting woman in the UK. Cancer Research UK reported 55,213 newly diagnosed cases of invasive breast cancer in 2014 - 2016 with 11,563 deaths in 2016. In spite of improvements in diagnosis and therapeutic treatments, breast cancer is the second leading cause of cancer deaths in British women. Similar statistics apply across the diversified world. Genetic and epigenetic heterogeneity are key characteristics of breast cancer [1]. A sequential process of genetic and epigenetic alterations during tumour progression dramatically diversifies cancer cell characteristics. Global analysis of gene expression in ductal carcinoma (DC) has identified five major breast cancer subtypes, luminal A, luminal B, human epidermal growth factor receptor 2^+ ($HER2^+$), basal-like, and claudin-low tumours (Figure1-1) [2]. Among them, luminal A and B cells express oestrogen receptor (ER) gene (ESR1). Approximately 75% of breast cancer is expected to be ER positive. In contrast, basal-like and claudin-low cells do not express ER, progesterone receptor (PR), and HER2. Transcription levels of 50 genes (PAM50) and epigenetic modifications have been analysed to discriminate breast cancer subtypes [3]. Breast cancer has inter- and intra-tumoural heterogeneity and gene expression profiling has been used for the analysis of biological phenotypes. Endocrine therapy is widely used for luminal A and B breast cancer, and Trastuzumab is a common chemotherapy drug for $HER2^+$ breast cancer. Other therapies such as surgery, radiation, and chemotherapies are used for basal-like, and claudin-low breast cancers [4].

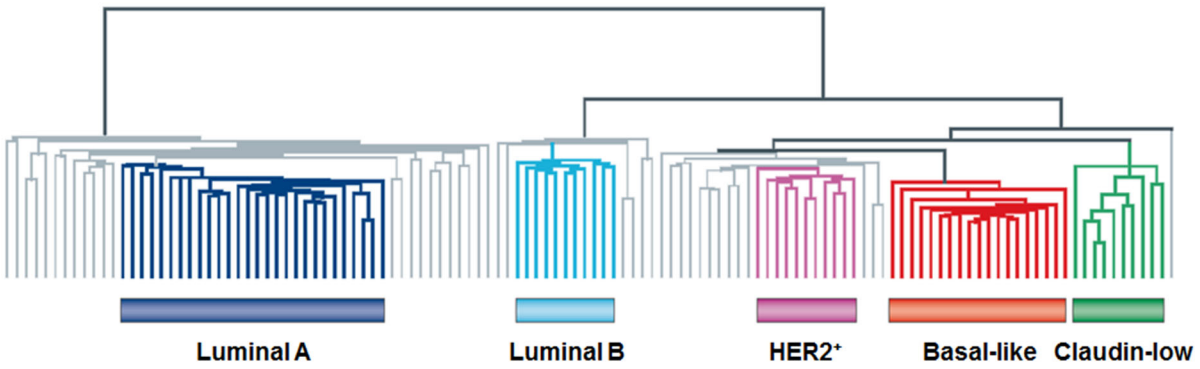


Figure 1-1 Gene expression profile of breast cancer.
Gene expression profile of 115 breast cancers. Breast cancers are divided into five subtypes, luminal A, luminal B, $Her2^+$, basal-like, and claudin-low. Breast cancers in the grey branches do not correlate with five main subtypes. The diagram is adapted from [1].

1.1.2 Breast cancer cell lines

A wide variety of breast cancer cell lines have been established for the analysis of biological phenotypes, molecular functions, cancer cell metabolism, and the therapeutic response of heterogeneous breast cancer. The first breast cancer cell line, BT-20, was established in 1958. One of the most commonly used breast cancer cell lines, MCF-7, was established in 1973. In addition, the MD Anderson series were established in 1978. The subtypes of these breast cancer cell lines were determined and their profile of genomic alterations and gene expression were analysed by DNA microarrays, RNA sequencing (RNA-Seq), and array-based comparative genomic hybridization (aCGH) (Table 1-1) [5, 6].

Cell Line	Classification	ER	PR	HER2	PI3K	PTEN
BT-474	Luminal B	+	+	+	K111N, G333C	Wt
MDA-MD-361	Luminal B	+	+	+	E545K, K567R G1633A, A1700G	Wt
MCF-7	Luminal A	+	+	-	E542K, E545K G1624A, G1633A	Wt
BT-483	Luminal A	+	+	-	E542K, G1624A	Wt
T47D	Luminal A	+	+	-	H1047R, A3140G	Wt
ZR-75-1	Luminal A	+	-	-	Wt	L108R, T323G
MDA-MD-453	Her2	-	-	+	H1047R, A3140G	E307K, G919A
MDA-MD-468	Basal-like	-	-	-	Wt	Deletion
BT-549	Claudin-low	-	-	-	Wt	Deletion
BT-20	Claudin-low	-	-	-	P539R, H1047R C1616G, A3140G	Wt
HCC1143	Claudin-low	-	-	-	Wt	Wt
MDA-MB-231	Claudin-low	-	-	-	Wt	Wt

Table 1-1 Subtypes and genetic mutations of breast cancer cell lines.

Genomic mutations in breast cancer have been reported and the Memorial Sloan Kettering integrated mutation profiling of actionable cancer targets (MSK-IMPACT) platform has identified many DNA alterations and amplifications. Alterations in CDH1, TP53, GATA3, CCND1, MYC, PIK3CA, and PTEN are frequently detected in breast cancers [7]. Among many mutations and amplifications, 32 genes such as ESR1 and TP53 are commonly altered in metastases compared with primary tumours [7].

Activating mutations in the PI3K signalling pathway are frequently found in ER positive breast cancer cell lines. The frequencies of alterations and amplifications of the PI3K

signalling pathway in ER^+ breast cancers are 41-48% for insulin-like growth factor 1 receptor (IGF-1R), 28-47% for p110α PI3K, 29-44% for Phosphatase and tensin homolog (PTEN), 22% for phosphoinositide-dependent kinase-1 (PDPK1), and 2.6-3.8% for AKT1 [8]. The majority of mutations of p110α PI3K are found at E542K/E545K in exon 9 and H1047R/H1047L in exon 20 [9]. This activation of PI3K signalling can promote tumour proliferation and progression [10, 11].

1.1.3 PI3K signalling pathway in breast cancer

The PI3K signalling pathway is a well-characterized signalling pathway which has oncogenic properties. PI3K has three different classes (I, II and III) and class I is further subdivided into class IA and class IB. Class IA PI3K has three isoforms of p110 which are transcribed from PIK3CA, PIK3CB, and PIK3CD. Among them, PIK3CA and PIK3CB are widely expressed in all cell types [12]. The p110 subunit consists of five domains including a p85 binding domain (p85-BD) and a catalytic domain (Figure 1-2). The p85-BD of p110 subunit can interact with the inter Src homology 2 (iSH2) domain of p85 regulatory subunits. The establishment of heterodimers supresses PI3K activity. Binding of the p85 subunit with receptor tyrosine kinases (RTKs) can relieve this inhibitory effect on PI3K.

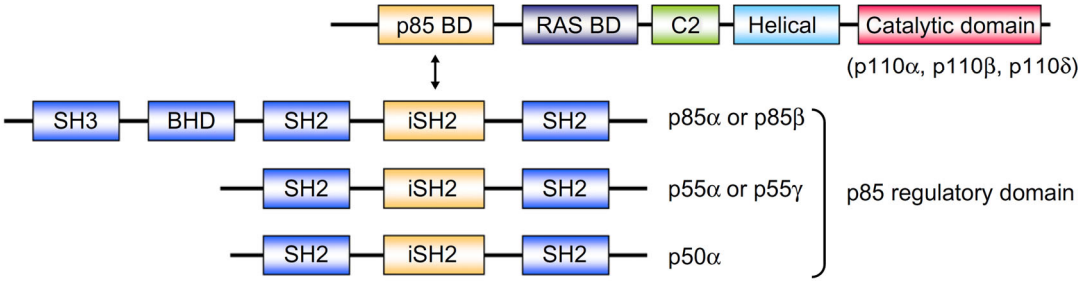


Figure 1-2 Structure of class IA PI3K.
The p110 subunit consists of five domains; p85-binding domain (p85-BD), RAS-binding domain (RBD), putative membrane-binding domain (C2), helical domain, and catalytic domain. The p85 subunits consists of three core domains; inter-Src homology 2 (iSH2), Src homology 2 (SH2), Src homology 3 (SH3), and a BCR homology domain (BHD). The diagram is adapted from [13].

PIK3CA mutations were first discovered in various human solid tumours in 2004 [9]. Human colorectal cancers (32%), glioblastomas (27%), gastric cancers (25%), breast cancers (8%), and lung cancers (4%) had PIK3CA mutations. In particular $PIK3CA^{H1047R}$ can initiate tumour progression in the mammary epithelium, hyper-activation of PI3K is a key molecular mechanism of carcinogenesis [14]. The PI3K signalling pathway starts from

the activation of RTKs by growth factors. Among many upstream receptors of PI3K, insulin-like growth factor 1 (IGF-1) is well linked to PTEN, PI3K, and serine/threonine kinase AKT activity. IGF-1 can stimulate IGFR-1 and recruit PI3K to the plasma membrane. PI3K phosphorylates phosphatidylinositol 4,5-bisphosphate (PIP2) and generates phosphatidyl-inositol 3,4,5-trisphosphate (PIP3). In contrast, PTEN dephosphorylates PIP3 at position D3 and regenerates PIP2. Therefore, PTEN works as an inactivator of the PI3K signalling cascade. PIP3 then recruits AKT and PDPK1 to the plasma membrane. Recruited AKT is phosphorylated by PDPK1 and subsequently phosphorylates downstream substrates (Figure 1-3). Activation of mTORC1 promotes mRNA translation, glucose metabolism, nucleotide synthesis, and protein turnover. In addition, activated AKT promotes transport of the glucose transporter 4 (GLUT4) to the plasma membrane and accelerates glucose metabolism [15]. Glucose metabolism is also promoted by the inactivation of glycogen synthase kinase- β (GSK3β). In addition, PI3K enhances angiogenesis and promotes nutrient accessibility [16]. Thus, the PI3K/AKT signalling pathway regulates cell metabolism and tumour proliferation.

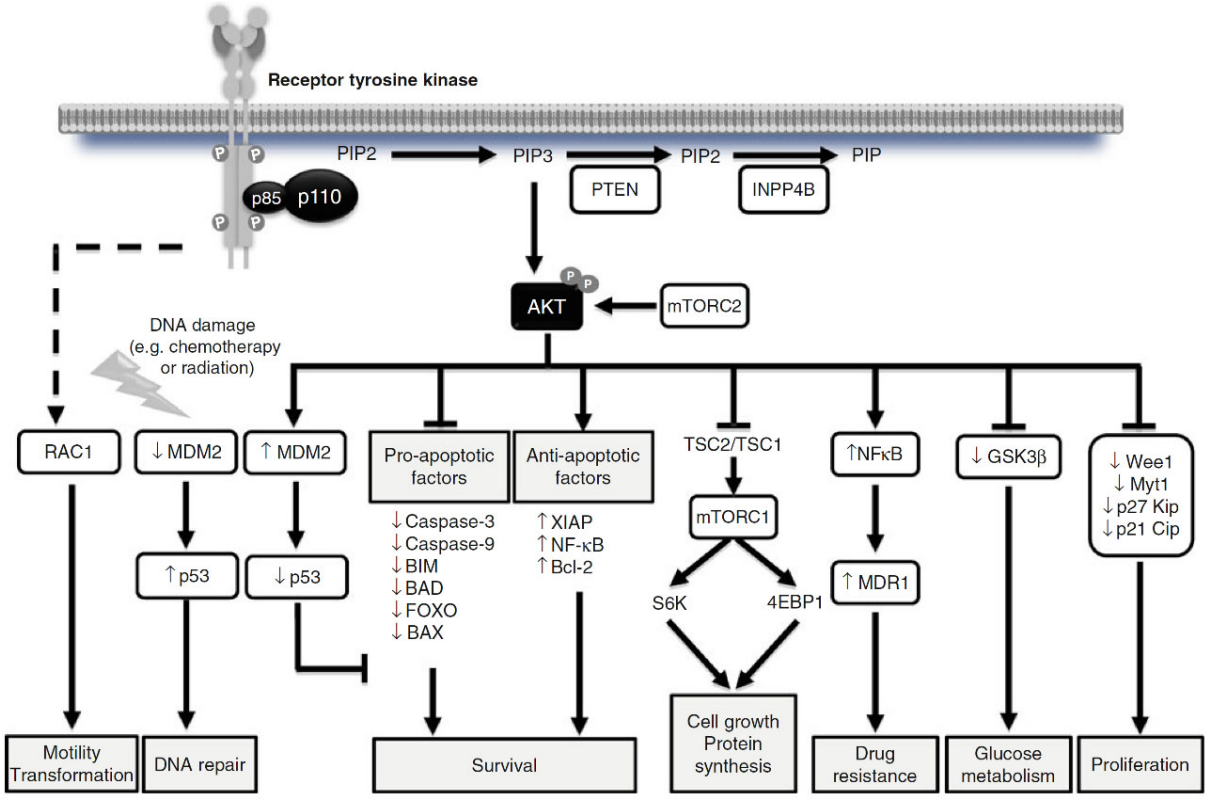


Figure 1-3 PI3K/AKT signalling pathway in cancer.
Activated RTK can promote cell migration via RAC1 activation. Phosphorylated AKT is a signalling hub of PI3K signalling pathway which regulates metabolism, proliferation, and drug resistance. The diagram is adapted from [17].

1.1.4 Hormone and targeted therapy

Endocrine therapy for breast cancer is a standard treatment in patients with ER expression. Approximately 70 - 80% of breast cancer patients are expected to express ER and Tamoxifen has commonly been used for adjuvant therapy. Tamoxifen treatment can reduce recurrence of ER^+ breast cancer by 40% and mortality by 30% [18]. Aromatase inhibitors (AI), which prevents oestrogen production, can be used in post-menopausal woman following several years of Tamoxifen treatment. This combination endocrine therapy has been shown to improve disease-free survival compared with Tamoxifen alone [19]. AI include non-steroidal (Letrozole) and steroidal (Exemestane) inhibitors which can both improve overall survival.

HER2 is overexpressed in roughly 20% of breast cancer patients. Trastuzumab is a targeted therapy drug which binds with the extracellular domain of the HER2 protein. The combinatorial treatment of the monoclonal antibody Trastuzumab with chemotherapy can decrease the recurrence of $HER2^+$ breast cancer by 50% and the risk of death by 30% [18]. Lapatinib is an inhibitor of the internal component of HER1 and HER2. Combinatorial treatment with Lapatinib and Trastuzumab can improve progression-free survival of metastatic breast cancer [20]. There are many therapeutic treatments in breast cancer and the clinical strategy is completely different depending on the individual breast cancer characteristics.

1.1.5 Therapeutic resistance of ER^+ breast cancer

There are multiple causes of therapy resistant ER^+ breast cancer. Highly frequent mutations and alterations in the PI3K signalling pathway increase the resistance to endocrine therapy because of cross-talk between PI3K and ER signalling pathways. Tamoxifen is a common endocrine therapy in ER^+ breast cancer patients. This established drug can improve disease-free survival but some patients develop recurrent breast cancer [21]. PI3K signalling can activate ER transcriptional activity independent from oestrogen. In addition, oestrogen-bound ERα can activate PI3K signalling pathway by directly interacting with PI3K p85 subunit [22, 23]. In some cases, ER^+ breast cancer cells have a resistance to oestrogen deprivation because of overlap in these two signalling pathways [24]. PI3K activated ER^+ breast cancers have worse prognostic clinic-pathological feature [25, 26]. When comparing PIK3CA mutants and wild-type patients, PIK3CA mutated

patients had a better prognosis at least in the first three years [25]. On the other hand, PIK3CA mutated breast cancer patients frequently have tumour recurrence. ER^+ breast cancers acquire many other oncogenic alterations in Met and c-Myc during tumour progression, with c-Myc amplification linked to PI3K inhibitor resistance [14]. Therefore, a new clinical approach is required to improve the prognosis of heterogeneous breast cancer. In order to overcome PI3K inhibitor resistance in a subset of breast cancers, there are many ongoing clinical trials using PI3K inhibitors and combination drugs for the effective suppression of ER^+ breast cancers (Table 1-2).

Identifier	PI3K inhibitor	Combination drugs	Trial	PI3KCA	Patients (n)
NCT01790932	Buparlisib	Placebo	Phase 2	Wt	50
NCT01576666	Buparlisib	LDE225	Phase 1	Wt	120
NCT01816594	Buparlisib	Trastuzumab, Paclitaxel	Phase 2	Mutant	50
NCT01339442	Buparlisib	Fulvestrant	Phase 1	Mutant	31
NCT02404844	Buparlisib	Tamoxifen	Phase 2	Wt	48
NCT02088684	Buparlisib, Alpelisib	LEE011, Fulvestrant	Phase 1/Phase 2	Wt	70
NCT01219699	Alpelisib	Fulvestrant	Phase 1	Mutant	221
NCT01872260	Alpelisib	LEE011	Phase 1	Mutant	256
NCT02389842	Pictilisib	Palbociclib	Phase 1	Mutant	93
NCT01918306	Pictilisib	Cisplatin	Phase 1/Phase 2	Mutant	11
NCT02260661	AZD8835	Fulvestrant	Phase 1	Mutant	20
NCT02457910	Taselisib	Enzalutamide	Phase 1/Phase 2	Wt	73
NCT02340221	Taselisib	Fulvestrant	Phase 3	Mutant	631
NCT03439046	Alpelisib	Fulvestrant, Letrozole	Phase 3	Mutant	287
NCT02437318	Alpelisib	Fulvestrant	Phase 3	Wt	572
NCT01923168	Alpelisib	Buparlisib	Phase 2	Wt/Mutant	340
NCT01082068	XL147, XL765	Letrozole	Phase 1/Phase 2	Wt	78
NCT02273973	Taselisib	Letrozole	Phase 2	Mutant	334
NCT02738866	Palbociclib	Fulvestrant	Phase 2	Mutant	100
NCT01430585	PF-04691502	Letrozole	Phase 2	Wt	14
NCT02626507	Gedatolisib	Placebo	Phase 1	Wt	18

Table 1-2 Clinical trials of PI3K inhibitors in ER^+ breast cancer

1.2 Cancer cell metabolism

1.2.1 Inter-cellular metabolic heterogeneity

Proliferating and non-proliferating cells have different metabolic characteristics. The metabolism of proliferating cancer cells is characterized by aerobic glycolysis. In the 1920s, Otto Warburg first discovered the cancer cell-specific metabolic feature known as the Warburg effect. Differentiated cells mainly use glucose for mitochondrial tricarboxylic acid (TCA) cycle under sufficient oxygen supply. These cells in a hypoxic environment employ anaerobic glycolysis and produce lactate. Thus, the oxygen level is a key metabolic

regulator in differentiated and non-proliferating cells. In contrast, cancer cells mainly employ glycolysis in aerobic conditions (Figure 1-4). A key feature of aerobic glycolysis is the inefficient but fast energy production [27]. Cancer cells can overcome the disadvantage of inefficient ATP generation by uptake and consuming large amounts of glucose. High glucose consumption leads to high lactate production, resulting in an acidic micro-environment.

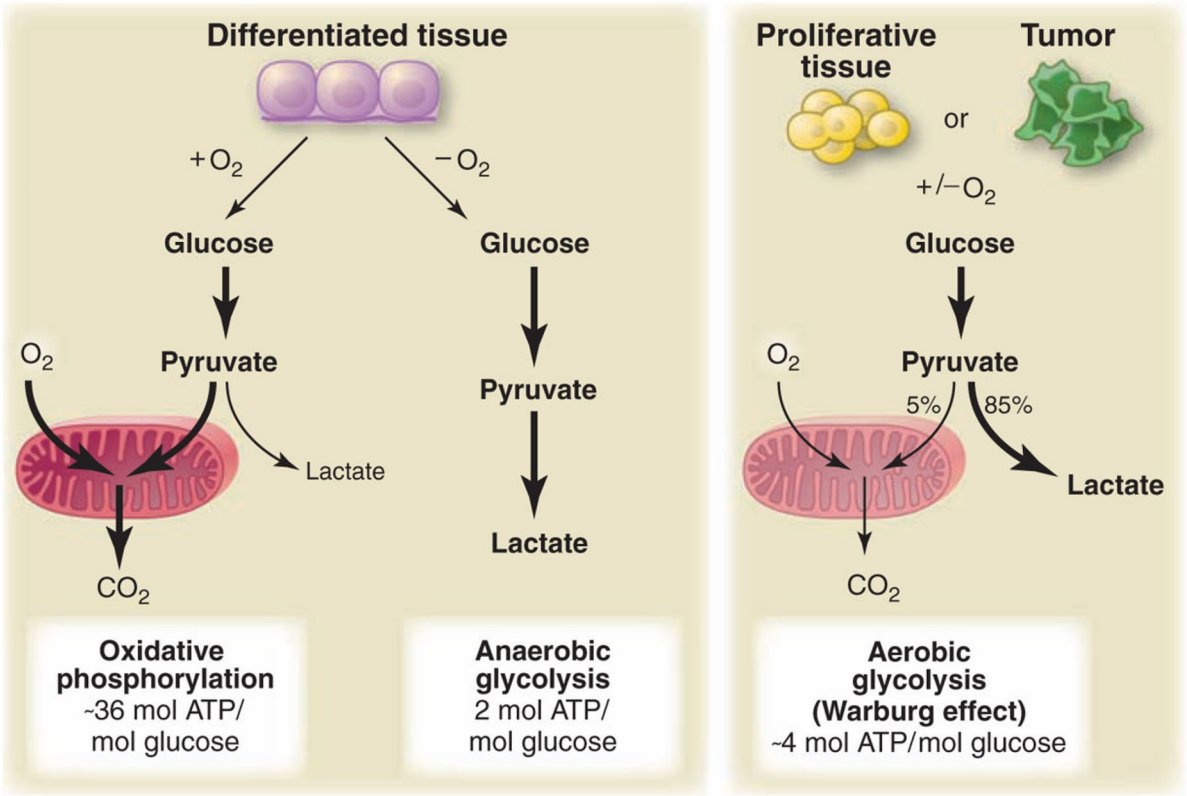


Figure 1-4 Metabolic strategies of differentiated and cancer cells.
Differentiated cells change the balance of metabolic pathways depending on oxygen concentration. In contrast, proliferating tissues and tumours highly utilize glycolysis in aerobic conditions (Warburg effect). The diagram is adapted from [28].

The recent consensus in the tumour metabolism field is that cancer cells engage in both glycolysis and OXPHOS to synthesize biomass and ATP for continuous proliferation. The balance of these different metabolic pathways can vary even among genetically homogeneous cells. In particular, the tumour microenvironment has gradients of nutrient, oxygen, and extracellular pH [29]. Cancer cells can adapt to complex microenvironments by metabolic alterations that extend beyond the Warburg effect [30-32]. These alterations further contribute to the establishment of metabolic heterogeneity of cancer cells.

1.2.2 Metabolic regulation

Cell metabolism has several routes such as glycolysis, glutaminolysis, glycogen metabolism, the TCA cycle, and the pentose phosphate pathway (PPP). One metabolic route can partially compensate another metabolic pathway because each metabolic pathway contributes to both ATP and biomass production. For instance, inhibition of glucose uptake leads to the enhancement of glutaminolysis, therefore inhibition of glucose transporters in the plasma membrane may not supress tumour growth. These metabolic shifts are very important for cancer cell proliferation and survival in different microenvironments. Metabolic reprogramming in response to the complex tumour microenvironment allows cancer cells to sustain higher proliferation.

The main mechanisms by which tumours change their metabolic states are altering the expression levels and post-transcriptional modifications of metabolic enzymes. There are several crucial metabolic regulators including HIF, PI3K/AKT/mTORC1 signalling, MYC, and p53 (Figure 1-5). In particular, IGFR1 is a crucial receptor which activates the PI3K/AKT signalling pathway. Phosphorylated AKT can transport GLUT to the plasma membrane and accelerate glucose uptake. In contrast, p53 negatively regulates glycolysis by inhibiting GLUT transport to the plasma membrane and expression of glycolytic enzymes [33]. In addition, AKT and MYC promote Glucose 6-phosphate (G6P) production from glucose by activating Hexokinase [34, 35]. G6P is a key intermediate of cell metabolism, this metabolite can be used for both energy and biomass production. Active AKT also promotes Fructose 1,6-bisphosphate (FBP) production from Fructose 6-phosphatate (F6P) by activating phosphofructokinase-1 (PFK-1). Aldolase A is also a critical enzyme to facilitate glycolysis, which can bind with filamentous actin (F-actin) [36]. Therefore, cell migration can regulate cell metabolism through actin cytoskeletal dynamics. AKT further induces MYC expression through mTORC1 activation [37]. MYC induction can accelerate glycolysis through activating pyruvate kinase and lactate dehydrogenase. Thus, PI3K/AKT signalling is a key regulator of cell metabolism. As I stated in chapter 1.1.2, breast cancer cell lines have genetic alterations in the PI3K signalling pathway which accelerate glycolytic cell metabolism and enhance tumour malignancy.

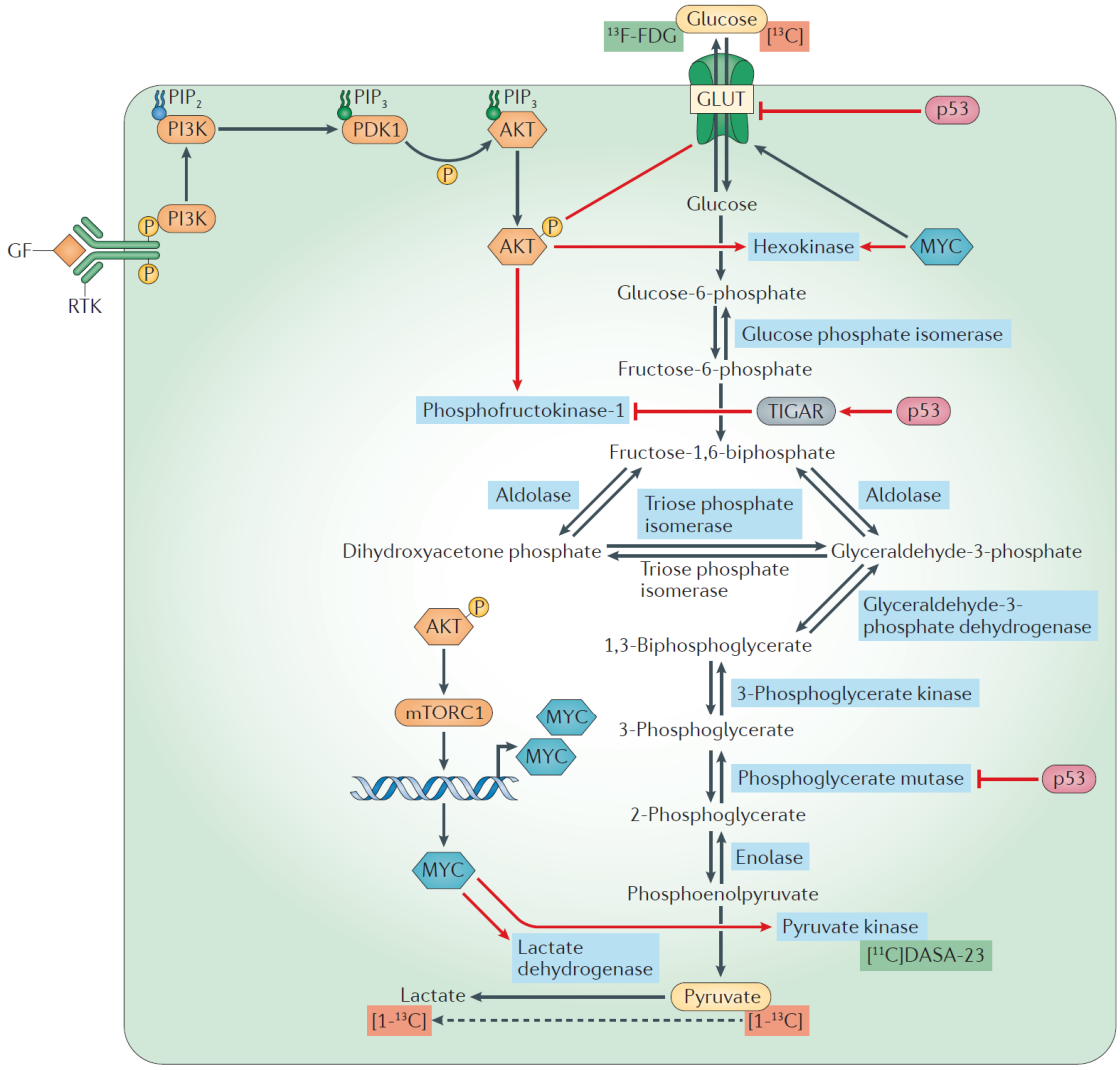


Figure 1-5 Oncogenic regulation of cancer cell metabolism.
Red arrows are the common oncogenic signalling pathways in cancer cell metabolism. PI3K/AKT signalling pathway and MYC promote and p53 inhibits glycolysis. PET tracers are highlighted in green, and MRS tracers in red. Glucose isotopes ^{18}F-FDG and ^{13}C-labelled glucose can be used for PET imaging and MRS in patients. The diagram is adapted from [38].

1.3 Tumour microenvironment

1.3.1 Non-cellular tumour microenvironmental factors

The tumour microenvironment consists of cellular and non-cellular components which contribute to cancer cell heterogeneity. The key non-cellular microenvironmental factors are nutrient accessibility, oxygen levels, extracellular pH, and ECM stiffness (Figure 1-6). In particular, nutrient accessibility and oxygen levels can vary depending on the distance from blood vessels. Vascularisation can accelerate aerobic metabolism by increasing the supply of nutrients and oxygen. Furthermore, blood flow removes cellular waste such as

lactate and helps to maintain a neutral extracellular pH. These microenvironmental conditions support sustainable tumour proliferation. In contrast, cancer cells in hypoxic areas have anaerobic metabolism. Hypoxia induces the expression of glycolytic enzymes mediated by hypoxia-inducible factor 1 (HIF-1) [28]. Anaerobic glucose metabolism such as that induced by HIF1α generates only 2 moles of ATP and NADH from a single molecule of glucose. The efficiency of energy production in anaerobic glycolysis is relatively lower than OXPHOS, anaerobic glycolysis helps to compensate for the lower ATP production. In addition, cancer cells in hypoxic regions can be supported by oxygenated cancer cells. Hypoxic cancer cells secrete large amounts of lactate using monocarboxylate transporter 4 (MCT4). Oxygenated cancer cells take in secreted lactate and use it as a fuel for mitochondrial metabolism [39]. In spite of lactate utilisation by oxygenated cancer cells, elevated lactate and proton production significantly reduce extracellular pH to a range of pH 5.8 to 7.0 in the tumour [40]. Thus, cancer cells reprogram their metabolism in order to survive and proliferate in different tumour microenvironments.

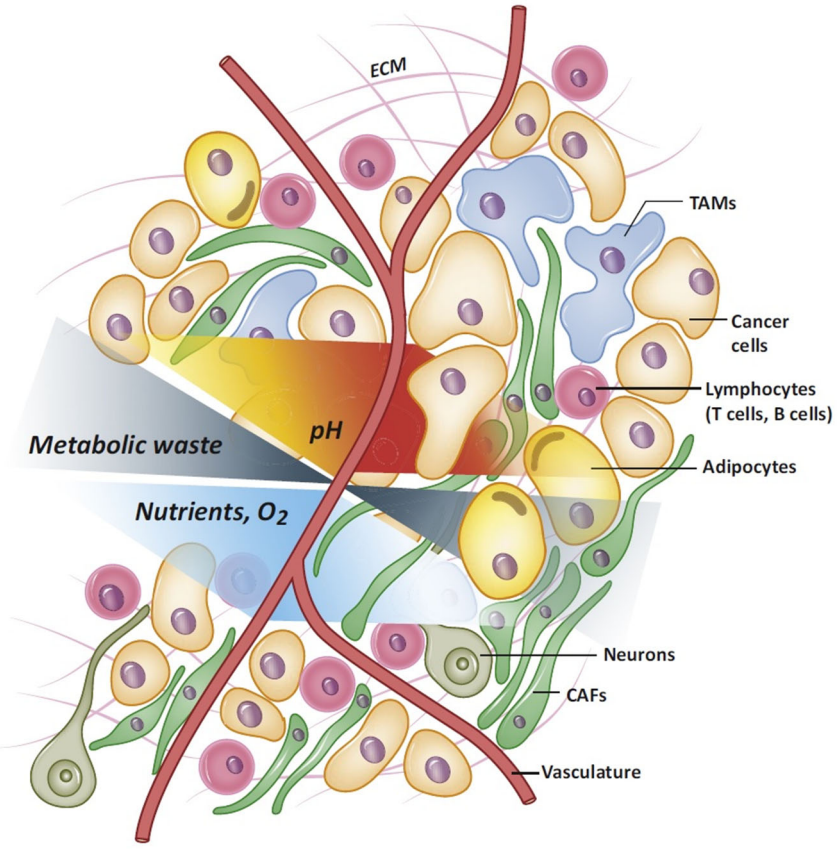


Figure 1-6 Tumour microenvironmental factors.
Complex tumour microenvironments with different nutrient accessibility, oxygen levels, metabolic waste concentration, extracellular pH, extracellular matrix (ECM) stiffness, and cellular populations. Tumour associated macrophages: TAMs. The diagram is adapted from [41].

1.3.2 Cancer Associated Fibroblasts (CAFs)

Cellular populations in the tumour microenvironment are also very important factors to regulate tumour heterogeneity. CAFs, adipocytes, macrophages, and immune cells can interact with cancer cells and change cancer cell characteristics. CAFs are the most abundant cellular component of the tumour stroma and a key modifier of cancer progression [42]. In addition to cancer cells, CAFs also have high heterogeneity possibly because of their wide variety of origin. Many cell types such as resident fibroblasts, adipocytes, and stem cells can transform into CAFs [43]. Many factors secreted by cancer cells, such as transforming growth factor β (TGF-β), can activate normal fibroblasts and induce CAFs. Because CAFs are derived from several different types of cells, characteristics of CAFs are different depending on the activation processes [44]. For example, conditioned medium (CM) of MCF-7 cells and MDA-MB-231 cells can induce a CAF-like phenotype in human adipose tissue-driven stem cells (hASCs) [45]. CM from CAFs also significantly promotes proliferation of MCF-7 cells by increasing 17β-estrodiol dehydrogenase (E2DH) activity [46]. Thus, cancer cells and CAFs have a reciprocal relationship in tumour microenvironmental adaptation and continuous proliferation.

Another crucial role of established CAFs in tumour microenvironments is secretion of ECM components such as collagen type1 and Matrix metalloproteinases (MMPs). These ECM components can form connective tissue networks and facilitate tumour growth and malignancy [47]. In mouse models, subcutaneous co-injection of MCF-7 cells and CAFs exhibits faster tumour development compared with the injection without CAFs [48]. In addition, collagen type 1 secretion from CAFs inhibits chemotherapeutic drug uptake in breast cancer [49].

CAFs have a great impact on tumour characteristics through remodelling gene expression and cell metabolism. CAFs secrete alanine [50], glutamine [51], and cysteine [52] which are consumed by cancer cells (Figure 1-7). In addition, exosomes secreted by CAFs can remodel cancer cell phenotype by altering gene expression [53, 54]. Cancer cells also secrete lactate [55], glutamate [51], and citrulline [56] which are consumed by the surrounding cells. CAFs and cancer cells have a reciprocal relationship to facilitate proliferation because the effect of cellular communication is bidirectional. CAFs and other types of cells such as effector T (Teff) cells and adipocytes can exchange metabolites with cancer cells [50, 51, 57, 58]. Therefore, targeting CAFs in cancer therapy may be important for effective tumour suppression.

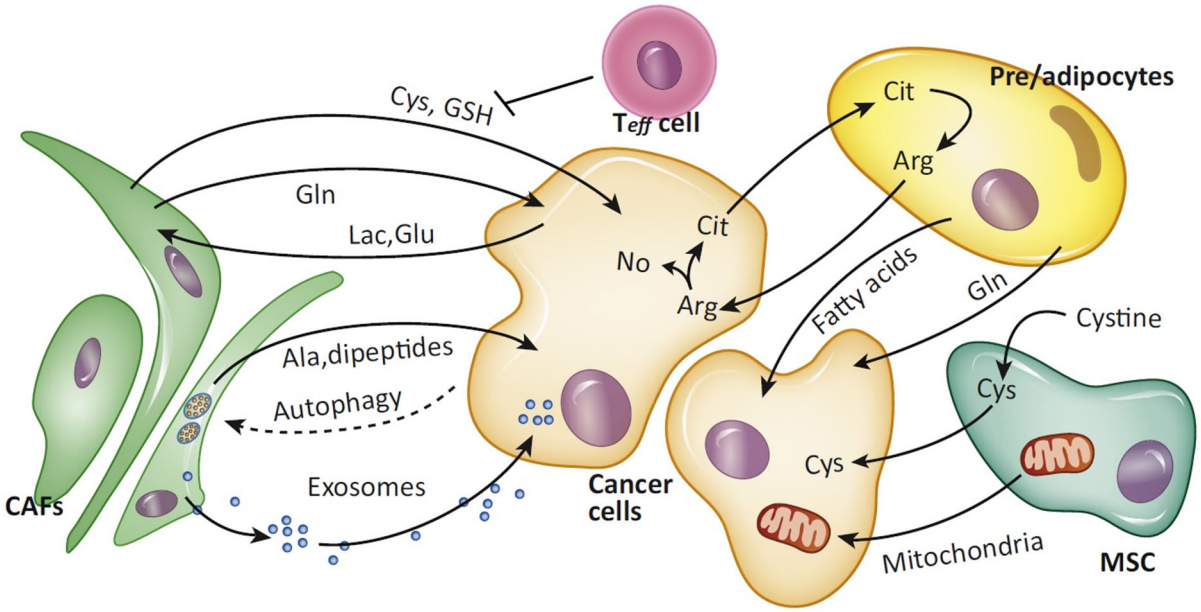


Figure 1-7 Nutrient exchange among different types of cells.
The tumour microenvironment consists of heterogeneous cancer cells, CAFs, adipocytes, macrophages, and immune cells. Their metabolism and nutrient requirements are different, cancer cells exchange nutrients with other cell types. Alanine: Ala, Arginine: Arg, Citrulline: Cit, Cysteine: Cys, Glutamine: Gln, Glutamate: Glu, Glutathione: GSH, Lactate: Lac, Nitric oxide: NO. The diagram is adapted from [41].

In addition to metabolite exchange among different types of cells, CAFs can also induce Tamoxifen resistance in endocrine therapy. For instance, co-culture of MCF7 cells and CAFs can promote mitochondrial activity and increase resistance to Tamoxifen and Fulvestrant by 4.4-fold and 2.5-fold, respectively [59]. The mechanism of acquiring resistance to Tamoxifen includes that CAFs promote mitochondrial activity of cancer cells by providing lactate and ketones as a fuel of OXPHOS. Therefore, Tamoxifen-resistant cancer cells are re-sensitised by mitochondrial inhibitors such as metformin.

1.4 Epigenetic regulation of gene expression

1.4.1 Epigenetic modifications

Epigenetic regulators and transcription factors are frequently mutated in breast cancer. Epigenetic alterations can drive tumour initiation, progression, and therapeutic response. During tumour progression, cancer cells acquire epigenetic alterations which are closely linked with tumour heterogeneity. In particular, specific covalent modifications of chromatin components including DNA methylation, histone methylation and acetylation of particular regions can remodel gene expression (Figure 1-8). The structure of chromatin consists of

nucleosomes which have 147 bp of DNA and 8 histone components [60]. Epigenetic modifications dictate chromatin accessibility, and in many cases are inheritable non-genetic cancer cell characteristics [61]. DNA methylation is a highly stable epigenetic modification because DNA methylation is a covalent modification of genetic material. These established DNA methylation patterns can be copied during DNA replication. DNA methylation patterns found in the cancer cells often reflect the modification patterns of cell origins. The metastasized cancer cells might have similar DNA methylation patterns to the primary tumour. Thus, DNA methylation is a stable and inheritable epigenetic mechanism of regulating gene expression. DNA methylation states can work as a long-term memory for the cells and DNA methylation represents a sophisticated mechanism of regulation of gene expression. In contrast to covalent modification of DNA, methyl and acetyl groups on histone are not permanent modifications because of histone turnover. In addition, histone modifications are gradually changed by different tumour microenvironments. Modification patterns of histones are written in different conditions by nutrient accessibility and oxygen concentrations. Histone methylation and acetylation states are profoundly affected by the microenvironment. The stability of epigenetic modifications are key to improve our understanding of heterogeneous cancer cell characteristics.

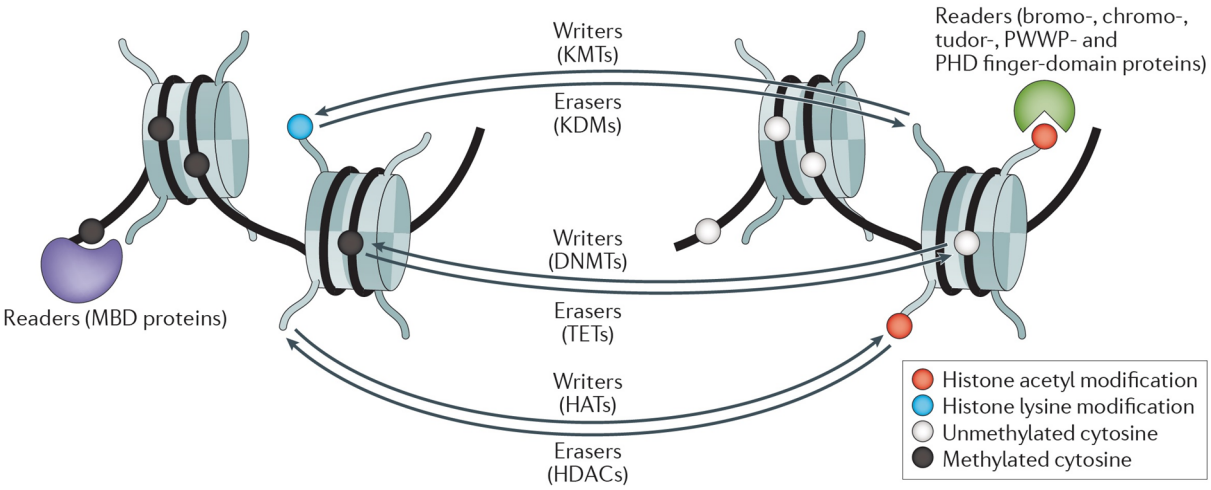


Figure 1-8 Covalent modification of DNA and histones.
Chromatin is covalently modified by DNA methylation, histone methylation, and histone acetylation. Writers and erasers of these covalent modifications generate heterogeneous modification patterns and gene expression. Lysine methyltransferases: KMTs, Lysine demethylases: KDMs, DNA methyltransferases: DNMTs, Ten-eleven translocations: TETs, Histone acetyltransferases: HATs, Histone Deacetylases: HDACs, Methyl-CpG-binding domain: MBD. The diagram is adapted from [62].

1.4.2 DNA methylation

Cancer cells acquire DNA methylation during progression. The key characteristics of DNA methylation in cancer cells are hyper-methylation in promoter regions [63, 64]. DNA methyltransferases (DNMT1, DNMT3A, DNMT3B) and demethylases (TET1, TET2, TET3) regulate DNA methylation levels and these enzymes can establish specific DNA methylation patterns. In particular, excessively methylated cytosine nucleotides in CpG islands in promoter regions have a crucial role in carcinogenesis by silencing tumour suppressor genes [65, 66]. In addition, hypo-methylation promotes chromosomal instability and activation of oncogenes. Thus, modifications of DNA methylation regulate tumour proliferation. In addition, microenvironmental factors can regulate DNA methylation. For example, oxygen stress regulates the recruitment of DNA methyltransferases to specific genes [67]. Nutrient accessibility in the tumour microenvironment can be an important regulator of DNA methylation. Methionine is a major donor of methyl groups and the depletion of methionine decreases DNA methylation levels [68].

1.4.3 Histone methylation

As I stated in chapter 1.4.2, methionine is a major donor for methylation. Methionine is converted to S-adenosylmethionine (SAM) and histone methyltransferase (HMT) utilizes this metabolite for histone methylation especially at H3K4, H3K9, H3K27, H3K36, H3K79, and H4K20. Among them, tri-methylation of lysine-9, -27, and -20 suppresses transcription and methylation of lysine-4, -36, and -79 promotes transcription [69]. Therefore, histone methylation patterns as well as histone methylation levels regulate gene expression. For example, low histone methylation of H3K4 reduces gene expression levels of AKT1, MYC, and MAPK [70]. High methylation levels of H3K4 were found in human breast cancers [71]. H3K4 de-methylase KDM5A is a target of AKT and phosphorylated KDM5A down-regulates its activity [72]. Therefore, PI3K/AKT signalling increases methylation levels of H3K4 and maintains high expression levels of AKT1. On the other hand, MYC amplification suppresses PI3K/AKT signalling pathway through up-regulation of PTEN [73]. MYC can promote H3K27 methylation by inactivating the PI3K/AKT signalling pathway because AKT inactivates Enhancer of Zeste homolog 2 (Ezh2), a methyltransferase of H3K27. Thus MYC and PI3K signalling can establish specific histone methylation patterns. The methionine salvage cycle and folate metabolism can also supply methionine for histone

methylation, defects in these metabolic pathways increases cancer cell dependence of extracellular methionine [74, 75]. Individual cancer cells have different nutrient accessibility and oxygen levels depending on the intra-tumoural location. For example, glucose and glutamine levels are extremely low in the core of solid tumours compared with the periphery [76]. Cancer cell metabolism and different tumour microenvironments can establish heterogeneous histone methylation patterns, gene expression, and cancer cell characteristics.

1.4.4 Histone acetylation

Nucleosomes have dynamic and reversible acetylation processes in all four histones. Histone acetylation can remodel chromatin structure and accelerate gene expression, cell metabolism, and therapeutic resistance [77]. Perturbation of histone acetylation patterns is influenced by the activity of histone acetyltransferases (HATs) and histone deacetylases (HDACs). These enzymes regulate the transfer of acetyl groups from Acetyl-CoA to lysine residues in histones. Therefore, Acetyl-CoA synthesis is a key metabolic pathway to supply acetyl groups for histone acetylation. Intracellular Acetyl-CoA levels can fluctuate according to diet, microenvironment, and PI3K/AKT signalling [78, 79]. Increased glucose concentration in the extracellular microenvironment can induce high histone acetylation, and glucose starvation decreases histone acetylation levels because glucose is a key nutrient source of Acetyl-CoA [80-82]. Through glucose metabolism, glucose is converted to pyruvate and then transported into mitochondria. Glucose-derived citrate is exported from the mitochondria and ATP citrate lyase (ACLY) converts it to Acetyl-CoA in the cytoplasm [83]. In particular, PI3K/AKT signalling can promote Acetyl-CoA production and histone acetylation through ACLY activation [78]. In addition to glucose, some other metabolites including glutamine, acetate, and fatty acids are used for histone acetylation [84, 85]. In most cases, production of nuclear and cytoplasmic Acetyl-CoA depends on export of citrate from the mitochondria. Therefore, histone acetylation may be very sensitive to nutrient accessibility and manipulation of nutrient levels could remodel histone acetylation levels [78]. Thus, PI3K/AKT signalling and nutrient accessibility are key regulators of histone acetylation patterns.

1.5 Fluorescence imaging

1.5.1 Fluorescence microscopy

Since the development of fluorescence microscopy, demands to visualise biological structures, protein localisations, and kinase activities in live cells have been increasing. Immunofluorescence imaging has been used for the analysis of intracellular protein localisation and its modification including phosphorylation, acetylation, and methylation in fixed cells using antibodies. In Immunofluorescence imaging, primary antibodies detect target proteins and its modification. Fluorescence-labelled secondary antibodies can visualise their localization in cells. The development of fluorescent dyes has had a great impact on cancer research because fluorescent dyes can analyse live cells at the single cell scale. For example, the fluorescence-labelled glucose analog, 2-NBDG, can measure glucose uptake speed. In addition, TMRE and CellRox can measure mitochondrial membrane potential and intracellular ROS levels, respectively. TMRE can measure mitochondrial membrane potential because it has an ester group to facilitate mitochondrial membrane permeability. Further advantages in live cell imaging have been established by the discovery of fluorescent proteins. Green fluorescent protein (GFP) was purified from jellyfish *Auquorea Victoria* in 1962 and many new variants were developed based on GFP. Fluorescent proteins have been used for tracking protein localisation in live cells. Kinetic microscopy techniques such as fluorescence recovery after photobleaching (FRAP), fluorescence loss in photobleaching (FLIP), and photo-activation were developed for the investigations of protein tracking and dynamics (Figure 1-9). In FRAP, the fluorophore in selected regions of the cell is bleached and the kinetics of molecular diffusion are quantified by measuring fluorescence recovery. In FLIP, the fluorophore in the selected region of the cell is repeatedly bleached and the kinetics of molecular diffusion are quantified by measuring fluorescence decay. In photo-activation, photo-activatable fluorophores in the selected region of cells are activated and fluorescence diffusion throughout the cells are quantified by measuring fluorescence intensity. In addition to the analysis of protein localisation and diffusion by live cell imaging, the first genetically-encoded FRET biosensor was developed in 1997 [86].

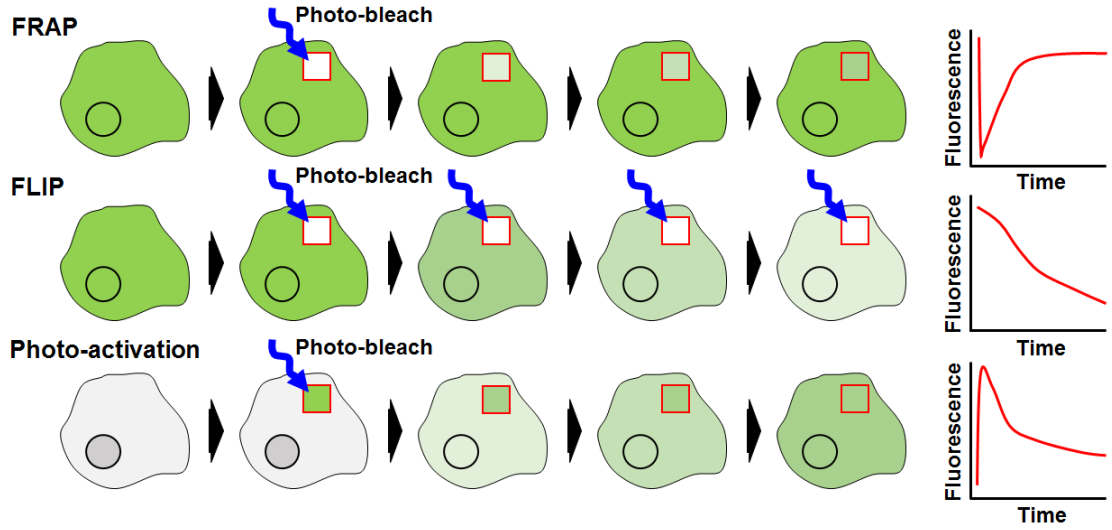


Figure 1-9 Kinetic microscopy techniques.
Schematic representation of FRAP, FLIP, and photo-activation for tracking protein diffusion in live cells.

1.5.2 Fluorescence resonance energy transfer (FRET)

The mechanism of FRET is based on the process of excitation by photon absorption and its de-excitation by another photon emission. These processes are well described by Jablonski diagram (Figure 1-10A). The fluorescent protein is excited by photon absorption which transits the electronic energy state from ground singlet state (S_0) to excited singlet state (S_1). Excitation energy is represented by excitation (hv_1), electric state is subdivided into vibrational and rotational states. However, the emission spectrum is independent from hv_1 and electronic energy state shift to S_1 by thermal relaxation. The fluorescent protein then releases the energy by emission (hv_2) or non-radiative relaxation.

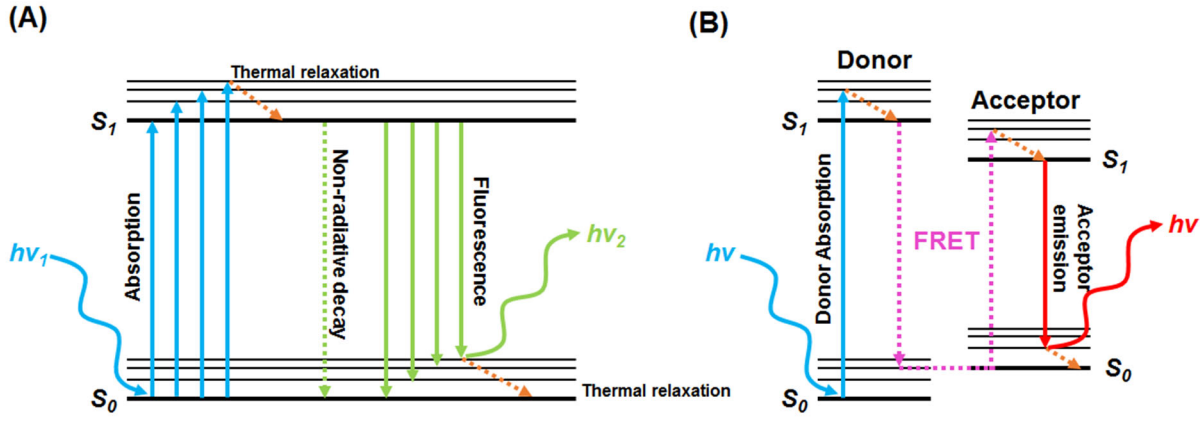


Figure 1-10 Mechanism of fluorescence excitation and emission.
(A) A fluorophore is excited and the electronic energy state shifts from ground singlet state (S_0) to excited singlet state (S_1). The longer arrows are the more energetic transitions. (B) The electronic energy of the donor fluorophore transfers to the acceptor fluorophore in FRET.

In FRET, energy can transfer from donor to acceptor fluorescent protein (Figure 1-10B). The electronic energy of the donor fluorophore can only transfer to the acceptor fluorophore in specific conditions. First, the emission spectrum of the donor fluorescent protein must overlap with the absorption spectrum of the acceptor fluorescent protein. The fluorescence emission of the donor excites the acceptor in the overlapping spectrum (Figure 1-11A). Next, the donor fluorescent protein must orient in parallel with the acceptor fluorescent protein (Figure 1-11B, C). If the angle of the donor and the acceptor is in a perpendicular orientation, the energy of the donor cannot transfer to the acceptor. In addition, the distance between the donor and the acceptor must be close enough, the typical distance is 10 nm. Sensitivity of FRET biosensors are different because these conditions are different. FRET biosensors change conformational structure by binding with molecules and due to modifications such as phosphorylation. Therefore, FRET ratio shifts depending on the molecular concentrations or kinase activities. Thus, FRET biosensors can read out cellular information at the single cell scale. The FRET ratio can be calculated by the spectral ratiometric measurement. In this approach, the ratio of acceptor intensity divided by donor intensity is calculated as FRET ratio. In the intensity measurement of two spectral channels in FRET, the intensity of the donor fluorescent protein declines and the acceptor fluorescent protein increases the emission intensity.

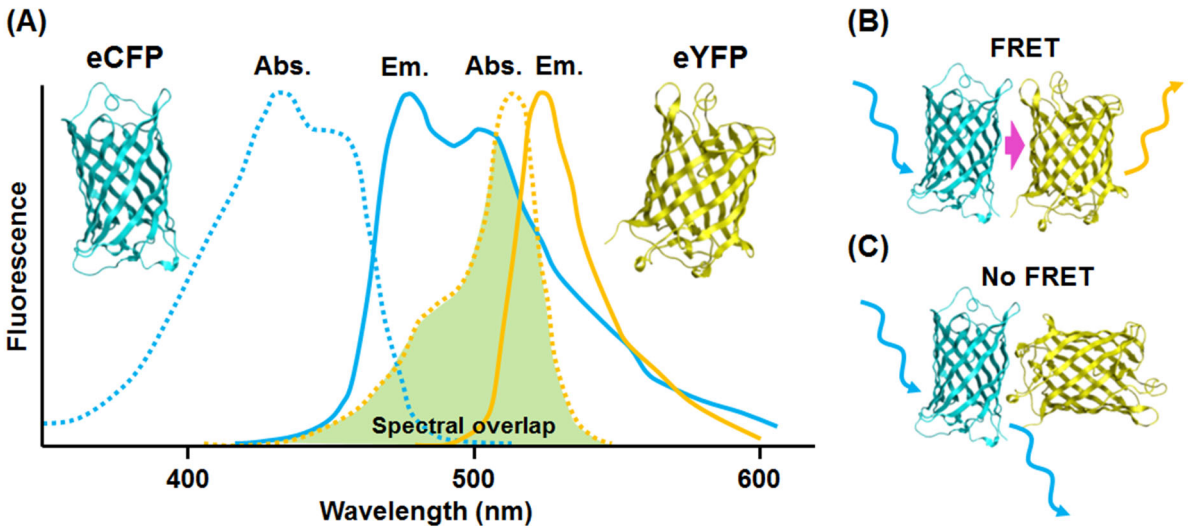


Figure 1-11 FRET mechanism.
(A) Fluorescence spectrum of eCFP (donor) and eYFP (acceptor). The emission spectra of eCFP overlaps with the absorption spectra of eYFP (green area). (B) eCFP and eYFP aligned in parallel, the electric energy of eCFP can transfer to eYFP. (C) eCFP aligned perpendicular to eYFP, the electric energy of eCFP cannot transfer to eYFP.

The genetically-encoded FRET biosensor has rapidly developed in the recent two decades in order to analyse signalling pathways and metabolism at single cell resolution. FRET biosensors employ several mechanisms to change conformational structure by molecular events. Among them, inter- and intra-molecular FRET-based biosensors are widespread FRET technology (Figure 1-12A, B). Both FRET-based biosensors increase FRET ratio by binding of the sensory domain with a substrate. FRET-based biosensors in my research employ inter-molecular FRET technology. A key advantage of imaging cancer cell metabolism using FRET-based biosensors is the ability to perform metabolic measurements with spatiotemporal resolution. However, FRET imaging is limited in its capacity to read out multiple different types of information from single cells. In order to solve this problem, FRET biosensors with different fluorophore combinations have been developed for multiplexed imaging. Simultaneous imaging of two different FRET sensors can analyse multiple different types of information at the single cell scale.

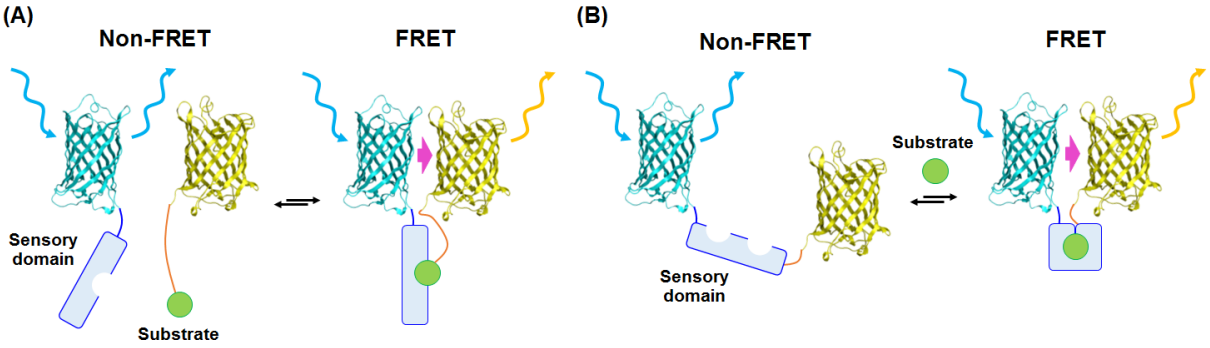


Figure 1-12 The mechanisms of FRET-based biosensors.
(A) Intramolecular FRET-based biosensor. Two independent fluorescent proteins can reduce distances by binding events. (B) Intermolecular FRET-based biosensor. FRET biosensor changes conformational structure by binding with a substrate.

Ratiometric FRET is an ideal approach to analyse intracellular protein interactions, ion levels, and second messenger levels in live cells with spatiotemporal resolution. However, this imaging approach has technical problems such as photostability, and different fluorescence tissue penetration between the donor and acceptor fluorescence proteins. The photostability of fluorescent proteins could be associated with the possible number of excitation-emission cycles. The expected average number of this cycle is 10,000 -100,000 and fluorescent proteins are irreversibly degraded by repeating this cycle. In addition, the FRET ratio is higher at deep sections of the specimen because longer emission wavelength has better tissue penetration. In order to avoid these risks of FRET inaccuracy, fluorescence lifetime imaging microscopy of FRET biosensors has been used, especially for *in vivo* imaging.

1.5.3 Fluorescence lifetime imaging microscopy (FLIM)

The excited fluorescent proteins emit fluorescence and the fluorescence intensity homogeneously and exponentially decays to the ground state. Fluorescence lifetime (τ) is the average time to keep the excited singlet state as defined in the following equation.

$$\tau = \frac{1}{K_\gamma + K_{n\gamma}}$$

Each fluorescent protein has their original radiative decay rate ($K\gamma$) but non-radiative decay rate ($Kn\gamma$) is mostly affected by microenvironmental factors including viscosity, temperature, and pH [87-89]. In addition, exponential fluorescence decay time $I(t)$ is defined in the following equation.

$$I(t) = I_o e^{\frac{-t}{\tau}}$$

In this equation, fluorescence decay time $I(t)$ is the time to decrease the fluorescence intensity by e^{-1} or about 36.8% of initial value (I_0). Fluorescence lifetime can be measured by time-domain and frequency-domain techniques. Frequency-domain FLIM demodulates fluorescence signals followed by the excitation. Fluorescence lifetime is calculated by the comparison between fluorescence signals with a standard such as a fluororesin which has a fluorescence lifetime of 4.0 ns. In contrast, time-domain FLIM records fluorescence signals in time following excitation by pulsed laser. Time-correlated single-photon counting (TCSPS) records individual photons in each arrival time after a short optical pulse (Figure 1-13). Because TCSPS commonly employs the laser scanning fluorescence lifetime imaging microscope, it is possible to measure fluorescence lifetime decay in each pixel. On the other hand, longer acquisition time due to single pixel scanning and low count rates are the main limitation of this imaging technology.

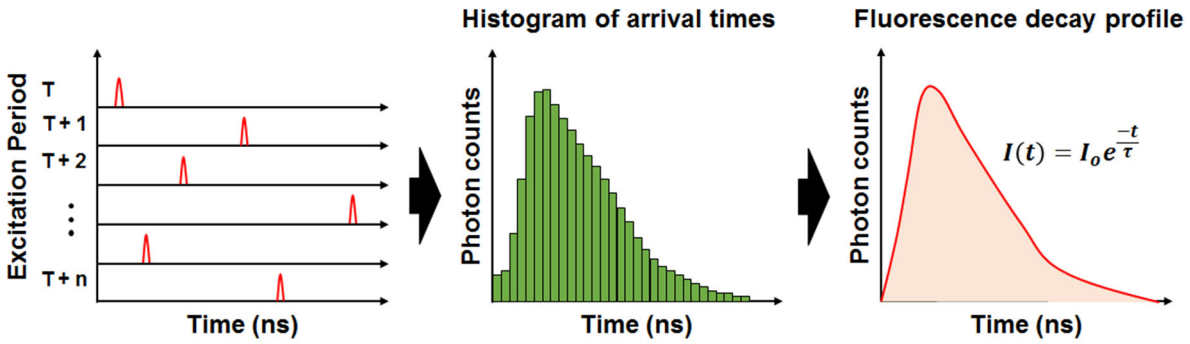


Figure 1-13 Principle of TCSPC-based fluorescence lifetime measurement.
The laser pulse excites the fluorophore and detects photons at each arrival time. Several hundreds of photons are counted in each arrival time and build a histogram. Fluorescence decay reflects this histogram.

1.5.4 FRET and FLIM applications in tumour cell biology

Since the establishment of the first FRET biosensor, a wide variety of genetically encoded FRET biosensors have been generated to analyse intracellular protein-protein interactions, intracellular ion levels, second messenger levels, metabolite levels, small GTPase activities, and kinase activities [86, 90]. Among them, the ERK FRET biosensor is widely used in the research of cell signalling. The ERK FRET biosensor revealed that ERK activity can spread towards the neighbouring cells and support cell proliferation [91, 92]. In addition, the mechanism of BRAF inhibitor failure in melanoma cells *in vivo* was clarified using the ERK FRET biosensor [93]. Thus, FRET biosensors can read out spatiotemporal information. Measurement of fluorescence lifetime of the donor fluorophore of FRET biosensors can quantify the FRET efficiency. In FLIM-FRET, the fluorescence lifetime of the donor fluorophore with FRET (τ_{DA}) and without FRET (τ_D) are defined in the following equation. In FRET state, the donor fluorophore of FRET biosensor always has shorter fluorescence lifetime.

$$\tau_D = \frac{1}{K_\gamma + K_{n\gamma}}$$

$$\tau_{DA} = \frac{1}{K_\gamma + K_{nr} + K_{FRET}}$$

In addition to FLIM-FRET, label free autofluorescence lifetime imaging has been studied as an attractive non-invasive approach to acquire cellular information. Nicotinamide adenine dinucleotide (NADH) and nicotinamide adenine dinucleotide phosphate (NADPH)

are reducing agents involved in many bio-synthetic reactions. These electron carriers have autofluorescence in a reduced state and they can serve as informative biomarkers for cell metabolism [94]. NAD(P)H has protein-bound and protein-unbound forms which have unique fluorescence lifetime [95]. There are many factors such as the mitochondrial respiration chain and glycolytic enzymes which can influence NAD(P)H, fluorescence lifetime of NAD(P)H represents the relative rates of glycolysis and OXPHOS [95-97]. Recent researches have employed fluorescence lifetime imaging of NAD(P)H auto-fluorescence for *in vivo* analysis of cell metabolism [98]. Intravital imaging of NAD(P)H fluorescence lifetime has further found that circadian rhythm in live mice regulates the balance of glycolysis and OXPHOS [99]. Taken together, FRET and FLIM are the ideal analysis tools for visualising small molecules and enzyme activities in live cells.

Chapter 2. Materials & Methods

2.1 Cell culture and transfection

2.1.1 Cell culture

Human breast cancer cell lines were cultured in Dulbecco's modified Eagle medium (DMEM) with 10% fetal bovine serum (FBS) and 1% Penicillin Streptomycin (Pen Strep) at 37 °C in 5% CO_2. Human breast cancer-associated fibroblast cell line 1255T IDC was cultured in DMEM with 10% FBS, 1% Insulin-Transferrin-Selenium (ITS), and 1% Pen Strep at 37 °C in 5% CO_2. Cell Services in the Francis Crick institute screened T47D, MCF-7, ZR-75-1, JimT-1, MDA-MB-231, and 1255T IDC cells for mycoplasma. 24 hours before experiments, the cells were detached from cell culture dishes by 0.1% trypsin (Thermo Fisher Scientific) and 0.02% versene solution (Thermo Fisher Scientific). Cells were plated on glass bottom dishes at 1 x 10^4 cells / cm^2 and media was changed to phenol red free DMEM with 10% FBS at 3 hours before imaging.

Components	Concentration (mg/L)	Concentration (mM)
Amino Acids		
Glycine	30	0.4
L-Arginine hydrochloride	84	0.39810428
L-Cystine 2HCl	63	0.20127796
L-Glutamine	580	3.9726028
L-Histidine hydrochloride-H2O	42	0.2
L-Isoleucine	105	0.8015267
L-Leucine	105	0.8015267
L-Lysine hydrochloride	146	0.7978142
L-Methionine	30	0.20134228
L-Phenylalanine	66	0.4
L-Serine	42	0.4
L-Threonine	95	0.79831934
L-Tryptophan	16	0.078431375
L-Tyrosine	72	0.39779004
L-Valine	94	0.8034188
Vitamins		
Choline chloride	4	0.028571429
Niacinamide	4	0.032786883
Pyridoxine hydrochloride	4	0.019417476
Thiamine hydrochloride	4	0.011869436
i-Inositol	7.2	0.04
Inorganic Salts		
Calcium Chloride	264	1.7959183
Magnesium Sulfate	200	0.8130081
Potassium Chloride	400	5.3333335
Sodium Bicarbonate	3700	44.04762
Sodium Chloride	6400	110.344826
Sodium Phosphate monobasic	141	0.91558444
Other Components		
D-Glucose	4500	25

Table 2-1 DMEM formulation

Components	Concentration
Total Protein	3.7 g/dL
Glucose	151 mg/dL
Calcium	14.40 mg/dL
Sodium	140 MMOL/L
Potassium	13.50 MMOL/L
Bicarbonate	14.0 MMOL/L
Chloride	96 MMOL/L
Cholesterol	25 mg/dL
Creatinine	2.90 mg/dL
Blood Urea Nitrogen (BUN)	14 mg/dL
Uric Acid	3.30 mg/dL
Hormone Profile: Estradiol	27.80 pg/mL
Hormone Profile: Insulin	8.21 uIU/mL
Hormone Profile: Progesterone	<0.05 ng/mL
Hormone Profile: Testosterone	<0.10 ng/mL
Hormone Profile: Thyroxine (T4)	10.10 ug/dL
Lactic Dehydrogenase (LDH)	699 u/L
Low Density Lipoproteins (LDL)	0.0 mg/dL
High Density Lipoproteins (HDL)	10 mg/dL
Phosphorous (Inorganic)	10.40 mg/dL
pH	7.2

Table 2-2 FBS formulation

2.1.2 Lipofectamine 2000 transfection

For measuring intracellular metabolite levels in breast cancer cell lines, FRET biosensors were stably expressed using the PiggyBac transposon system. A day before the transfection, breast cancer cells were plated on 60 mm dishes at 5 x 10^4 cells / cm^2. For one 60 mm dish, a total of 5 µg DNA and 10 µl of Lipofectamine 2000 reagent (Thermo Fisher Scientific) were diluted in 500 µl of Opti-MEM medium. These two solutions were mixed and incubated for 20 minutes at room temperature. Culture media was changed from DMEM to Opti-MEM and then the cells were incubated with the transfection complex for 3 hours. After incubation, cells were washed with PBS and cultured in DMEM with 10% FBS. After selection of FRET biosensor expressing cells using puromycin, cells were sorted by BD fluorescence-activated cell sorting (FACS) Aria™ III. The cells were excited by 405 nm and 488 nm for cyan and yellow fluorescent proteins. Fluorescence of these two fluorescent proteins was detected using 450/50 nm and 525/50 nm band pass filters.

2.1.3 X-tremeGENE™ HP DNA Transfection

A day before transfection, breast cancer cells were plated on 60 mm dishes at 5 x 10^4 cells / cm^2. For one 60 mm dish, a total of 5 µg DNA and 20 µl of X-tremeGENE™ HP DNA Transfection Reagent (Sigma-Aldrich) was diluted in 500 µl of Opti-MEM medium. These two solutions were mixed and incubated for 15 minutes at room temperature. The cells were incubated with the transfection complex without changing media. After puromycin selection, FRET biosensor expressing cells were sorted by FACS as described above.

2.2 Plasmids and DNA maps

2.2.1 Plasmids

FRET biosensors in the PiggyBac transposon vector were cloned from Glucose FRET biosensor (Addgene, 17866) [100], Pyruvate FRET biosensor (Addgene, 51308) [101], Lactate FRET biosensor (Addgene, 44238) [102], and ATP FRET biosensor (Addgene, 51958) [103]. The glucose FRET biosensor was amplified using “Glucose Biosensor For.” and “Glucose Biosensor Rev.” primers (Table 2-3). The pyruvate FRET biosensor was amplified using “Pyruvate Biosensor For.” and “Pyruvate Biosensor Rev.” primers. The

lactate FRET biosensor was amplified using “Lactate Biosensor For.” and “Lactate Biosensor Rev.” primers. The ATP FRET biosensor was amplified using “ATP Biosensor For.” and “ATP Biosensor Rev.” primers. In transposition of the FRET biosensor into genomic DNA, the piggyBac transposase cuts out transposon-specific inverted terminal repeat sequences (ITRs) and the FRET biosensor from the transposon vector (Figure 2-1). This FRET biosensor is then randomly integrated into TTAA genetic locations.

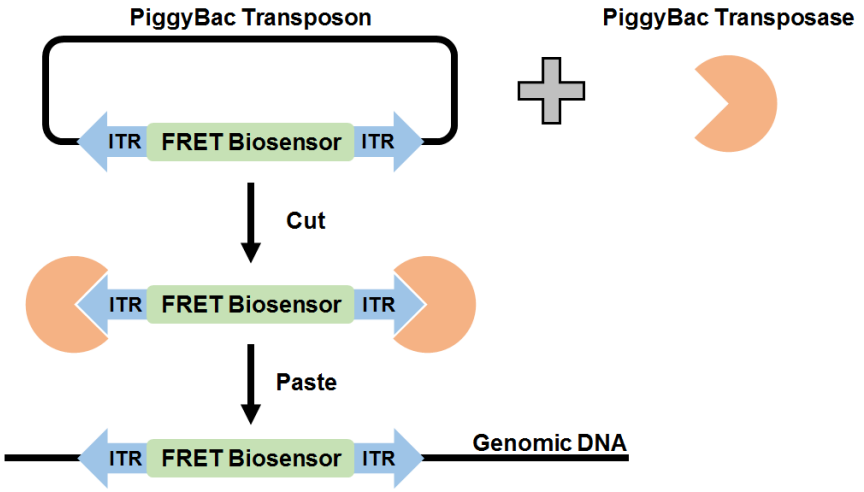


Figure 2-1 Mechanism of PiggyBac transposon system.
The piggyBac transposase recognises and cuts out transposon-specific ITRs and FRET biosensor from the transposon vector. The FRET biosensor is then randomly integrated into genetic DNA.

D183A point mutation in the glucose FRET biosensor was generated by site-directed mutagenesis kit (NEB). The glucose FRET biosensor with mTurquoise2-sReACh combination was constructed using a series of primers (Figure 2-2). Amplified DNA fragments were joined using Gibson Assembly (NEB). QIAfilter Plasmid Maxi kit (Qiagen) was used for plasmid DNA purification and DNA concentration was measured by the Nanodrop Spectrophotometer (Nanodrop) at 260 nm absorbance.

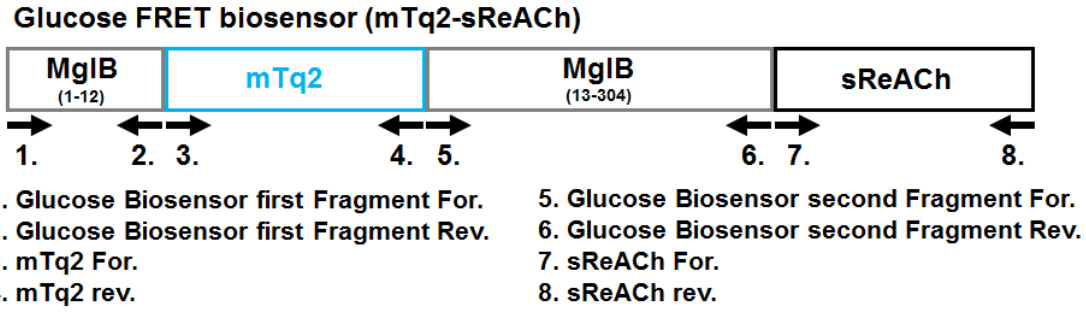


Figure 2-2 Cloning of the glucose FRET biosensor
The glucose FRET biosensor with mTurquoise2-sReACh combination was constructed using eight different primers.

2.2.2 Gibson Assembly

Gibson Assembly is a new technology to assemble multiple DNA fragments using three different enzymes. For primer designing, the forward primers including restriction enzyme site has a "G" nucleotide inserted between the overlap and the N-terminal sequence of the gene to ensure the gene is in the frame. DNA fragments of the glucose FRET biosensor with overlapping ends (15 - 25 nt) were mixed with Gibson Assembly Master Mix (Figure 2-3). Endonuclease chewed back 5' end and created single-stranded 3´ overhangs. These DNA fragments were annealed and then DNA polymerase filled in gaps within each annealed DNA fragment. Finally, DNA ligase sealed nicks in the assembled DNA.

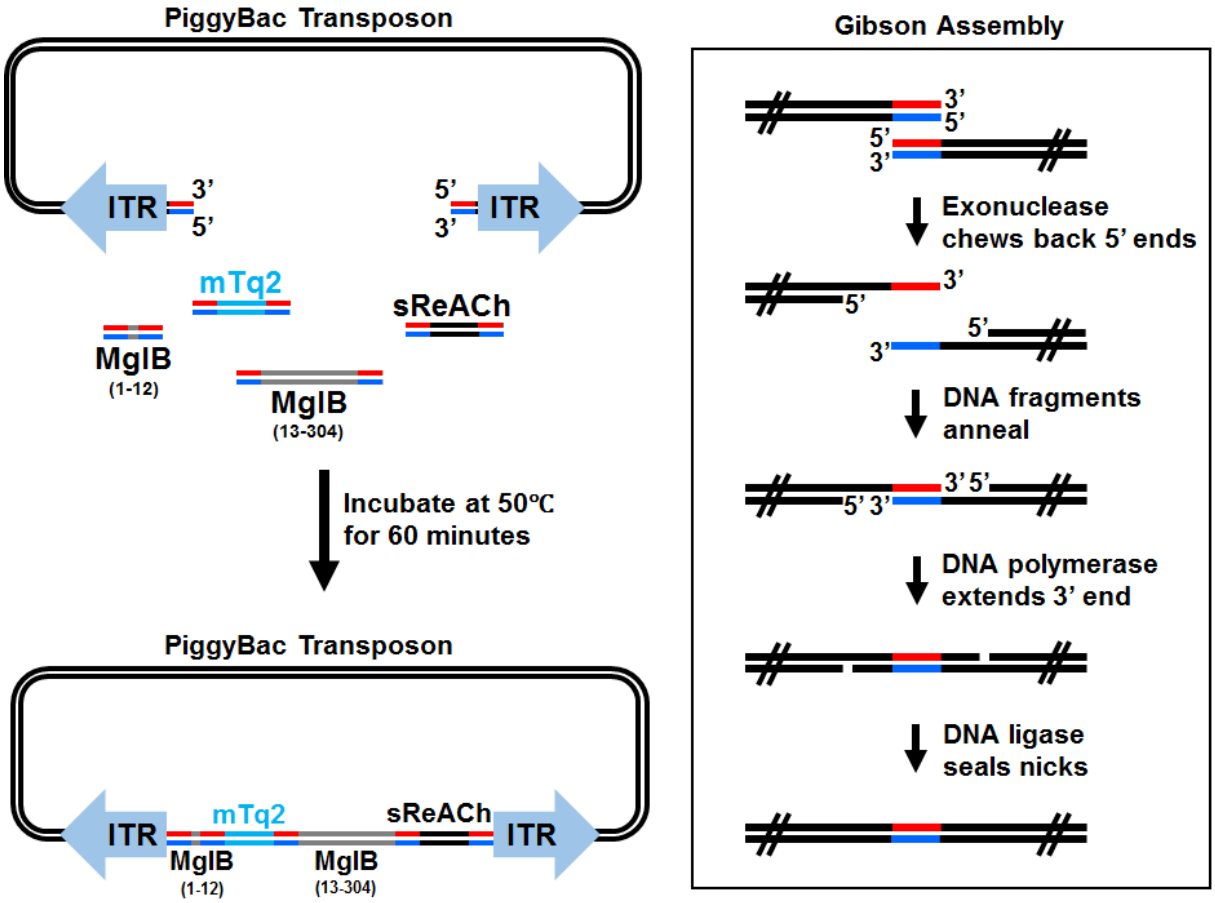


Figure 2-3 Overview of the Gibson Assembly
The glucose FRET biosensor with mTurquoise2 and sReACh pair was constructed using Gibson Assembly.

Primers	Sequences
Glucose Biosensor For.	5'- TCTCATCATTTTGGCAAA**g**CTCGAGCCGACC**ATG**GCTGATACTCGC -3'
Glucose Biosensor Rev.	5'- CGCTAGAGGGAAACCGTTGCTAGCTTAAGCTT**TTA**GTACAGCTCGTCCATGCC -3'
Glucose biosensor first Fragment For.	5'- TCTCATCATTTTGGCAAA**g**CTCGAGCCGACC**ATG**GCTGATACTCGCATTGGTGTAACAATCTATAAGTCGGCTGGT**ATG**GTGAGCAAGGGCGAGGAG -3'
Glucose biosensor first Fragment Rev.	5'- CTCCTCGCCCTTGCTCAC**CAT**ACCAGCCGACTTATAGATTGTTACACCAATGCGAGTATCAGC**CAT**GGTCGGCTCGAG**c**TTTGCCAAAATGATGAGA -3'
mTq2 For.	5'- ATCTATAAGTCGGCTGGT**ATG**GTGAGCAAGGGCGAGGAG -3'
mTq2 Rev.	5'- AAAGTTATCTCGGCTACCGTACAGCTCGTCCATGCC -3'
Glucose biosensor second Fragment For.	5'- GGCATGGACGAGCTGTACGGTAGCCGAGATAACTTT -3'
Glucose biosensor second Fragment Rev.	5'- CTCGCCCTTGCTCAC**CAT**TTTCTTGCTGAATTCAGC -3'
sReACh For.	5'- GCTGAATTCAGCAAGAAA**ATG**GTGAGCAAGGGCGAGGAG -3'
sReACh Rev.	5'- CGCTAGAGGGAAACCGTTGCTAGCTTAAGCTT**TTA**GTACAGCTCGTCCATGCC -3'
glucose Biosensor D183A For.	5'- ACCGCAATGTGGGCCACCGCTCAGGCG -3'
glucose Biosensor D183A Rev.	5'- CGCCTGAGCGGTGGCCCACATTGCGCT -3'
Pyruvate Biosensor For.	5'- TCTCATCATTTTGGCAAA**g**GAATTCCGAAC**ATG**GTGAGCAAGGGC -3'
Pyruvate Biosensor Rev.	5'- CGCTAGAGGGAAACCGTTGCTAG**c**AAGCTT**TTA**CTTGTACAGCTCGTC -3'
Lactate Biosensor For.	5'- TCTCATCATTTTGGCAAA**g**GAATTCCCGAAC**ATG**GTGAGCAAGGGC -3'
Lactate Biosensor Rev.	5'- CGCTAGAGGGAAACCGTTGCTAGGTTAAC**TTA**GTACAGCTCGTCCATGCC -3'
ATP Biosensor For.	5'- TCTCATCATTTTGGCAAA**g**CTCGAGCCGACC**ATG**GTGAGCAAGGGCGAG -3'
ATP Biosensor Rev.	5'- CGCTAGAGGGAAACCGTTGCTAGCTTAAG**TTA**CTCGATGTTGTGGCGGATC -3'

Table 2-3 Primers

2.2.3 DNA map of Glucose FRET biosensor (eCFP-Citrine)

XhoI - MglB (1-12) - eCFP - MglB (13-304) - Citrine - AflII

CTCGAGCCGACC **ATG** GCT GAT ACT CGC ATT GGT GTA ACA ATC TAT AAG TCG GCT GGT
ATG GTG AGC AAG GGC GAG GAG CTG TTC ACC GGG GTG GTG CCC ATC CTG GTC GAG
CTG GAC GGC GAC GTA AAC GGC CAC AAG TTC AGC GTG TCC GGC GAG GGC GAG GGC
GAT GCC ACC TAC GGC AAG CTG ACC CTG AAG TTC ATC TGC ACC ACC GGC AAG CTG
CCC GTG CCC TGG CCC ACC CTC GTG ACC ACC CTG ACC TGG GGC GTG CAG TGC TTC
AGC CGC TAC CCC GAC CAC ATG AAG CAG CAC GAC TTC TTC AAG TCC GCC ATG CCC
GAA GGC TAC GTC CAG GAG CGC ACC ATC TTC TTC AAG GAC GAC GGC AAC TAC AAG
ACC CGC GCC GAG GTG AAG TTC GAG GGC GAC ACC CTG GTG AAC CGC ATC GAG CTG
AAG GGC ATC GAC TTC AAG GAG GAC GGC AAC ATC CTG GGG CAC AAG CTG GAG TAC
AAC TAC ATC AGC CAC AAC GTC TAT ATC ACC GCC GAC AAG CAG AAG AAC GGC ATC
AAG GCC AAC TTC AAG ATC CGC CAC AAC ATC GAG GAC GGC AGC GTG CAG CTC GCC
GAC CAC TAC CAG CAG AAC ACC CCC ATC GGC GAC GGC CCC GTG CTG CTG CCC GAC
AAC CAC TAC CTG AGC ACC CAG TCC GCC CTG AGC AAA GAC CCC AAC GAG AAG CGC
GAT CAC ATG GTC CTG CTG GAG TTC GTG ACC GCC GCC GGG ATC ACT CTC GGC ATG
GAC GAG CTA TAC GGT AGC CGA GAT AAC TTT ATG TCT GTA GTG CGC AAG GCT ATT
GAG CAA GAT GCG AAA GCC GCG CCA GAT GTT CAG CTG CTG ATG AAT GAT TCT CAG
AAT GAC CAG TCC AAG CAG AAC GAT CAG ATC GAC GTA TTG CTG GCG AAA GGG GTG
AAG GCA CTG GCA ATC AAC CTG GTT GAC CCG GCA GCT GCG GGT ACG GTG ATT GAG
AAA GCG CGT GGG CAA AAC GTG CCG GTG GTT TTC TTC AAC AAA GAA CCG TCT CGT
AAG GCG CTG GAT AGC TAC GAC AAA GCC TAC TAC GTT GGC ACT GAC TCC AAA GAG
TCC GGC ATT ATT CAA GGC GAT TTG ATT GCT AAA CAC TGG GCG GCG AAT CAG GGT
TGG GAT CTG AAC AAA GAC GGT CAG ATT CAG TTC GTA CTG CTG AAA GGT GAA CCG
GGC CAT CCG GAT GCA GAA GCA CGT ACC ACT TAC GTG ATT AAA GAA TTG AAC GAT
AAA GGC ATC AAA ACT GAA CAG TTA CAG TTA GAT ACC GCA ATG TGG **GAC** ACC GCT
CAG GCG AAA GAT AAG ATG GAC GCC TGG CTG TCT GGC CCG AAC GCC AAC AAA ATC
GAA GTG GTT ATC GCC AAC AAC GAT GCG ATG GCA ATG GGC GCG GTT GAA GCG CTG
AAA GCA CAC AAC AAG TCC AGC ATT CCG GTG TTT GGC GTC GAT GCG CTG CCA GAA
GCG CTG GCG CTG GTG AAA TCC GGT GCA CTG GCG GGC ACC GTA CTG AAC GAT GCT
AAC AAC CAG GCG AAA GCG ACC TTT GAT CTG GCG AAA AAC CTG GCC GAT GGT AAA
GGT GCG GCT GAT GGC ACC AAC TGG AAA ATC GAC AAC AAA GTG GTC CGC GTA CCT
TAT GTT GGC GTA GAT AAA GAC AAC CTG GCT GAA TTC AGC AAG AAA ATG GTG AGC
AAG GGC GAG GAG CTG TTC ACC GGG GTG GTG CCC ATC CTG GTC GAG CTG GAC GGC
GAC GTA AAC GGC CAC AAG TTC AGC GTG TCC GGC GAG GGC GAG GGC GAT GCC ACC
TAC GGC AAG CTG ACC CTG AAG TTC ATC TGC ACC ACC GGC AAG CTG CCC GTG CCC
TGG CCC ACC CTC GTG ACC ACC TTC GGC TAC GGC CTG ATG TGC TTC GCC CGC TAC
CCC GAC CAC ATG AAG CAG CAC GAC TTC TTC AAG TCC GCC ATG CCC GAA GGC TAC
GTC CAG GAG CGC ACC ATC TTC TTC AAG GAC GAC GGC AAC TAC AAG ACC CGC GCC
GAG GTG AAG TTC GAG GGC GAC ACC CTG GTG AAC CGC ATC GAG CTG AAG GGC ATC
GAC TTC AAG GAG GAC GGC AAC ATC CTG GGG CAC AAG CTG GAG TAC AAC TAC AAC
AGC CAC AAC GTC TAT ATC ATG GCC GAC AAG CAG AAG AAC GGC ATC AAG GTG AAC
TTC AAG ATC CGC CAC AAC ATC GAG GAC GGC AGC GTG CAG CTC GCC GAC CAC TAC
CAG CAG AAC ACC CCC ATC GGC GAC GGC CCC GTG CTG CTG CCC GAC AAC CAC TAC
CTG AGC TAC CAG TCC GCC CTG AGC AAA GAC CCC AAC GAG AAG CGC GAT CAC ATG
GTC CTG CTG GAG TTC GTG ACC GCC GCC GGG ATC ACT CTC GGC ATG GAC GAG CTG
TAC AAG **TAA** CTTAAG

2.2.4 DNA map of Glucose FRET biosensor (mTurquoise2 - sReACh)

XhoI - MglB (1-12) – mTq2 - MglB (13-304) - sReACh - AflII

CTCGAGCCGACC **ATG** GCT GAT ACT CGC ATT GGT GTA ACA ATC TAT AAG TCG GCT GGT
ATG GTG AGC AAG GGC GAG GAG CTG TTC ACC GGG GTG GTG CCC ATC CTG GTC GAG
CTG GAC GGC GAC GTA AAC GGC CAC AAG TTC AGC GTG TCC GGC GAG GGC GAG GGC
GAT GCC ACC TAC GGC AAG CTG ACC CTG AAG TTC ATC TGC ACC ACC GGC AAG CTG
CCC GTG CCC TGG CCC ACC CTC GTG ACC ACC CTG TCC TGG GGC GTG CAG TGC TTC
GCC CGC TAC CCC GAC CAC ATG AAG CAG CAC GAC TTC TTC AAG TCC GCC ATG CCC
GAA GGC TAC GTC CAG GAG CGC ACC ATC TTC TTC AAG GAC GAC GGC AAC TAC AAG
ACC CGC GCC GAG GTG AAG TTC GAG GGC GAC ACC CTG GTG AAC CGC ATC GAG CTG
AAG GGC ATC GAC TTC AAG GAG GAC GGC AAC ATC CTG GGG CAC AAG CTG GAG TAC
AAC TAC TTT AGC GAC AAC GTC TAT ATC ACC GCC GAC AAG CAG AAG AAC GGC ATC
AAG GCC AAC TTC AAG ATC CGC CAC AAC ATC GAG GAC GGC GGC GTG CAG CTC GCC
GAC CAC TAC CAG CAG AAC ACC CCC ATC GGC GAC GGC CCC GTG CTG CTG CCC GAC
AAC CAC TAC CTG AGC ACC CAG TCC AAG CTG AGC AAA GAC CCC AAC GAG AAG CGC
GAT CAC ATG GTC CTG CTG GAG TTC GTG ACC GCC GCC GGG ATC ACT CTC GGC ATG
GAC GAG CTG TAC GGT AGC CGA GAT AAC TTT ATG TCT GTA GTG CGC AAG GCT ATT
GAG CAA GAT GCG AAA GCC GCG CCA GAT GTT CAG CTG CTG ATG AAT GAT TCT CAG
AAT GAC CAG TCC AAG CAG AAC GAT CAG ATC GAC GTA TTG CTG GCG AAA GGG GTG
AAG GCA CTG GCA ATC AAC CTG GTT GAC CCG GCA GCT GCG GGT ACG GTG ATT GAG
AAA GCG CGT GGG CAA AAC GTG CCG GTG GTT TTC TTC AAC AAA GAA CCG TCT CGT
AAG GCG CTG GAT AGC TAC GAC AAA GCC TAC TAC GTT GGC ACT GAC TCC AAA GAG
TCC GGC ATT ATT CAA GGC GAT TTG ATT GCT AAA CAC TGG GCG GCG AAT CAG GGT
TGG GAT CTG AAC AAA GAC GGT CAG ATT CAG TTC GTA CTG CTG AAA GGT GAA CCG
GGC CAT CCG GAT GCA GAA GCA CGT ACC ACT TAC GTG ATT AAA GAA TTG AAC GAT
AAA GGC ATC AAA ACT GAA CAG TTA CAG TTA GAT ACC GCA ATG TGG **GAC** ACC GCT
CAG GCG AAA GAT AAG ATG GAC GCC TGG CTG TCT GGC CCG AAC GCC AAC AAA ATC
GAA GTG GTT ATC GCC AAC AAC GAT GCG ATG GCA ATG GGC GCG GTT GAA GCG CTG
AAA GCA CAC AAC AAG TCC AGC ATT CCG GTG TTT GGC GTC GAT GCG CTG CCA GAA
GCG CTG GCG CTG GTG AAA TCC GGT GCA CTG GCG GGC ACC GTA CTG AAC GAT GCT
AAC AAC CAG GCG AAA GCG ACC TTT GAT CTG GCG AAA AAC CTG GCC GAT GGT AAA
GGT GCG GCT GAT GGC ACC AAC TGG AAA ATC GAC AAC AAA GTG GTC CGC GTA CCT
TAT GTT GGC GTA GAT AAA GAC AAC CTG GCT GAA TTC AGC AAG AAA ATG GTG AGC
AAG GGC GAG GAG CTG TTC ACC GGG GTG GTG CCC ATC CTG GTC GAG CTG GAC GGC
GAC GTA AAC GGC CAC AAG TTC AGC GTG TCC GGC GAG GGC GAG GGC GAT GCC ACC
TAC GGC AAG CTG ACC CTG AAG CTC ATC TGC ACC ACC GGC AAG CTG CCC GTG CCC
TGG CCC ACC CTC GTG ACC ACC TTC GGC TAC GGC CTG ATG TGC TTC GCC CGC TAC
CCC GAC CAC ATG AAG CAG CAC GAC TTC TTC AAG TCC GCC ATG CCC GAA GGC TAC
GTC CAG GAG CGC ACC ATC TTC TTC AAG GAC GAC GGC AAC TAC AAG ACC CGC GCC
GAG GTG AAG TTC GAG GGC GAC ACC CTG GTG AAC CGC ATC GAG CTG AAG GGC ATC
GAC TTC AAG GAG GAC GGC AAC ATC CTG GGG CAC AAG CTG GAG TAC AAC TGG AAC
AGC GTC AAC GTC TAT ATC ATG GCC GAC AAG CAG AAG AAC GGC ATC AAG GTG AAC
TTC AAG ATC CGC CAC AAC ATC GAG GAC GGC AGC GTG CAG CTC GCC GAC CAC TAC
CAG CAG AAC ACC CCC ATC GGC GAC GGC CCC GTG CTG CTG CCC GAC AAC CAC TAC
CTG AGC TAC CAG TCC GCC CTG AGC AAA GAC CCC AAC GAG AAG CGC GAT CAC ATG
GTC CTG CTG GAG AGA GTG ACC GCC GCC GGG ATC ACT CTC GGC ATG GAC GAG CTG
TAC AAG **TAA** CTTAAG

2.2.5 DNA map of Pyruvate FRET biosensor

EcoRI - mTFP - PdhR - Venus - AflII

GAATCCGAAC **ATG** GTG AGC AAG GGC GAG GAG ACC ACA ATG GGC GTA ATC AAG CCC GAC ATG AAG ATC AAG CTG AAG ATG GAG GGC AAC GTG AAT GGC CAC GCC TTC GTG ATC GAG GGC GAG GGC GAG GGC AAG CCC TAC GAC GGC ACC AAC ACC ATC AAC CTG GAG GTG AAG GAG GGA GCC CCC CTG CCC TTC TCC TAC GAC ATT CTG ACC ACC GCG TTC GCC TAC GGC AAC AGG GCC TTC ACC AAG TAC CCC GAC GAC ATC CCC AAC TAC TTC AAG CAG TCC TTC CCC GAG GGC TAC TCT TGG GAG CGC ACC ATG ACC TTC GAG GAC AAG GGC ATC GTG AAG GTG AAG TCC GAC ATC TCC ATG GAG GAG GAC TCC TTC ATC TAC GAG ATA CAC CTC AAG GGC GAG AAC TTC CCC CCC AAC GGC CCC GTG ATG CAG AAG AAG ACC ACC GGC TGG GAC GCC TCC ACC GAG AGG ATG TAC GTG CGC GAC GGC GTG CTG AAG GGC GAC GTC AAG CAC AAG CTG CTG CTG GAG GGC GGC GGC CAC CAC CGC GTT GAC TTC AAG ACC ATC TAC AGG GCC AAG AAG GCG GTG AAG CTG CCC GAC TAT CAC TTT GTG GAC CAC CGC ATC GAG ATC CTG AAC CAC GAC AAG GAC TAC AAC AAG GTG ACC GTT TAC GAG AGC GCC GTG GCC CGC AAC TCC ACC GAC GGC ATG GAC GAG CTG TAC AAG AGA TCT GGT ACC ACA AGT TTG TAC AAA AAA GCA GGC TCC GAA TTC GCC CTT GGT ACC ATG GCC TAC AGC AAA ATC CGC CAA CCA AAA CTC TCC GAT GTG ATT GAG CAG CAA CTG GAG TTT TTG ATC CTC GAA GGC ACT CTC CGC CCG GGC GAA AAA CTC CCA CCG GAA CGC GAA CTG GCA AAA CAG TTT GAC GTC TCC CGT CCC TCC TTG CGT GAG GCG ATT CAA CGT CTC GAA GCG AAG GGC TTG TTG CTT CGT CGC CAG GGT GGC GGC ACT TTT GTC CAG AGC AGC CTA TGG CAA AGT TTC AGC GAT CCG CTG GTG GAG CTG CTC TCC GAC CAT CCT GAG TCA CAG TAT GAC TTG CTC GAA ACA CGA CAC GCC CTG GAA GGT ATC GCC GCT TAT TAC GCC GCG CTG CGT AGT ACC GAT GAA GAC AAG GAA CGC ATC CGT GAA CTC CAC CAC GCC ATA GAG CTG GCG CAG CAG TCT GGC GAT CTG GAC GCG GAA TCA AAC GCC GTA CTC CAG TAT CAG ATT GCC GTC ACC GAA GCG GCC CAC AAT GTG GTT CTG CTT CAT CTG CTA AGG TGT ATG GAG CCG ATG TTG GCC CAG AAT GTC CGC CAG AAC TTC GAA TTG CTC TAT TCG CGT CGC GAG ATG CTG CCG CTG GTG AGT AGT CAC CGC ACC CGC ATA TTT GAA GCG ATT ATG GCC GGT AAG CCG GAA GAA GCG CGC GAA GCA TCG CAT CGC CAT CTG GCC TTT ATC GAA GAA ATT TTG CTC GAC AGA AGT CGT GAA GAG AGC CGC CGT GAG CGT TCT CTG CGT CGT CTG GAG CAA CGA AAG AAT CTT AAG AGA TCT ACC ATG GTG AGC AAG GGC GAG GAG CTG TTC ACC GGG GTG GTG CCC ATC CTG GTC GAG CTG GAC GGC GAC GTA AAC GGC CAC AAG TTC AGC GTG TCC GGC GAG GGC GAG GGC GAT GCC ACC TAC GGC AAG CTG ACC CTG AAG CTG ATC TGC ACC ACC GGC AAG CTG CCC GTG CCC TGG CCC ACC CTC GTG ACC ACC CTG GGC TAC GGC CTG CAG TGC TTC GCC CGC TAC CCC GAC CAC ATG AAG CAG CAC GAC TTC TTC AAG TCC GCC ATG CCC GAA GGC TAC GTC CAG GAG CGC ACC ATC TTC TTC AAG GAC GAC GGC AAC TAC AAG ACC CGC GCC GAG GTG AAG TTC GAG GGC GAC ACC CTG GTG AAC CGC ATC GAG CTG AAG GGC ATC GAC TTC AAG GAG GAC GGC AAC ATC CTG GGG CAC AAG CTG GAG TAC AAC TAC AAC AGC CAC AAC GTC TAT ATC ACC GCC GAC AAG CAG AAG AAC GGC ATC AAG GCC AAC TTC AAG ATC CGC CAC AAC ATC GAG GAC GGC GGC GTG CAG CTC GCC GAC CAC TAC CAG CAG AAC ACC CCC ATC GGC GAC GGC CCC GTG CTG CTG CCC GAC AAC CAC TAC CTG AGC TAC CAG TCC GCC CTG AGC AAA GAC CCC AAC GAG AAG CGC GAT CAC ATG GTC CTG CTG GAG TTC GTG ACC GCC GCC GGG ATC ACT CTC GGC ATG GAC GAG CTG TAC AAG **TAA** CTTAAG

2.2.6 DNA map of Lactate FRET biosensor

EcoRI - mTFP - LldR - Venus - AflII

GAATCCGAAC **ATG** GTG AGC AAG GGC GAG GAG ACC ACA ATG GGC GTA ATC AAG CCC GAC ATG AAG ATC AAG CTG AAG ATG GAG GGC AAC GTG AAT GGC CAC GCC TTC GTG ATC GAG GGC GAG GGC GAG GGC AAG CCC TAC GAC GGC ACC AAC ACC ATC AAC CTG GAG GTG AAG GAG GGA GCC CCC CTG CCC TTC TCC TAC GAC ATT CTG ACC ACC GCG TTC GCC TAC GGC AAC AGG GCC TTC ACC AAG TAC CCC GAC GAC ATC CCC AAC TAC TTC AAG CAG TCC TTC CCC GAG GGC TAC TCT TGG GAG CGC ACC ATG ACC TTC GAG GAC AAG GGC ATC GTG AAG GTG AAG TCC GAC ATC TCC ATG GAG GAG GAC TCC TTC ATC TAC GAG ATA CAC CTC AAG GGC GAG AAC TTC CCC CCC AAC GGC CCC GTG ATG CAG AAG AAG ACC ACC GGC TGG GAC GCC TCC ACC GAG AGG ATG TAC GTG CGC GAC GGC GTG CTG AAG GGC GAC GTC AAG CAC AAG CTG CTG CTG GAG GGC GGC GGC CAC CAC CGC GTT GAC TTC AAG ACC ATC TAC AGG GCC AAG AAG GCG GTG AAG CTG CCC GAC TAT CAC TTT GTG GAC CAC CGC ATC GAG ATC CTG AAC CAC GAC AAG GAC TAC AAC AAG GTG ACC GTT TAC GAG AGC GCC GTG GCC CGC AAC TCC ACC GAC GGC ATG GAC GAG CTG TAC AAG AGA TCT GGT ACC ATG ATT GTT TTA CCC AGA CGC CTG TCA GAC GAG GTT GCC GAT CGT GTG CGG GCG CTG ATT GAT GAA AAA AAC CTG GAA GCG GGC ATG AAG TTG CCC GCT GAG CGC CAA CTG GCG ATG CAA CTC GGC GTA TCA CGT AAT TCA CTG CGC GAG GCG CTG GCA AAA CTG GTG AGT GAA GGC GTG CTG CTC AGT CGA CGC GGC GGC GGG ACG TTT ATT CGC TGG CGT CAT GAC ACA TGG TCG GAG CAA AAC ATC GTC CAG CCG CTA AAA ACA CTG ATG GCC GAT GAT CCG GAT TAC AGT TTC GAT ATT CTG GAA GCC CGC TAC GCC ATT GAA GCC AGC ACC GCA TGG CAT GCG GCA ATG CGC GCC ACA CCT GGC GAC AAA GAA AAG ATT CAG CTT TGC TTT GAA GCA ACG CTA AGT GAA GAC CCG GAT ATC GCC TCA CAA GCG GAC GTT CGT TTT CAT CTG GCG ATT GCC GAA GCC TCA CAT AAC ATC GTG CTG CTG CAA ACC ATG CGC GGT TTC TTC GAT GTC CTG CAA TCC TCA GTG AAG CAT AGC CGT CAG CGG ATG TAT CTG GTG CCA CCG GTT TTT TCA CAA CTG ACC GAA CAA CAT CAG GCT GTC ATT GAC GCC ATT TTT GCC GGT GAT GCT GAC GGG GCG CGT AAA GCA ATG ATG GCG CAC CTT AGT TTT GTT CAC ACC ACC ATG AAA CGA TTC GAT GAA GAT CAG GCT CGC CAC GCA CGG ATT ACC CGC CTG CCC GGT GAG CAT AAT GAG CAT TCG AGG GAG AAA AAC GCA CTT AAG AGA TCT ACC **ATG** GTG AGC AAG GGC GAG GAG CTG TTC ACC GGG GTG GTG CCC ATC CTG GTC GAG CTG GAC GGC GAC GTA AAC GGC CAC AAG TTC AGC GTG TCC GGC GAG GGC GAG GGC GAT GCC ACC TAC GGC AAG CTG ACC CTG AAG CTG ATC TGC ACC ACC GGC AAG CTG CCC GTG CCC TGG CCC ACC CTC GTG ACC ACC CTG GGC TAC GGC CTG CAG TGC TTC GCC CGC TAC CCC GAC CAC ATG AAG CAG CAC GAC TTC TTC AAG TCC GCC ATG CCC GAA GGC TAC GTC CAG GAG CGC ACC ATC TTC TTC AAG GAC GAC GGC AAC TAC AAG ACC CGC GCC GAG GTG AAG TTC GAG GGC GAC ACC CTG GTG AAC CGC ATC GAG CTG AAG GGC ATC GAC TTC AAG GAG GAC GGC AAC ATC CTG GGG CAC AAG CTG GAG TAC AAC TAC AAC AGC CAC AAC GTC TAT ATC ACC GCC GAC AAG CAG AAG AAC GGC ATC AAG GCC AAC TTC AAG ATC CGC CAC AAC ATC GAG GAC GGC GGC GTG CAG CTC GCC GAC CAC TAC CAG CAG AAC ACC CCC ATC GGC GAC GGC CCC GTG CTG CTG CCC GAC AAC CAC TAC CTG AGC TAC CAG TCC GCC CTG AGC AAA GAC CCC AAC GAG AAG CGC GAT CAC ATG GTC CTG CTG GAG TTC GTG ACC GCC GCC GGG ATC ACT CTC GGC ATG GAC GAG CTG TAC AAG **TAA** CTTAAG

2.2.7 DNA map of ATP FRET biosensor

XhoI - CFP - F0F1 ATP synthase ε subunit - YFP - AflII

CTCGAGCCGACC **ATG** GTG AGC AAG GGC GAG GAG CTG TTC ACC GGG GTG GTG CCC ATC CTG GTC GAG CTG GAC GGC GAC GTA AAC GGC CAC AGG TTC AGC GTG TCC GGC GAG GGC GAG GGC GAT GCC ACC TAC GGC AAG CTG ACC CTG AAG TTC ATC TGC ACC ACC GGC AAG CTG CCC GTG CCC TGG CCC ACC CTC GTG ACC ACC CTG ACC TGG GGC GTG CAG TGC TTC GCC CGC TAC CCC GAC CAC ATG AAG CAG CAC GAC TTC TTC AAG TCC GCC ATG CCC GAA GGC TAC GTC CAG GAG CGT ACC ATC TTC TTC AAG GAC GAC GGC AAC TAC AAG ACC CGC GCC GAG GTG AAG TTC GAG GGC GAC ACC CTG GTG AAC CGC ATC GAG CTG AAG GGC ATC GAC TTC AAG GAG GAC GGC AAC ATC CTG GGG CAC AAG CTG GAG TAC AAC TAC ATC AGC CAC AAC GTC TAT ATC ACC GCC GAC AAG CAG AAG AAC GGC ATC AAG GCC CAC TTC AAG ATC CGC CAC AAC ATC GAG GAC GGC GGC GTG CAG CTC GCC GAC CAC TAC CAG CAG AAC ACC CCC ATC GGC GAC GGC CCC GTG CTG CTG CCC GAC AAC CAC TAC CTG AGC ACC CAG TCC GCC CTG AGC AAA GAC CCC AAC GAG AAG CGC GAT CAC ATG GTC CTG CTG GAG TTC GTG ACC GCC GCC ATC GAT ATG AAA ACT GTG AAA GTG AAT ATA ACA ACC CCT GAT GGG CCA GTC TAC GAC GCT GAT ATC GAG ATG GTG TCC GTG CGG GCC GAG AGT GGT GAT CTC GGC ATC CTC CCC GGT CAC ATT CCC ACA AAG GCC CCA CTG AAG ATC GGA GCT GTG CGG CTG AAG AAG GAC GGC CAA ACC GAG ATG GTC GCA GTC TCA GGC GGC ACT GTT GAA GTG CGG CCT GAC CAC GTT ACC ATT AAT GCT CAA GCC GCT GAA ACA GCC GAA GGA ATC GAC AAA GAG AGA GCA GAA GCC GCA AGA CAG AGG GCC CAG GAG CGG CTG AAC TCT CAA TCC GAT GAC ACC GAT ATT CGC CGG GCC GAG CTG GCA CTG CAG AGG GCC CTG AAC AGA CTG GAC GTG GCT GGG AAG GCA AAC GAA TTC ATG GAC GGC GGC GTG CAG CTC GCC GAC CAC TAC CAG CAG AAC ACC CCC ATC GGC GAC GGC CCC GTG CTG CTG CCC GAC AAC CAC TAC CTG AGC TAC CAG TCC GCC CTG AGC AAA GAC CCC AAC GAG AAG CGC GAT CAC ATG GTC CTG CTG GAG TTC GTG ACC GCC GCC GGG ATC ACT CTC GGC ATG GAC GAG CTG TAC AAG GGT GGC AGC GGT GGC ATG GTG AGC AAG GGC GAG GAG CTG TTC ACC GGG GTG GTG CCC ATC CTG GTC GAG CTG GAC GGC GAC GTA AAC GGC CAC AAG TTC AGC GTG TCC GGC GAG GGC GAG GGC GAT GCC ACC TAC GGC AAG CTG ACC CTG AAG CTG ATC TGC ACC ACC GGC AAG CTG CCC GTG CCC TGG CCC ACC CTC GTG ACC ACC CTG GGC TAC GGC CTG CAG TGC TTC GCC CGC TAC CCC GAC CAC ATG AAG CAG CAC GAC TTC TTC AAG TCC GCC ATG CCC GAA GGC TAC GTC CAG GAG CGC ACC ATC TTC TTC AAG GAC GAC GGC AAC TAC AAG ACC CGC GCC GAG GTG AAG TTC GAG GGC GAC ACC CTG GTG AAC CGC ATC GAG CTG AAG GGC ATC GAC TTC AAG GAG GAC GGC AAC ATC CTG GGG CAC AAG CTG GAG TAC AAC TAC AAC AGC CAC AAC GTC TAT ATC ACC GCC GAC AAG CAG AAG AAC GGC ATC AAG GCC AAC TTC AAG ATC CGC CAC AAC ATC GAG **TAA** CTTAAG

2.3 Western Blot

Protein expression levels were measured by western blot. MCF-7 cells were grown to roughly 80% confluence in 60 mm dishes and lysed with ice-cold lysis buffer (50 mM HEPES pH 7.4, 150 mM NaCl, 5% Glycerol, 1% NP-40, Proteinase inhibitor tablet, Phosphatase inhibitor tablet). Cell lysates were mixed with 4 x SDS sample buffer (180 mM HEPES pH 7.4, 40% glycerol, 4% SDS, 4% beta-mercaptoethanol, 0.04% bromophenol blue) and heated at 95ºC for 5 minutes. Next, these samples were loaded to 4-15% Mini-PROTEAN® TGX™ precast gels (Bio-Rad) along with a prestained protein ladder (Benchmark, Invitrogen) for electrophoresis. Proteins were then transferred to 0.2 µm Trans-Blot® Turbo™ Mini PVDF membrane (Bio-Rad). The membrane was blocked with 5% BSA in Tris buffer saline containing 0.1% Tween-20 for 1 hour at room temperature and incubated with primary antibodies overnight at 4ºC (Table 2-4). The membrane was next incubated with Horseradish peroxidase (HRP) coupled secondary antibodies for 1 hour at room temperature. Protein bands were revealed by Immobilon Luminata Crescendo Western HRP substrate (EMD Millipore) and chemiluminescence signals were detected by Amersham Imager 600 (GE Healthcare Life Sciences). Protein bands intensity were measured and quantified by Image J software.

Antibody	Company	Catalog number	Origin	Dilution
GLUT1	Abcam	ab15309	rabbit	1 / 1,000
GLUT4	Abcam	ab654	rabbit	1 / 1,000
phospho AKT (Ser473)	Cell Signaling	4060	rabbit	1 / 500
AKT	Cell Signaling	2920	mouse	1 / 1,000
Phospho S6 Ribosomal Protein (Ser235/236)	NEB	2211S	rabbit	1 / 2,000
S6 Ribosomal Protein	NEB	2317	mouse	1 / 2,000
phospho Cofilin (Ser3)	Cell signalling	3311S	rabbit	1 / 1,000
cofilin	Cell signalling	3312	rabbit	1 / 1,000
phospho Erk1/2 (Thr202/Thr204)	Cell Signaling	4376	rabbit	1 / 1,000
Erk1/2	Cell signalling	4695	rabbit	1 / 1,000
phospho FAK (Tyr397)	Cell signalling	8556S	rabbit	1 / 1,000
FAK	Cell signalling	3285S	rabbit	1 / 1,000
phospho Src (Tyr416)	Cell Signaling	6943	rabbit	1 / 1,000
phospho MLC 2 (Ser19)	NEB	3671L	rabbit	1 / 1,000
phospho YAP (Tyr357)	Abcam	ab62751	rabbit	1 / 1,000
YAP	Cell signalling	14074	rabbit	1 / 1,000
Ac-lysine (AKL5C1)	Santa Cruz	sc-32268	mouse	1 / 2,000
ß-Actin	Sigma-Aldrich	A1978	mouse	1 / 5,000

Table 2-4 Primary antibodies

2.4 Inhibitors and siRNA

2.4.1 Inhibitors

MCF-7 cells were plated on glass bottom dishes at 1 x 10^4 cells / cm^2. The inhibitors were diluted in DMEM with 10% FBS and cells were incubated with inhibitors for 24 hours at 37 °C in 5% CO_2 (Table 2-5). 3 hours before imaging, the media was changed to phenol red free DMEM with 10% FBS including each inhibitor.

Inhibitor	Targets	Company	Catalog number
WEB117	GLUT1	Stratech	S7927
AR-C155858	MCT1 and MCT2	Sigma-Aldrich	HY13248
Phloretin	MCT1 and MCT2	Sigma-Aldrich	P7912
Linsitinib	IGF-1R	Selleckchem	S1091
VO-Ohpic trihydrate	PTEN	Selleckchem	S8174
Pictilisib (GDC-0941)	PI3Kα/δ	Selleckchem	S1065
Alpelisib (BYL719)	PI3Kα	Selleckchem	S2814
AZD8186	PI3Kδ/β	Cambridge Bioscience	17384
Capivasertib (AZD5363)	Akt1/Akt2/Akt3	Cambridge Bioscience	15406
MK-2206 2HCl	Akt1/Akt2/Akt3	Selleckchem	S1078
Rapamycin	mTOR	Selleckchem	S1039
Dorsomorphin	AMPK	Tocris	3093
Phenformin	AMPK	Selleckchem	S2542
PD325901	MEK	LC Labs	P9688
BX-795	PDK1	Selleckchem	S1274
Dasatinib	Src	LC Labs	D3307
NSC23766	Rac1	Tocris	2161
CK-666	Arp2/3	Tocris	3950/10
Cytochalasin D	Actin polymerization	Tocris	1233
Jasplakinolide	Actin depolymerization	Tocris	2792/100
Y27632	ROCK	Tocris	1254
Nocodazole	Microtubule polymerization	Selleckchem	S2775
5-Aza-2-deoxicit	DNA methyltransferase	Sigma-Aldrich	A3656
Tazemetostat (EPZ-6438)	Histone methyltransferase	Selleckchem	S7128
GSK J4 HCl	Histone demethylase	Selleckchem	S7070
C646	Histone acetyltransferase	Selleckchem	S7152
Vorinostat	HDAC	Selleckchem	S1047
JQ1	BET bromodomain	Selleckchem	S7110
ZL0420	BRD4	Selleckchem	S8363
AZD5153	BRD4	Selleckchem	S8344
2-DG	Glucose metabolism	Sigma-Aldrich	D8375
Antimycin A	Mitochondrial Complex 3	Sigma-Aldrich	A8674
FCCP	Proton uncoupler in mitochondria	Sigma-Aldrich	C2920
Rotenone	Mitochondrial electron transport	Bio-techne	3616/50
Tamoxifen	Estrogen receptor	Sigma-Aldrich	T5648

Table 2-5 Inhibitors

2.4.2 siRNA

A day before transfection, MCF-7 cells were plated on glass bottom dishes at 1 x 10^4 cells / cm^2. For one 35 mm dish, a total of 5 µl of 20 µM siRNA and 2 µl of DharmaFECT 2 reagent (Dharmacon) were diluted in 100 µl of Opti-MEM medium (Table 2-6). These two solutions were gently mixed and incubated for 20 minutes at room temperature. Culture media was changed to serum free DMEM and cells were incubated with the transfection complex for 24 hours. After incubation, cells were washed with PBS and then cultured in DMEM with 10% FBS. The cells were analysed 48 hours after siRNA transfection.

siRNA	Code	Sequences
Non-Targeting Control	D-001210-01	UAGCGACUAAACACAUCAA
Non-Targeting Control	D-001210-02	UAAGGCUAUGAAGAGAUAC
E-Cadherin	D-003877-02	GGAGAGCGGUGGUCAAAGAUU
E-Cadherin	D-003877-05	GCAGUACAUUCUACACGUAUU
E-Cadherin	D-003877-06	GAGAACGCAUUGCCACAUAUU
E-Cadherin	D-003877-07	ACCAGAACCUCGAACUAUAUU
p120 Catenin	D-012572-01	GCUAUGAGCUCUUAUUUCAUU
p120 Catenin	D-012572-02	GAAGUGAUCAUUCCUCAUUUU
p120 Catenin	D-012572-03	UAGCUGACCUCCUGACUAAUU
p120 Catenin	D-012572-04	GGACCUUACUGAAGUUAUUUU
RhoA	D-003860-01	GAGAUAUGGCAAACAGGAUUU
RhoA	D-003860-02	GAAAGACAUGCUUGCUCAUUU
RhoA	D-003860-03	GAACUAUGUGGCAGAUAUCUU
RhoA	D-003860-04	AUGGAAAGCAGGUAGAGUUUU
Rac1	D-003560-05	AGACGGAGCUGUAGGUAAAUU
Rac1	D-003560-07	UAAGGAGAUUGGUGCUGUAUU
Rac1	D-003560-08	UAAAGACACGAUCGAGAAAUU
Rac1	D-003560-09	CGGCACCACUGUCCCAACAUU
ROCK 1	D-003536-01	GGACACAGCUGUAAGAUUGUU
ROCK 1	D-003536-02	GAAGAAACAUUCCCUAUUCUU
ROCK 1	D-003536-03	GAGAUGAGCAAGUCAAUUAUU
ROCK 1	D-003536-05	GCCAAUGACUUACUUAGGAUU
Cofilin	D-012707-01	UGACAGGGAUCAAGCAUGAUU
Cofilin	D-012707-02	GCGGUGCUCUUCUGCCUGAUU
Cofilin	D-012707-03	GUCAAGAUGCUGCCAGAUAUU
Cofilin	D-012707-04	GCUAUGCCCUCUAUGAUGCUU
MST1	D-004157-01	CCAGAGCUAUGGUCAGAUA
MST1	D-004157-02	GUGAAACAGUGUCUUGUAA
MST1	D-004157-03	GAUGGGCACUGUCCGAGUA
MST1	D-004157-05	GCAGGUCAACUUACAGAUA
YAP1	D-012200-01	GGUCAGAGAUACUUCUUA
YAP1	D-012200-02	CCACCAAGCUAGAUAAAGA
YAP1	D-012200-03	GAACAUAGAAGGAGAGGAG
YAP1	D-012200-04	GCACCUAUCACUCUCGAGA

Table 2-6 siRNA

2.5 Immunofluorescence analysis

MCF-7 cells were plated on glass bottom dishes at 1 x 10^4 cells / cm^2 and cultured in DMEM with 10% FBS at 37 °C in 5% CO_2. Cells were fixed with 4% paraformaldehyde (PFA) in PBS at room temperature for 10 minutes and subsequently permeabilized with 0.1% Triton X-100 in PBS for 5 minutes. Inhibitor-treated cells were fixed 24 hours after inhibitor incubation and siRNA infected cells were fixed 48 hours after transfection. The cells were blocked with 1% BSA in PBS for 1 hour at room temperature and then incubated with primary antibodies at 4 ºC overnight (Table 2-7). The cells were next incubated with Alexa Fluor dye coupled secondary antibodies for 1 hour at room temperature. Nuclei were stained with DAPI (Sigma-Aldrich) and F-actin was stained with Phalloidin-Atto 633 (Sigma-Aldrich).

In the combinatorial imaging of FRET biosensor and immunostaining, images of the FRET biosensor must take in live cells because fixation with 4% PFA destroys FRET signals. Therefore, immunofluorescence images were taken after live cell imaging of FRET biosensor (Figure 2-4). The FRET biosensor-expressing MCF-7 cells were plated on glass bottom dishes and cultured in DMEM with 10% FBS at 37 °C in 5% CO_2. 3 hours before imaging, the media was changed to the phenol red free DMEM with 10% FBS. After FRET imaging, cells were fixed and stained as described above. Immunofluorescence images were acquired at the same position as live cell imaging.

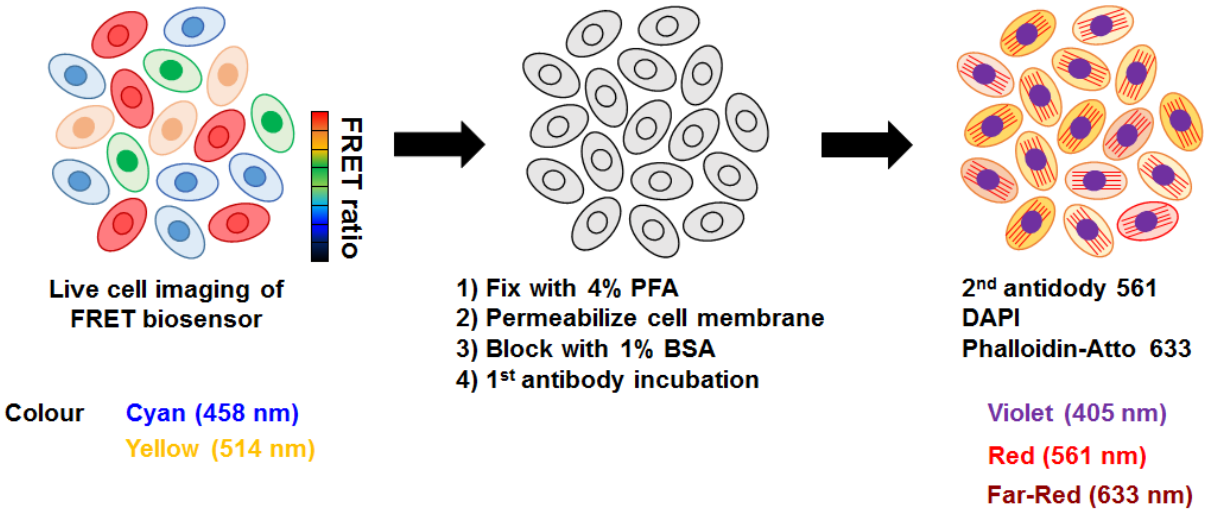


Figure 2-4 Experimental outline of immunofluorescence imaging.
Schematic representation of FRET imaging and immunofluorescence imaging. Combinatorial imaging of FRET biosensor and immunofluorescence can compare heterogeneous cell metabolism and other signalling information such as AKT phosphorylation levels and YAP nuclear/cytoplasm localisation.

1st Antibody	Company	Catalog number	Origin	Dilution
GLUT1	Abcam	ab15309	rabbit	1 / 500
phospho AKT (Ser473)	Cell Signaling	4060	rabbit	1 / 500
YAP	Cell signalling	14074	rabbit	1 / 500
2nd Antibody	Company	Catalog number	Origin	Dilution
Goat anti-Rabbit IgG, Alexa Fluor 555	Thermofisher Scientific	A-21429	Goat	1 / 2,000

Table 2-7 Antibodies for Immunofluorescence imaging

2.6 Immunohistochemistry

Immunohistochemical stains were performed on 5 µm tissue sections from xenograft tumours (see chapter 2.13). Xenograft tumours were quickly resected from the mice after intravital imaging and fixed with 4% PFA at 4 °C overnight. Fixed tumours were incubated with 30% sucrose in PBS at 4 °C until tumours sank to the bottom of the tube. The tumours were then immersed in OCT (Thermo Fisher Scientific) and frozen by ethanol chilled on dry ice. OCT blocks were sliced in 5 µm sections using a CM3050s Cryostat (Leica). The slices were permeabilized with 0.1% Triton X-100 in PBS for 5 minutes and blocked with 5% BSA in PBS for 1 hour at 4 °C. The sections were incubated with primary antibodies at 4ºC overnight and then incubated with Alexa Fluor dye-coupled secondary antibodies for 1 hour at room temperature (Table 2-7). Nuclei were stained with DAPI and F-actin was stained with Phalloidin-Atto 633.

2.7 Viability tests

2.7.1 Crystal violet staining

MCF-7 cells were plated on 12 well plates at 1 x 10^4 cells / cm^2. The cells were incubated with inhibitors for 7 days in DMEM with 10% FBS and then fixed with 4% PFA at room temperature for 10 minutes. Cells were washed with PBS and stained with 0.1% crystal violet in distilled water (DW) at room temperature for 30 minutes. Cells were washed with DW and plates were dried. Crystal violet intensity was measured using Epson Perfection V700 Photo scanner and quantified by Image J software.

2.7.2 IncuCyte S3 Live-Cell Analysis

MCF-7 cells were plated on 96 well plates at 1 x 10^4 cells / cm^2. The cells were incubated with inhibitors in DMEM with 10% FBS and the plates were placed into an IncuCyte S3 inside of incubator. Phase contrast images of the cells were acquired every 3 hours for 7

days using 10x objective. The average cell confluence was calculated from 3 phase contrast images acquired in each well. The growth rate of the cells was calculated as the change in cell confluence over time.

2.8 Seahorse assay

One day before oxygen consumption rate (OCR) and extracellular acidification rate (ECAR) measurements, the Seahorse XFe96 Analyser (Agilent) was turned on and warmed up to 37 °C. MCF-7 cells were plated on XF96 Cell Culture Microplates at 1 x 10^4 cells / well and cultured in DMEM with 10% FBS at 37 °C. XFe96 Sensor Cartridges were hydrated by calibrant solution at 37 °C in a non-CO_2 incubator overnight.

For OCR measurements, culture media was changed to Seahorse XF media (1 mM Pyruvate, 2 mM Glutamine, 25 mM Glucose, pH7.4) and incubated at 37 °C in the absence of CO_2 for 1 hour. OCR was measured 3 times after drug treatments with 6 minute intervals. Oligomycin, FCCP, and AntimycinA / Rotenone were added to final concentrations of 1 μM, 0.5 μM, and 0.5 μM respectively to measure “basal respiration”, “ATP production”, and “maximal respiration” (Figure 2-5A). For ECAR measurements, culture media was changed to Seahorse XF media (0 mM Pyruvate, 1 mM Glutamine, 0 mM Glucose, pH7.4) and incubated at 37 °C in the absence of CO_2 for 1 hour. ECAR was measured 3 times after drug treatments with 6 minute intervals. Glucose, Oligomycin, and 2-DG were added to final concentrations of 25 mM, 1 μM, and 50 mM respectively to measure “Glycolysis” and “Glycolytic capacity” (Figure 2-5B).

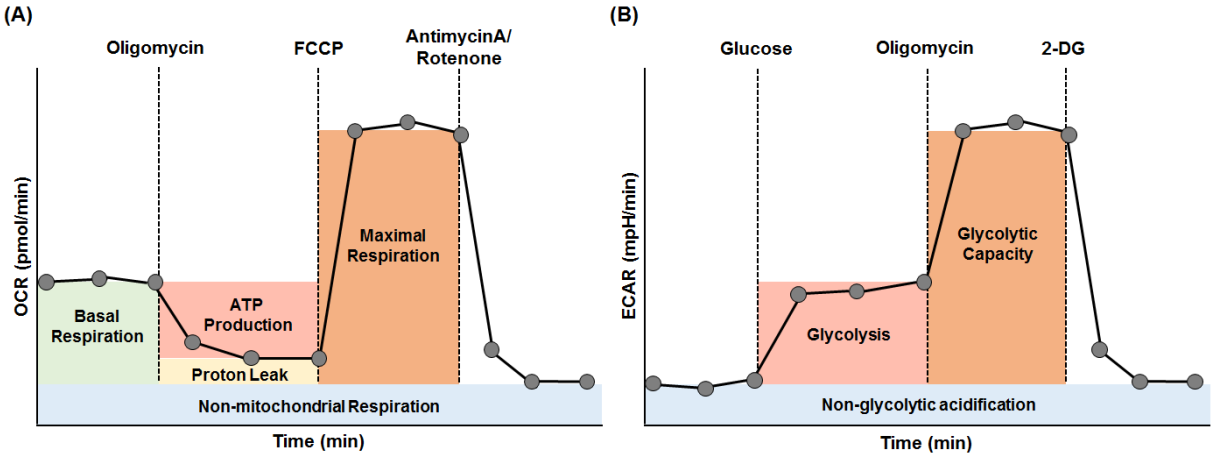


Figure 2-5 Seahorse analysis of OCR and ECAR.
(A) Seahorse analysis of OCR. Oligomycin inhibits ATP synthesis and FCCP uncouples proton gradient in mitochondria. AntimycinA and Rotenone inhibit mitochondrial complex I and III. (B) Seahorse analysis of ECAR. Glucose addition increases glucose-dependent glycolysis and inhibition of ATP synthesis by oligomycin maximizes glycolysis. 2-DG inhibits glycolysis.

2.9 Metabolomics

Metabolite profiling of MCF-7 cells under different conditions was performed by gas chromatography-mass spectrometry (GC-MS) analysis. For the metabolomic analysis of high and low glucose MCF-7 cells, FACS-isolated high and low glucose cells were plated on 60 mm dishes at 5 x 10^5 cells / dish and cultured in DMEM with 10% dialyzed FBS (Sigma) overnight at 37 °C (Figure 2-6A). For the metabolomic analysis of scratched and non-scratched cells, MCF-7 cells were plated on 60 mm dishes at 5 x 10^5 cells / dish and cultured in DMEM with 10% dialyzed FBS overnight at 37 °C. Plated cells were scratched roughly 50 times and cultured for an additional 24 hours (Figure 2-6B). For stable isotope labelling, cells were cultured in glucose-free DMEM with 10% dialyzed FBS and 25 mM U-^{13}C-glucose (CK isotope) for 90 minutes at 37 °C. The cells were washed with ice-cold PBS and suspended with 1.5 ml of metabolite extraction solution (water: methanol: chloroform = 1:3:1). The cell suspension was then sonicated and centrifuged at 13,000 g for 15 minutes. The supernatant was dried in a Speed Vac vacuum concentrator and resuspended in 50 µl chloroform, 150 µl methanol, and 150 µl water. The upper aqueous phase contained polar metabolites, and was derivatized by methoxyamine. Isotope tracer analysis of polar metabolites were performed using GS-MS (Agilent 7890A-5975C). These experiments were performed with the assistance of James Macrae and Jim Ellis in the metabolomics Science Technology Platform (STP).

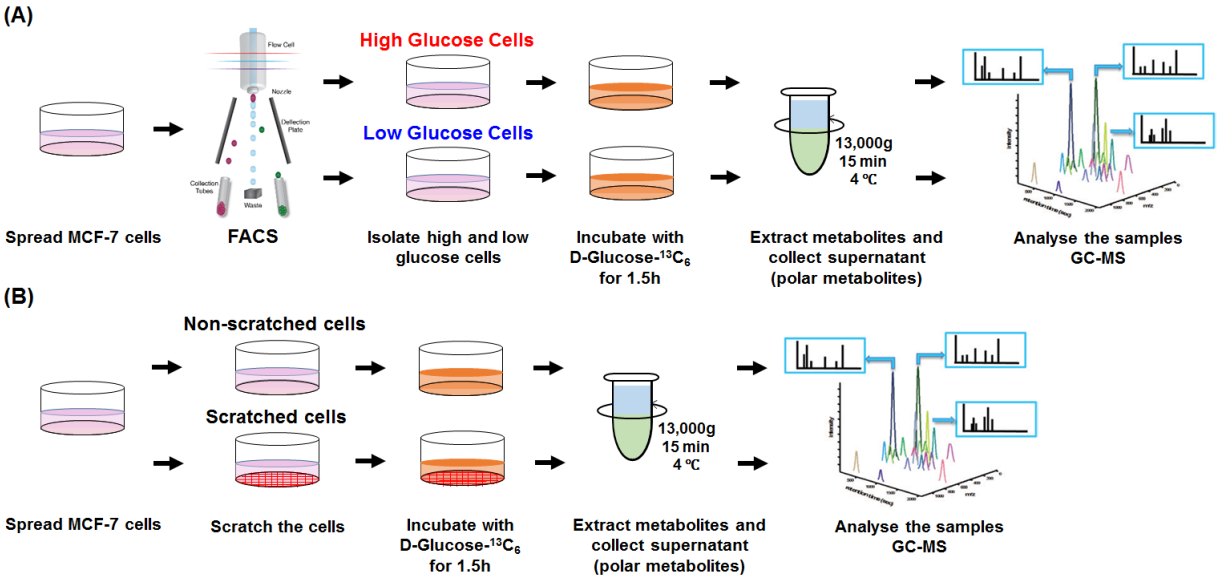


Figure 2-6 Experimental outline of metabolomic analysis.
(A, B) Schematic representation of metabolomic analysis in FACS-isolated high and low glucose cells, and scratched and non-scratched cells.

2.10 Migration Assays

2.10.1 Scratch assay

MCF-7 cells were plated on glass bottom dishes at 1 x 10^5 cells / cm^2 and cultured in phenol red free DMEM with 10% FBS for 24 hours at 37 °C. The cells were scratched at the centre of the well and time-lapse images were acquired every 5 minutes using an inverted Zeiss LSM 780 confocal microscope. Cells were imaged using a Plan-Apochromat 20x/0.8 NA objective lens and the emission signals were detected using Gallium arsenide phosphide (GaAsP) detectors. Cell migration and FRET ratio were measured and quantified by Image J software.

2.10.2 Wound healing assay

Removable culture inserts (Ibidi) were placed on glass bottom dishes and MCF-7 cells were plated at 2 x 10^4 cells / insert. Cells were cultured in phenol red free DMEM with 10% FBS for 24 hours at 37 °C. The removable culture inserts were removed from the glass bottom dishes and time-lapse images were acquired every 5 minutes using an inverted Zeiss LSM 780 confocal microscope. Cells were imaged using a Plan-Apochromat 20x/0.8 NA objective lens and the emission signals were detected using GaAsP detectors. Wound closures and FRET ratio were measured and quantified by Image J software.

2.11 Confocal microscopy

Confocal images were acquired using an inverted Zeiss LSM 780 confocal microscope. Cells were plated on glass bottom dishes at 1 x 10^4 cells / cm^2 and media was changed to phenol red free DMEM with 10% FBS at 3 hours before imaging. Imaging started 3 hours after changing media because FRET biosensors are very sensitive to temperature and pH. Excitation light from the Argon, DPSS 561 nm, and HeNe 633 nm lasers passed through MBS 458 or MBS 488/561/633 dichroic beam splitters. Cells were imaged using Plan-Apochromat 20x/0.8 NA objective lens and the emission signals were detected using GaAsP detectors. FRET images of glucose and ATP FRET biosensor were acquired with 458 nm excitation. Fluorescence was separated by beam splitters into 464-508 nm for eCFP and a 516-550 nm for FRET. FRET images of pyruvate and lactate FRET biosensors were also acquired with 458 nm excitation. Fluorescence was separated by beam splitters into 464-499 nm for mTFP and 520-560 nm for FRET. The emission signals of two

channels were simultaneously acquired with 458 nm excitation. Nuclei were stained with DAPI and images were acquired with 405 nm excitation and 410-460 nm signal detection. F-actin was stained with Phalloidin-Atto 633 and images were acquired with 633 nm excitation and 638-676 nm signal detection. In immunofluorescence imaging, Alexa Fluor 555 images were acquired with 561 nm excitation and 566-601 nm signal detection.

2.12 Mouse xenograft model

Animal experiments were performed in accordance with UK regulations under project license PPL/70/8380 and personal licence PIL/16907F0AA. Mouse xenograft tumours of MCF-7 cells were prepared by mammary fat pad injection in NOD SCID mice. NOD SCID mice have a severe immune deficiency due to mutation of the PRKDC gene (Table 2-8). Beta-estradiol pellets (0.72mg/pellet, 90 day release, Innovative Research of America) were implanted in NOD SCID mice a week before cell injection in order to provide estrogen required by MCF-7 cells for proliferation. After a week of pellet implantation, glucose FRET biosensor-expressing MCF-7 cells were trypsinized and re-suspended in 20% Matrigel (2 mg / ml) and 20% collagen I (2 mg / ml) in PBS at 2 x 10^7 cells / ml. 2 x 10^6 cells were injected under the fourth nipple into the mammary fat pad in Beta-estradiol pellet-implanted NOD SCID mice. Tumour size was monitored and measured twice a week. 10 - 14 days after cell injection, tumour size reached around 3 - 4 mm and images of developed tumours were acquired under terminal anesthesia using isofluorane.

Mouse xenograft tumours of MDA-MB-231 cells were prepared by mammary fat pad injection in BALB/c Nude mice. Glucose FRET biosensor-expressing MDA-MB-231 cells were trypsinized and re-suspended in 20% Matrigel (2 mg / ml) and 20% collagen I (2 mg / ml) in PBS at 2 x 10^7 cells / ml. 2 x 10^6 cells were injected under the fourth nipple into the mammary fat pad in BALB/c Nude mice. Tumour size was monitored and measured twice a week. 10 - 14 days after cell injection, tumour size reached around 3 - 4 mm and images of developed tumours were acquired under terminal anesthesia using isofluorane. These experiments were performed with the assistance of Steven Hooper in the Tumour Cell Biology Laboratory and Biological Research Facility (BRF) staff.

Strains	Hair	Thymus	T-Cells	B-Cells	NK-Cells	Complement
BALB/c Nude	-	-	-	+	+	+
NOD SCID	+	+	-	-	+	-

Table 2-8 Mouse models

2.13 Intravital imaging

Intravital images of the glucose FRET biosensor were acquired using an inverted Zeiss LSM 780 confocal microscope. Mice having 3-4 mm sized tumours underwent intravital imaging under terminal anaesthesia using isofluorane. A small incision was made in the skin to expose the tumour surface. The mouse was positioned on a heated microscope stage and the tumour surface was placed on the cover glass. The mouse was anesthetized throughout the imaging session. FRET images of the glucose FRET biosensor were acquired with 850 nm excitation using Mai Tai laser. Excitation light from the Mai Tai laser passed through MBS +690 dichroic beam splitters. Tumours were imaged using Plan-Apochromat 10x/0.45 NA or Plan-Apochromat 20x/0.8 NA objective lens and the emission signals were detected using GaAsP detectors. Fluorescence was separated by beam splitters into 464-508 nm for eCFP and a 516-550 nm for FRET. The emission signals of two channels were simultaneously acquired with 850 nm excitation. The images of second harmonic generation (SHG) were acquired with 850 nm excitation, and 390-450 nm signal detection. SHG images were sequentially acquired following with glucose FRET biosensor image acquisition.

2.14 Fluorescence lifetime imaging

A Simple-Tau TCSPC system (Becker & Hickl) with SPC-150 modules was connected to a Zeiss LSM 780. A Hybrid GaAsP detector was put in place for signal detection. Excitation light from the Mai Tai laser (90 MHz) passed through a 690 nm dichroic and a 690 nm short pass emission filter was employed to block far-red signals. eCFP signals of the glucose FRET biosensor were acquired with 850 nm excitation. Fluorescence was collected using a 465-495 nm band pass filter. Autofluorescence of NAD(P)H was acquired with 760 nm excitation. Fluorescence was collected using a 430-490 nm band pass filter. Fluorescence lifetime was measured using multifunctional 64 bit Data Acquisition Software. Images of 256 x 256 pixels with 256 time bins were acquired with 60 seconds exposure in order to acquire ~1000 photons per pixel. In order to accurately calculate the fluorescence lifetime, the fluorescence lifetime of gold nanorods (Sigma Aldrich) were measured for the instrument response function (IRF).

2.15 Image analysis

2.15.1 Ratiometric FRET

In the calculation of FRET ratio, individual cells were segmented and the intensities of donor and acceptor channels were measured following subtraction of background intensity. The FRET ratio was then calculated from the acceptor intensity divided by the donor intensity. FRET ratio was defined in the following equation.

$$\text{FRET ratio} = \frac{\text{Acceptor fluorescence intensity} - \text{background intensity}}{\text{Donor fluorescence intensity} - \text{background intensity}}$$

The 16 colours ratiometric images were created using ImageJ software. The background intensity of donor and acceptor images was subtracted using “Image Calculator”. Acceptor fluorescence intensity was then divided by donor fluorescence intensity using “Image Calculator”. Gray scale FRET images were converted to 16 colour ratiometric images using “Lookup Tables > 16 colors”. The range of ratiometric FRET images were optimized for each FRET biosensor. For time-lapse single cell analysis, individual cells were manually segmented and the FRET ratio in each time point was calculated as described above.

2.15.2 Kymographs

Kymographs were created from time-lapse images of glucose FRET biosensor-expressing breast cancer cells in the scratch and wound healing assay using Image J software. A kymograph of the scratch and wound healing assay represents cell migration over time with dynamic shifts of FRET ratio. Time-lapse images were rotated in vertical orientation to the wound. The images were then re-sliced from top to bottom using “Stacks > Reslice”. Re-sliced images of the donor and acceptor channels were processed to yield average-intensity projections. The average intensity of acceptor fluorescence intensity was then divided by the average intensity donor fluorescence intensity using “Image Calculator”. Gray scale images were converted to 16 colour ratiometric images using “Lookup Tables > 16 colors”. The range of ratiometric FRET images were optimized for each FRET biosensor.

2.15.3 Quantification of FRET ratio in xenograft tumours

The FRET ratio of the glucose FRET biosensor in xenograft tumours was quantified in centre-periphery axis using Image J software. Glucose FRET biosensor-expressing tumours were circled by a segmented line with 2,000 pixel line width (Figure 2-7). The circled tumours were aligned in a straight line using “Edit > Selection > Straighten”. Straightened images were then re-sliced from right to left using “Stacks > Reslice”. Re-sliced images of donor and acceptor channels were processed to yield average-intensity projections. The average intensity of acceptor fluorescence intensity was then divided by the average intensity donor fluorescence intensity using “Image Calculator”. The FRET ratio of the glucose FRET biosensor of the xenograft tumour in the centre-periphery axis was calculated using “Analyze > Plot profile”. The FRET ratio of glucose FRET biosensor in xenograft tumours was thus quantified from the whole tumour. The quantified FRET ratio of the glucose FRET biosensor represents the average FRET signals of tumours.

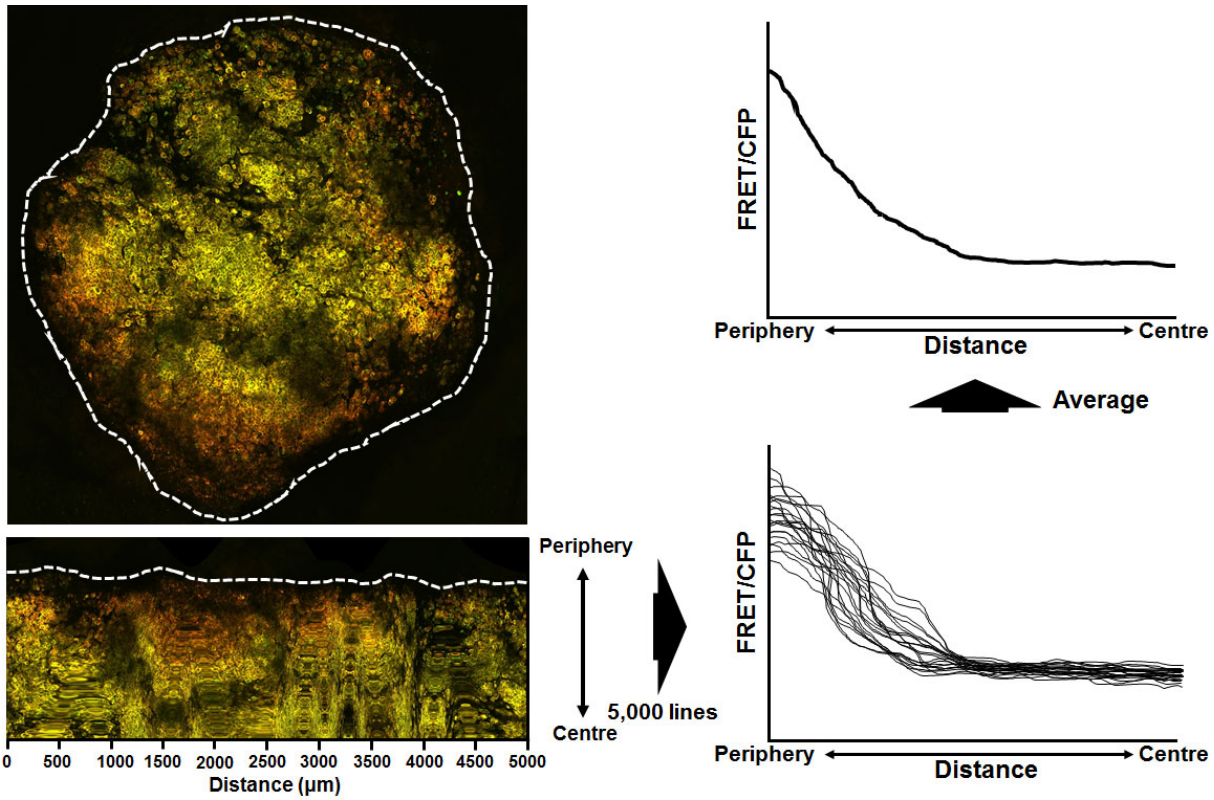


Figure 2-7 Quantification of FRET ratio in xenograft tumours

Schematic representation of FRET signal quantification in xenograft tumours.

2.15.4 Quantification of nuclei density in xenograft tumours

Nuclei density of xenograft tumours was quantified in centre-periphery axis using Image J software. DAPI stained xenograft tumours were circled by segmented line with 2,000 pixel line width (Figure 2-8). The circled tumours were aligned in a straight line using “Edit > Selection > Straighten”. Straightened images were converted to thresholded images using “Adjust > Threshold”. Straightened thresholded images were then re-sliced from right to left using “Stacks > Reslice”. Re-sliced images were processed to yield average-intensity projections. The nuclei density of xenograft tumours in the centre-periphery axis was quantified using “Analyze > Plot profile”. The nuclei density in xenograft tumours was thus quantified from whole tumours. The quantified nuclei density represents the average cell confluence of tumours.

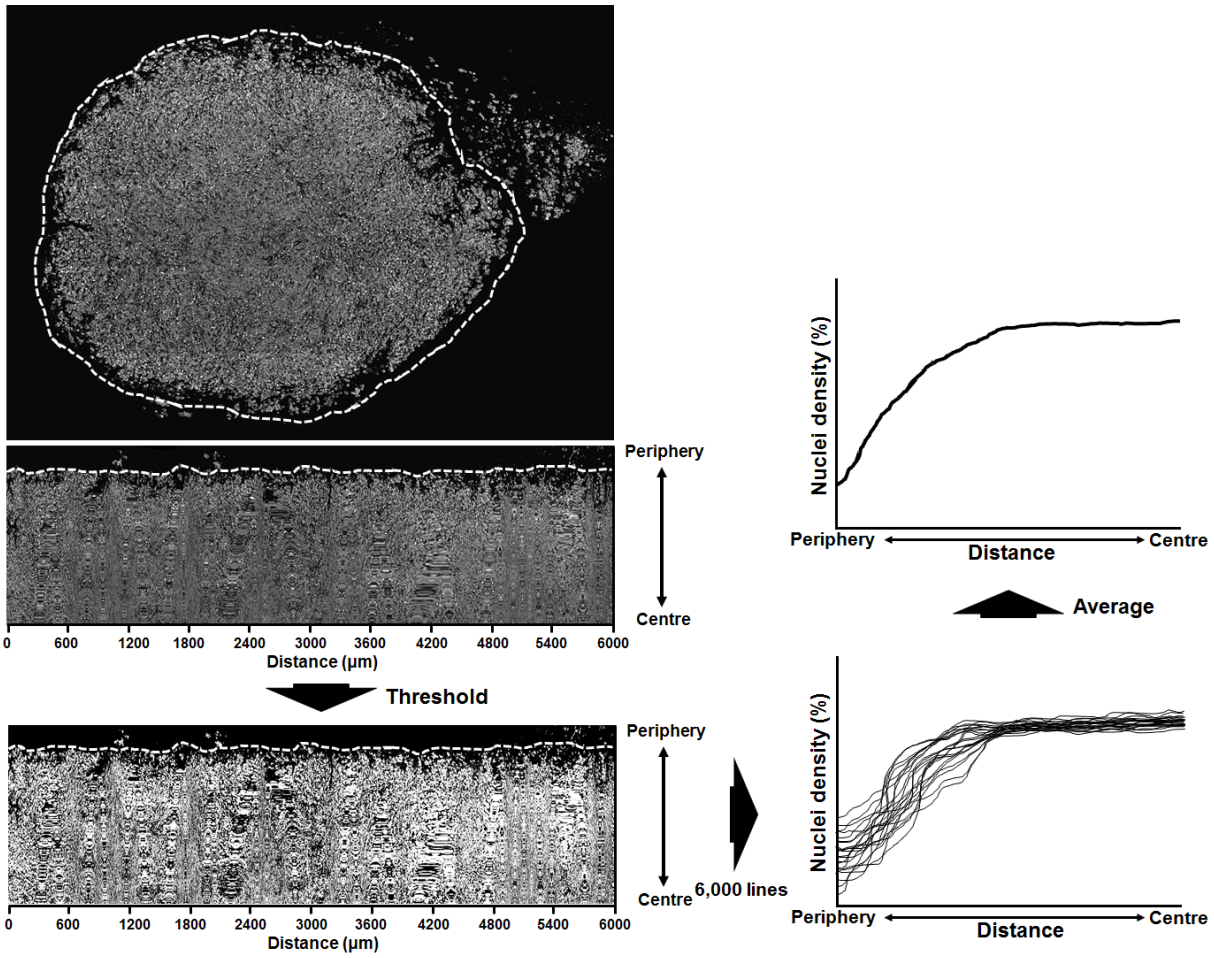


Figure 2-8 Quantification of nuclei density in xenograft tumours
Schematic representation of quantification of nuclei density in xenograft tumours.

2.15.5 FLIM-FRET

In the calculation of fluorescence lifetime of the glucose FRET biosensor, FLIM images and IRF were uploaded to FLIMfit software (Figure 2-9). The uploaded FLIM images were smoothed with 3x3 spatial averaging to reduce noise. In order to remove auto-fluorescence and the other weaker signals, the integrated minimum photon was set at 100 - 200. Fluorescence lifetime of the glucose FRET biosensor was analyzed by double exponential decay with automatic estimation. Two decay components represented FRET and non-FRET fluorescence decay. Fluorescence lifetime in FRET state is shorter than non-FRET state. A fluorescence lifetime fitting curve was calculated from photon counts in each time bin. Normalised residual represented the accuracy of fitting.

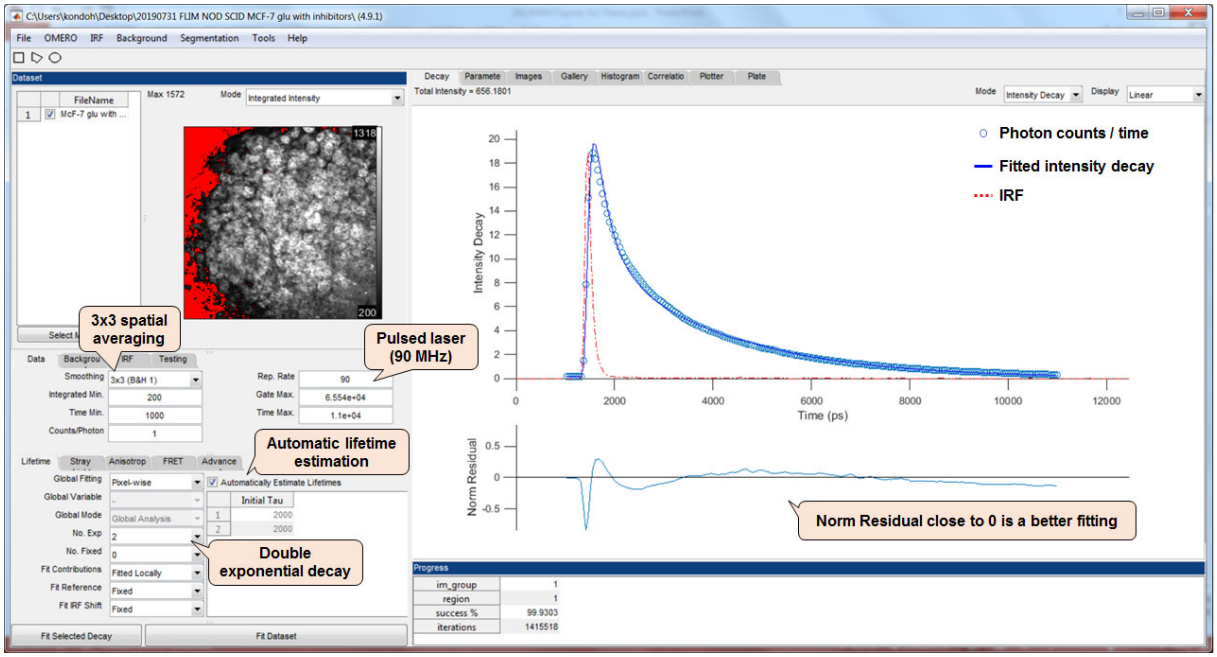


Figure 2-9 Fluorescence lifetime calculation using FLIMfit.
Overview of fluorescence lifetime calculation using FLIMfit software.

2.15.6 NAD(P)H fluorescence lifetime

In the calculation of fluorescence lifetime of NAD(P)H, FLIM images and IRF were uploaded to FLIMfit software. The uploaded FLIM images were smoothed with 3x3 spatial averaging to reduce noise. In order to remove auto-fluorescence and the other weaker signals, the integrated minimum photon was set at 100 - 200. Fluorescence lifetime of NAD(P)H was analyzed by triple exponential decay with fixed fluorescence lifetime, because this fitting process was better than double exponential decay with automatic

estimation and triple exponential decay with automatic estimation (Figure 2-10). NAD(P)H has a protein-bound and a protein-unbound form which have unique fluorescence lifetime. The fluorescence lifetime of protein-unbound form of NAD(P)H, protein-bound form of NADH, and protein-bound form of NADPH are estimated in 400 ps, 1,500 ps, and 4,400 ps, respectively [95]. The fluorescence lifetime of NAD(P)H represents the ratio of these three components. A fluorescence lifetime fitting curve was calculated from the photon counts in each time bin.

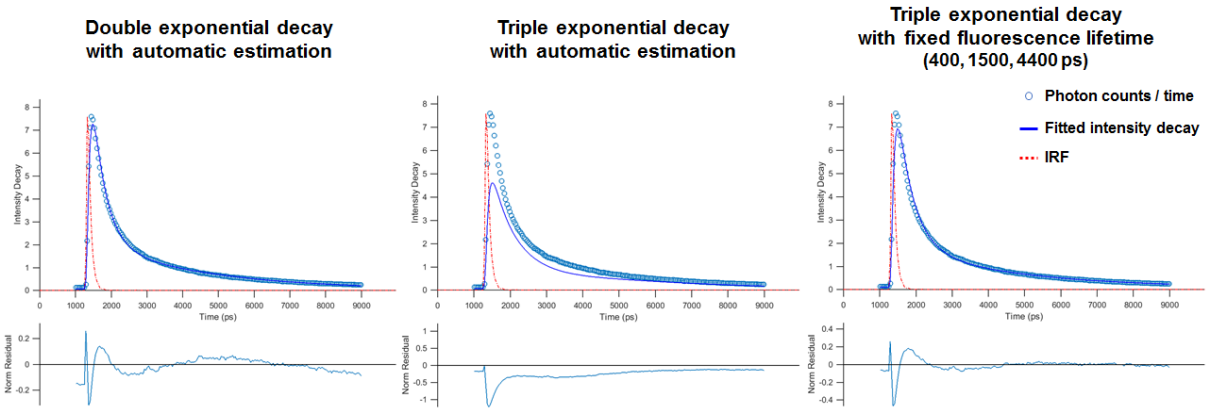


Figure 2-10 Fluorescence lifetime fitting curves of NAD(P)H.
Fluorescence lifetime fitting curves of NAD(P)H in three different conditions.

2.16 Statistics

P value and R square were calculated using GraphPad Prim. The unpaired T test compares the means of two unmatched groups with a Gaussian distribution and the same variances. Welch unpaired T test compares the means of two unmatched groups with different standard assumption. The Mann-Whitney test compares the median of two unmatched groups with equal variance. The Kolmogorov-Smirnov test compares the median of two unmatched groups with un-equal variance. The Mann-Whitney test has more power to detect a difference in the median but the Kolmogorov-Smirnov test has more power to detect differences in the shapes of the distributions. The P value is calculated to ask if there is a statistically significant difference between the mean of two groups. Each symbol has the following meanings. ns ($P > 0.05$), *($P < 0.05$), **($P < 0.01$), ***($P < 0.001$), ****($P < 0.0001$). The R^2 value quantifies the fraction of all the variation in the samples that is accounted for by a difference between the group means.

Chapter 3. Imaging metabolic heterogeneity of breast cancer

3.1 Chapter summary

In this chapter, I show breast cancer cell lines have heterogeneous cell metabolism. In cell metabolism research, metabolomic analysis has been widely used for the measurement of metabolic flux and metabolite levels. Multiplicity and complexity of cancer cell metabolism are expected. However, limitations of the available techniques have not allowed for accurate analysis of metabolic heterogeneity at the single cell scale. In order to analyse cancer cell metabolism at single cell resolution, I optimise nine different metabolic biosensors in MCF-7 cells, and modify the glucose FRET biosensor for multiplexed imaging. Multiplexed imaging of the glucose FRET biosensor with 2-NBDG, TMRE, and CellRox clarify that intracellular glucose levels indicate the balance of glycolysis and OXPHOS. In particular, high glucose cells have high glucose uptake and consumption. In contrast, low glucose cells have high mitochondrial membrane potential and ROS levels. Metabolomic analysis further reveals the details of glucose metabolism in high and low glucose cells.

3.2 Metabolic Biosensors

3.2.1 Glucose FRET Biosensor

A genetically encoded glucose FRET biosensor “FLIPglu-600u” was constructed by Takanaga H. *et al.* using bacterial mature glucose/galactose-binding protein MglB, eCFP, and Citrine [104]. The new glucose FRET biosensor “FLII^{12}Pglu-700μδ 6” divided MglB in two parts and improved the working range to detect intracellular glucose levels [100]. The mechanism of the glucose FRET biosensor is a conformational structural change of the biosensor by binding with glucose. The glucose-binding FRET biosensor can transfer the electric energy from eCFP to Citrine (Figure 3-1). Therefore, the FRET ratio of the glucose FRET biosensor is increased in high glucose conditions. This genetically encoded FRET biosensor can read out intracellular glucose levels at the single cell scale. Intracellular glucose levels are expected to represent metabolic states and extracellular glucose levels in tumour microenvironments. In the spheroid assay, multicellular spheroids of HEK293 cells showed that cells in the central area of spheroids have higher intracellular glucose levels [105]. Moreover, RasV12 transformed MDCK cells increased intracellular glucose levels but substantially diminished by the interaction with normal cells [106].

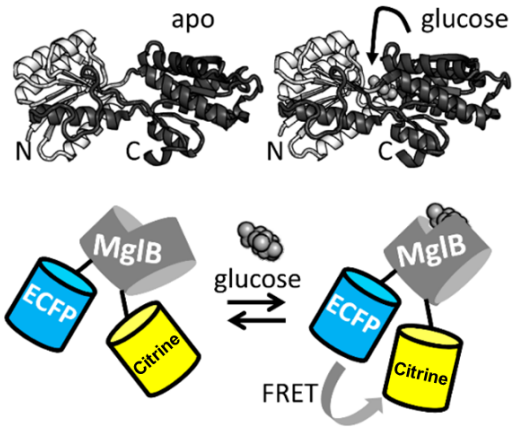


Figure 3-1 Glucose FRET biosensor.
Schematic representation of conformational shift of glucose FRET biosensor. Glucose FRET biosensor binds with intracellular glucose and then changes its conformational structure. The diagram is adapted from [107].

Glucose FRET biosensor "FLII^{12}Pglu-700μδ 6" expressing MCF-7 cells were established, and a point mutant of D183A in glucose FRET biosensor was constructed in order to reduce the glucose affinity of the MglB domain. First, I wished to exclude that glucose binding had a detrimental effect. The glucose FRET biosensor can bind with glucose and glucose captured by the FRET biosensor cannot be used for cell metabolism. Therefore, expression of the glucose FRET biosensor is expected to inhibit glucose metabolism. I analysed the effect of the glucose FRET biosensor expression on cell proliferation of MCF-7 cells using the IncuCyte S3 Live-Cell Analysis System (Figure 3-2). As a result, growth of wild type glucose FRET biosensor-expressing MCF-7 cells did not have a significant difference in proliferation compared with D183A mutant expressing MCF-7 cells.

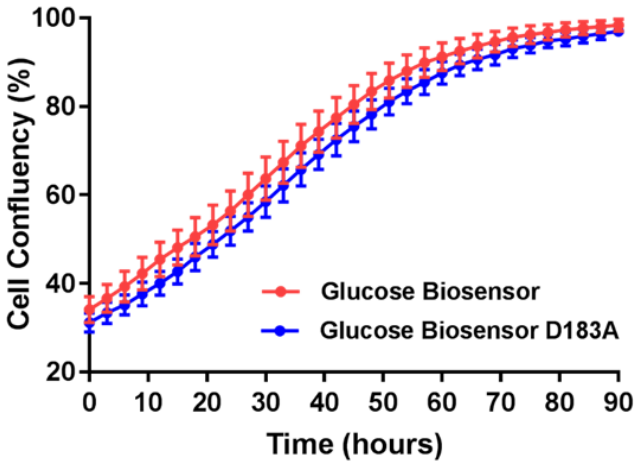


Figure 3-2 Proliferation of glucose FRET biosensor expressing MCF-7 cells.
Growth curve of stable cell lines of wild type and D183A glucose FRET biosensor expressing MCF-7 cells. Cell confluence was measured every 3 hours using IncuCyte S3 Live-Cell Analysis System. n > 20 wells for each condition from at least three independent experiments.

Next, the working range of the biosensor and the effect of biosensor expression levels on the FRET ratio were measured in different glucose concentrations (Figure 3-3A). Glucose FRET biosensor-expressing MCF-7 cells were incubated in media with different glucose concentrations for 1 hour and then the FRET ratio of individual cells was measured by live cell imaging. In 0 mM glucose media, the glucose FRET biosensor showed very low FRET ratio. On the other hand, MCF-7 cells in 25 mM glucose media showed a wide range of FRET ratios. This will be shown in more detail in chapter 3.3. Because the average FRET ratio of the glucose FRET biosensor was high in high glucose media, the biosensor indicated intracellular glucose levels were responding to extracellular glucose levels. The different FRET ratios of individual cells in the same condition indicates that the cells have heterogeneous metabolic states.

High biosensor expression is expected to increase the FRET ratio because the distance of each biosensor in the cells are closer than low biosensor expression. In this case, the donor fluorophore has more chance to transfer the electric energy to the acceptor fluorophore of the other biosensors. In order to exclude the effect of glucose biosensor expression levels on FRET ratio, I isolated the cell population which had similar biosensor expression levels by FACS. Next, I compared intracellular glucose levels and biosensor expression levels of MCF-7 cells in different glucose concentrations (Figure 3-3B). In all conditions, intracellular glucose levels were independent from biosensor expression levels.

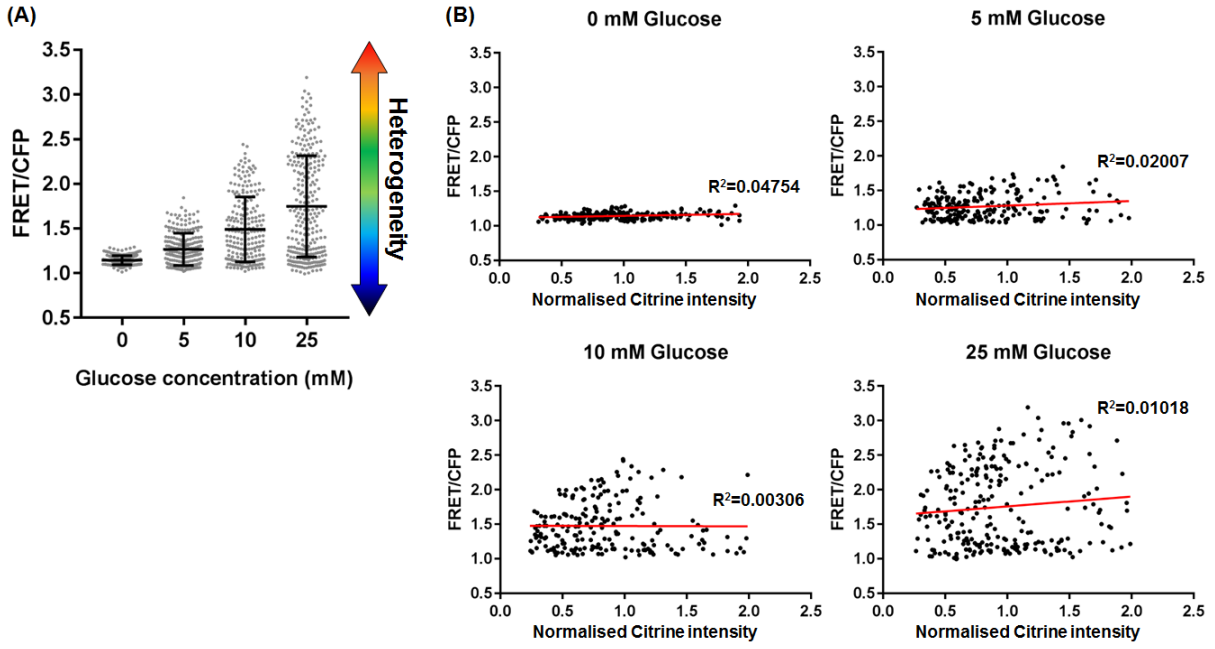


Figure 3-3 Working range of the glucose FRET biosensor in MCF-7 cells.
(A) Intracellular glucose levels of MCF-7 cells in 0, 5, 10, and 25 mM glucose media. Each dot represents FRET signals of individual cells. (B) Each plot show FRET signals against their normalised Citrine intensity in individual cells. n > 200 cells for each condition from at least three independent experiments.

3.2.1.1 Glucose FRET biosensor modification for multiplexed imaging

The fluorophore combination of the glucose FRET biosensor was changed from eCFP-Citrine to eCFP-sReACh and mTurquoise2-sReACh for multiplex imaging (Figure 3-4A). Because eCFP has a complex fluorescence decay and sensitivity to pH and temperature, mTurquoise2 was employed for the new biosensor [89]. For the purpose of multiplex imaging, sReACh is an ideal acceptor because this fluorophore can receive electric energy from a donor fluorophore but does not emit the light [108-110]. Fluorescence lifetime imaging of this single-color glucose FRET biosensor can read out intracellular glucose levels. In order to measure the working range of the new glucose FRET biosensors, the fluorescence lifetime of the donor fluorophore in each glucose FRET biosensor was measured by TCSPC FLIM (Figure 3-4B). The glucose FRET biosensors of the eCFP-Citrine pair and the eCFP-sReACh pair showed very similar working ranges. Fluorescence lifetime of the glucose FRET biosensor in 25 mM glucose is around 100 ps shorter than 0 mM glucose media. In addition, glucose FRET biosensors of the mTurquoise2-Venus pair and the mTurquoise2-sReACh pair also had very similar fluorescence lifetime. These two glucose FRET biosensors have longer fluorescence lifetime because the fluorescence lifetime of Turquoise2 is longer than eCFP. The fluorescence lifetime shifts of mTurquoise2-Venus and mTurquoise2-sReACh pair between 0 and 25 mM glucose were around 200 ps. Therefore, mTurquoise2-sReACh pair of the glucose FRET biosensor is the best candidate for multiplex imaging.

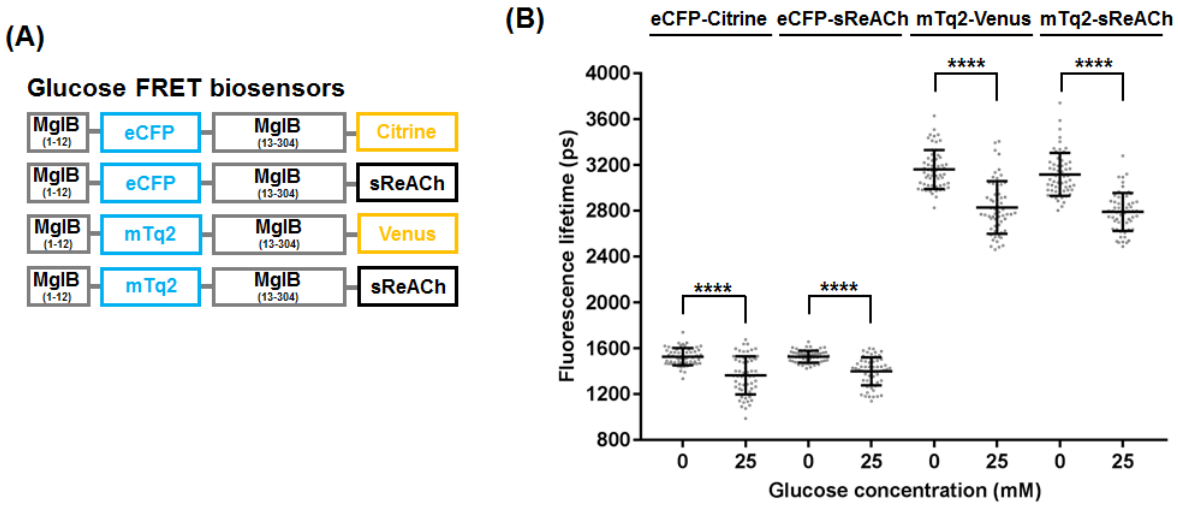


Figure 3-4 Fluorescence lifetime of four different glucose FRET biosensors.
(A) Glucose FRET biosensors with different fluorophore pairs. (B) Fluorescence lifetime of glucose FRET biosensors. Glucose FRET biosensor expressing MCF-7 cells were established and the cells were incubated in 0 or 25 mM glucose media for 1 hour. Fluoresce lifetime of donor fluorophore was measured by TCSPC FLIM. n > 60 cells for each condition from three independent experiments. ****p < 0.0001 Welch unpaired T test.

3.2.2 ATP FRET Biosensor

A genetically encoded ATP FRET biosensor "ATeam" was constructed by Imamura H. *et al.* using the ε subunit of Bacillus subtilis F_0F_1-ATP synthase, CFP (mseCFP), and YFP (cp173-mVenus) [103]. The mechanism of the ATP FRET biosensor is a conformational structural change of the biosensor by binding with ATP. The F_0F_1-ATP synthase domain can bind with ATP and increase the FRET ratio (Figure 3-5A). The ATP FRET biosensor is a common FRET biosensor in the field of neuroscience. Neurons require a large amount of ATP to keep ion gradients for signal transduction. Therefore, the ATP FRET biosensor has been used for the analysis of glycolysis and OXPHOS which have an impact on ATP production [111]. In addition, the ATP FRET biosensor can analyse intracellular ATP levels with spatiotemporal resolution. Migrating cells have different ATP demands within the cells and imaging ATP levels clarified that migrating cells increase ATP levels especially at invadopodia by promoting actin polymerization [112].

ATP FRET biosensor expressing MCF-7 cells were established and the working range of the biosensor was measured by comparing the FRET ratio in two conditions (Figure 3-5B). ATP FRET biosensor-expressing MCF-7 cells were incubated in 0 mM glucose with 2-DG and 25 mM glucose media for 1 hour and then the FRET ratio of individual cells was measured by live cell imaging. The difference in FRET ratio between 0 mM glucose with 2-DG and 25 mM glucose media is around 0.5, this wide working range can detect inter-cellular heterogeneous ATP levels.

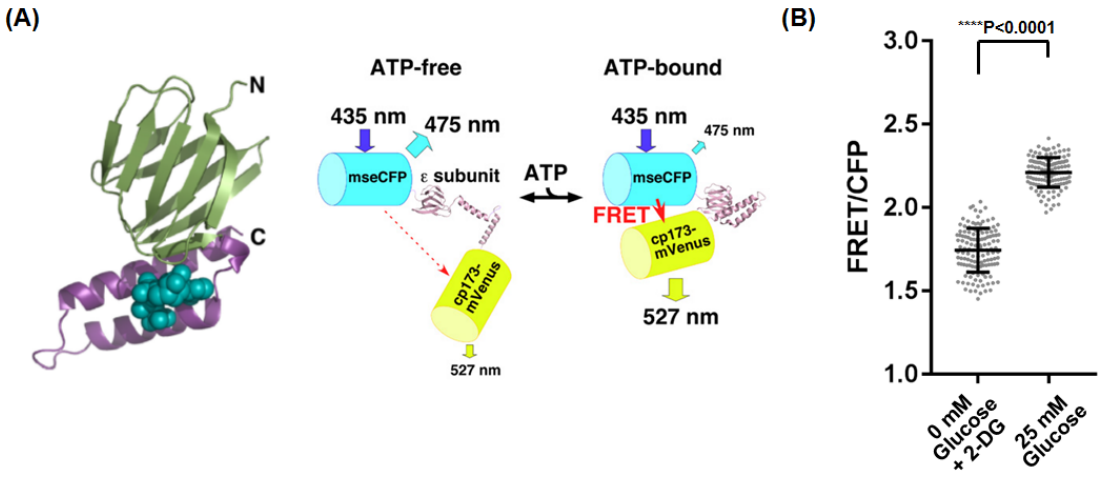


Figure 3-5 ATP FRET biosensor.
(A) Structure of the ε subunit of F_0F_1-ATP synthase and the ATP FRET biosensor consisting of mseCFP, ε subunit, and cp173-mVenus. The diagram is adapted from [103]. (B) ATP FRET biosensor expressing MCF-7 cells were incubated in 0 mM Glucose with 25 mM 2-DG and 25 mM glucose media for 1 hour and FRET signals were measured in individual cells. n > 100 cells for each condition from at least three independent experiments. . ****p < 0.0001 Welch unpaired T test.

3.2.3 AMPK FRET Biosensor

A genetically encoded AMPK FRET biosensor was constructed by Tsou P. *et al.* using forkhead-associated domain 1 (FHA1), AMPK substrate Acetyl-CoA carboxylase, eCFP, and Venus [113]. The dynamic range of the AMPK FRET biosensor was improved by changing its fluorophore combination to mTurquoise2 and Venus [114]. In this biosensor, the FRET ratio is increased by the phosphorylation of Serine 79 in the AMPK substrate Acetyl-CoA carboxylase (Figure 3-6A). Recently, the AMPK FRET biosensor consisting of α2β2γ1 AMPK heterotrimer, eCFP, and Venus was established [115]. The AMPK FRET biosensor has been used to read out energetic states and allosteric AMPK activity with spatiotemporal resolution. Specifically, transgenic mice of AMPK FRET biosensor were established and heterogeneous drug response was identified by intravital imaging [116]. AMPK FRET biosensor-expressing MCF-7 cells were established and the working range of the biosensor was measured by comparing the FRET ratio in two conditions (Figure 3-6B). MCF-7 cells were incubated in 0 mM glucose with 2-DG and 25 mM glucose media for 1 hour and then the FRET ratio of individual cells was measured by live cell imaging. 0 mM glucose with 2-DG media slightly increased AMPK activity and biosensor detected heterogeneous AMPK activity.

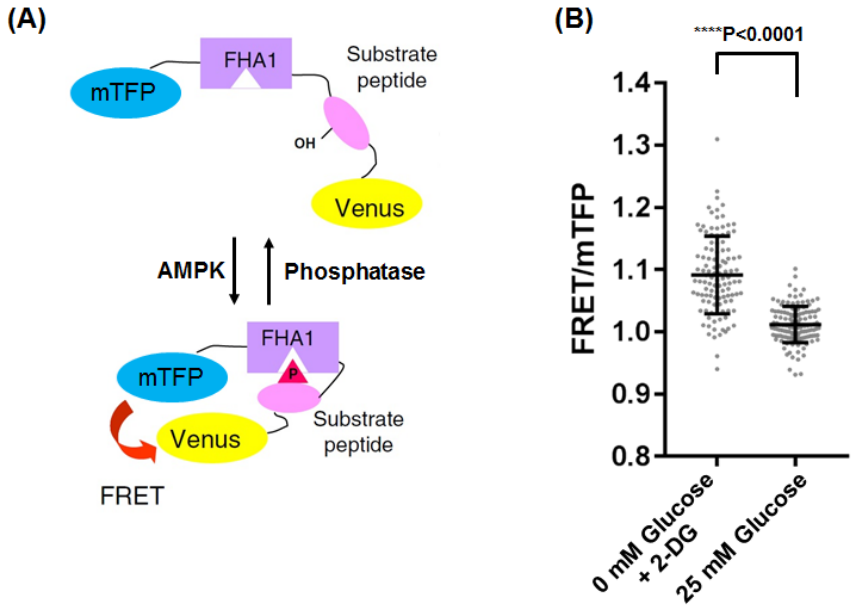


Figure 3-6 AMPK FRET biosensor.
(A) Structure of AMPK FRET biosensor consisting of eCFP, FHA1, AMPK substrate, and Venus. AMPK phosphorylates its substrate and changes the conformational structure of the AMPK FRET biosensor. The diagram is adapted from [113]. (B) AMPK FRET biosensor expressing MCF-7 cells were incubated in 0 mM Glucose with 25 mM 2-DG and 25 mM glucose media for 1 hour and FRET signals were measured in individual cells. n > 100 cells for each condition from at least three independent experiments. . ****p < 0.0001 Welch unpaired T test.

3.2.4 Pyruvate FRET Biosensor

A genetically-encoded pyruvate FRET biosensor "Pyronic" was constructed by San Martín A. *et al.* using bacterial pyruvate dehydrogenase complex regulator (PdhR), mTFP, and Venus (Figure 3-7A) [101]. In contrast to the glucose biosensor, the pyruvate FRET biosensor has a lower FRET ratio upon pyruvate binding. The original structure of the pyruvate FRET biosensor has a shorter distance between mTFP and Venus, pyruvate binding can open this structure. A pyruvate FRET biosensor reporter mouse line was generated and imaging of intracellular pyruvate levels revealed a dynamic change of cytosolic pyruvate levels during embryonic development [117].

Pyruvate FRET biosensor-expressing MCF-7 cells were established and the working range was measured by comparing the FRET ratio in two different conditions (Figure 3-7B). Pyruvate FRET biosensor-expressing MCF-7 cells were incubated in 0 mM and 25 mM glucose media for 1 hour and then the FRET ratio of the individual cells was measured by live cell imaging. The FRET ratio of the pyruvate FRET biosensor shifted 0.05 on average from 0 mM to 25 mM glucose media. Because extracellular glucose level can change intracellular pyruvate levels, glucose is a key nutrient source to generate pyruvate in MCF-7 cells. Although the working range of the pyruvate FRET biosensor is smaller than the glucose FRET biosensor, this biosensor can detect heterogeneous intracellular pyruvate levels.

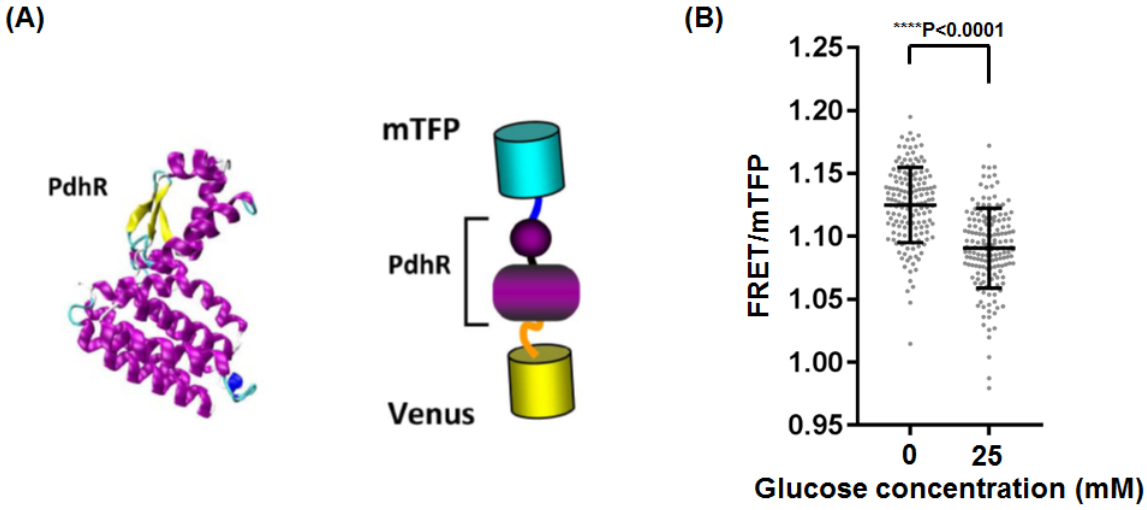


Figure 3-7 Pyruvate FRET biosensor.
(A) Structure of PdhR and pyruvate FRET biosensor consisting of mTFP, PdhR and Venus. The diagram is adapted from [101]. (B) Pyruvate FRET biosensor expressing MCF-7 cells were incubated in 0 mM and 25 mM glucose media for 1 hour and then FRET signals were measured at single cell resolution. n > 100 cells for each condition from at least three independent experiments. ****p < 0.0001 unpaired T test.

3.2.5 Lactate FRET Biosensor

A genetically encoded lactate FRET biosensor “Laconic” was constructed by San Martín A. *et al.* using bacterial L-lactate dehydrogenase regulator (LldR), mTFP, and Venus (Figure 3-8A) [102]. The lactate FRET biosensor has a similar FRET mechanism with the pyruvate FRET biosensor. The lactate FRET biosensor can bind with lactate and reduce the FRET ratio. This FRET biosensor has been used for the research of cell metabolism. Recent research using the lactate FRET biosensor clarified that hyperglycaemia induces an increase of intracellular lactate concentration [118]. In addition, the lactate FRET biosensor was used for the measurement of lactate uptake in Huntington’s disease cells [119]. Huntington’s disease cells change the expression levels of GLUT3 and remodel lactate metabolism.

Lactate FRET biosensor-expressing MCF-7 cells were established and the working range was measured by comparing the FRET ratio in the two different conditions (Figure 3-8B). Lactate FRET biosensor-expressing MCF-7 cells were incubated in 0 mM and 25 mM glucose media for 1 hour and then the FRET ratio of individual cells was measured by live cell imaging. The difference of FRET ratio between 0 mM and 25 mM glucose media is around 0.08. Although the working range of the lactate FRET biosensor is small, this biosensor can detect heterogeneous intracellular lactate levels.

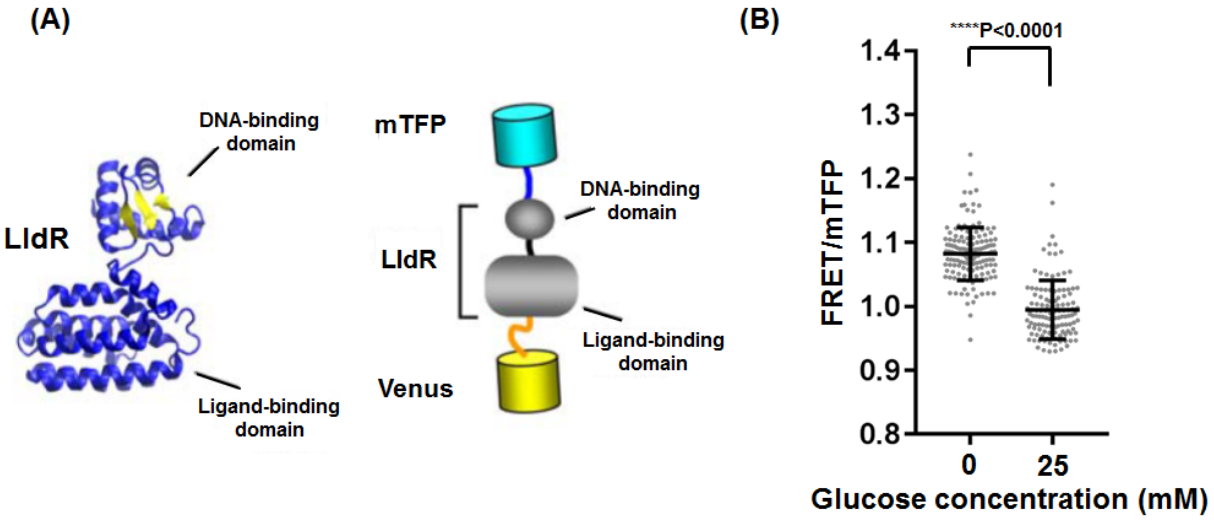


Figure 3-8 Lactate FRET biosensor.
(A) Structure of LldR and lactate FRET biosensor consisting of mTFP, LldR, and Venus. The diagram is adapted from [102]. (B) Lactate FRET biosensor expressing MCF-7 cells were incubated in 0 mM and 25 mM glucose media for 1 hour and then FRET signals were measured at single cell resolution. n > 100 cells for each condition from at least three independent experiments. ****p < 0.0001 unpaired T test.

3.2.6 NAD(P)H

Many metabolic pathways utilize NAD^+/NADH and $NADP^+$/NADPH to facilitate both catabolism and anabolism. The fluorescence lifetime of the protein-unbound form of NAD(P)H is 400 ps and mitochondrial complex 1 utilises the protein-unbound form of NADH to transport protons into the inter-membrane space [95]. This reaction reduces the ratio of the protein-unbound form of NADH from the total population of NAD(P)H. In contrast, fluorescence lifetime of the protein-bound form of NAD(P)H is longer than the protein-unbound from of NAD(P)H. Therefore, a shorter fluorescence lifetime of NAD(P)H indicates high glycolysis/OXPHOS ratio, and a longer fluorescence lifetime represents low glycolysis/OXPHOS ratio.

Fluorescence lifetime imaging can determine the relative proportion of protein-bound and protein-unbound NAD(P)H in living cells. MCF-7 cells were incubated with the proton uncoupler, FCCP, or the mitochondrial complex I inhibitor, Rotenone, and the fluorescence lifetime of NAD(P)H was measured at four time points (Figure3-9). The fluorescence lifetime of NAD(P)H is increased by treatment with FCCP, and decreased by Rotenone. Thus, autofluorescence of NAD(P)H can be used as a non-invasive metabolic indicator.

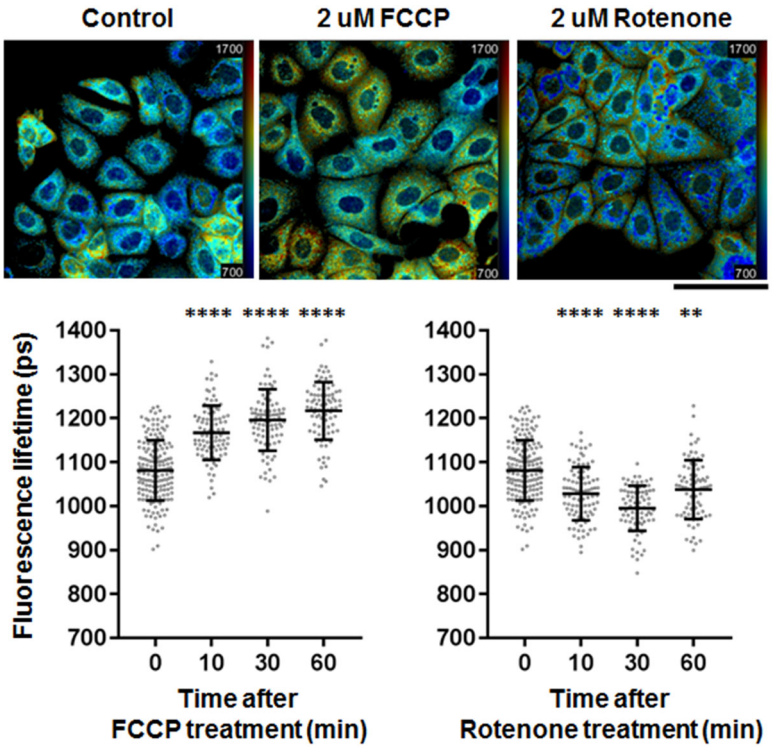


Figure 3-9 Fluorescence lifetime imaging of NAD(P)H
Fluorescence lifetime of NAD(P)H was measured after 2 μM FCCP or 2 μM Rotenone treatment. The FLIM images of NAD(P)H were acquired 60 minutes after inhibitor treatment. Scale=100 μm. n > 100 cells for each condition from at least three independent experiments. **P < 0.01, ****P < 0.0001 unpaired T test.

3.2.7 2-NBDG

2-NBDG is a fluorescence labelled glucose which is an indicator of glucose uptake (Figure 3-10A). Once 2-NBDG is taken into the cells, it is phosphorylated at the C-6 position and well retained in the cells. 2-NBDG has been widely used for the analysis of glucose metabolism, especially in tumour cell biology. 2-NBDG high throughput fluorescence screening has clarified that lung cancer cells having high glucose uptake ability frequently acquire mutations at EGFR and PIK3CA [120]. In addition, multiplexed imaging of 2-NBDG and TMRE has revealed that $Her2^{+}$ breast cancer can switch glycolysis and OXPHOS depending on Her2 expression levels [121]. Thus, a multiplexed imaging approach can be applied for intravital imaging [122], 2-NBDG is a good indicator of glucose metabolism.

MCF-7 cells were plated and cultured in 25 mM glucose DMEM. The cells were then incubated with 100 μM 2-NBDG for 1 - 3 hours and the glucose uptake speed was measured by fluorescence intensity measurement (Figure 3-10B, C). The difference of 2-NBDG average intensity between 2 and 3 hours incubation was smaller than the difference between 1 and 2 hours incubation. 2-NBDG is well retained in the cells, long term incubation can gradually saturate intracellular 2-NBDG levels. In addition, minimising the 2-NBDG concentration is very important because saturated 2-NBDG inhibits glucose metabolism. Furthermore, the standard deviation of 2-NBDG intensity at 1 hour of incubation was smaller than at 2 hour of incubation. From these reasons, 2 hours incubation is the best labelling time to analyse heterogeneous glucose metabolism in MCF-7 cells.

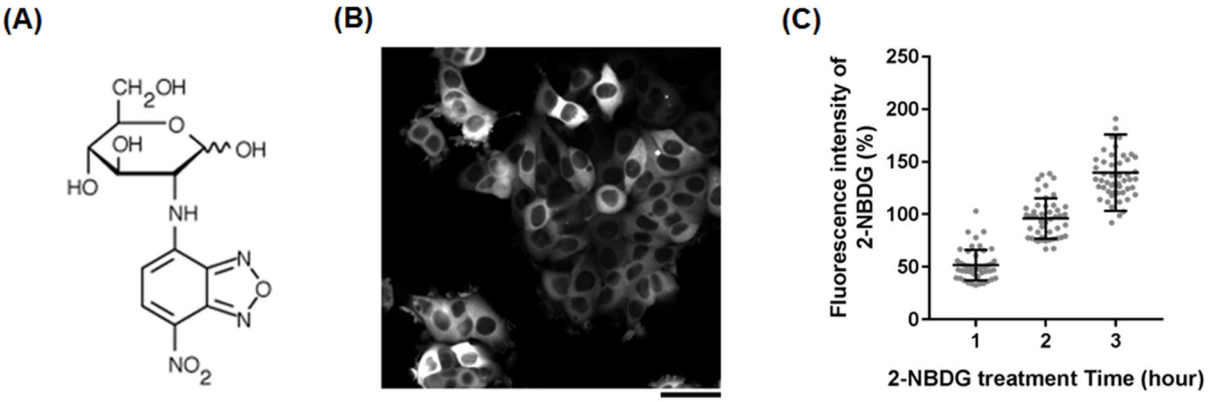


Figure 3-10 Fluorescence imaging of 2-NBDG.
(A) Chemical structure of 2-NBDG. Its molecular formula is $C_{12}H_{14}N_4O_8$ and molecular weight is 342.2646. (B) Fluorescence image of MCF-7 cells labelled with 100 μM 2-NBDG for 2 hours. Scale = 50 μm (C) Normalised fluorescence intensity of 2-NBDG in MCF-7 cells. The cells were incubated with 100 μM 2-NBDG for 1-3 hours and then fluorescence intensity was measured at single cell resolution. n > 50 cells for each condition from at least three independent experiments.

3.2.8 TMRE

Mitochondrial membrane potential can be measured using lipophilic cationic probes. The ester group of TMRE provides lipophilicity and the positive charge of the oxidized iminium cation facilitates mitochondrial membrane permeability (Figure 3-11A) [123]. TMRE can accumulate within the mitochondria depending on the mitochondrial membrane potential. The basic mitochondrial membrane potential of cancer cells is around 150 - 180 mV across the mitochondrial inner membrane and TMRE accumulation increases 10-fold for every 61.5 mV at 37 °C [124].

MCF-7 cells were plated and cultured in 25 mM glucose DMEM. The cells were then incubated with 100 nM TMRE for 10 - 60 minutes and the mitochondrial membrane potential was analysed by fluorescence intensity measurement (Figure 3-11B, C). There was no significant difference of TMRE intensity among three different time points, indicating that TMRE can accumulate in mitochondria within 10 minutes. In addition, the ATP synthase inhibitor, Olygomycin, can increase TMRE intensity. Oligomycin can stop proton transport from the inter-membrane space to the matrix, mitochondrial membrane potential is increased by Oligomycin treatment. In contrast, the proton gradient uncoupler, FCCP, dramatically reduced TMRE intensity. FCCP can reduce the proton gradient in mitochondria by diffusing protons through the mitochondrial membrane. Thus, TMRE can read out heterogeneous mitochondrial membrane potential in MCF-7 cells.

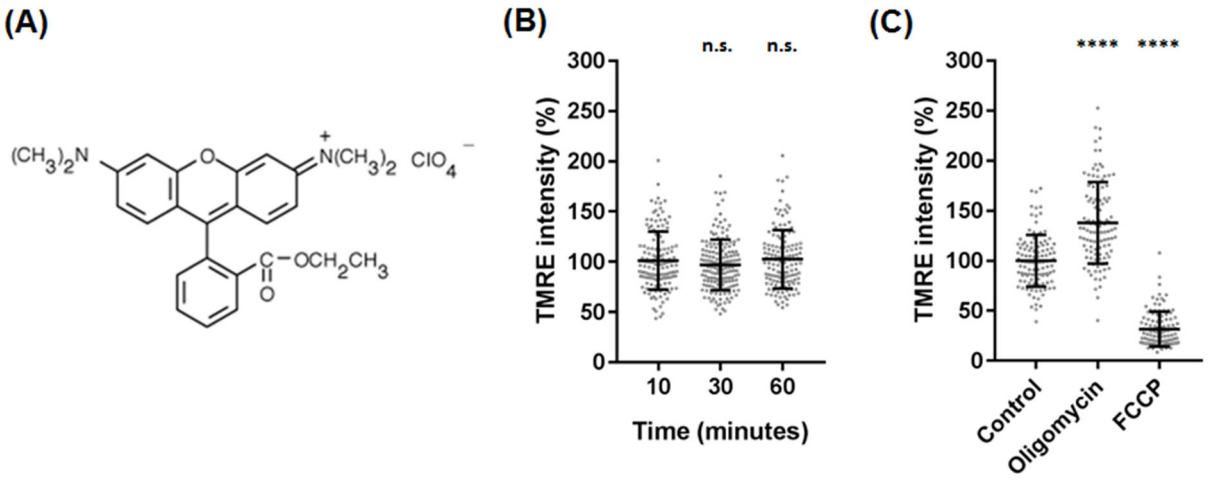


Figure 3-11 Fluorescence imaging of TMRE.
(A) Chemical structure of TMRE. Its molecular formula is $C_{26}H_{27}ClN_2O_7$ and molecular weight is 514.9615. (B) Normalised fluorescence intensity of TMRE in MCF-7 cells incubating for 10, 30, 60 minutes. (C) Normalised fluorescence intensity of TMRE in MCF-7 cells incubating for 10 minutes with 2 μM oligomycin and 2 μM FCCP. n > 100 cells for each condition from at least three independent experiments. n.s. $p > 0.05$, ****$P < 0.0001$ unpaired T test.

3.2.9 CellRox

CellRox is an indicator of ROS levels which has a strong positive correlation with mitochondrial membrane potential [125, 126]. ROS production is dramatically increased above 140 mV of mitochondrial membrane potential. CellRox can measure ROS production through changing its fluorescence intensity. CellRox does not emit fluorescence in a reduced state but oxidation can enhance fluorescence intensity (Figure 3-12A). CellRox has a series of colour regents such as green, orange, and far red. Therefore, this ROS sensitive fluorescence dye is useful for the multiplexed imaging of cell metabolism. Recent researches have used CellRox for the analysis of inhibitors in cell metabolism [127-129].

MCF-7 cells were plated and cultured in 25 mM glucose DMEM. The cells were incubated with 2 μM FCCP and 2 μM Oligomycin for 1 hour at 37 °C. Inhibitor-treated cells were then stained with 5 μM CellRox Deep Red Reagent for 30 minutes at 37 °C. Intracellular ROS levels were analysed by measuring fluorescence intensity of CellRox (Figure 3-12B). The proton gradient uncoupler, FCCP, significantly reduced and the ATP synthase inhibitor, Oligomycin, increased CellRox intensity. An increase of the mitochondrial membrane potential by inhibition of ATP synthase can increase ROS production [130]. On the other hand, lower mitochondrial membrane potential and decreased respiratory chain activity reduce ROS production [131]. Thus, CellRox imaging data matched with previous reports and fluorescence imaging of CellRox can read out ROS levels at single cell resolution.

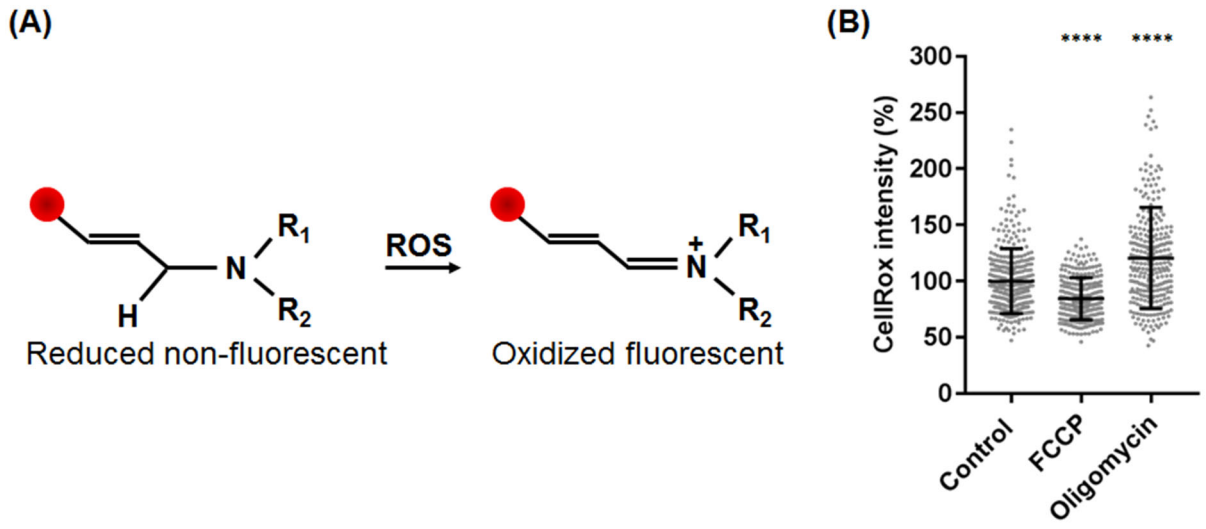


Figure 3-12 Fluorescence imaging of CellRox.
(A) The mechanism of CellRox to change fluorescence intensity. (B) Normalised fluorescence intensity of CellRox in MCF-7 cells incubating with 2 μM FCCP or 2 μM oligomycin. n > 200 cells for each condition from at least three independent experiments. ****P < 0.0001 Welch unpaired T test.

3.2.10 Summary of biosensor optimisation

In my research, I optimised a total of nine different biosensors in MCF-7 cells in order to analyse metabolic heterogeneity. Each biosensor has a different working range and their sensitivities are very important to read out heterogeneous metabolic states (Table 3-1). Among FRET-based biosensors, the glucose FRET biosensor has a great working range to detect intracellular glucose levels. In particular, the cells in high glucose media showed highly heterogeneous glucose levels. The ATP biosensor is also a good biosensor to read out different energetic conditions at the single cell scale. On the other hand, AMPK, pyruvate, and lactate FRET biosensors have small working ranges. The design of the FRET-based biosensors is a fundamental reason for these different sensitivities. In addition, fluorescence lifetime imaging of NAD(P)H is also a good candidate for imaging heterogeneous metabolism. Its working range is around 500 ps and it can analyse heterogeneous glycolysis/OXPHOS ratio at single cell resolution. 2-NBDG, TMRE, and CellRox are also excellent biosensor to read out heterogeneous glucose uptake, the mitochondrial membrane potential, and intracellular ROS levels. Specifically, TMRE and CellRox have a wide range of intensity and their fluorescence colours do not overlap with FRET-based biosensors. Taken together, the glucose FRET biosensor is the primary biosensor and the other three dyes can be used for multiplexed imaging.

FRET-based Biosensors	Donor	Acceptor	Working range (FRET ratio)	Heterogeneity detection
Glucose biosensor	eCFP	Citrine	1.0 - 3.5	◎
ATP biosensor	mseCFP	mVenus	1.5 - 2.5	○
AMPK biosensor	mTFP	Venus	0.9 - 1.2	△
Pyruvate biosensor	mTFP	Venus	1.0 - 1.2	△
Lactate biosensor	mTFP	Venus	0.9 - 1.2	△
FRET-based Biosensors	**Donor**	**Acceptor**	**Working range (lifetime)**	**Heterogeneity detection**
Glucose biosensor	eCFP	Citrine	1,000 - 1,700 ps	◎
Glucose biosensor	eCFP	sReACh	1,000 - 1,700 ps	◎
Glucose biosensor	mTq2	Venus	2,500 - 3,300 ps	◎
Glucose biosensor	mTq2	sReACh	2,500 - 3,300 ps	◎
Autofluorescence	**Colour**		**Working range (lifetime)**	**Heterogeneity detection**
NAD(P)H	Blue		900 - 1,400 ps	○
Dyes	**Colour**		**Working range (intensity)**	**Heterogeneity detection**
2-NBDG	Green		70 - 140 %	○
TMRE	Red		20 - 250 %	◎
CellRox	Far-Red		50 - 250 %	◎

Table 3-1 Working range of biosensors.
Heterogeneity detection (◎ Great, ○ Good, △ Bad)

3.3 Metabolic heterogeneity of breast cancer cell lines

3.3.1 Heterogeneity of intracellular glucose levels

In biosensor optimisation, I found MCF-7 cells have heterogeneous intracellular glucose levels. Although the cells were cultured in the same media, cells had heterogeneity of intracellular glucose levels (Figure 3-13A). The FRET distribution of the glucose FRET biosensor in MCF-7 cells showed that many cells can keep low glucose states in high glucose DMEM (Figure 3-13B). These different intracellular glucose levels could be established by different demands for cellular glucose as a nutrient source. Cancer cells can utilise many nutrient sources such as glucose, glutamine, fatty acids, and amino acids. Because glycolytic and OXPHOS cells have different nutrient demands to facilitate their metabolic routes, the amount of glucose uptake and consumption should be different in each cell (Figure 3-13C). If cellular intake of glucose is larger than glucose consumption, intracellular glucose levels of the cells may be high. On the other hand, if cellular intake of glucose is smaller than glucose consumption, intracellular glucose levels of the cells may be low. Thus, intracellular glucose levels can be established by the balance of glucose uptake and consumption.

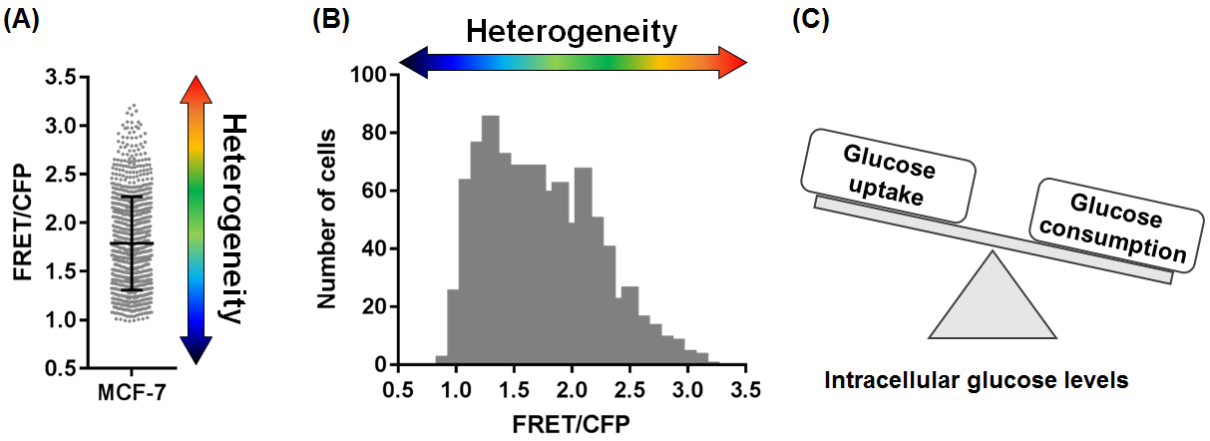


Figure 3-13 Heterogeneity of intracellular glucose levels.
(A, B) Intracellular glucose levels of MCF-7 cells in 25 mM glucose media. Following single cell segmentation, distribution of intracellular glucose levels were analysed in MCF-7 cells. n > 500 cells from three independent experiments. (C) Expected model to determine intracellular glucose levels.

3.3.2 Intracellular glucose levels discriminate glycolysis and OXPHOS

Breast cancer cells have heterogeneous intracellular glucose levels. In order to analyse the mechanism to establish different intracellular glucose levels, I measured glucose uptake and consumption of MCF-7 cells by changing the glucose concentration of media (Figure 3-14A). Glucose uptake and consumption speed can be calculated from the shifts of FRET ratio at single cell resolution. Individual cells were segmented and glucose levels were tracked during cell incubation in 0 mM and 25 mM glucose media. In 25 mM glucose the cells showed heterogeneous glucose levels and intracellular glucose levels dramatically declined by incubating in 0 mM glucose media. High glucose cells could have higher glucose consumption because of sharp intracellular glucose reduction. In contrast, low glucose cells had a slower rate of intracellular glucose decline. After 30 minutes incubation in 0 mM glucose DMEM, the media was replaced with 25 mM glucose DMEM and intracellular glucose levels were further measured for an additional 60 minutes. The increase of intracellular glucose levels indicates the rate of “glucose uptake - glucose consumption”. Because high glucose cells returned to the high glucose states, high glucose cells could have higher glucose uptake.

From the segmentation of single cells and tracked intracellular glucose levels, I found intracellular glucose levels were highly correlated with glucose uptake speed (Figure 3-14B). Glucose uptake of high glucose cells was significantly higher than low glucose cells. In addition, glucose consumption of high glucose cells was also higher than low glucose cells (Figure 3-14C). These results indicate that high glucose cells use glucose faster than low glucose cells. In addition, comparing glucose uptake and consumption speed, glucose uptake speed was slightly higher than glucose consumption speed in most of the cells. Therefore, glucose uptake rate would be a key regulator of glucose metabolism. Breast cancer cell lines have different expression levels of glucose transporters and monocarboxylate transporters (MCTs) [132-134]. The difference of glucose transporter expression in individual cells could change glucose metabolism and establish metabolic heterogeneity. In particular, GLUT1 and GLUT4 are the key glucose transporters in breast cancer cells [135], analysis of the expression levels of these two glucose transporters in high and low glucose cells will help to clarify the mechanism to establish heterogeneous glucose metabolism.

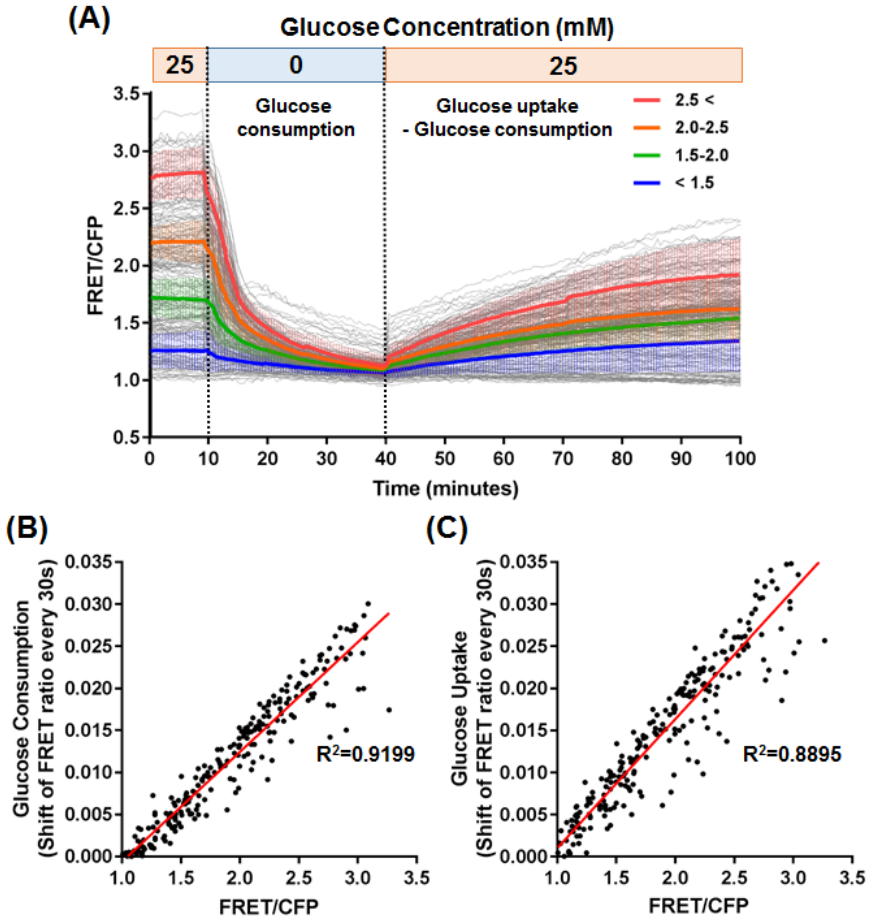


Figure 3-14 Imaging glucose uptake and consumption.
(A) Glucose biosensor expressing MCF-7 cells were incubated in 25 mM glucose DMEM. The media was changed to 0 mM glucose DMEM at time 10 minutes, and then re-changed to 25 mM glucose DMEM at time 40 minutes. Images were acquired every 30 seconds. (B, C) Glucose uptake and consumption speed of MCF-7 cells. Plots show single cell tracing of FRET signals and their rate of change. n > 200 cells from three independent experiments.

I further analysed the relationship between intracellular glucose levels and glucose uptake speed by multiplexed imaging. Intracellular glucose levels were measured by fluorescence lifetime imaging of the glucose FRET biosensor, and glucose uptake was measured by fluorescence imaging of 2-NBDG. For multiplexed imaging of the glucose FRET biosensor and 2-NBDG, the glucose FRET biosensor with mTurquoise2-sReACh combination expressing MCF-7 cells were incubated with 100 μM 2-NBDG for 2 hours (Figure 3-15A). The fluorescence lifetime of the glucose FRET biosensor is shorter in high glucose conditions because the energy of mTurquoise2 can transfer to sReACh. Multiplexed imaging showed that fluorescence lifetime shorter high glucose cells had high 2-NBDG intensity (Figure 3-15B). Thus, multiplexed imaging of the glucose FRET biosensor and 2-NBDG also indicates that intracellular glucose levels and glucose uptake speed have a significant relationship.

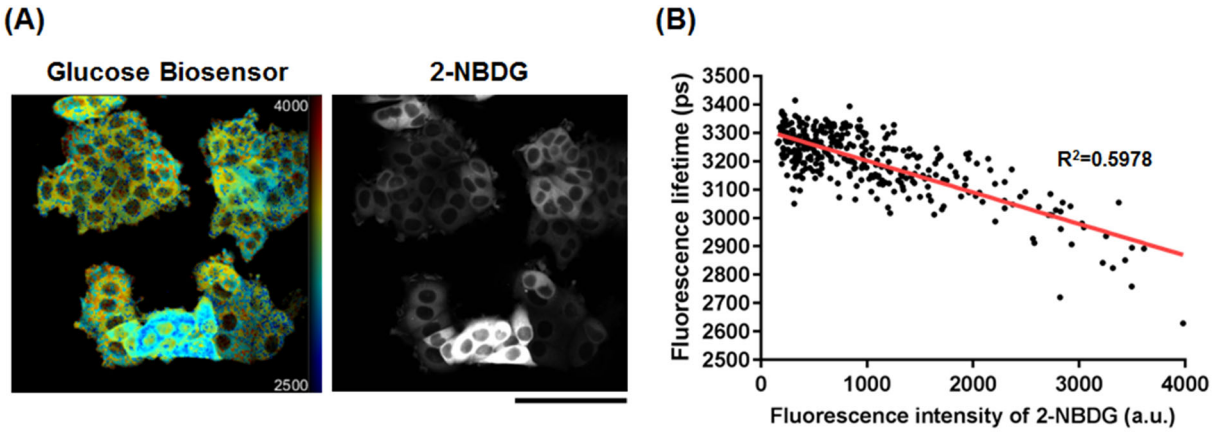


Figure 3-15 Multiplexed imaging of glucose FRET biosensor and 2-NBDG.
(A) FLIM-FRET of glucose FRET biosensor expressing MCF-7 cells and 2-NBDG intensity. MCF-7 cells were incubated with 100 μM 2-NBDG for 2 hours. Scale=100 μm. (B) The fluorescence lifetime of the glucose FRET biosensor was plotted against the fluorescence intensity of 2-NBDG. n > 300 cells from three independent experiments.

Intracellular glucose levels can distinguish the cells with different glucose demands. However, the relationship between intracellular glucose levels and the other metabolic characteristics such as mitochondrial activity and energetic stress are still unknown. Therefore, I characterized cell metabolism of high and low glucose cells by multiplexed imaging of the glucose FRET biosensor and TMRE. Multiplexed imaging identified that low glucose cells have slightly higher mitochondrial membrane potential (Figure 3-16A). However, the difference of TMRE intensity between high and low glucose cells was very small probably because transported protons would be rapidly used for ATP production. Therefore, I incubated the cells with the ATP synthase inhibitor, Oligomycin, and measured mitochondrial membrane potential. As a result, the difference of TMRE intensity dramatically increased between high and low glucose cells (Figure 3-16B). This result indicates that low glucose cells have higher ability of proton transport into the inter-membrane space. Thus, double imaging of the glucose FRET biosensor and TMRE identified the clear relationship between intracellular glucose levels and mitochondrial activities. During proton transport into the inter-membrane space in mitochondria, superoxide is produced by mitochondrial complex 1 and 3. Because low glucose cells have higher mitochondrial activities, this cell population could have high intracellular ROS levels. In order to analyse the relationship between intracellular glucose and ROS levels, I acquired multiplexed images of the glucose FRET biosensor and CellRox. Multiplexed imaging identified that low glucose cells have higher ROS levels (Figure 3-16C). In addition, the relationship between intracellular ATP levels and mitochondrial membrane potential

was analysed using ATP FRET biosensor-expressing MCF-7 cells. Multiplexed imaging of the ATP FRET biosensor and TMRE clarified that intracellular ATP levels had mild correlation with the mitochondrial membrane potential. The cells having high intracellular ATP levels had high mitochondrial membrane potential (Figure 3-16D). Taken together, imaging intracellular glucose levels can read out heterogeneous mitochondrial membrane potential, ROS levels, and intracellular ATP levels.

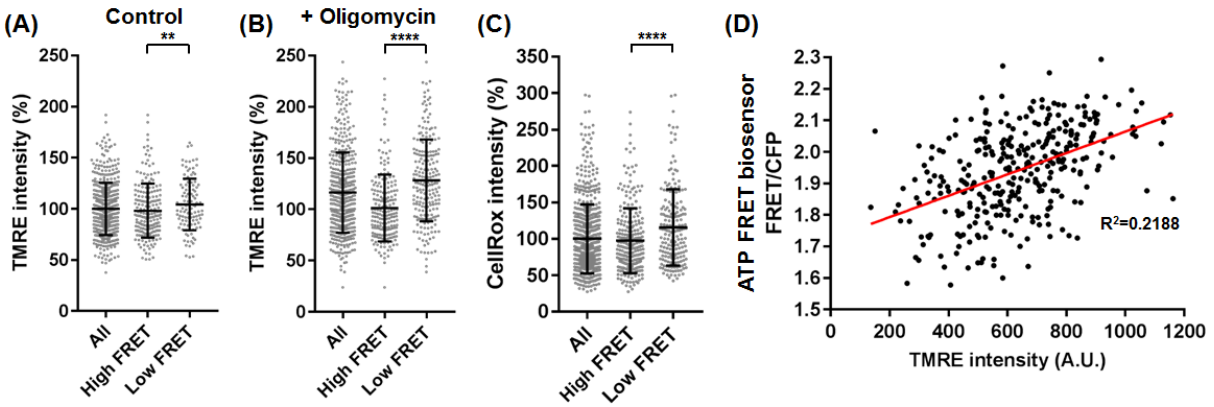


Figure 3-16 Multiplexed imaging of intracellular glucose levels and energetic states.
(A) TMRE distribution in high and low glucose cells. Glucose biosensor expressing MCF-7 cells were incubated with 100 nM TMRE for 10 minutes. (B) Glucose biosensor expressing MCF-7 cells were incubated with 2 μM Oligomycin for 1 hour and then incubated with 100 nM TMRE for 10 minutes. (C) CellRox distribution in high and low glucose cells. Glucose biosensor expressing MCF-7 cells were incubated with 5 μM CellRox for 30 minutes. (D) FRET ratio of ATP biosensor was plotted against fluorescence intensity of TMRE. n > 300 cells for each condition from at least three independent experiments. **P < 0.01, ****P < 0.0001 Welch unpaired T test.

Multiplexed imaging identified that intracellular glucose levels indicate different mitochondrial membrane potential, ROS levels, and ATP levels. However, the differences of these factors between high and low glucose cells were very small. In order to measure mitochondrial activities in high and low glucose cells with high accuracy, I need to carefully link these factors because mitochondrial membrane potential and ROS levels have a complex relationship. High mitochondrial membrane potential increases ROS production through the mitochondrial electron transport [136]. However, ROS reduces mitochondrial membrane potential and induces mitophagy to eliminate defective mitochondria [137]. Thus, mitochondrial conditions also contribute to the balance of mitochondrial membrane potential and ROS levels. Because the relationships of these metabolic indicators are complicated, multiplexed imaging is a strong tool for correlation. Triple imaging of intracellular glucose levels, mitochondrial membrane potential, and ROS levels in MCF-7 cells identified that low glucose cells have a higher ratio of “ROS / mitochondrial membrane

potential" (Figure 3-17). This result indicates that low glucose cells have high mitochondrial activities, but ROS produced by the mitochondrial respiratory chain reduces mitochondrial membrane potential. In order to keep high energy production, low glucose may have high mitochondrial turnover.

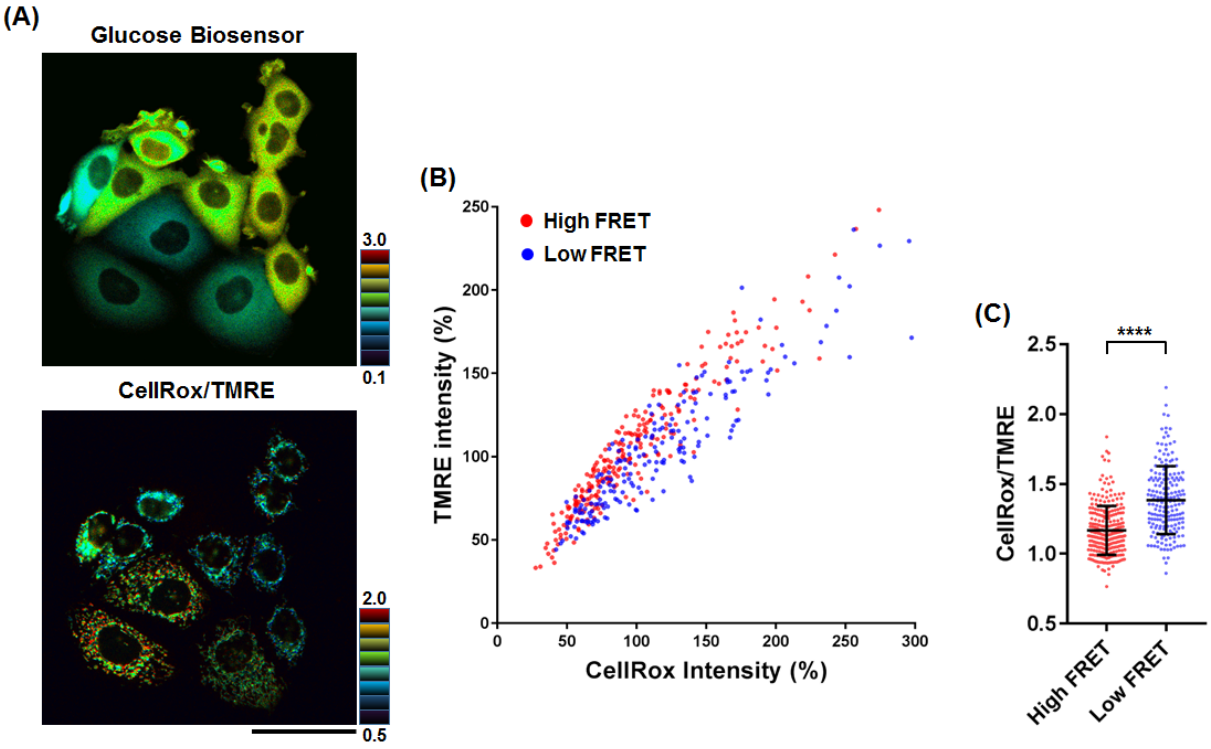


Figure 3-17 Multiplexed imaging of glucose FRET biosensor, TMRE, and CellRox.
(A) Intracellular glucose levels and the rate of "CellRox / TMRE" intensity in MCF-7 cells. Scale = 50 μm. (B) TMRE intensity was plotted against CellRox intensity. Red dots are high glucose cells (High FRET) and blue dots are low glucose cells (Low FRET). (C) CellRox/TMRE distribution in high and low glucose cells. n > 200 cells for each condition from three independent experiments. ***p < 0.001 unpaired T test.

3.3.3 Intracellular glucose levels of breast cancer cell lines

Cancer cells commonly have higher glucose uptake compared with normal cells, 2-[18F] fluoro-2-deoxy-D-glucose (FDG) PET/CT can detect solid tumours [138]. In addition to high glucose uptake and consumption of cancer metabolism, cancer cells are expected to have metabolic heterogeneity [139]. In order to analyse heterogeneous cell metabolism, glucose FRET biosensor-expressing breast cancer cell lines were established in T47D, MCF-7, ZR-75-1, JimT-1, and MDA-MB-231 cells. In all cell lines, the cells with high and low expression of the biosensor were removed by FACS. Among five breast cancer cell lines, highly malignant cell lines, JimT-1 and MDA-MB-231 cells, have higher intracellular

glucose levels (Figure 3-18A). Luminal A and B breast cancer cells are less aggressive and have better prognosis [140]. In contrast, $Her2^{+}$ and triple negative breast cancer cells have a more aggressive phenotype. Therefore, intracellular glucose levels are matched with the biological phenotype of breast cancer. In addition to the different intracellular glucose levels among breast cancer cell lines, all five cell lines showed heterogeneity of intracellular glucose levels (Figure 3-18B). Within a cancer, all cell lines are expected to have the same driver of cell metabolism although recent research has questioned this mechanism. There are some key metabolic regulators such as MYC, p53, and PI3K signalling pathway. Breast cancer cell lines have different gene alterations in these metabolic regulators, all five breast cancer cell lines have highly heterogeneous intracellular glucose levels. Therefore, there might be a principal regulation mechanism of metabolic heterogeneity.

Heterogeneous gene expression can establish inter-cellular metabolic heterogeneity. In this case, metabolic heterogeneity should be stable because genetically regulated gene expression is stable. In contrast, epigenetic regulation of gene expression is another possibility to establish metabolic heterogeneity. Cancer cell metabolism can reprogram epigenetic modifications such as histone methylation and acetylation [76, 80]. Therefore, epigenetic regulation of gene expression could generate unstable metabolic heterogeneity.

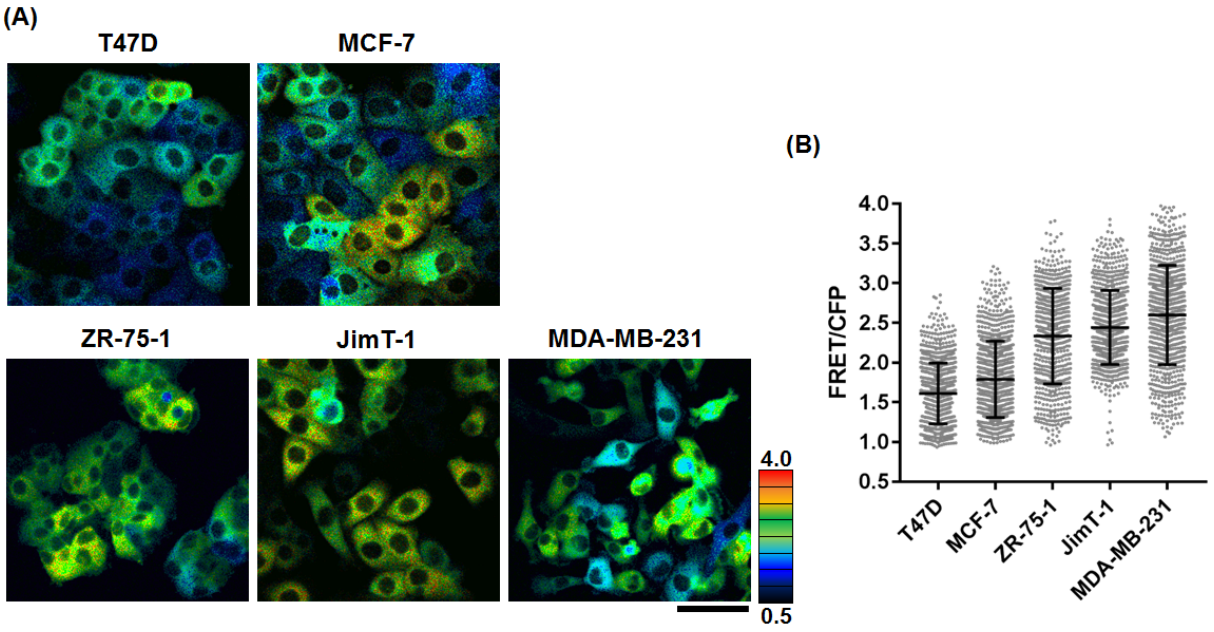


Figure 3-18 Intracellular glucose levels of breast cancer cell lines.
(A) Ratiometric images of glucose FRET biosensor in breast cancer cell lines. Scale=100 μm (B) Following single cell segmentation, distribution of intracellular glucose levels were analysed in five breast cancer cell lines. n > 300 cells for each condition from at least three independent experiments.

There are different possibilities to generate heterogeneous intracellular glucose levels such as genetic, epigenetic, and signalling regulation. These sources of heterogeneity might be expected to have different stability. Among them, genetic alterations and DNA methylation could have higher stability. On the other hand, histone acetylation and signal transductions could have short term stability. In order to analyse the stability regulation mechanisms governing heterogeneous intracellular glucose levels, I measured the stability of intracellular glucose levels by time lapse imaging. Glucose FRET biosensor-expressing breast cancer cells were plated and cultured in 25 mM glucose DMEM. The stability of intracellular glucose levels was analysed by measuring the FRET ratio of individual cells for 10 hours (Figure 3-19). The cells were segmented and intracellular glucose levels of individual cells were tracked every 30 seconds. The average and standard deviation of intracellular glucose levels were calculated, and intracellular glucose levels were aligned from low to high. This graph shows the relationship between intracellular glucose levels and their short term stability. Furthermore, glucose FRET signals at time 0 hour against signals at time 10 hours were plotted with the standard deviation over 10 hours. These dot plots show the stability of intracellular glucose levels at single cell resolution.

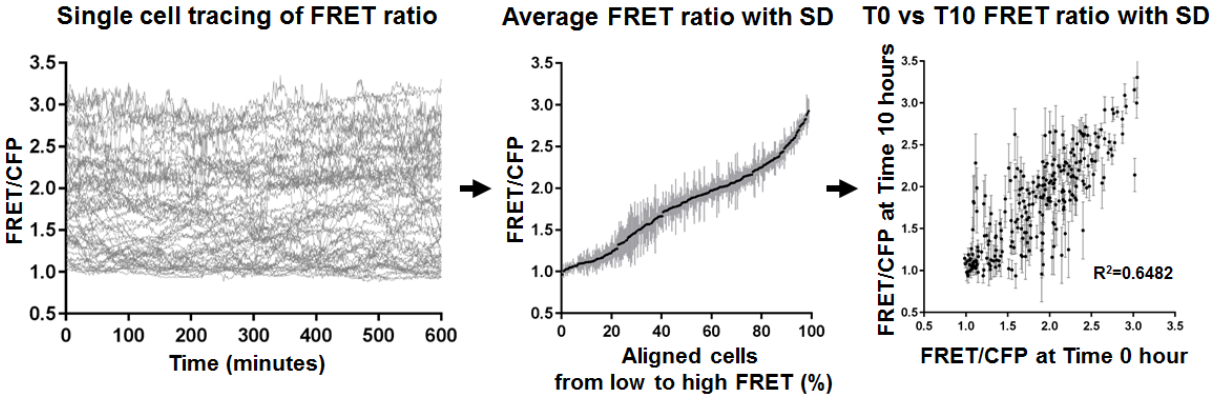


Figure 3-19 Imaging stability of intracellular glucose levels.
Glucose biosensor expressing MCF-7 cells were imaged for 10 hours every 30 seconds. Following cell segmentation, glucose levels were tracked and average FRET ratio and standard deviation were calculated from 10-hour time-lapse imaging. Glucose FRET signals at T=0 against signal at T=10 were plotted with the standard deviation over 10 hours.

As a result of time-lapse imaging of intracellular glucose levels in five breast cancer cell lines, each cell line showed their specific characteristics of intracellular glucose stability (Figure 3-20). Among them, T47D and MCF-7 cells have very similar stability of intracellular glucose levels. Especially high and low glucose cells have higher stability and intracellular glucose levels were almost same during the 10 hours. However, cells with

intermediate glucose levels fluctuated their intracellular glucose levels very quickly. On the other hand, JimT-1 cells have very stable intracellular glucose levels in the whole cell population. ZR-75-1 and MDA-MB-231 cells also have stable high glucose cells, but intracellular glucose levels of low glucose cells fluctuated very quickly. Thus, breast cancer cell lines have very unique characteristics of intracellular glucose levels and their regulation mechanism might be different in each cell line. Recent research clarified that leukemia-initiating cells (LICs) have metabolic heterogeneity and pyruvate dehydrogenase kinase isoform 2 (PDK2) activity can establish metabolic heterogeneity [141, 142]. In this research, NAD^+/NADH sensor was expressed in LICs and the heritability of NAD^+/NADH ratio was analysed by tracking individual cells from the first to the third generation. High NAD^+/NADH cells had high stability of cell metabolism and daughter cells inherit metabolic characteristics from the mother cells. In contrast, low NAD^+/NADH cells rapidly change NAD^+/NADH ratio. Thus, stability and heritability of metabolic characteristics are different among individual cells.

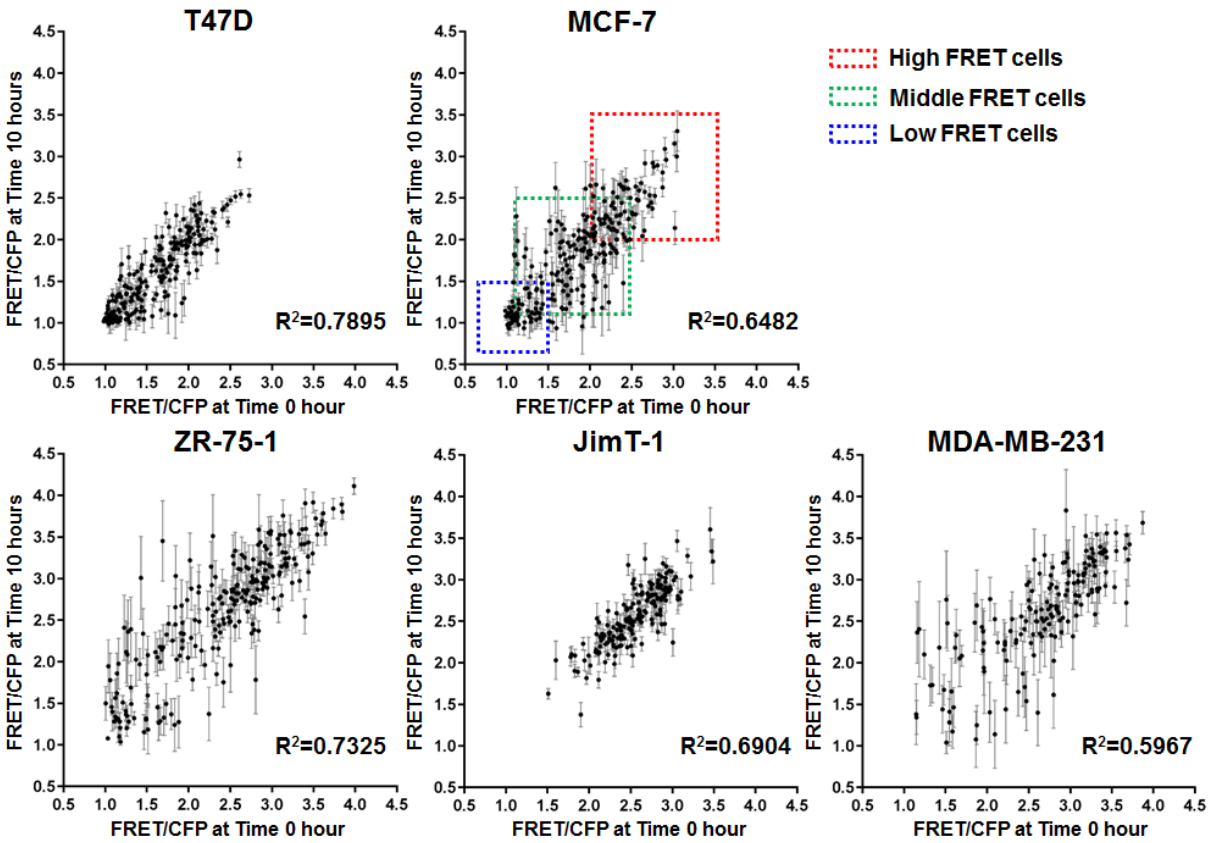


Figure 3-20 Stability of intracellular glucose level in breast cancer cell lines.
Glucose biosensor expressing breast cancer cell lines were imaged for 10 hours. Following cell segmentation, the glucose levels were tracked and glucose FRET signal at T=0 against signal at T=10 plotted with the standard deviation over 10 hours. n > 150 cells for each condition from at least three independent experiments.

In order to analyse the effect of cell cycle and heritability of cell metabolism, intracellular glucose levels of MCF-7 cells were tracked for 45 hours and relabelled to the first mitosis at time 0 (Figure 3-21A). Intracellular glucose levels of MCF-7 cells rapidly dropped and increased during cell division. In particular low glucose cells have a larger range in this dramatic perturbation of intracellular glucose levels. Second cell divisions were observed at around 1,500 - 2,100 minutes after first mitosis. Intracellular glucose levels were stable after mitosis and the cells kept their metabolic states for at least 45 hours. On the other hand, intracellular glucose levels of individual cells can fluctuate and the cells have heterogeneity of metabolic stability. Therefore, I further analysed intracellular glucose levels among all these generations of MCF-7 cells from single cell tracing data sets. Intracellular glucose levels of first generation cells were well correlated with second generation cells (Figure 3-21B). In particular, high and low glucose cells had almost the same intracellular glucose levels between the first and second generation. However, this correlation was reduced at third generation (Figure 3-21C). Thus, daughter cells can inherit metabolic characteristics from parental cells. However after another generation, there was less correlation of intracellular glucose levels which indicates progressive loss of heritable information. Intracellular glucose levels could be a short term stable but long term unstable metabolic characteristic.

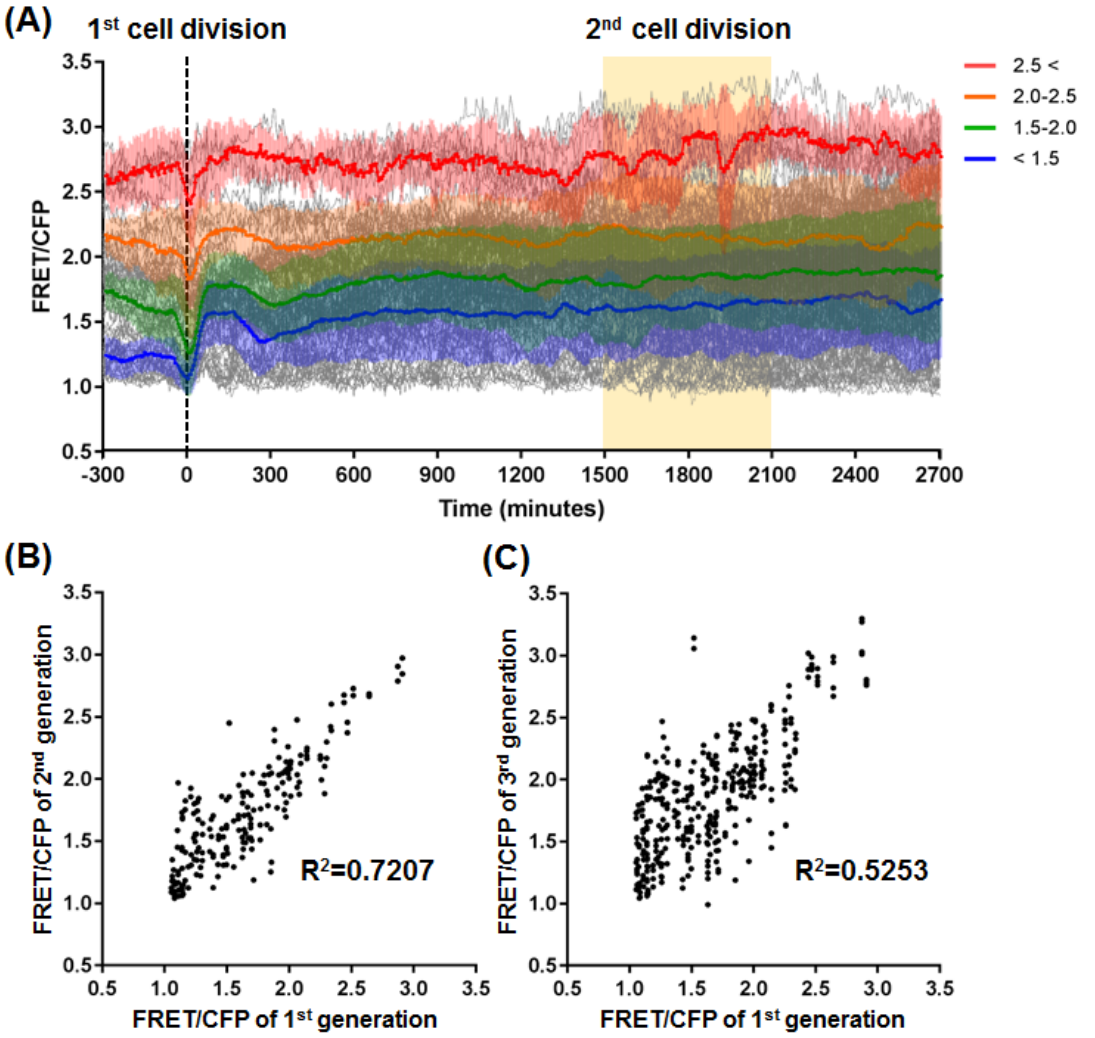


Figure 3-21 Long term stability of intracellular glucose levels.
(A) Glucose FRET biosensor expressing MCF-7 cells were imaged for 2,700 minutes. Following cell segmentation, intracellular glucose levels were tracked in individual cells. (B) Glucose FRET signals at 1st generation against signals at 2nd generation. (C) Glucose FRET signals at 1st generation against signals at 3rd generation. n > 200 cells for each condition from three independent experiments.

Single cell tracking of intracellular glucose levels indicates that glucose levels are heritable but long term unstable metabolic characteristics. Time-lapse imaging is an ideal approach to measure intracellular glucose levels at the single cell scale but it is difficult to track the cells in the longer term. In order to solve this problem, high and low glucose cells were isolated by FACS and intracellular glucose levels were measured in a time course (Figure 3-22). Time course imaging of intracellular glucose levels in FACS-isolated high and low glucose cells can trace metabolic states in longer term. For high and low glucose cell isolation, the cells must be detached from culture dishes by trypsinization. However, cell detachment can change cell metabolism possibly by metabolite leakage [143].

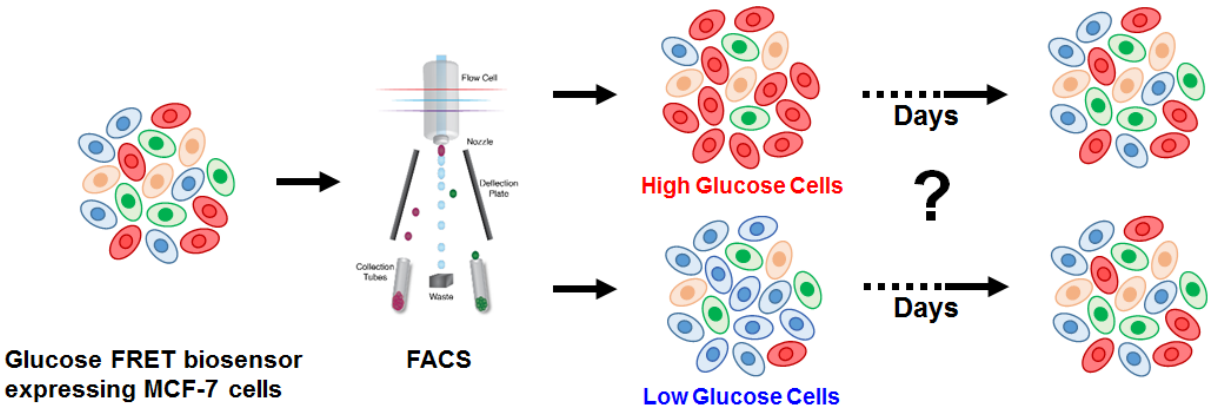


Figure 3-22 Experimental outline of imaging FACS-isolated breast cancer cells.
Schematic representation of imaging intracellular glucose levels of FACS-isolated high and low glucose cells. High and low glucose cells were isolated by FACS, cultured in glass bottom dishes, and images were acquired in time course.

The effect of trypsinization on metabolites leakage would be different among cell lines, FRET distribution of intracellular glucose levels in flow cytometry was measured in five breast cancer cell lines (Figure 3-23). As might be expected, FRET distribution was different from the quantification data of live cell imaging. Among them, T47D and MCF-7 cells did not fit a simple distribution. Because these two cell lines had stable high and low glucose cells in live cell imaging, FRET distributions in flow cytometry were matched with imaging data. In contrast, the other three cell lines had a single population in flow cytometry. The characteristics of intracellular glucose levels in ZR-75-1 and MDA-MB-231 cells in imaging were of having stable high glucose cells and unstable low glucose cells. Unstable low glucose cells might shift to high glucose state.

In the process of cell sorting, there are many steps affecting cell metabolism such as cell detachment, changing media, and flow stress during cell sort. These multiple factors could change FRET distribution of ZR-75-1 and MDA-MB-231 cells. JimT-1 cells also had a single population in flow cytometry, and this FRET distribution was matched with intracellular glucose levels in the live cell imaging data. Thus, the cells with unstable glucose levels could rapidly change intracellular glucose levels in flow cytometry. Because these unstable cells could change intracellular glucose levels during cell sorting, T47D and MCF-7 cells are better cell lines to isolate stable high and low glucose cells.

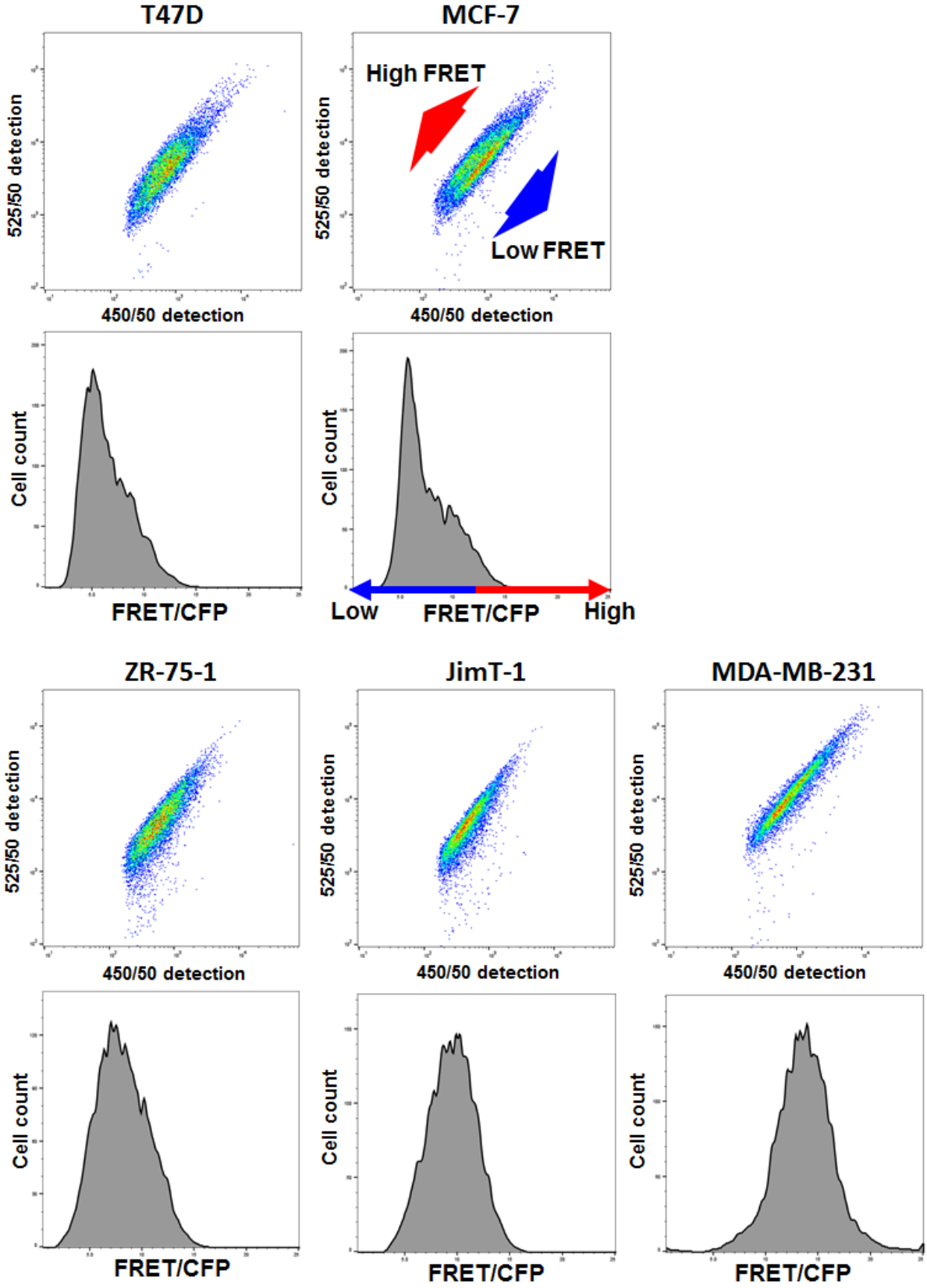


Figure 3-23 FRET distribution of intracellular glucose levels in flow cytometry.
Panels show the FRET distribution of intracellular glucose levels in breast cancer cell lines. The cells were excited by 405 nm fluorescence wavelength and fluorescence signals were detected at 450/50 and 525/50 nm gates.

Breast cancer cell lines have different stability of intracellular glucose levels during cell sorting. In addition, the effect of cell detachment on metabolic state was also different among five breast cancer cell lines. Therefore, metabolic stability was analysed by isolating high and low glucose cells by FACS. In cell sorting, the top and bottom 10% of the cells were isolated from the total population (Figure 3-24A). In MCF-7 cells, the proportion of low FRET cells was higher than high glucose cells in flow cytometry. In addition, isolated high and low glucose cells were re-analysed by flow cytometry. Purity analysis clarified that FACS-isolated low glucose cells had high accuracy but FACS-isolated high glucose cells included middle-low glucose cells (Figure 3-24B). These isolated cells were plated on glass bottom dishes and cultured in 25 mM glucose DMEM for 24 hours. Intracellular glucose levels of FACS-isolated high and low glucose cells were then measured using an inverted Zeiss LSM 780 confocal microscope (Figure 3-24C). Intracellular glucose levels of FACS-isolated high and low glucose cells were very similar with purity analysis of flow cytometry. Both high and low glucose cells could keep similar metabolic states at least 24 hours after cell isolation.

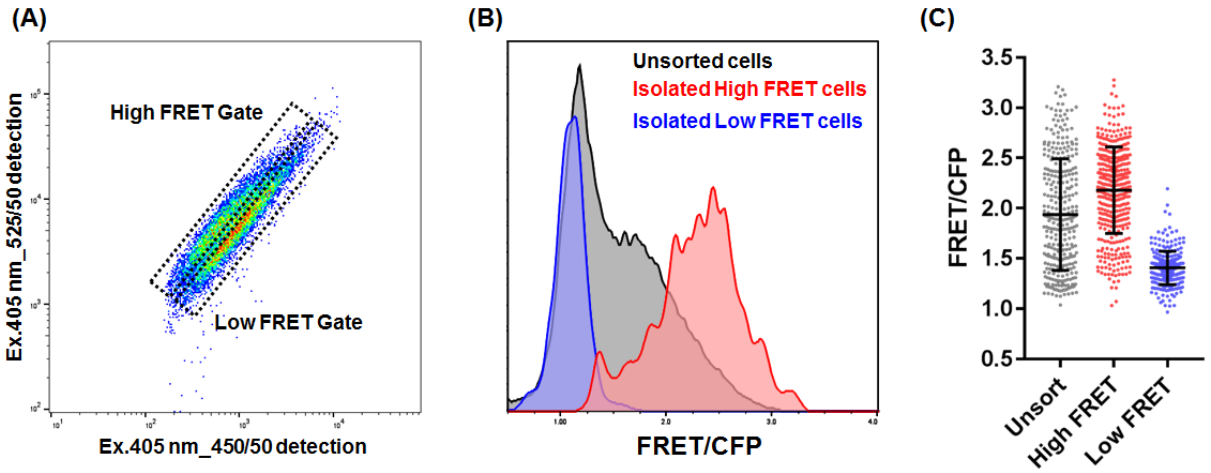


Figure 3-24 High and low glucose cell isolation in MCF-7 cells.
(A) Panel shows FRET distribution of glucose FRET biosensor expressing MCF-7 cells. High and low glucose cells were isolated from the dashed squares. (B) Panel shows the histogram of FRET distribution of glucose FRET biosensor expressing MCF-7 cells. Red and blue histograms are purity analysis of isolated high and low glucose cells. (C) Imaging intracellular glucose levels of isolated high and low glucose cells using confocal microscope. n > 300 cells for each condition from three independent experiments.

In five breast cancer cell lines, high and low glucose cells were successfully isolated from T47D, MCF-7, ZR-75-1, and JimT-1 cells. However, high and low glucose cells of MDA-MB-231 cells were rapidly returned to the average of unsorted population because of the instability of intracellular glucose levels (Figure 3-25).

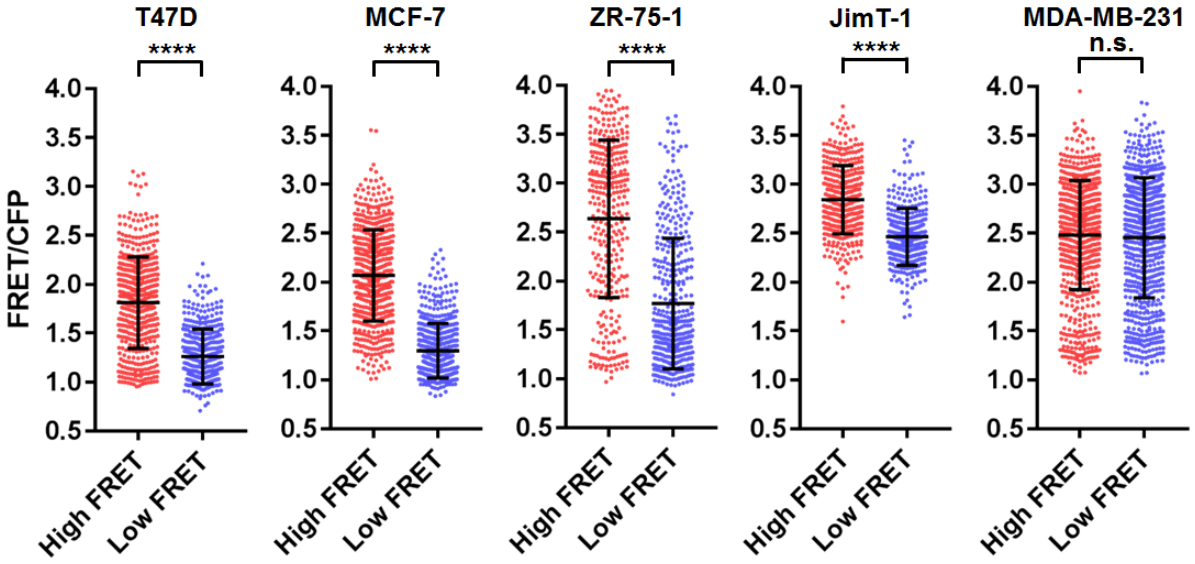


Figure 3-25 High and low glucose cell isolation in breast cancer cell lines.
Imaging intracellular glucose levels of isolated high and low glucose in T47D, MCF-7, ZR-75-1, JimT-1, and MDA-MB-231 cells using confocal microscope. n > 300 cells for each condition from three independent experiments. ****p < 0.0001 Kolmogorov-Smirnov test.

Long term stability of intracellular glucose levels was analysed by sequential 4-day time-course imaging in ER$^+$ T47D, MCF-7, and ZR-75-1 cells after high and low glucose cell isolation by flow cytometry (Figure 3-26). In T47D cells, isolated high glucose cells gradually returned to the unsorted glucose levels. Unsorted and 4 days-cultured high glucose cells had no significant difference of intracellular glucose levels. In contrast, low glucose cells of T47D cells were highly stable. Intracellular glucose levels slightly increased but unsorted and 4 days-cultured low glucose cells had significant difference of intracellular glucose levels. MCF-7 cells had very similar characteristics of intracellular glucose levels to T47D cells. Isolated high glucose cells of MCF-7 cells also gradually returned to the unsorted glucose levels within 4 days. The decline of intracellular glucose levels was largest between days 1 and 2, and stability of high glucose cells of MCF-7 cells were lower than T47D cells. Low glucose cells of MCF-7 cells were highly stable and 4 days-cultured low glucose cells had significant difference compared with unsorted cells. ZR-75-1 cells have clearly different characteristics of intracellular glucose levels. 24 hours after cell isolation, intracellular glucose levels of high and low glucose cells were significantly different from unsorted cells. However, high glucose cells of ZR-75-1 cells rapidly returned to the average of unsorted glucose levels. Low glucose cells of ZR-75-1 cells had high stability and 4 days-cultured low glucose cells had significant difference of intracellular glucose levels. Taken together, stability of low glucose cells are higher than high glucose cells in all ER$^+$ breast cancer cell lines.

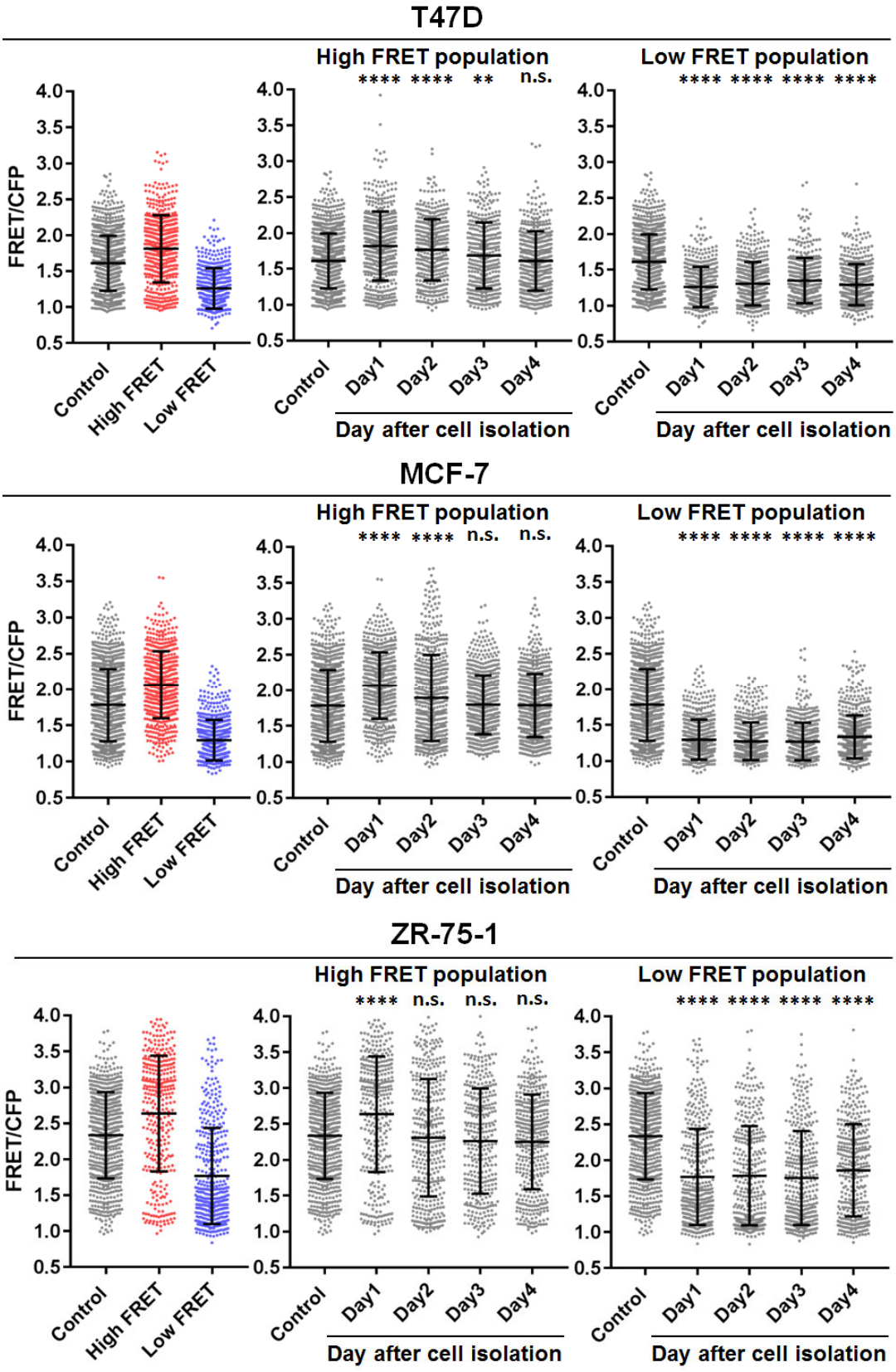


Figure 3-26 Stability of FACS-isolated high and low glucose cells.
High and low glucose cells were isolated by flow cytometry and intracellular glucose levels were traced for continuous 4 days in T47D, MCF-7, and ZR-75-1 cells. n > 400 cells for each condition from three independent experiments. n.s. $p > 0.05$, **$p < 0.01$, ****$p < 0.0001$ unpaired Kolmogorov-Smirnov test.

3.3.4 OCR and ECAR measurements

Multiplexed imaging of intracellular glucose levels, ATP levels, 2-NBDG, TMRE, and CellRox clarified that high and low glucose cells mainly employ glycolysis and OXPHOS, respectively. In order to further analyse cell metabolism based on this imaging result, I measured OCR and ECAR in FACS-isolated high and low glucose MCF-7 cells. OCR can read out cellular basal respiration, ATP-linked respiration, and maximal respiration capacity by sequential mitochondrial inhibitor treatments (see chapter 2.8). OCR measurement clarified that low glucose cells highly utilise OXPHOS (Figure 3-27A). Basal respiration of low glucose cells was significantly higher than high glucose cells because the OCR of low glucose cells was higher than high glucose cells before Oligomycin treatment. FCCP treatment can maximise respiration capacity, and the OCR of low glucose cells was significantly higher than high glucose cells. These OCR measurements suggest that low glucose cells have high OXPHOS. Imaging cell metabolism showed that low glucose cells have higher mitochondrial membrane potential, intracellular ROS levels, and intracellular ATP levels. OCR measurements were matched with these imaging data. In order to analyse glycolysis in high and low glucose cells, I measured ECAR. ECAR can read out glycolysis and glycolytic capacity by sequential glucose addition and inhibitor treatments (see chapter 2.8). Unexpectedly, ECAR measurement showed that low glucose cells have a significantly higher extracellular acidification rate (Figure 3-27B). Cells can start glycolysis by adding glucose and glycolysis of low glucose cells was significantly higher than high glucose cells. Oligomycin treatment can maximise glycolysis by inhibiting ATP synthetase in mitochondria. The glycolytic capacity of low glucose cells was also significantly higher than high glucose cells. These results contradicts imaging results which showed that high glucose cancer cells are a glycolytic cell population. However, carbon dioxide generated by the tricarboxylic acid (TCA) cycle in mitochondria can increase ECAR. At this point, ECAR cannot simply measure glycolytic capacity because of non-separation of lactate and CO_2 production. Therefore, I analysed the details of cell metabolism in high and low glucose cells by metabolomic analysis.

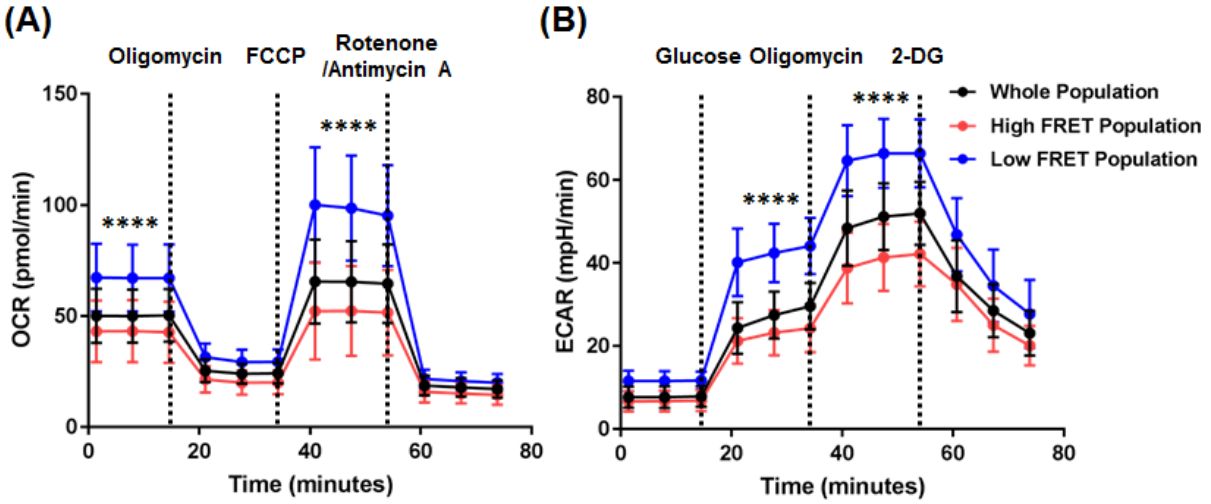


Figure 3-27 OCR and ECAR in FACS-isolated high and low glucose cells.
(A) OCR measurement in FACS-isolated high and low glucose cells. OCR was measured every 6 minutes by adding 1 μM Oligomycin, 0.5 μM FCCP, and 0.5 μM Rotenone/Actinomycin. (B) ECAR measurement in FACS-isolated high and low glucose cells. ECAR was measured every 6 minutes by adding 25 mM glucose, 1 μM Oligomycin, and 50 mM 2-DG. n > 30 wells for each condition from at least three independent experiments. ****p < 0.0001 unpaired T test.

3.3.5 Metabolomic analysis

Imaging cell metabolism is a strong experimental approach to understand cell metabolism with spatiotemporal resolution. However, multiplexed imaging can read out a maximum of 3-4 types of metabolic information from a single cell. Therefore, I analysed the details of cell metabolism in FACS-isolated high and low glucose cells by metabolomic analysis. Metabolites in high and low glucose cells were extracted and polar metabolites were analysed using GC-MS (Figure 3-28). In addition, metabolites of CM in high and low glucose cells were also analysed using GC-MS. Metabolomic analysis can trace whole glucose metabolism by labelling the metabolites with stable isotope $^{13}C_6$. In this experiment, FACS-isolated high and low glucose cells were incubated with D-Glucose-$^{13}C_6$ for 90 minutes. Although metabolites in glycolysis and PPP are rapidly labelled with the stable isotope $^{13}C_6$, metabolites in the TCA cycle require a longer incubation time. In order to read out the metabolic differences of high and low glucose cells in glycolysis and OXPHOS, the cells should be cultured with D-Glucose-$^{13}C_6$ for different incubation times.

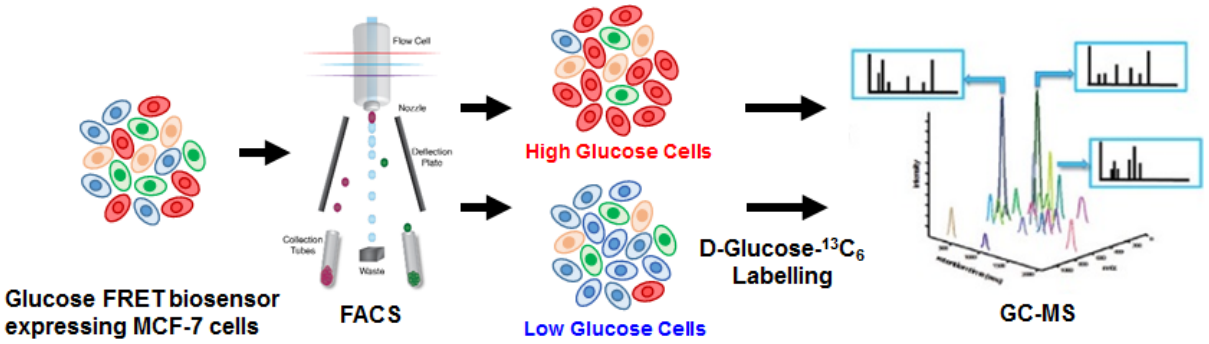


Figure 3-28 Experimental outline of metabolomics in high and low glucose cells.
Schematic representation of metabolomic analysis of FACS-isolated high and low glucose cells. High and low glucose cells were isolated from glucose FRET biosensor expressing MCF-7 cells by flow cytometry. FACS-isolated high and low glucose cells were incubated with D-Glucose-$^{13}C_6$ for 90 minutes and then extracted metabolites were analysed using GC-MS.

Glucose metabolism in MCF-7 cells was profiled by metabolomic analysis. In metabolic profiling, relative abundance and $^{13}C_6$ labelled percentage of metabolites were measured in the glycolysis pathway and the TCA cycle (Figure 3-29). First, I confirmed the relative abundance of glucose in high and low glucose cells. The intracellular glucose level of FACS-isolated high glucose cells was more than double that of low glucose cells, FACS successfully isolated high and low glucose cells (Figure 3-29B). In addition, metabolomic analysis revealed that low glucose cells have higher abundance of metabolites in the TCA cycle such as citrate, succinate, and malate (Figure 3-29C). The abundance of alanine, glutamine, and aspartate of low glucose cells were also significantly higher than high glucose cells (Figure 3-29D). Furthermore, high glucose cells excreted slightly larger amount of lactate to the media (Figure 3-29E). These results suggest that high glucose cells mainly employ glycolysis and low glucose cells highly utilize mitochondrial metabolism. Incubation of FACS-isolated high and low glucose cells with stable isotope-labelled glucose further clarified that high glucose cells have a higher percentage of $^{13}C_6$ labelled Ribose 5-P (Figure 3-29F). Glucose, glucose 6-P, and ribulose 5-P were saturated with carbon isotope $^{13}C_6$ because metabolic reactions in glycolysis are very fast. Metabolites of TCA cycle and amino acids in low glucose cells were highly labelled with $^{13}C_6$ (Figure 3-29G, H). In addition, there was no significant difference of $^{13}C_6$ labelled pyruvate and lactate in CM (Figure 3-29I). These results suggest that high glucose cells use high levels of glucose for PPP compare with low glucose cells. In contrast, low glucose cells consume glucose for energy production in mitochondria. Thus, metabolomic analysis clarified that intracellular glucose levels can discriminate glycolysis and OXPHOS in MCF-7 cells.

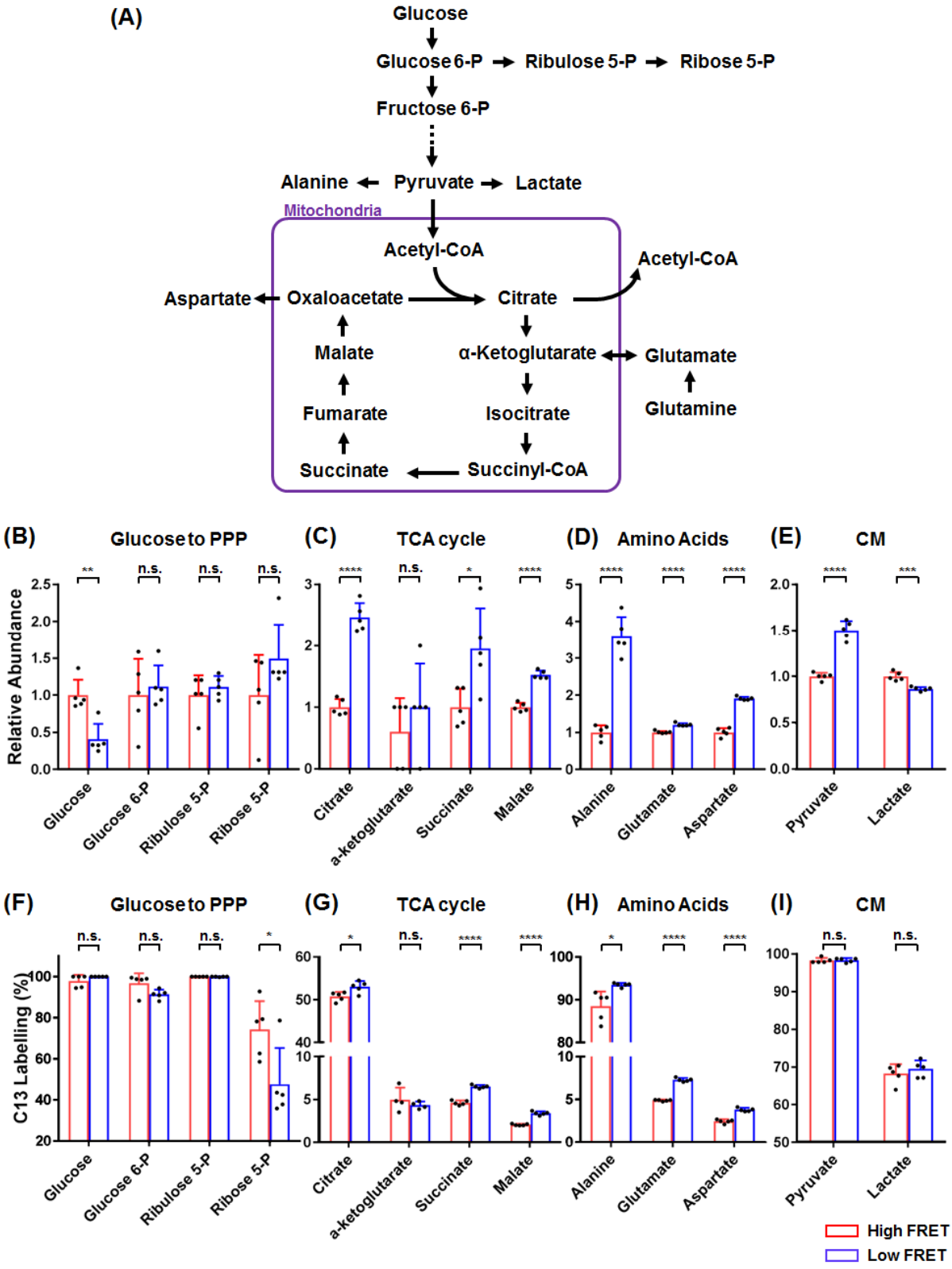


Figure 3-29 Metabolomic analysis of high and low glucose cells.
(A) Schematic representation of the key metabolic pathways of glycolysis and TCA cycle. (B-I) High and low glucose cells were incubated with D-Glucose-$^{13}C_6$ for 90 minutes and then extracted metabolites were analysed using GC-MS. Relative Relative abundance and $^{13}C_6$ labelled percentage of metabolites in PPP, TCA cycle, amino acids, and media were measured in high and low glucose cells. n=5 replicates for one condition. n.s. $p > 0.05$, *$p < 0.05$, **$p < 0.01$, ***$p < 0.001$, ****$p < 0.0001$ unpaired T test.

3.4 Growth of high and low glucose cells

Multiplexed imaging and metabolic analysis of MCF-7 cells clarified that the cells have metabolic heterogeneity. Because high intracellular glucose level is a novel cancer characteristic, glycolytic high glucose cells are expected to have a highly invasive and proliferative phenotype. In order to characterize the functional significance of high and low glucose cells, I measured the growth rate *in vitro* and *in vivo*. First, FACS-isolated high and low glucose cells were cultured in DMEM with different glucose and pyruvate concentration for 7 days in order to confirm the effect of nutrient condition for cell growth. Proliferation of high and low glucose cells was then analysed by crystal violet staining (Figure 3-30A). Although growth of FACS-isolated low glucose cells were slightly higher than high glucose cells in complete DMEM, high glucose cells proliferated significantly slower under pyruvate depletion. Glycolytic high glucose cells can produce amino acids, nucleic acids as well as ATP from glucose. In addition, high glucose consumption can promote glutaminolysis through C-terminal-binding protein (CtBP) activity [144]. However, low glucose cells had significantly higher proliferation under pyruvate depletion. One possibility to accelerate cell proliferation of low glucose cells is that high glucose DMEM can facilitate glycolysis in both high and low glucose cells without pyruvate. Low glucose cells originally have high mitochondrial activity, promotion of glycolysis might be able to enhance cell proliferation. Pyruvate can be used for TCA cycle and amino acids production. Therefore, high glucose cells might have a high demand for pyruvate for proliferation. Thus, individual cells have different demands for nutrient sources and nutrient conditions in the tumour microenvironment could be a key regulator of cell metabolism and proliferation. Next, I measured the cell growth of high and low glucose cells *in vivo*. FACS-isolated high and low glucose cells were injected into NOD SCID mice and tumour sizes were measured twice a week (Figure 3-30B). The tumour sizes of low glucose cells were significantly larger than high glucose cells only in the first week. Intracellular glucose levels are long term unstable metabolic characteristics, metabolic difference could have disappeared within a week. Because FACS-isolated high and low glucose cells have significant differences in cell growth *in vivo*, the nutrient conditions of the tumour microenvironment could be similar with pyruvate depletion media *in vitro*. Thus, different nutrient preference of high and low glucose cells could make a difference in tumour growth.

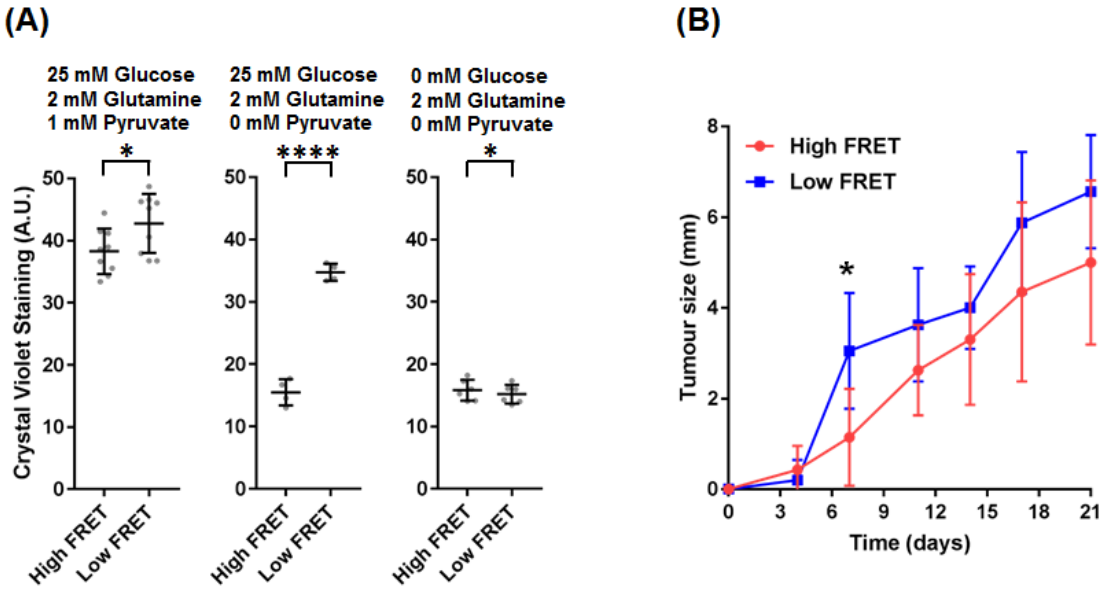


Figure 3-30 Proliferation of FACS-isolated high and low glucose cells.
(A) MCF-7 cells were cultured in the different nutrient condition for 7 days and stained with crystal violet. n > 9 wells from three independent experiments. (B) Growth of FACS-isolated high and low glucose cells *in vivo*. n=9 in high glucose cells, and n=5 in low glucose cells from two independent experiments. *p < 0.05, ****p < 0.0001 unpaired T test.

3.5 Chapter discussion

In this chapter, I optimised nine different biosensors to analyse heterogeneous breast cancer cell metabolism. Among them, the glucose FRET biosensor has a great working range to read out heterogeneous metabolic states. Imaging intracellular glucose levels could distinguish glycolysis and OXPHOS. Metabolomic analysis further clarified that high and low glucose cells consume glucose for the different metabolic routes. These results indicate that breast cancer cells have a mechanism to establish metabolic heterogeneity. Heterogeneous cell metabolism can reversibly fluctuate between glycolytic and OXPHOS metabolism. Therefore, epigenetic regulation of gene expression and signalling regulation are expected to make a reversibly variable cancer cell metabolism. Unsurprisingly, nutrient accessibility is a key regulator of heterogeneous tumour growth. Although high and low glucose cells have similar growth in complete media, high glucose cells proliferated more slowly under pyruvate depletion. Tumour microenvironments dynamically change nutrient accessibility, extracellular pH, oxygen concentration, and ECM stiffness. Cancer cells have to remodel cell metabolism in order to adapt to different microenvironmental conditions for survival. Having heterogeneous and reversibly variable cell metabolism could be a great mechanism for tumour microenvironmental adaptation.

Chapter 4. Regulatory mechanism of heterogeneous glucose metabolism

4.1 Chapter summary

In this chapter, I analyse the regulatory mechanism of heterogeneous glucose metabolism in breast cancer. Tumour microenvironmental factors such as cell confluence, ECM stiffness, extracellular pH, and oxygen concentration are known to regulate glucose metabolism. However, their effect on single cells with different characteristics is not clear. Among different microenvironmental factors, cell confluence negatively correlates with intracellular glucose levels. Cells in high cell confluence reduce expression levels of GLUT1 and GLUT4. In addition, the phosphorylation level of Colifin is significantly higher than the cells in low cell confluence. These characteristics of key metabolic regulators are similar with FACS-isolated high and low glucose cells. Functional analysis of high and low glucose cells indicates that activity of PI3K/AKT signalling and actin cytoskeletal dynamics regulate the balance of glycolysis and OXPHOS in breast cancer cells. In addition, I find a subset of high glucose cells that can regulate glycolysis independently of their PI3K/AKT activity.

4.2 The effect of microenvironmental factors on cell metabolism

Cancer cells reprogram cell metabolism in order to adapt the tumour microenvironment. Tumour microenvironmental factors such as nutrient accessibility, oxygen levels, extracellular pH, and ECM stiffness are regulators of cell metabolism. Although cancer cells in the core of tumour are known to have high glycolysis, the effect of individual microenvironmental factors on glucose metabolism at the single cell scale is unclear. Therefore, I analysed the effect of nutrient conditions, extracellular pH, ECM stiffness, co-culture with CAFs, and oxygen concentration on intracellular glucose levels in MCF-7 cells. As I described in chapter 3.4, the nutrient balance of glucose and pyruvate can change tumour growth. Extracellular pH also has a great impact on glucose metabolism. In order to analyse the effect of extracellular pH on glucose metabolism, glucose FRET biosensor-expressing MCF-7 cells were incubated in DMEM with different pH. As a result, cells in the acidic media dramatically reduced intracellular glucose levels (Figure 4-1A). Because glycolysis produces lactate and reduces extracellular pH, an acidic microenvironment could inhibit glycolytic metabolism *in vivo*. In addition, I measured intracellular glucose levels of MCF-7 cells on different stiffness. The cells were cultured on glass bottom dishes

and collagen gel for 24 hours. The cells plated on glass bottom dishes had slightly higher intracellular glucose levels compared with those cells plated on collagen gels (Figure 4-1B). Mechanical stress from the stiffer surface might increase glycolysis through actin cytoskeletal remodelling because F-actin can bind with Aldolase A and regulate glycolysis [36, 145]. In the tumour microenvironment, cancer cells can exchange metabolites with CAFs [50, 51, 57]. Cancer cells excrete unnecessary metabolites such as lactate and uptake metabolites such as alanine and glutamine excreted from CAFs. Therefore, interactions between cancer cells and CAFs can regulate cancer cell metabolism. In order to analyse the effect of CAFs on glucose metabolism, glucose FRET biosensor-expressing MCF-7 cells were co-cultured with human breast CAFs for 24 hours. As a result, intracellular glucose levels of MCF-7 cells were slightly decreased by co-culture with CAFs (Figure 4-1C). Cancer cells might be able to promote the TCA cycle by receiving glutamine and alanine from CAFs. Interactions of cancer cells and CAFs thus change metabolic states of cancer cells.

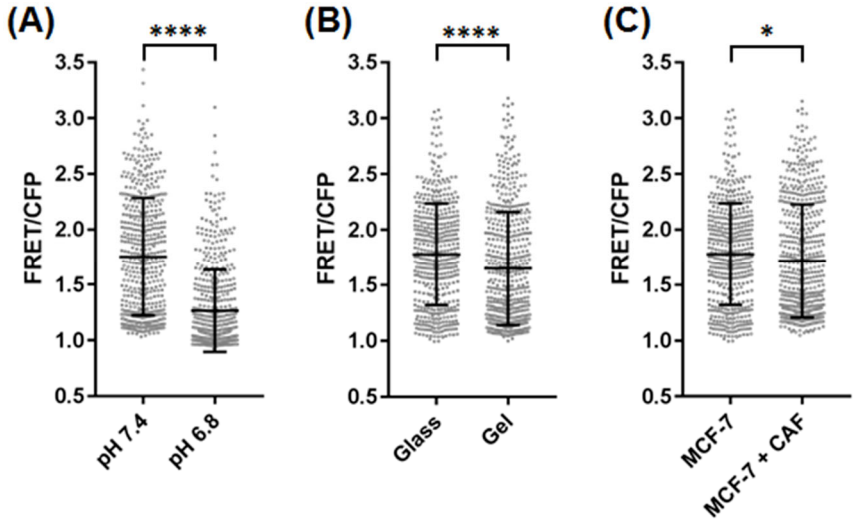


Figure 4-1 Tumour microenvironmental factors regulate glucose metabolism.
(A, B, C) FRET distribution of intracellular glucose levels of MCF-7 cells in the different extracellular pH, stiffness, and co-culture with CAFs. n > 500 cells for each condition from at least three independent experiments. *p < 0.05, ****p < 0.0001 Kolmogorov-Smirnov test.

I further analysed the effect of oxygen concentration on glucose cell metabolism. Oxygen levels in the tumour microenvironment are different depending on the distance from blood vessels. Cancer cells in low oxygen concentration mainly employ anaerobic glycolysis. HIF-1 is activated by dimerization of the α and β subunits in hypoxic conditions. Because HIF-1 is a transcription factor of genes encoding glycolytic enzymes, hypoxia is a key microenvironmental factor to accelerate glycolysis [146, 147]. In addition, HIF-1 inactivates the TCA cycle and mitochondrial metabolism [148, 149].

In order to analyse the metabolic remodelling response to oxygen concentration, I measured cell metabolism of MCF-7 cells in normoxia and hypoxia using seven different biosensors. MCF-7 cells and FRET biosensor-expressing MCF-7cells were incubated in 1% oxygen for 24 hours. Glucose uptake was measured by 2-NBDG labelling of MCF-7 cells, and mitochondrial membrane potential was measured by TMRE staining. In addition, intracellular glucose, pyruvate, lactate, ATP levels and AMPK activity were measured by FRET imaging (Figure 4-2A, B). As a result, the cells in hypoxia significantly increased glucose uptake but reduced intracellular glucose levels. Furthermore, hypoxia significantly increased intracellular pyruvate and lactate levels. As expected, mitochondrial activity and ATP levels in hypoxia were lower than control condition. Unexpectedly, AMPK activity in hypoxia was also kept low. These result indicate that the cells in hypoxia accelerate glycolysis to cover low mitochondrial respiration. Although many studies have reported metabolic reprogramming in hypoxia, the experimental approach to analyse cell metabolism at single cell resolution was limited. Single cell imaging of cell metabolism using biosensors is an ideal way to reveal metabolic reprogramming with spatiotemporal resolution.

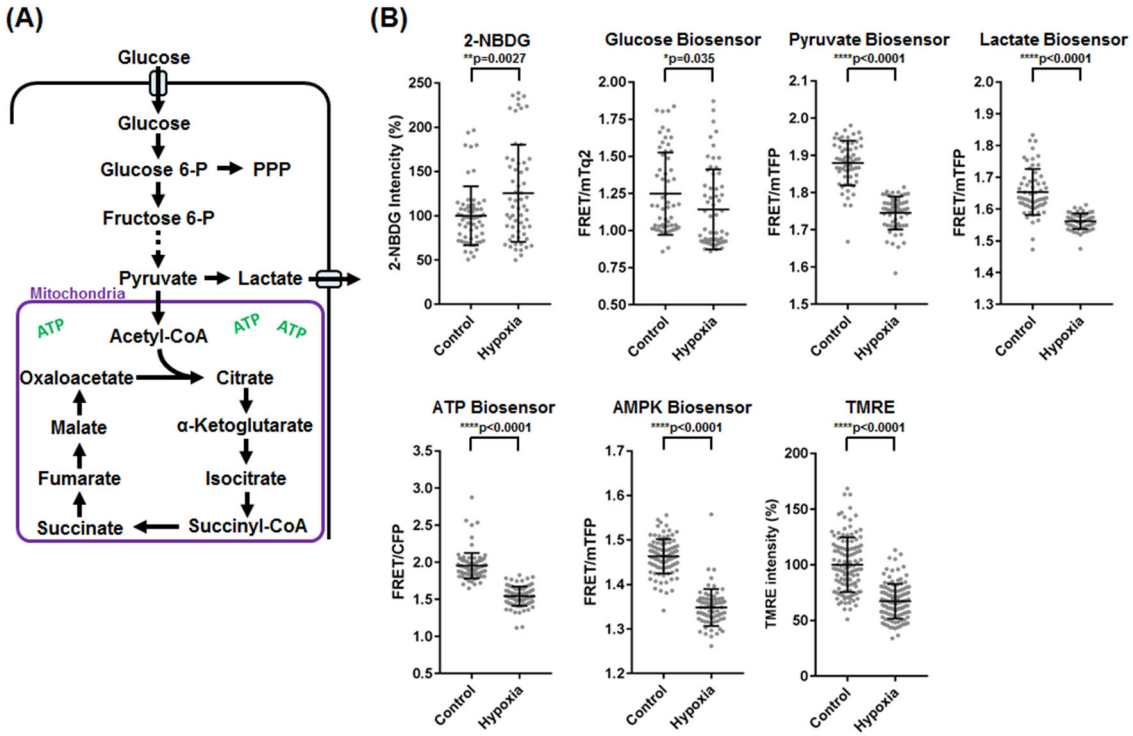


Figure 4-2 Cell metabolism of MCF-7 cells in normoxia and hypoxia.
(A) Schematic representation of the key metabolic pathways of glycolysis and TCA cycle. (B) Quantified cell metabolism of MCF-7 cells in control and hypoxia. In hypoxia the cells were incubated in 1% O_2 for 24 hours. 2-NBDG intensity, intracellular glucose levels, pyruvate levels, lactate levels, ATP levels, AMPK activity, and TMRE intensity were measured by live cell imaging. n > 60 cells for each condition from two independent experiments.

4.3 Intracellular glucose levels of different cell confluence

High cell confluence supresses cancer cell proliferation due to the inhibition of pyruvate transported from the cytoplasm into mitochondria [150, 151]. Actin cytoskeletal remodelling and cell adhesion are also key regulators of cell metabolism at different cell density [36, 152]. Thus, cell confluence is expected to regulate cell metabolism. In order to analyse the impact of cell confluence on glucose metabolism, I measured intracellular glucose levels of MCF-7 cells at three different cell confluences (Figure 4-3). Glucose FRET biosensor-expressing MCF-7 cells were plated with three different cell confluences and cultured for 24 hours. As a result, MCF-7 cells at 5.0 x 10^4 cells/cm^2 slightly reduced intracellular glucose levels. In addition, intracellular glucose levels of MCF-7 cells were dramatically reduced at 1.0 x 10^5 cells/cm^2. These results indicate that cells at high cell confluence supress glycolysis.

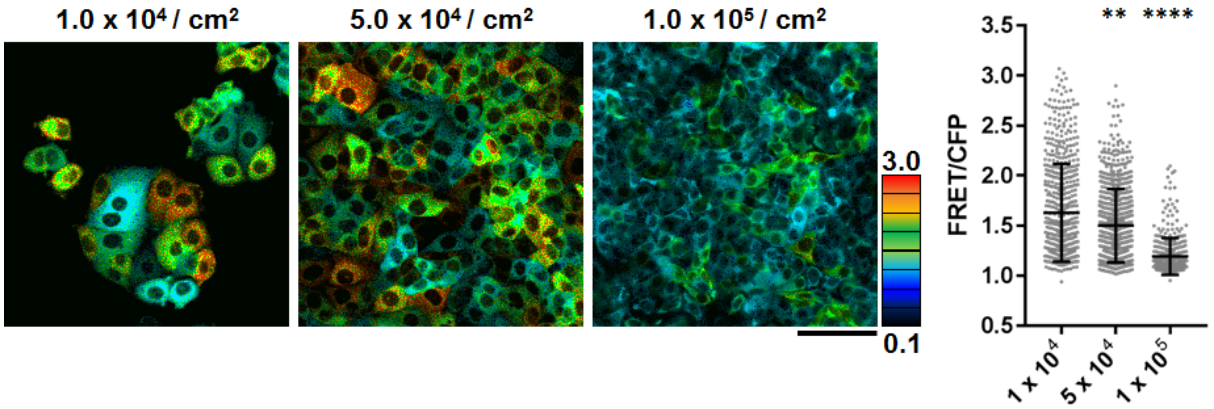


Figure 4-3 Intracellular glucose levels with different cell confluences.
Ratiometric FRET images of intracellular glucose levels of MCF-7 cells at 1.0 x 10^4 cells/cm^2, 5.0 x 10^4 cells/cm^2, and 1.0 x 10^5 cells/cm^2. Scale=50 μm. n > 400 cells for each condition from at least three independent experiments. **p < 0.01, ****p < 0.0001 Kolmogorov-Smirnov test.

In addition, YAP localisation of nucleus/cytoplasm (N/C) ratio in MCF-7 cells was measured by immunostaining in three different cell confluences. Mechanical stress is known to regulate YAP phosphorylation and its localisation [153-156]. Dephosphorylated active YAP is translocated into nucleus and promotes glycolysis through GLUT3, HK2, and PFKFB3 transcription [157, 158]. As expected, the YAP N/C ratio was dramatically reduced at 1.0 x 10^5 cells/cm^2 (Figure 4-4). This dramatic shift of YAP localisation is matched with the dramatic reduction of intracellular glucose levels at 1.0 x 10^5 cells/cm^2. These results indicate that mechanical stress induced by high cell confluence could supress glycolysis through YAP translocation.

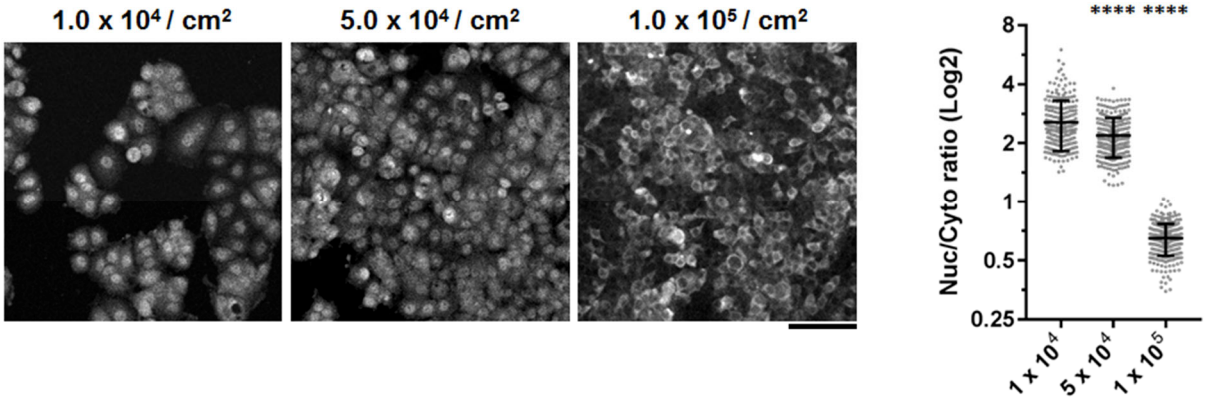


Figure 4-4 YAP localization with different cell confluence.
YAP localisation in MCF-7 cells at 1.0 x 10^4 cells/cm^2, 5.0 x 10^4 cells/cm^2, and 1.0 x 10^5 cells/cm^2. YAP localisation was detected by immunostaining using YAP antibody. YAP N/C ratio was calculated in single cell scale. Scale=100 μm. n > 400 cells for each condition from at least three independent experiments. ****p < 0.0001 Welch unpaired T test.

4.4 PI3K/AKT signalling regulates glucose metabolism

Breast cancer cell lines have heterogeneous cell metabolism which can regulate cell proliferation. However, the key regulators that establish metabolic heterogeneity in breast cancer is unclear. Because metabolic states are reversibly variable and long term unstable, metabolic heterogeneity could be regulated by either cell signalling or epigenetically controlled gene expression. Since activation of PIK3CA is frequently detected in breast cancer [7], I analysed the effect of inhibitors of different steps of the PI3K/AKT/mTOR signalling pathway on glucose metabolism. In addition, the effect of cell adhesion and actin cytoskeletal dynamics on cell metabolism was analysed due to the fact that cell confluence has a great impact on intracellular glucose levels.

In order to analyse the effect of PI3K/AKT/mTOR signalling on glucose metabolism, intracellular glucose levels of MCF-7 cells were measured after inhibitor treatments (Figure 4-5). Intracellular glucose levels of glucose FRET biosensor-expressing MCF-7 cells were measured after 24 hours incubation with each inhibitor. As a result, IGFR, PI3K, AKT, and mTOR inhibitor treatments dramatically reduced intracellular glucose levels. Therefore, the PI3K/AKT/mTOR signalling could promote glycolysis. However, there are a subset of high glucose cells maintaining high glucose states under inhibitor treatments (Figure 4-5, red dashed squares). This result indicates that there are different cell populations which regulate glycolysis dependently and independently from the PI3K/AKT signalling pathway.

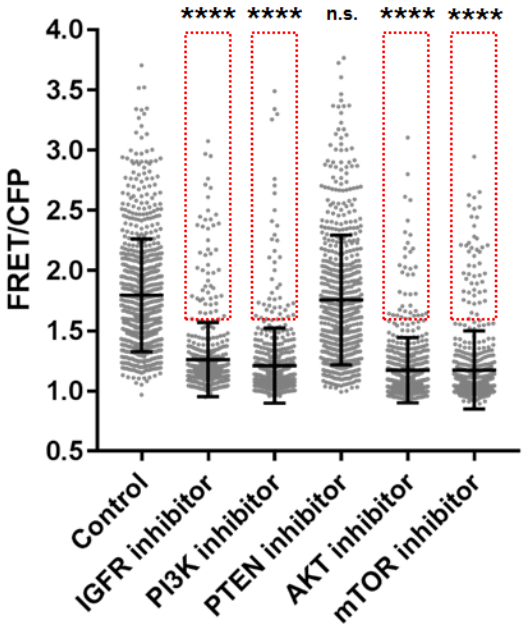


Figure 4-5 PI3K/AKT/mTOR signalling pathway regulates glucose metabolism.
Intracellular glucose levels of MCF-7 cells after inhibitor treatments for 24 hours. The cells in the red squares represent inhibitor resistant high glucose cells. n > 400 cells for each condition from at least three independent experiments. n.s. $p > 0.05$, ****$p < 0.0001$ Kolmogorov-Smirnov test.

Although most of the cells respond to PI3K inhibition and remodel cell metabolism, a subset of MCF-7 cells have resistance to PI3K inhibition. PI3K inhibitors can reduce intracellular glucose levels in most of the cells but a small percentage of cells can keep a high glucose state (Figure 4-6A, red dashed square). Therefore, MCF-7 cells might have a mechanism to keep glycolytic metabolism independent from PI3K signalling. In addition, I measured intracellular glucose levels after washing out the PI3K inhibitor in order to analyse the lasting effect on glucose metabolism (Figure 4-6A). Analysis of the lasting effect is very important to reduce a risk of secondary effects because long-lasting inhibitors can reduce drug dosage and frequency. However, intracellular glucose levels are rapidly returned to the original state after washing out the PI3K inhibitor. Because the PI3K inhibitor non-covalently binds with PI3K isoforms, wash out of inhibitor can quickly recover the PI3K activity. Therefore, the PI3K inhibitor should be continuously applied for the inhibition of glycolysis.

I hypothesized that PI3K inhibitor resistant cells might already have high intracellular glucose levels prior to inhibitor treatment. In order to analyse the metabolic state of this cell population, intracellular glucose levels of FACS-isolated high and low glucose cells were measured after PI3K inhibitor treatment. As a result, PI3K inhibitor treated FACS-isolated high glucose cells have large numbers of PI3K inhibitor-resistant high glucose

cells compared with PI3K inhibitor-treated unsorted cells (Figure 4-6A, B). On the other hand, PI3K inhibitor-treated FACS-isolated low glucose cells had few PI3K inhibitor-resistant cells (Figure 4-6C). Thus, a subset of PI3K inhibitor resistant cells originally have a high glucose state and cells within this population can regulate glycolysis independent from PI3K signalling.

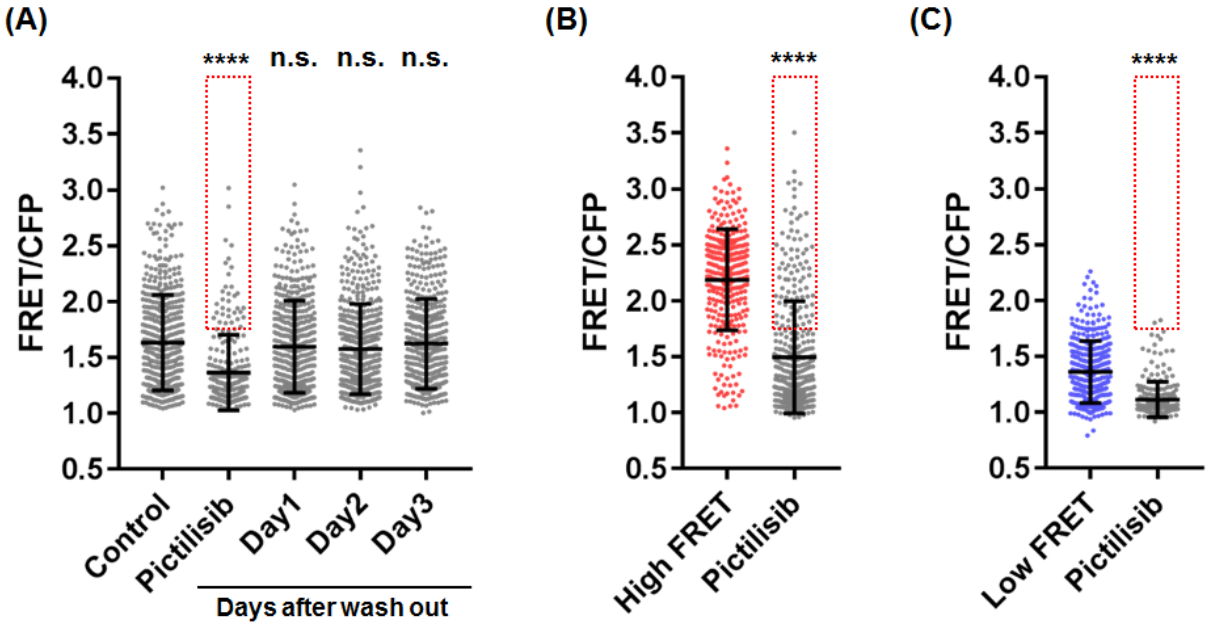


Figure 4-6 The effect of PI3K inhibitor on high and low glucose cells.
(A) FRET distribution of intracellular glucose levels in MCF-7 cells after 0.1 μM Pictilisib treatment and its wash out. Red dashed square represents PI3K inhibitor resistant population. (B, C) FRET distribution of intracellular glucose levels in FACS-isolated high and low glucose cells after 0.1 μM Pictilisib treatment. Red dashed square represents PI3K inhibitor resistant population. n > 300 cells for each condition from at least three independent experiments. n.s. $p > 0.05$, ****$p < 0.0001$ Kolmogorov-Smirnov test.

4.5 The effect of PI3K and PTEN inhibitor on cell metabolism

Inhibition of PI3K reduces intracellular glucose levels. However, details of the effect of the PI3K inhibitor on the other metabolite levels are unclear. In order to analyse the effect of PI3K signalling on glucose metabolism, I measured the metabolic states of MCF-7 cells under PI3K and PTEN inhibitor treatments using six different biosensors (Figure 4-7A, B). Because PTEN dephosphorylates PIP3 and generates PIP2, the PTEN inhibitor could have an opposite effect compared with the PI3K inhibitor. MCF-7 cells and FRET biosensor-expressing MCF-7 cells were incubated in 0.1 μM Pictilisib and 5 μM VO-Ohpic trihydrate for 24 hours. Glucose uptake was measured by 2-NBDG labelling, and mitochondrial membrane potential was measured by TMRE staining. In addition,

intracellular glucose, pyruvate, lactate, and ATP levels were measured by FRET imaging. PI3K inhibitor treatment significantly reduced glucose uptake and intracellular glucose levels. In addition, PI3K inhibition significantly increased intracellular pyruvate and lactate levels. On the other hand, ATP levels and mitochondrial membrane potential were not changed by PI3K inhibition. These results indicate that PI3K inhibition suppresses glucose uptake and consumption of glucose, pyruvate, and lactate.

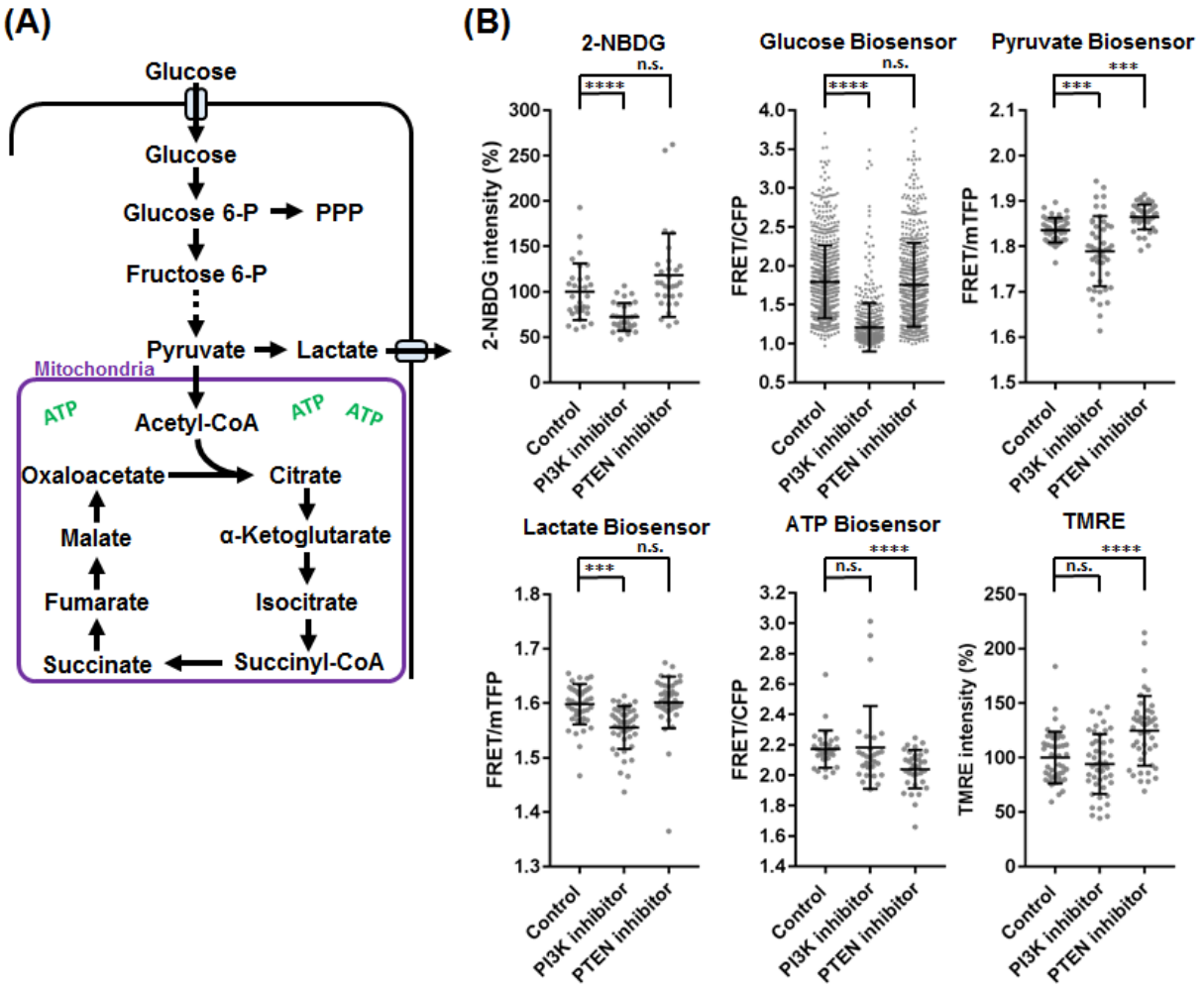


Figure 4-7 Cell metabolism of MCF-7 cells after inhibitor treatments.
(A) Schematic representation of the key metabolic pathways of glycolysis and TCA cycle. (B) Quantified cell metabolism of MCF-7 cells under 0.1 μM Pictilisib and 5 μM VO-Ohpic trihydrate treatments for 24 hours. 2-NBDG intensity, intracellular glucose levels, pyruvate levels, lactate levels, ATP levels, and TMRE intensity were measured by live cell imaging. n > 60 cells for each condition from two independent experiments. n.s. $p > 0.05$, ***$p < 0.001$, ****$p < 0.0001$ Welch unpaired T test.

The PI3K/AKT signalling pathway regulates heterogeneous glucose metabolism. However, the effect of PI3K/AKT signalling on glycolysis and OXPHOS is still unclear. It is important to analyse the metabolic states of inhibitor-treated cells because inhibitor-treated low glucose cells might have different metabolic state compared to low glucose cells without

inhibitor treatment. Therefore, I measured OCR and ECAR after inhibitor treatments. As a result, PI3K and AKT inhibition dramatically reduced OCR (Figure 4-8A). In addition, PI3K, AKT, and mTOR inhibitors reduced ECAR (Figure 4-8B). These results indicate that PI3K/AKT/mTOR signalling pathways regulate both glycolysis and OXPHOS.

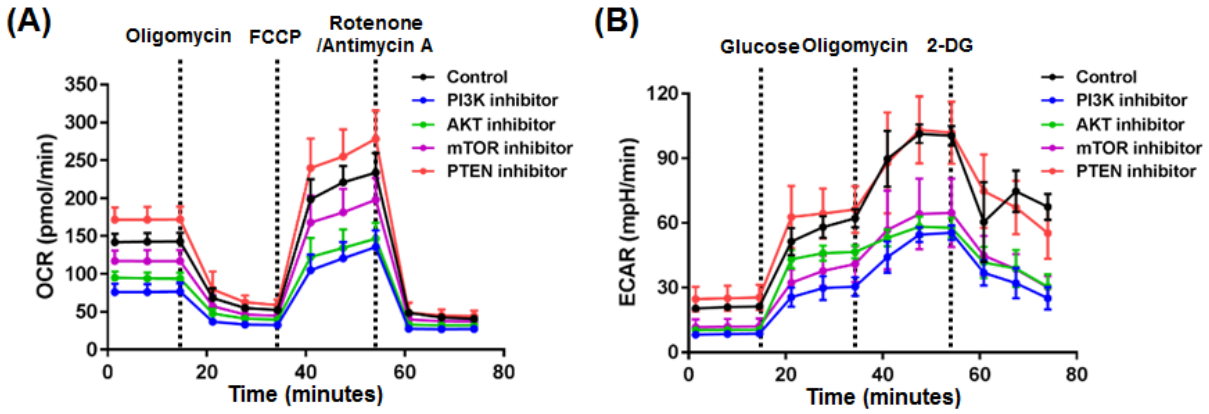


Figure 4-8 PI3K/AKT signalling pathway regulates OCR and ECAR.
(A, B) OCR and ECAR of MCF-7 cells after inhibitor treatments of PI3K/AKT/mTOR signalling pathway. n > 9 wells for each condition from two independent experiments.

4.6 Actin cytoskeletal remodelling regulates glucose metabolism

Cell metabolism is highly heterogeneous in breast cancer, and I have found that PI3K/AKT signalling regulates this metabolic heterogeneity. In addition to PI3K/AKT signalling, actin cytoskeletal remodelling is also expected to regulate glucose metabolism because cell confluence can remodel metabolic state as I described in chapter 4.3. In order to analyse the effect of actin cytoskeletal remodelling on cell metabolism, intracellular glucose levels of MCF-7 cells were measured after inhibitor treatments (Figure 4-9A). Intracellular glucose levels of glucose FRET biosensor-expressing MCF-7 cells were measured after 24 hours incubation with each inhibitor. As a result, actin cytoskeletal remodelling inhibitors also changed intracellular glucose levels. Src, ROCK, Arp2/3 inhibitors and Cytochalasin D reduced intracellular glucose levels. In contrast, Rac1 inhibitor and Jasplakinolide increased intracellular glucose levels. These results indicate that actin cytoskeletal remodelling regulates glucose metabolism. I further measured intracellular glucose levels after knock-down of gene expression using siRNA (Figure 4-9B). Gene knockdown of p120 Catenin, RhoA, ROCK1, and Cofilin reduced intracellular glucose levels. Among them, knockdown of Cofilin has a dramatic effect on reducing intracellular glucose levels. These results indicate that actin cytoskeletal dynamics as well as PI3K/AKT signalling regulate heterogeneous glucose metabolism.

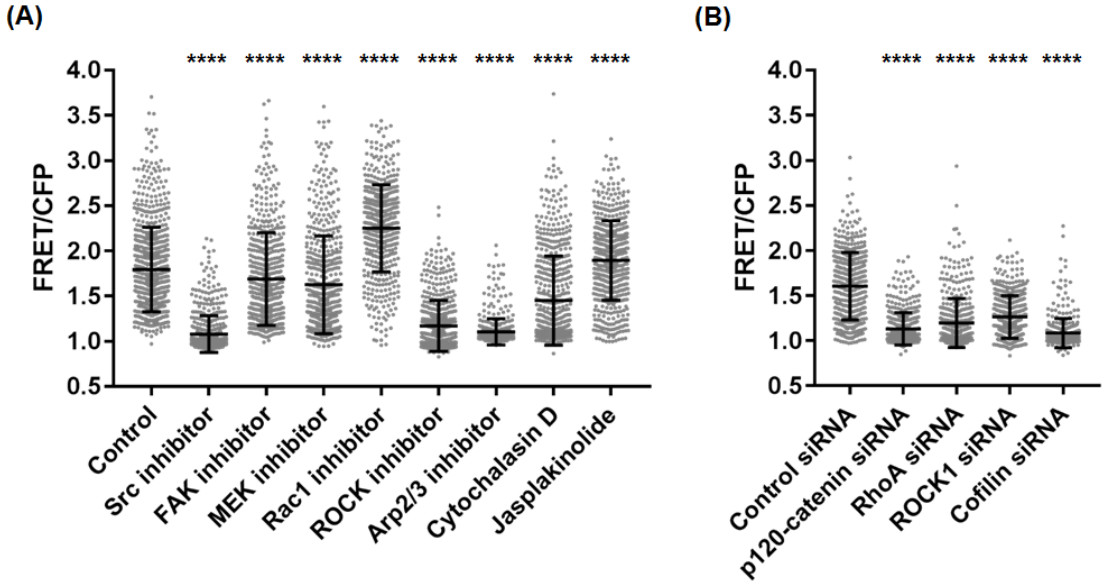


Figure 4-9 Actin cytoskeletal dynamics regulate glucose metabolism.
(A) Intracellular glucose levels of MCF-7 cells after inhibitor treatments for 24 hours. (B) Intracellular glucose levels of MCF-7 cells after gene knockdown with siRNA. n > 400 cells for each condition from at least three independent experiments. ****p < 0.0001 Kolmogorov-Smirnov test.

Actin cytoskeletal dynamics regulate heterogeneous glucose metabolism. However, the effect of actin cytoskeletal remodelling on glycolysis and OXPHOS is still unclear. In order to analyse glycolysis and OXPHOS in inhibitor-treated cells, I measured OCR and ECAR after Rac1 inhibitor, Arp2/3 inhibitor, Cytochalasin D, and Jasplakinolide treatments. As a result, Rac1 inhibitor, Cytochalasin D, and Jasplakinolide increased OCR (Figure 4-10A). On the other hand, Cytochalasin D treated cells increased ECAR but Rac1 inhibitor and Jasplakinolide reduced ECAR (Figure 4-10B). Thus, actin de-polymerization promotes both glycolysis and OXPHOS. In contrast, actin polymerization inhibits glycolysis.

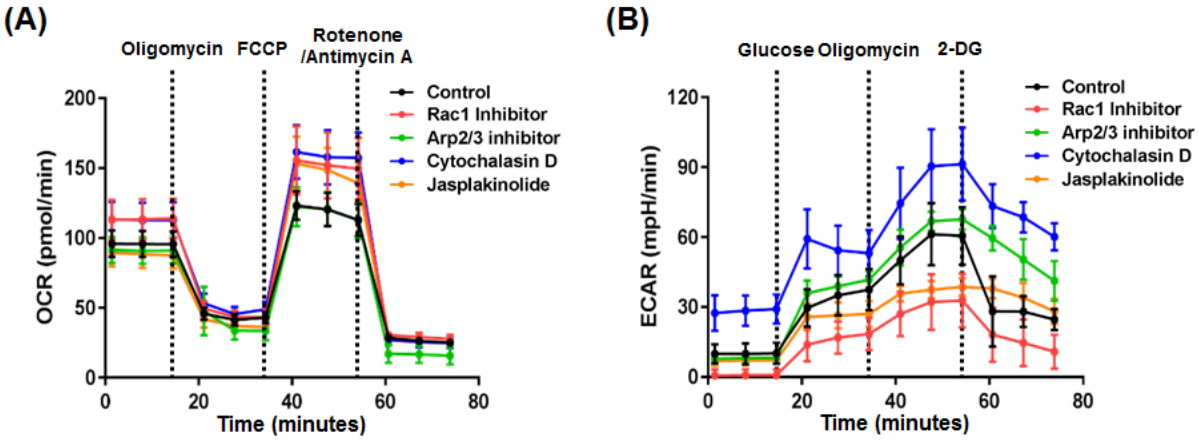


Figure 4-10 Actin cytoskeletal remodelling regulates OCR and ECAR.
(A) OCR and ECAR of MCF-7 cells after inhibitor treatments of PI3K-AKT signalling pathway. (B) OCR and ECAR of MCF-7 cells after inhibitor treatments of actin cytoskeletal remodelling. n > 9 wells for each condition from two independent experiments.

4.7 Signalling pathway of regulating heterogeneous glucose metabolism

Breast cancer cell lines have heterogeneous cell metabolism which can regulate cell proliferation. However, key regulators to establish metabolic heterogeneity in breast cancer are unclear. Because metabolic states are reversibly fluctuating and long term unstable, metabolic heterogeneity could be regulated by epigenetically controlled gene expression and signalling. First, I measured expression and phosphorylation levels of key metabolic regulators in FACS-isolated high and low glucose MCF-7 cells (Figure 4-11A, B). High glucose cells had higher expression levels of GLUT1 which is a key glucose transporter. In addition, AKT phosphorylation levels were high in high glucose cells. Active AKT can promote glycolysis through GLUT1 expression and GLUT4 translocation to the plasma membrane [15]. In contrast, low glucose cells had high expression of c-Myc. c-Myc can activate glycolysis, glutaminolysis, and mitochondrial metabolism [159]. Low glucose cells also had high Cofilin phosphorylation levels. Phosphorylated Cofilin is an inactivated form and low glucose cells could have low actin cytoskeletal dynamics. Thus, high and low glucose cells have different characteristics of gene expression and signalling.

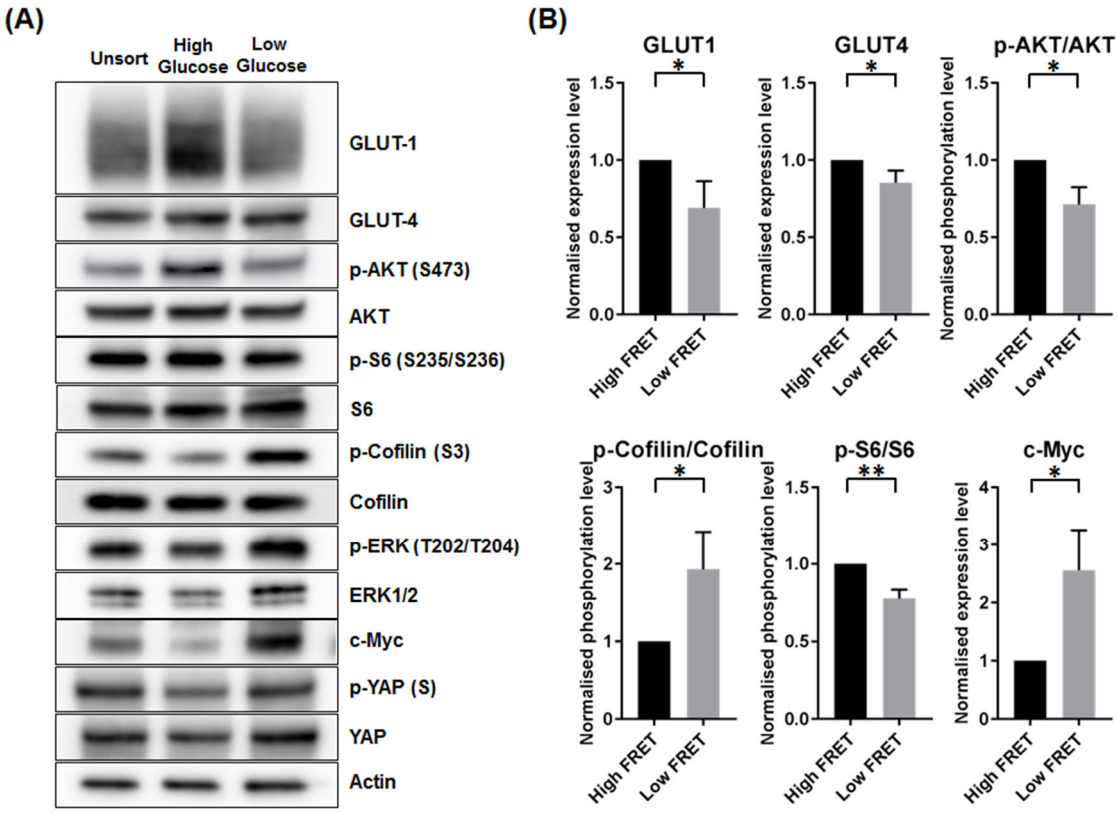


Figure 4-11 Expression levels of metabolism regulator proteins in high and low glucose cells. (A) Western blot of metabolism regulator proteins in FACS-isolated high and low glucose cells. (B) Quantification of western blot. Expression levels of metabolism regulator proteins were quantified from three independent blots. *p < 0.05, **p < 0.01 unpaired T test.

I further analysed acetylation levels of FACS-isolated high and low glucose cells. As I described in chapter 1.4.4, glucose-derived citrate is converted to acetyl-CoA which is a key supplier of acetyl groups for histone acetylation. Metabolomic analysis clarified that intracellular citrate levels of FACS-isolated low glucose cells are 2.5 times higher than FACS-isolated high glucose cells (see chapter 3.3.5). Therefore, low glucose cells might have high acetyl-CoA production and protein acetylation levels. In order to analyse lysine acetylation levels of high and low glucose cells, acetylated lysine residues in FACS-isolated high and low glucose cells were detected by Western Blot analysis (Figure 4-12). Acetyl-lysine antibody can detect proteins which have acetylated lysine in peptides. As a result, some peptides of low glucose cells have higher acetylation levels compared with high glucose cells. In particular, 30-35 kDa and 20-25 kDa proteins had extremely high acetylation levels. From the molecular weight, 20-25 kDa proteins might be histone H1. Histones have higher acetylation levels compared with other proteins and lysine of H1, H2A, H3, and H4 are highly acetylated by HATs. In order to determine these proteins and acetylation sites, histone acetylation levels in high and low glucose cells should be analysed using acetyl-histone antibodies. In addition, proteomic analysis of acetylated proteins is necessary to clarify the relationship between glucose metabolism and histone acetylation. Thus, histone acetylation might regulate metabolic heterogeneity.

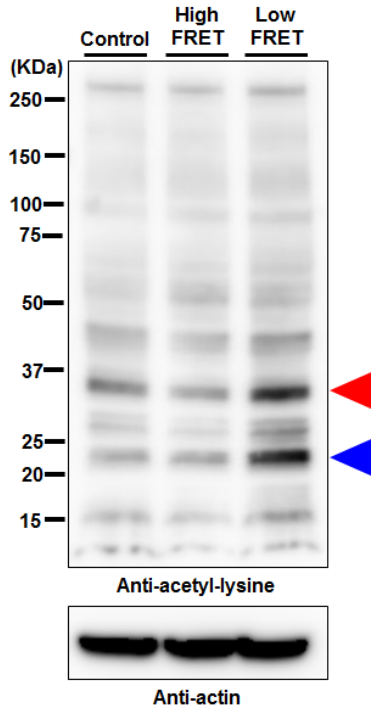


Figure 4-12 Western Blot of acetyl-lysine in high and low glucose cells.
Western blot analysis of acetyl-lysine in FACS-isolated high and low glucose cells. Acetylation levels of the proteins at the red and blue arrows are extremely high in low glucose cells.

4.8 Signalling pathway in different cell confluences

Glycolytic-high glucose cells and OXPHOS-low glucose cells have different characteristics of PI3K/AKT signalling and actin cytoskeletal dynamics. Because cell confluence regulates intracellular glucose levels, I expected that cell signals at high and low cell confluence might have similar characteristics to FACS-isolated low and high glucose cells. In order to compare characteristics of the key metabolic regulators between high and low cell confluence, I measured expression and phosphorylation levels of GLUT1, GLUT4, AKT, and Cofilin in MCF-7 cells at 1.0 x 10^4 cells/cm^2 and 1.0 x 10^5 cells/cm^2 (Figure 4-13A, B). As a result, the cells in low cell confluence had higher expression levels of GLUT1 and GLUT4. These glucose transporters can take in glucose from extracellular micro-environments. In addition, expression and phosphorylation levels of AKT were higher at high cell confluence. On the other hand, there was no significant difference of phospho-AKT/AKT ratio between the cells at high and low cell confluence. Low expression and high Cofilin phosphorylation levels is a hallmark of the cells in high cell confluence. High cell confluence induces mechanical stress and highly packed cells could stabilise the actin cytoskeletal structure through Cofilin activity. These characteristics of metabolic regulators are similar to FACS-isolated high and low glucose cells. Heterogeneous breast cancer cells have different regulatory mechanisms of glucose metabolism and micro-environmental factors can further increase metabolic complexity and heterogeneity.

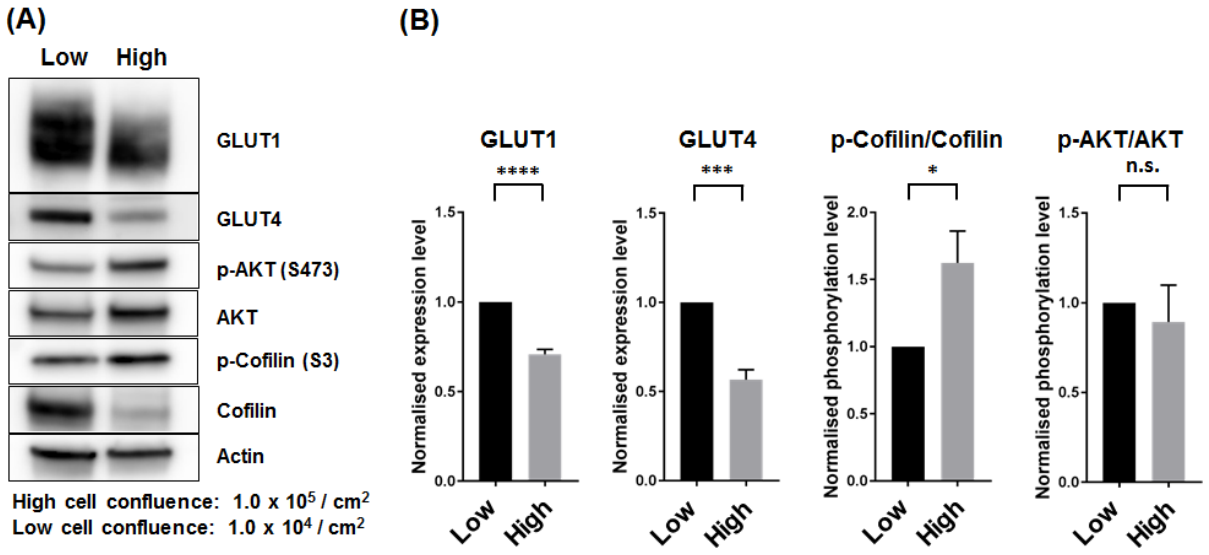


Figure 4-13 Expression levels of metabolism regulator proteins in high and low cell confluence. (A) Western blot of metabolism regulator proteins of MCF-7 cells at 1.0 x 10^4 cells/cm^2 and 1.0 x 10^5 cells/cm^2. (B) Quantification of western blot. Expression levels of metabolism regulator proteins were quantified from three independent blots. n.s. $p > 0.05$, *$p < 0.05$, ***$p < 0.001$ unpaired T test.

4.9 Chapter discussion

In this chapter, I found that many microenvironmental factors such as nutrient accessibility, cell confluence, ECM stiffness, extracellular pH, and oxygen concentration regulate glucose metabolism. Among them, cell confluence is a key regulator of glucose metabolism. The cells at high cell confluence reduce expression of glucose transporters and stabilize the actin cytoskeleton. These highly packed cancer cells suppress glycolysis, and the core of tumours could have similar metabolic characteristics. I showed that FACS-isolated high and low glucose cells have different activities of PI3K/AKT/mTOR signalling and actin cytoskeletal dynamics. Although most of the high glucose cells regulate glycolysis depending on PI3K activity, a subset of cells can promote glycolysis independently from PI3K signalling. PI3K inhibition can effectively suppress tumour growth, but this PI3K inhibitor-resistant cell population might recur after therapeutic treatments. In order to improve therapeutic options for breast cancer, combinatorial inhibitor treatment should be investigated for targeting PI3K inhibitor resistant high glucose cells.

Chapter 5. Migrating high glucose cells accelerate glycolysis

5.1 Chapter summary

In this chapter, I analyse the glucose metabolism of MCF-7 and MDA-MB-231 cells *in vivo*. Imaging intracellular glucose levels can determine the metabolic balance of glycolysis and OXPHOS at the single cell scale. Analysis of cancer cell metabolism *in vivo* could clarify the mechanisms of metabolic reprogramming and tumour microenvironmental adaptation. I clarify that intracellular glucose levels of MCF-7 and MDA-MB-231 cells are significantly higher at the tumour periphery. In both breast cancer cell lines, intracellular glucose levels are increased in gradient from central to peripheral axis. Linking to earlier data, I find that cells at the tumour periphery have low cell confluence, high GLUT1 expression levels, and high AKT phosphorylation levels. High glucose cells at the tumour periphery could promote glycolysis by activating glucose uptake and PI3K/AKT signalling in low cell confluence. The scratch assay can reduce cell confluence and facilitate cell migration. Scratch-induced migrating cells dramatically increase intracellular glucose levels. Because characteristics of scratch-induced migrating cells are similar to the cells at the tumour periphery, the scratch assay can analyse migrating high glucose cells in low cell confluence and non-migrating low glucose cell in high cell confluence. Both imaging and metabolomic analysis identify that migrating high glucose cells highly utilise glycolysis.

5.2 Intravital imaging of intracellular glucose levels

5.2.1 Intravital imaging of intracellular glucose levels in MCF-7 cells

In the previous chapter, I have shown that breast cancer cells have heterogeneous glucose metabolism which can reversibly fluctuate between glycolysis and OXPHOS. This metabolic fluctuation could be important for tumour microenvironmental adaptation. In particular, breast tumours are composed of heterogeneous cancer cells in complex microenvironments with different nutrient accessibility, oxygen concentration, and ECM stiffness. Cancer cells need to reprogram cell metabolism for sustainable proliferation in such different tumour microenvironments. In order to analyse the metabolic states of MCF-7 cells *in vivo*, I injected glucose FRET biosensor-expressing MCF-7 cells under the fourth nipple of NOD SCID mice and ratiometric FRET images of developed tumours were acquired by intravital imaging (Figure 5-1A). Intracellular glucose levels were high at the

tumour periphery and low at the core of the tumour. In addition, I quantified the glucose levels of the developed tumour in centre-periphery axis (Figure 5-1B). Intracellular glucose levels of the periphery were significantly higher than central areas. In particular, 50-100 μm of the tumour edge had extremely high intracellular glucose levels. These intracellular glucose levels of MCF-7 cells suggest that some microenvironmental pressures could change glucose metabolism. Cell confluence and actin cytoskeletal remodelling through cell migration could change glucose metabolism *in vivo* because cancer cells at the tumour periphery might have more space for proliferation and migration.

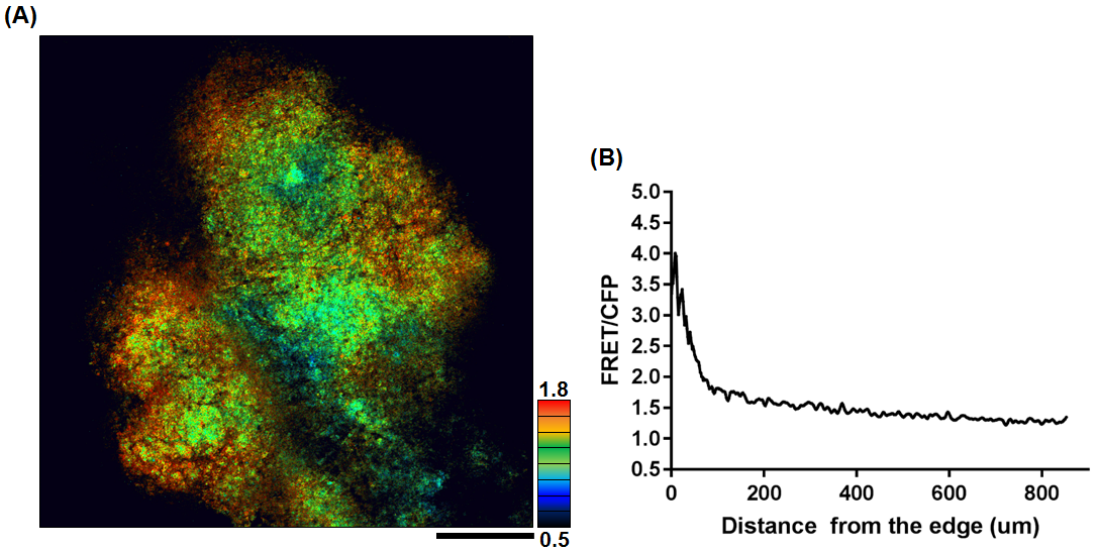


Figure 5-1 Intravital imaging of intracellular glucose levels in MCF-7 tumours.
(A) Intravital imaging of intracellular glucose levels of MCF-7 tumours in NOD SCID mice. Scale = 500 μm. (B) Quantified intracellular glucose levels of developed tumour in central-peripheral axis. n = 4

5.2.2 Intravital imaging of intracellular glucose levels in MDA-MB-231 cells

MCF-7 cells showed heterogeneous intracellular glucose levels in developed tumours. Peripheral regions of developed tumours had high glucose levels whereas central areas had low glucose levels. I further analysed intracellular glucose levels of MDA-MB-231 cells which have metabolic characteristics that are different to MCF-7 cells. MDA-MB-231 cells are low adhesive and high glycolytic breast cancer cell lines. Intravital imaging of intracellular glucose levels in different breast cancer cell lines is very important to analyse the fundamental mechanism of metabolic reprogramming in breast cancer. Glucose FRET biosensor-expressing MDA-MB-231 cells were injected under the fourth nipple of BALB/c Nude mice and FRET images of developed tumours were acquired. As with MCF-7 tumours, intracellular glucose levels of MDA-MB-231 cells were extremely high at the tumour periphery (Figure 5-2).

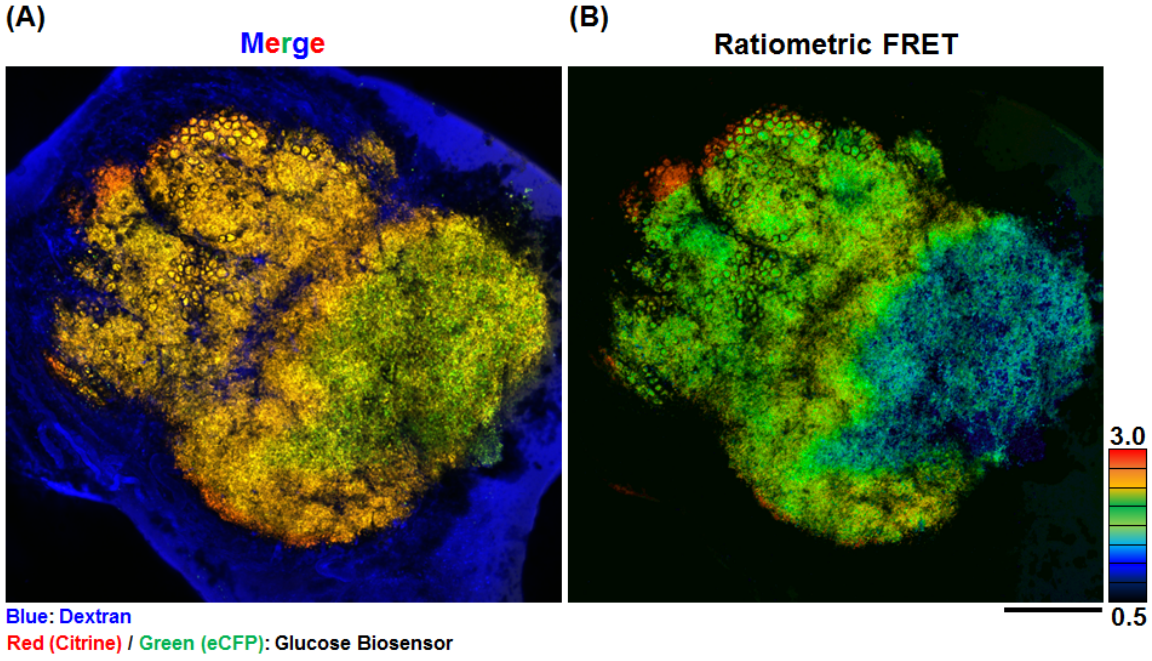


Figure 5-2 Intravital imaging of intracellular glucose levels in MDA-MB-231 tumours.
(A) Intravital imaging of intracellular glucose levels of MDA-MB-231 tumours in BALB/c Nude mice. Red and Green are FRET signals from glucose FRET biosensor. Blue is 155 KDa fluorescein-dextran. Scale=500 μm. (B) Ratiometri FRET image of glucose FRET biosensor of MDA-MB-231 tumour.

I measured fluorescence lifetime of the glucose FRET biosensor of MDA-MB-231 cells in the developed tumours. Especially with intravital imaging, the FRET ratio fluctuates depending on microenvironmental factors such as temperature, pH, and depth of imaging [87-89]. Fluorescence lifetime imaging can reduce the risk of different light scattering of eCFP and Citrine because FRET efficiency is measured from the fluorescence lifetime of the donor fluorophore. Fluorescence lifetime of the glucose FRET biosensor was matched with a pattern of FRET ratio, indicating that ratiometric FRET imaging is a reliable imaging approach *in vivo* (Figure 5-3). Therefore, I used ratiometric FRET imaging in the next sections. The patterns of intracellular glucose levels could be regulated by micro-environmental pressures. There are several possible explanations for the patterns of intracellular glucose levels I observed by intravital imaging. First, cancer cells at the tumour periphery might have more space for proliferation. Low cell confluence can promote glucose metabolism by increasing GLUT1 and GLUT4 expression levels. Second, cells at the tumour periphery might have high actin cytoskeletal dynamics because the cells can invade towards free space. Actin cytoskeletal remodelling promotes glycolysis and I have shown high glucose cells could have high actin dynamics. Nutrient accessibility is also a possible factor to make patterns of intracellular glucose levels. Cells might have different nutrient accessibility depending on tumour positions and the distance from blood vessels.

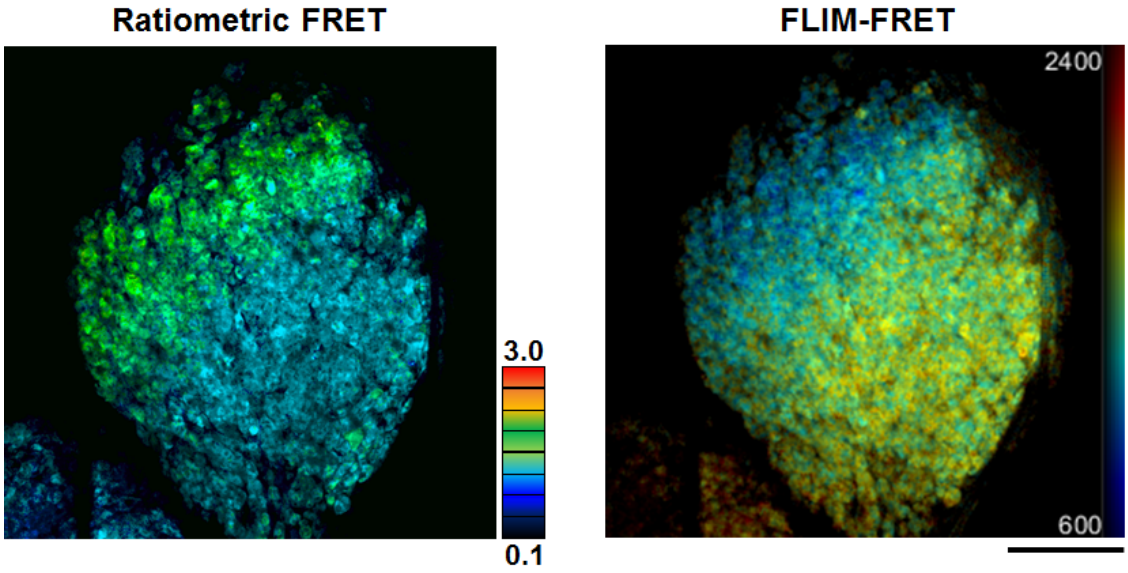


Figure 5-3 Ratiometric FRET and FLIM-FRET of intracellular glucose levels.
Intravital imaging of intracellular glucose levels of MDA-MB-231 tumours by ratiometric FRET and FLIM-FRET. Scale=100 μm.

5.2.3 Histopathology analysis

Breast cancer cells could be remodelling cell metabolism in the tumour microenvironment because xenograft tumours had patterns of intracellular glucose levels. GLUT1 expression level and PI3K activity could regulate metabolic remodelling in the process of tumour development. FACS-isolated high and low glucose cells have different characteristics of gene expression and signalling *in vitro*, xenograft tumours are expected to have similar characteristics. In order to analyse the role of GLUT1 and PI3K/AKT signalling for metabolic reprogramming *in vivo*, GLUT1 expression level and AKT phosphorylation level in MCF-7 tumours were measured by immunohistochemistry (IHC). First, I acquired intravital images of the glucose FRET biosensor in MCF-7 tumours and then tumours were resected, fixed, and incubated with antibodies. In FRET imaging, I confirmed the cells at the tumour periphery have high intracellular glucose levels (Figure 5-4A, B). Immuno-staining of GLUT1 clarified that GLUT1 expression was slightly high at the tumour periphery (Figure 5-4C, E). In addition, AKT phosphorylation level was relatively high at the tumour periphery (Figure 5-4D, F). These molecular characteristics are matched with high and low glucose cells *in vitro*. I showed in chapter 4.7 that FACS-isolated high glucose cells had high GLUT1 expression and high AKT phosphorylation levels. These data suggest that high and low glucose cells have similar metabolic characteristics *in vitro* and *in vivo*.

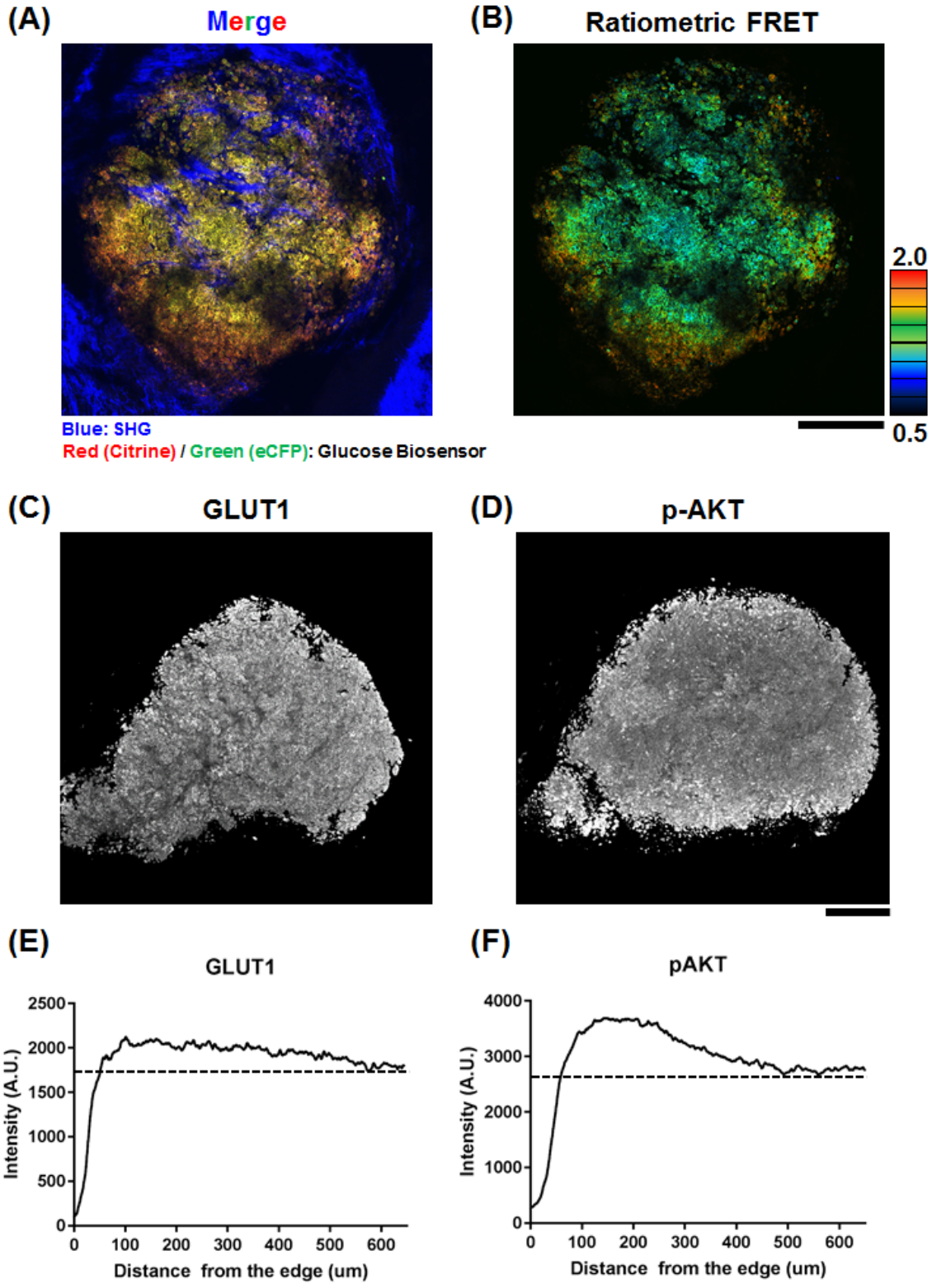


Figure 5-4 IHC imaging of GLUT1 and pAKT in MCF-7 tumours.
(A, B) Intravital imaging of intracellular glucose levels of MCF-7 tumours in NOD SCID mice. Red and Green are FRET signals from glucose FRET biosensor. Blue is second harmonic generation (SHG). Scale=500 μm. (C-D) IHC of GLUT1 and phosphorylated AKT. IHC images and FRET images were acquired from the same tumour. Scale = 500 μm. (E-F) Quantified GLUT1 and phosphorylated AKT intensity of MCF-7 tumour in central-peripheral axis. Average intensities of GLUT1 and pAKT were quantified from whole images. n = 3

MCF-7 and MDA-MB-231 xenograft tumours have the patterns of intracellular glucose levels. Different cell confluence of xenograft tumours could be one possible reason to make metabolic patterns *in vivo*. In order to analyse cell confluence of developed tumours, I measured the nuclei density of MCF-7 tumours. MCF-7 cells were injected under the fourth nipple of NOD SCID mice and developed tumours were resected after intravital imaging. Resected tumours were fixed, frozen, and sliced in 5 μm sections. The slices were stained with DAPI and nuclei images were acquired (Figure 5-5A). Because xenograft tumours have MCF-7 cells and other types of cells such as CAFs, I removed the cells which did not have glucose FRET biosensor expression. Nuclei density of MCF-7 cells in xenograft tumours was then measured in the centre-periphery axis (Figure 5-5B). As a result, averaged nuclei density was clearly low at the tumour periphery. This nuclei density indicates that cell confluence at the tumour periphery is lower than central areas, and cell confluence negatively correlated with intracellular glucose levels. This data indicates that cell confluence regulate glucose metabolism by changing glucose transporter expression and PI3K/AKT activities.

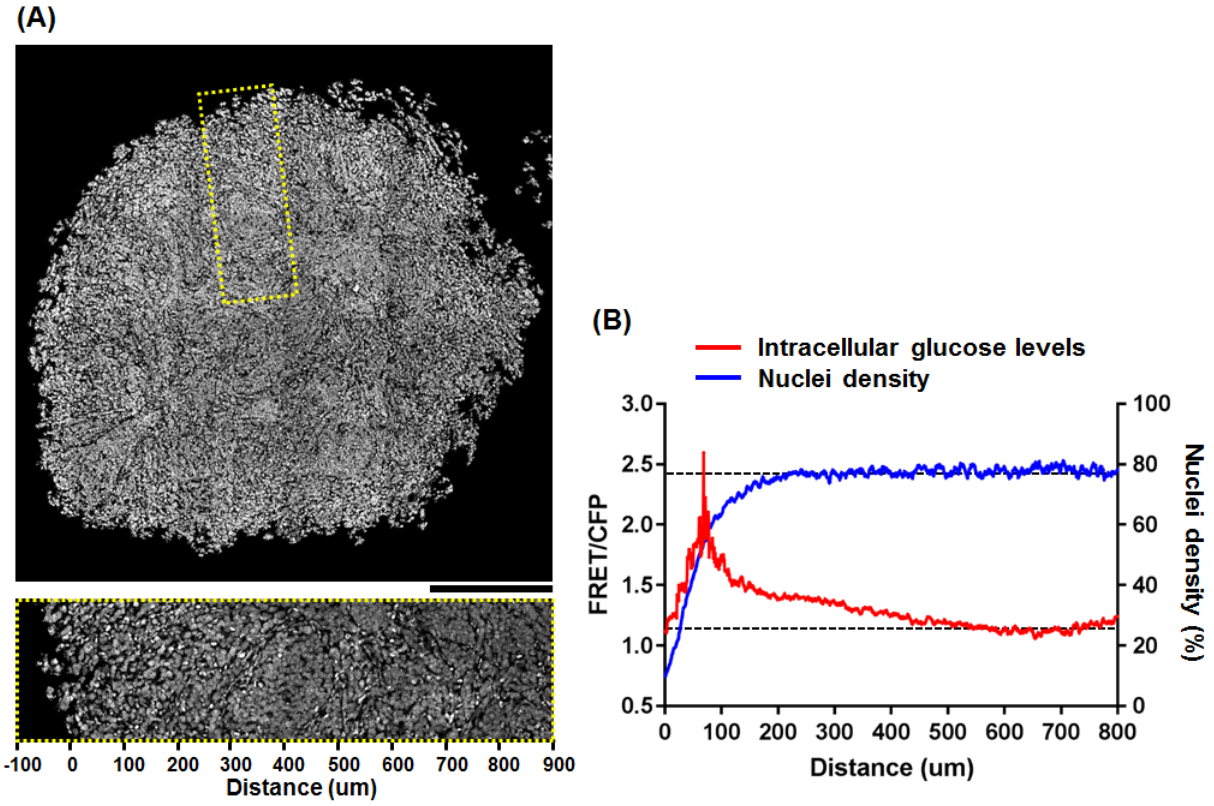


Figure 5-5 Cell confluence of MCF-7 xenograft tumours.
(A) DAPI staining of MCF-7 xenograft tumours. DAPI images and FRET images in Figure 5-4 images were acquired from the same tumour. Scale = 500 μm. (B) Quantified nuclei density of MCF-7 tumour in central-peripheral axis. Average nuclei density was quantified from whole image. n = 3

5.3 Scratch-induced high glucose cells promote glycolytic cell metabolism

5.3.1 Scratch-induced migrating cells increase glucose levels

Cell confluence and actin cytoskeletal remodelling can regulate cell metabolism. In order to analyse the effect of cell confluence and cell migration on glucose metabolism, I scratched the cells and compared intracellular glucose levels. The cells at the leading edge promote cell migration in low cell confluence, and the cells in the central area immobilise in high cells confluence. Therefore, the scratch assay can compare migrating cells in low cell confluence and non-migrating cells in high cell confluence. First, I plated glucose FRET biosensor-expressing breast cancer cells with high cell confluence and cultured them overnight. The cells were then scratched by a pipette tip and intracellular glucose levels were measured by time-lapse imaging. As a result, intracellular glucose levels of MCF-7 cells were dramatically increased at the leading edge (Figure 5-6). Because the cells were plated in high confluence, intracellular glucose levels of non-migrating cells were very low. Scratched cells started to migrate and intracellular glucose levels were increased about 10 hours after the scratch.

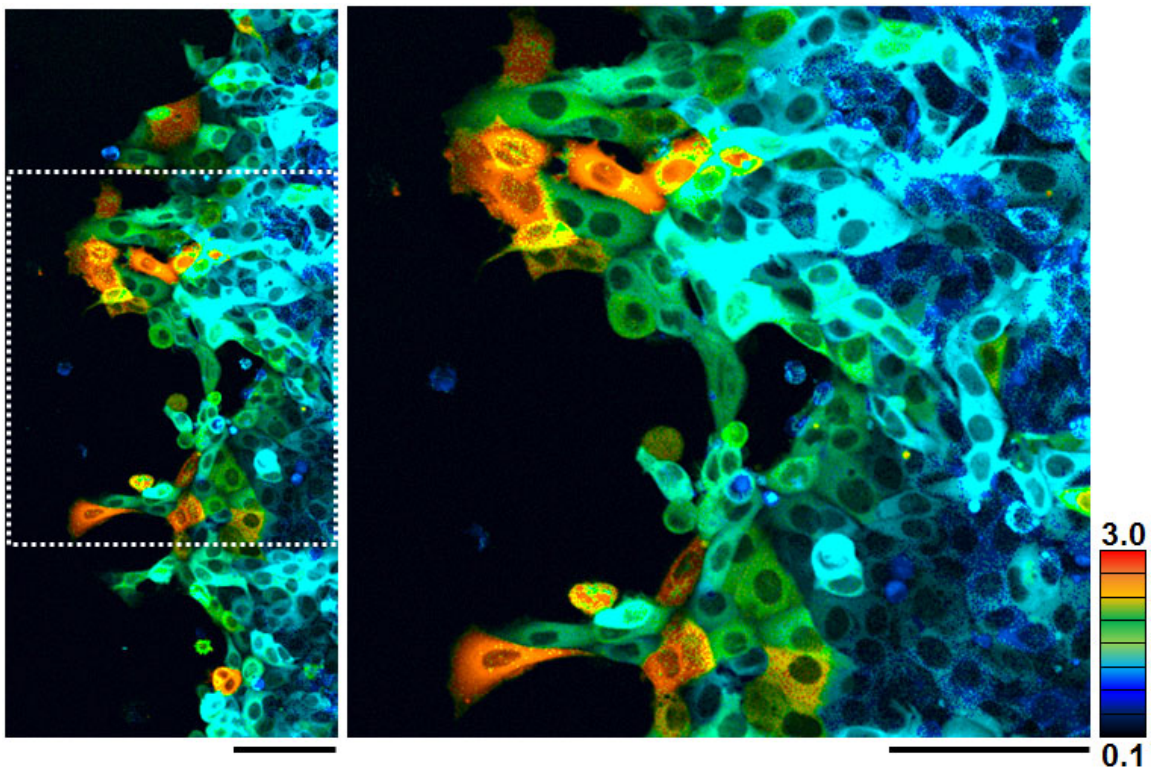


Figure 5-6 Scratch assay of glucose FRET biosensor expressing MCF-7 cells.
Ratiometric FRET images of glucose FRET biosensor in MCF-7 cells were acquired 10 hours after scratching of monolayer. Scale=100 μm.

In order to better characterise the dynamics of the changes in glucose levels and cell migration, kymographs were created from time-lapse imaging in five breast cancer cell lines. The kymographs were generated from three independent scratch assays, and intracellular glucose levels of the kymograph were the average of over 5,000 lines (Figure 5-7).

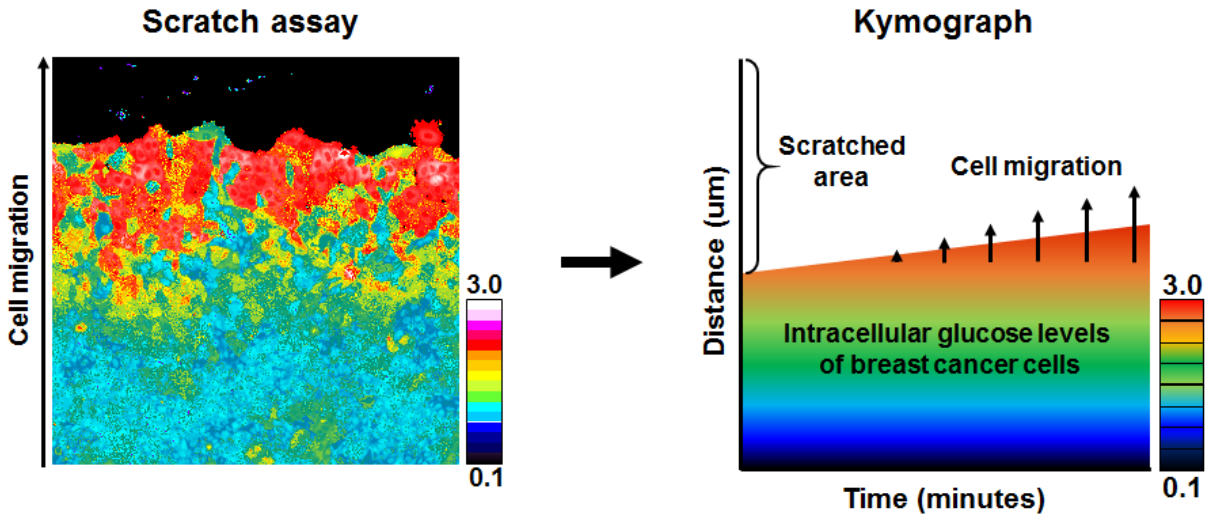


Figure 5-7 Outline of constructing kymograph.
Glucose FRET biosensor expressing breast cancer cells were scratched and time-lapse images were acquired for 40 hours. Kymograph represents intracellular glucose levels during cell migration.

Five breast cancer cell lines have different characteristics of cell adhesion and migration. T47D and MCF-7 cells have high cell adhesion but JimT-1 and MDA-MB-231 cells are low-adhesive cells. In addition, JimT-1 and MDA-MB-231 cells are highly migratory cell lines but ZR-75-1 cells have very low cell migration. Comparison of intracellular glucose levels of these cell lines during cell migration can analyse the relationship between glucose metabolism and cell migration. Among five breast cancer cell lines, MCF-7, ZR-75-1, and MDA-MB-231 cells had high intracellular glucose levels at the leading edge (Figure 5-8). These scratch assays indicate two different aspects of remodelling cell metabolism in migrating and non-migrating cells. As I stated, scratch-induced migrating cells dramatically increased glucose levels. In contrast, non-migrating cells reduced intracellular glucose levels which could be induced by increasing cell confluence. MCF-7 and MDA-MB-231 cells had similar patterns of intracellular glucose levels within tumours *in vivo*. The cells at the tumour periphery with low cell confluence had extremely high intracellular glucose levels. Thus, migrating cells at low cell confluence can accelerate intracellular glucose levels which are similar metabolic characteristics to the cells *in vivo*.

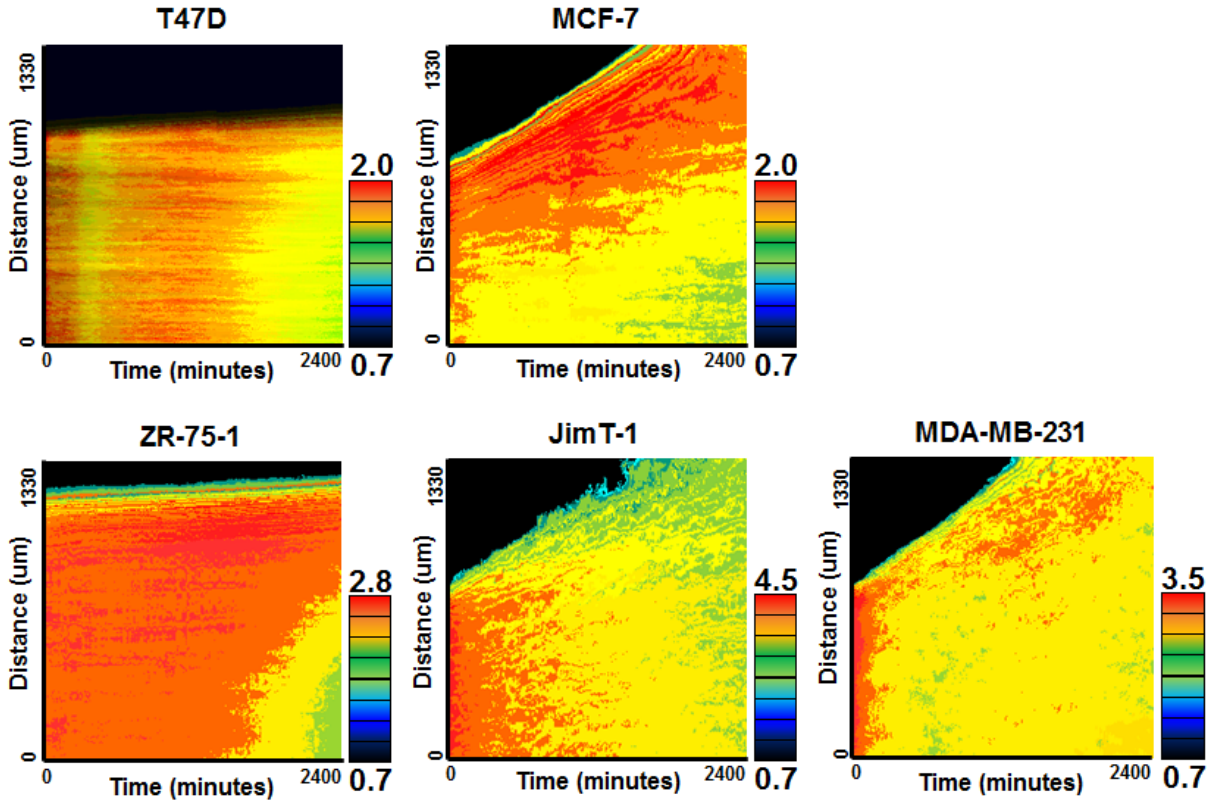


Figure 5-8 Scratch assay in breast cancer cell lines.
Kymograph of glucose FRET signals in scratch assay. Glucose FRET biosensor expressing breast cancer cell lines were scratched and time-lapse images were acquired for 40 hours. The kymographs were generated from three independent scratch assays.

5.3.2 Scratch and wound healing assay in MCF-7 cells

The scratch assay showed a dramatic intracellular glucose increase in migrating cells at the leading edge. The scratch assay physically removes the cells by scratch which could damage the cells. Therefore, there is a possibility that the scratch-induced high glucose level was induced by cell damage. In order to clarify the effect of scratch itself, I compared intracellular glucose levels in migrating cells by scratch assay and wound healing assay (Figure 5-9A, C). In wound healing assay, cells are plated in removable chambers which can create a wound without damaging the cells. As a result, migrating cells at the leading edge in wound healing assay also increased intracellular glucose levels. In addition, the cells in scratch and wound healing assay had very similar migration speed (Figure 5-9B). These results indicate that intracellular glucose increase in migrating cells was driven by cell migration and change in cell confluence. Migrating high glucose cells could promote glycolysis for proliferation and migration.

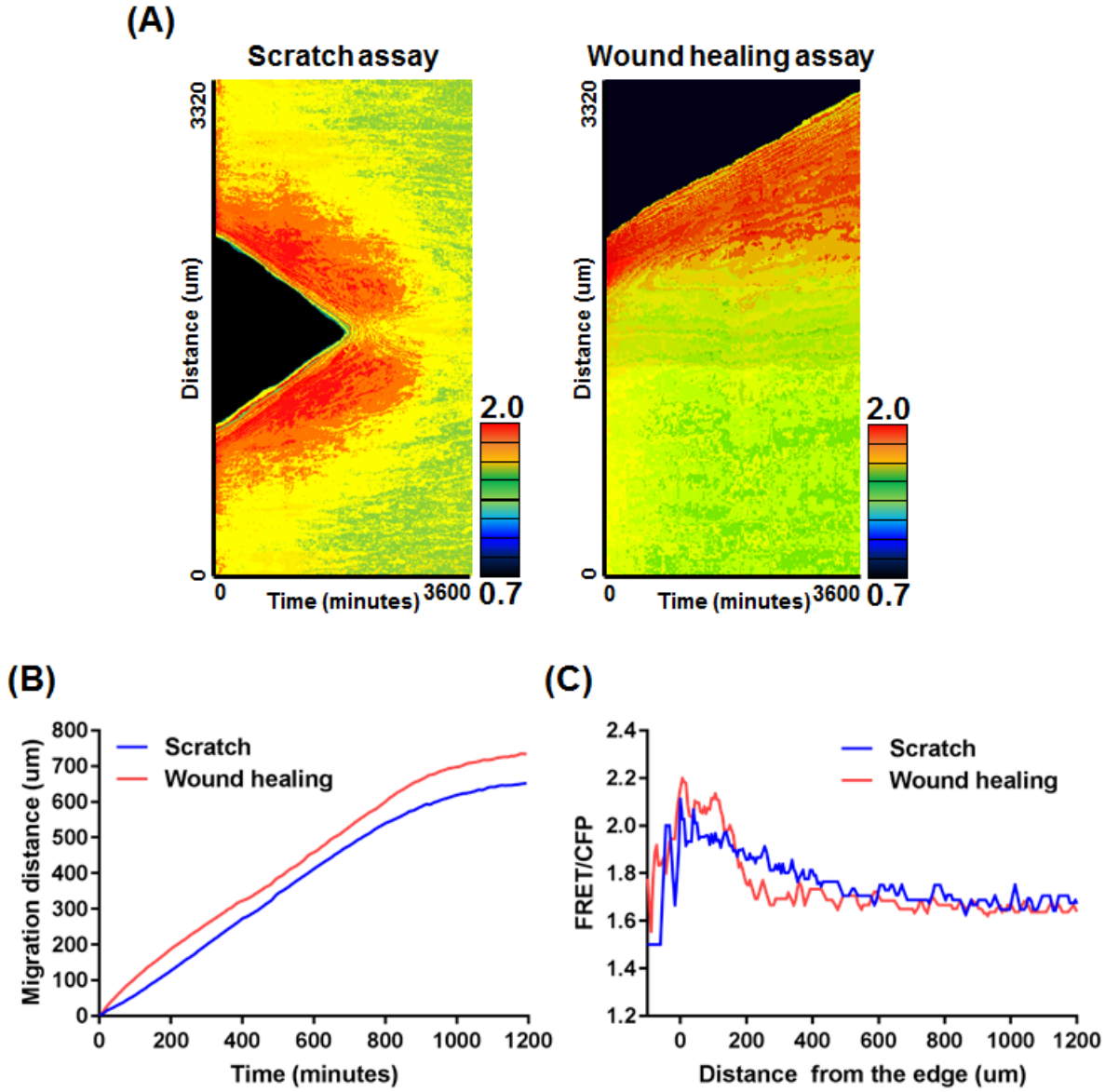


Figure 5-9 Comparison of scratch and wound healing assay.
(A) Kymograph of glucose FRET signals in scratch and would healing assay. (B) Quantification of cell migration in scratch and wound healing assay. (C) Quantification of intracellular glucose levels in scratch and wound healing assay.

5.3.3 Scratch-induced migrating cells decrease ATP levels

Imaging intracellular glucose levels thus suggests that cell migration and cell confluence can regulate glucose metabolism. Both scratch and would healing assays induce dramatic intracellular glucose increase in migrating cells at the leading edge. These migrating high glucose cells could have high ATP production because migrating cells require large amounts of ATP to facilitate cell migration [160]. In order to clarify the energetic stress in migrating and non-migrating cells, I measured intracellular ATP levels of MCF-7 cells in

the scratch assay (Figure 5-10A). Unexpectedly, scratch-induced migrating cells reduced intracellular ATP levels. In addition, I further measured AMPK activity in the scratch assay and I found that the cells at the leading edge have high AMPK activity (Figure 5-10B). There are two possible explanations to create this energetic condition. One possibility is that migrating cells have the same ATP production as non-migrating cells but consume larger amounts of ATP. In this case, intracellular ATP levels could decline due to rapid ATP consumption. Another possibility is that migrating cells promote glycolysis and it cannot supply sufficient ATP for cell migration. Glycolysis can produce amino acids and nucleic acids as well as ATP from glucose. However, the amount of ATP produced per glucose molecule is lower than OXPHOS. Therefore, glycolytic cells would also have low intracellular ATP levels. The metabolic regulation mechanisms of migrating and non-migrating cells are still unclear and further investigation is required.

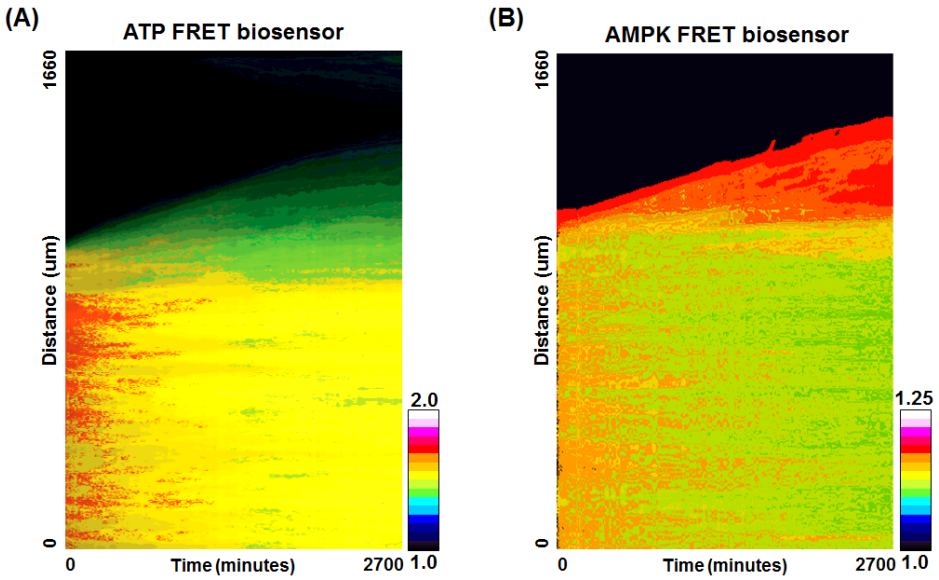


Figure 5-10 Scratch assay of ATP biosensor expressing MCF-7 cells.
(A, B) Kymograph of ATP and AMPK FRET signals in scratch assay. ATP and AMPK FRET biosensor expressing MCF-7 cells were scratched and time-lapse images were acquired for 45 hours.

5.3.4 Nutrient requirement during cell migration

Migrating cells increase intracellular glucose levels and reduce ATP levels. The cells at leading edge could take in large amounts of glucose but also consume more ATP than non-migrating cells. Therefore, efficient energy production is very important to facilitate cell migration. Cancer cells have different nutrient requirements in different developmental stages and microenvironments [161]. Glucose, glutamine, and lactate are the key nutrient source in tumour microenvironments. In order to analyse the nutrient requirement of

migrating cells, I cultured the cells in different nutrient conditions and then measured migration ability. First, I analysed cell metabolism of MCF-7 cells in 12 different nutrient conditions by ratiometric FRET imaging. Intracellular glucose levels declined in glutamine-starved media because the cells need to complement glutamine depletion by consuming large amounts of glucose for ATP and biomass production (Figure 5-11A). Intracellular ATP levels were stable in nutrient starvation. However, the glucose analog 2-DG dramatically reduced ATP levels (Figure 5-11B). 2-DG inhibits glycolysis because it has the 2-hydroxyl group replaced by hydrogen and accumulates in the cells as 2-deoxy-D-glucose-6-phosphate (2DG6P). Because the media in all 12 conditions includes 10% FBS, the cells might produce ATP from small amounts of glucose (Table 2-2). Glucose and glutamine are the key nutrient sources of ATP and biomass production. These two carbon source are crucial for proliferation because cells having access to glucose or glutamine can continuously proliferate (Figure 5-11C). Although there was no obvious difference of cell proliferation between glucose and glutamine starvation, glutamine starved MCF-7 cells significantly supressed cell migration compared with glucose starved cells (Figure 5-11D). Therefore, glutamine could be a key nutrient source for cell migration. These data indicate that each nutrient source is used for different biological events.

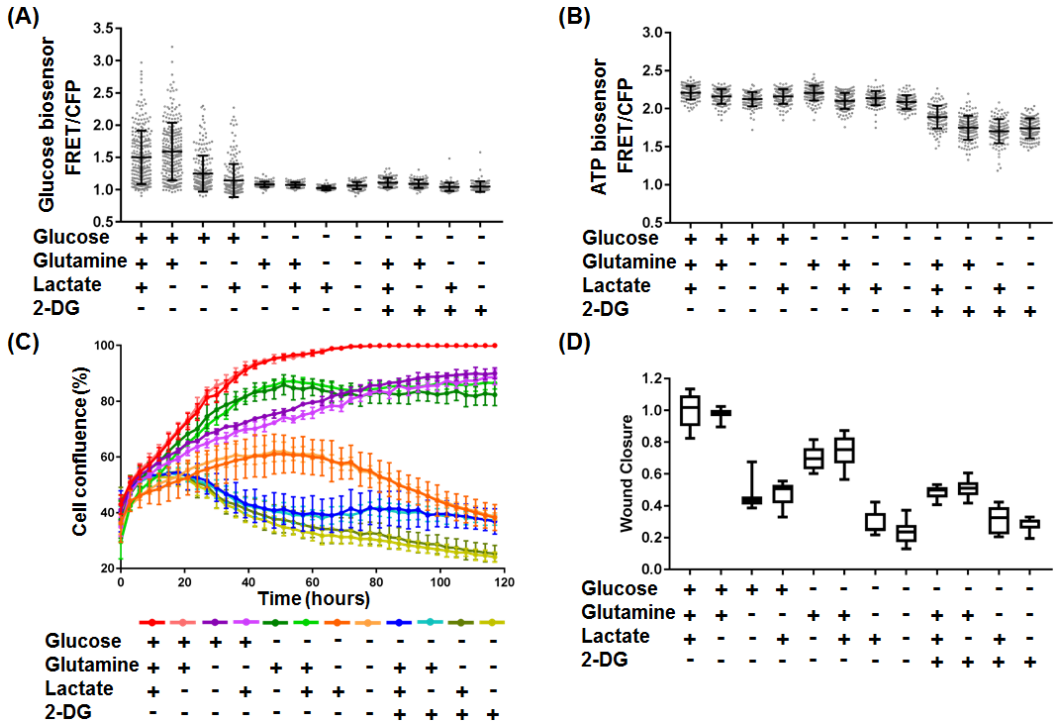


Figure 5-11 nutrient requirements of MCF-7 cells.
(A) Intracellular glucose level of MCF-7 cells. n > 100 (B) Intracellular ATP level of MCF-7 cells. n > 100 (C) Cell growth of MCF-7 cells. n = 5 (D) Wound healing assay of MCF-7 cells in 12 different nutrient conditions. Wound closure was calculated from the wound area at time 0 hour and 24 hours. n = 12 for each condition from three independent experiments.

5.3.5 Imaging cell metabolism in scratch-induced migrating cells

Scratch-induced migrating cells had a dramatic intracellular glucose increase and ATP decrease. However, details of cell metabolism in migrating high glucose cells and non-migrating low glucose cells are unclear. In order to analyse the glucose metabolism of these two cell populations, I measured glucose uptake and consumption speed as I analysed in chapter 3.3.2. MCF-7 cells were plated on glass bottom dishes and cultured for 24 hours after scratching the cells. The glucose uptake and consumption speeds of scratched MCF-7 cells were measured by incubating in 0 mM and 25 mM glucose media (Figure 5-12A). Glucose starvation dramatically reduced intracellular glucose levels and incubation in 25 mM glucose media gradually increased intracellular glucose levels. From the segmentation and tracking of intracellular glucose levels of individual cells, I found intracellular glucose levels were highly correlated with glucose uptake and consumption speed (Figure 5-12B, C). These results indicate that migrating high glucose cells take in and consume glucose faster than non-migrating low glucose cells.

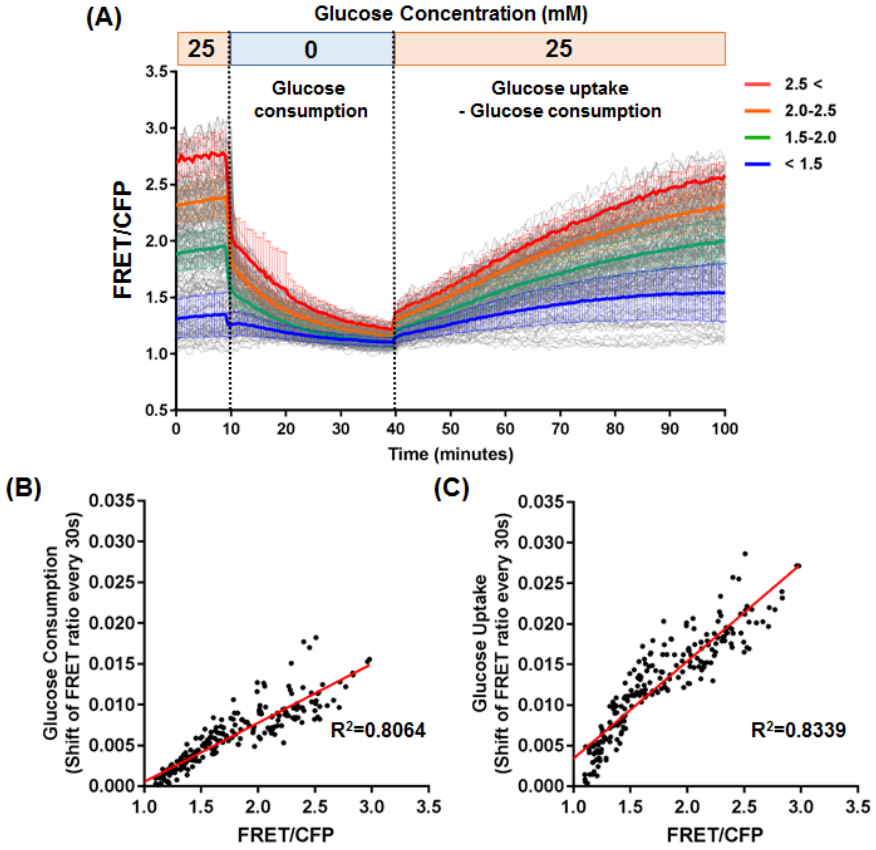


Figure 5-12 Imaging glucose uptake and consumption in scratch assay.
(A) Scratched MCF-7 cells were incubated with 0 mM glucose DMEM from time 10-40 minutes, and media was changed with 25 mM glucose DMEM at time 40 minutes. Images were taken every 30 seconds. (B, C) Glucose uptake and consumption speed of scratched MCF-7 cells. n > 200 cells from three independent experiments.

I further analysed the relationship between intracellular glucose levels and the glucose uptake speed in migrating and non-migrating cells by multiplexed imaging as I analysed in chapter 3.3.2. Intracellular glucose levels were measured by fluorescence lifetime imaging of the glucose FRET biosensor, and glucose uptake was measured by the fluorescence intensity of 2-NBDG. Glucose FRET biosensor with mTurquoise2-sReACh pair-expressing MCF-7 cells were plated and cultured for 24 hours after scratching the cells. Scratched cells were then incubated with 100 μM 2-NBDG for 2 hours (Figure 5-13A). Multiplexed imaging showed that migrating high glucose cells had slightly higher glucose uptake (Figure 5-13B). Thus, multiplexed imaging of glucose FRET biosensor and 2-NBDG also showed that intracellular glucose levels and glucose uptake speed are correlated in scratch-induced migrating cells and non-migrating cells.

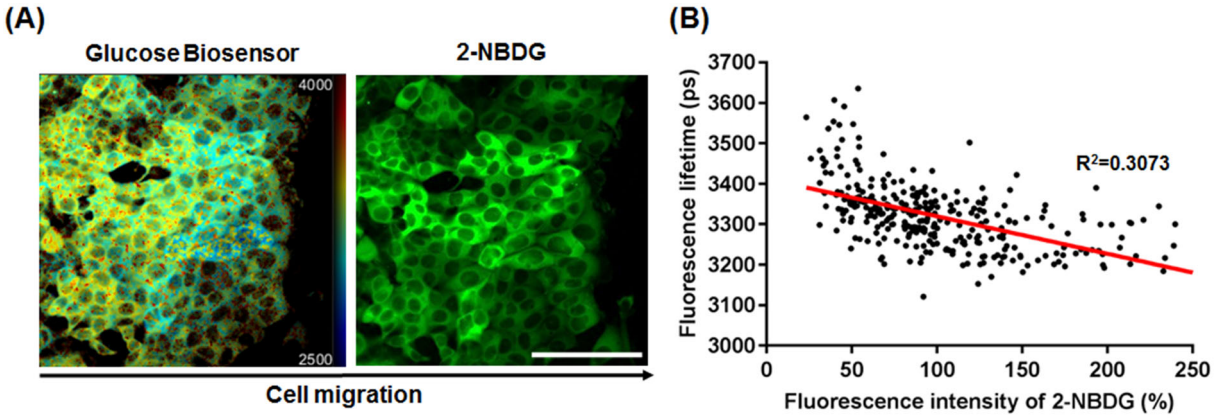


Figure 5-13 Multiplexed imaging of glucose levels and 2-NBDG in scratch assay.
(A) Scratched MCF-7 cells were incubated with 100 μM 2-NBDG for 2 hours. Scale=100 μm. (B) Fluorescence lifetime of single cells plotted against normalised fluorescence intensity of 2-NBDG. n > 300 cells from three independent experiments.

Intracellular glucose levels can distinguish the cells with different glucose demands. I further characterized migrating high glucose cells and non-migrating low glucose cells by multiplexed imaging of intracellular glucose levels and mitochondrial membrane potential, as I analysed in chapter 3.3.2. Multiplexed imaging of intracellular glucose levels and TMRE intensity identified that non-migrating low glucose cells have slightly higher mitochondrial membrane potential (Figure 5-14A). Because FACS-isolated low glucose cells have a high ability for proton transport into the inter-membrane space, I incubated the cells with the ATP synthase inhibitor, Oligomycin, and measured TMRE intensity. As a result, there was no difference of TMRE intensity before and after Oligomycin treatment (Figure 5-14B). These results indicate that non-migrating low glucose cells have significantly higher mitochondrial membrane potential but the ability of proton transport into

the inter-membrane space is similar between migrating and non-migrating cells. Therefore, non-migrating low glucose cells might have low ATP production.

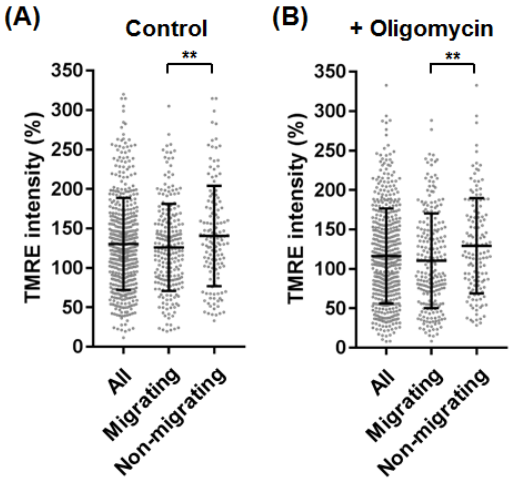


Figure 5-14 Multiplexed imaging of glucose FRET biosensor and TMRE in scratch assay.
(A) TMRE distribution in migrating high and non-migrating low glucose cells. Glucose FRET biosensor expressing MCF-7 cells were incubated with 100 nM TMRE for 10 minutes. (B) Glucose FRET biosensor expressing MCF-7 cells were incubated with 2 μM Oligomycin for 1 hour and then incubated with 100 nM TMRE for 10 minutes. n > 150 cells for each condition from three independent experiments. **p < 0.01 unpaired T test.

5.3.6 Metabolomic analysis of migrating and non-migrating cells

Imaging cell metabolism clarified the metabolic differences in migrating and non-migrating cells. In addition to multiplexed imaging, glucose metabolism in scratch-induced migrating and non-migrating cells were profiled by metabolomic analysis. Glucose FRET biosensor-expressing MCF-7 cells were cultured in 60 mm dishes and the cells were scratched roughly 50 times. After 24 hours of scratches, the percentage of high glucose cells was increased compared with non-scratch condition (Figure 5-15B). Metabolomic analysis identified that scratched cells had higher abundance of Ribulose 5-P (Figure 5-15C). In addition, scratched cells had higher abundance of α-ketoglutarate and Malate in TCA cycle (Figure 5-15D). On the other hand, there was no difference of amino acid abundance between scratched and non-scratched cells (Figure 5-15E). These results suggest that scratched cells promote both glycolysis and OXPHOS. Incubation of the cells with D-Glucose-$^{13}C_6$ further clarified that Glucose 6-P and Ribose 5-P in scratched cells are highly labelled with stable isotope $^{13}C_6$ (Figure 5-15G). In addition, metabolites of TCA cycle and amino acids in non-scratched low glucose cells were highly labelled with stable isotope $^{13}C_6$ (Figure 5-15H, I). Furthermore, scratched cells highly excreted stable isotope $^{13}C_6$ labelled pyruvate and lactate into the media (Figure 5-15J). These data suggest that scratched cells utilise high amounts of glucose for PPP and glycolysis. In contrast, non-

scratched cells use glucose for the TCA cycle and amino acid production. Taken together, scratched high glucose cells promote glycolysis, and other nutrient source such as glutamine might promote OXPHOS.

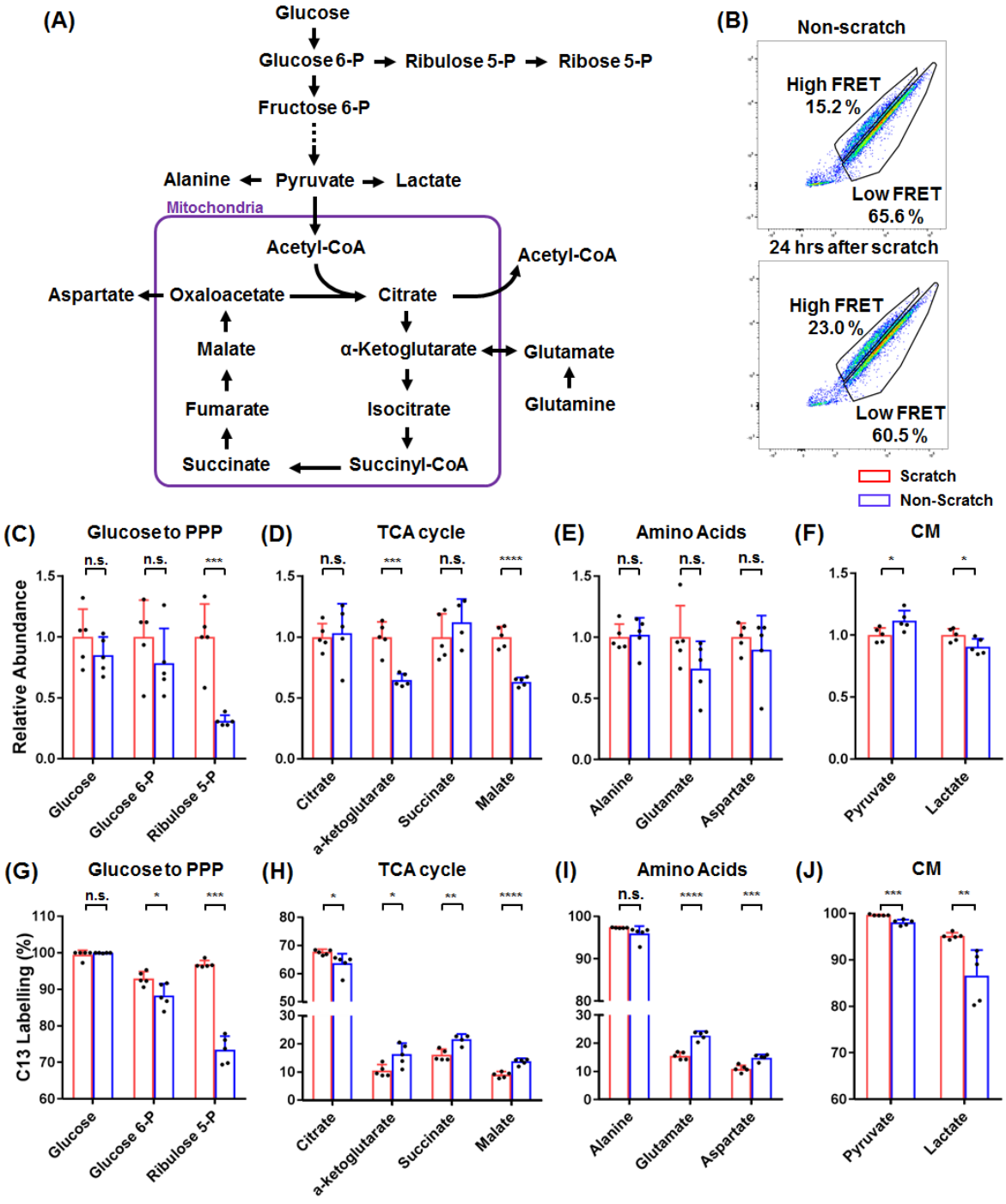


Figure 5-15 Metabolomic analysis of scratched and non-scratched MCF-7 cells.
(A) Schematic representation of the key metabolic pathways of glycolysis and TCA cycle. (B) Panels show the FRET distribution of intracellular glucose levels in scratched and non-scratched cells. (C) Scratched and non-scratched cells were incubated with D-Glucose-$^{13}C_6$.for 90 minutes and then extracted metabolites were analysed using GC-MS. Relative abundance and $^{13}C_6$ labelled percentage of metabolites in glucose, PPP, TCA cycle, amino acids, and media. n = 5 replicates for one condition. n.s. $p > 0.05$, *$p < 0.05$, **$p < 0.01$, ***$p < 0.001$, ****$p < 0.0001$ unpaired T test.

5.3.7 Signalling pathway for regulating scratch-induced glycolysis

Scratch-induced cell migration leads to increased intracellular glucose levels and a decrease in ATP levels at the leading edge. Migrating high glucose cells could have high actin cytoskeletal dynamics and PI3K activity [162-164]. Therefore, inhibition of PI3K/AKT signalling might be able to supress cancer cell migration and glycolytic metabolism. In order to analyse the effect of PI3K/AKT signalling and actin cytoskeletal remodelling on scratch-induced metabolic remodelling, I measured intracellular glucose levels of MCF-7 cells after inhibitor treatment in a scratch assay (Figure 5-16A). Glucose FRET biosensor-expressing MCF-7 cells were plated and incubated with IGFR, PI3K, PTEN, AKT inhibitors for 24 hours. Jasplakinolide and Cytochalasin D are actin de-polymerization and polymerization inhibitors, respectively. The cells were scratched by a pipette tip and time-lapse images were acquired for 40 hours. Among them, the IGFR inhibitor and PI3K inhibitor dramatically supressed cell migration and intracellular glucose increased at the leading edge (Figure 5-16B, C). The AKT inhibitor also slightly inhibited intracellular glucose increase and cell migration. On the other hand, the PTEN inhibitor did not have a significant effect on intracellular glucose increase and cell migration. These results suggest that PI3K/AKT signalling is a key regulator of both cell migration and glycolytic metabolism in migrating cells. However, inhibition of the PI3K/AKT signalling pathway cannot completely supress cell migration and intracellular glucose increase.

Inhibition of actin cytoskeletal remodelling also dramatically supressed cell migration and intracellular glucose increase. The actin polymerization inhibitor completely supressed cell migration and intracellular glucose increase (Figure 5-16A). Actin cytoskeletal dynamics have an important role in glycolytic metabolism. Aldolase A is a key enzyme to facilitate glycolysis and F-actin can bind with this enzyme. Therefore, actin cytoskeletal dynamics can promote glucose metabolism by mobilization of Aldolase A [36, 145]. I showed in chapter 4.6 that Cytochalasin D treatment can promote glycolysis. Although glycolytic cells are expected to have high intracellular glucose levels, Cytochalasin D-treated cells reduced intracellular glucose levels. Cytochalasin D-treated cells might reduce intracellular glucose levels by increasing glucose consumption. These results indicate that actin cytoskeletal dynamics is a crucial regulator of glucose metabolism. PI3K/AKT signalling could regulate metabolic remodelling probably through actin cytoskeletal dynamics.

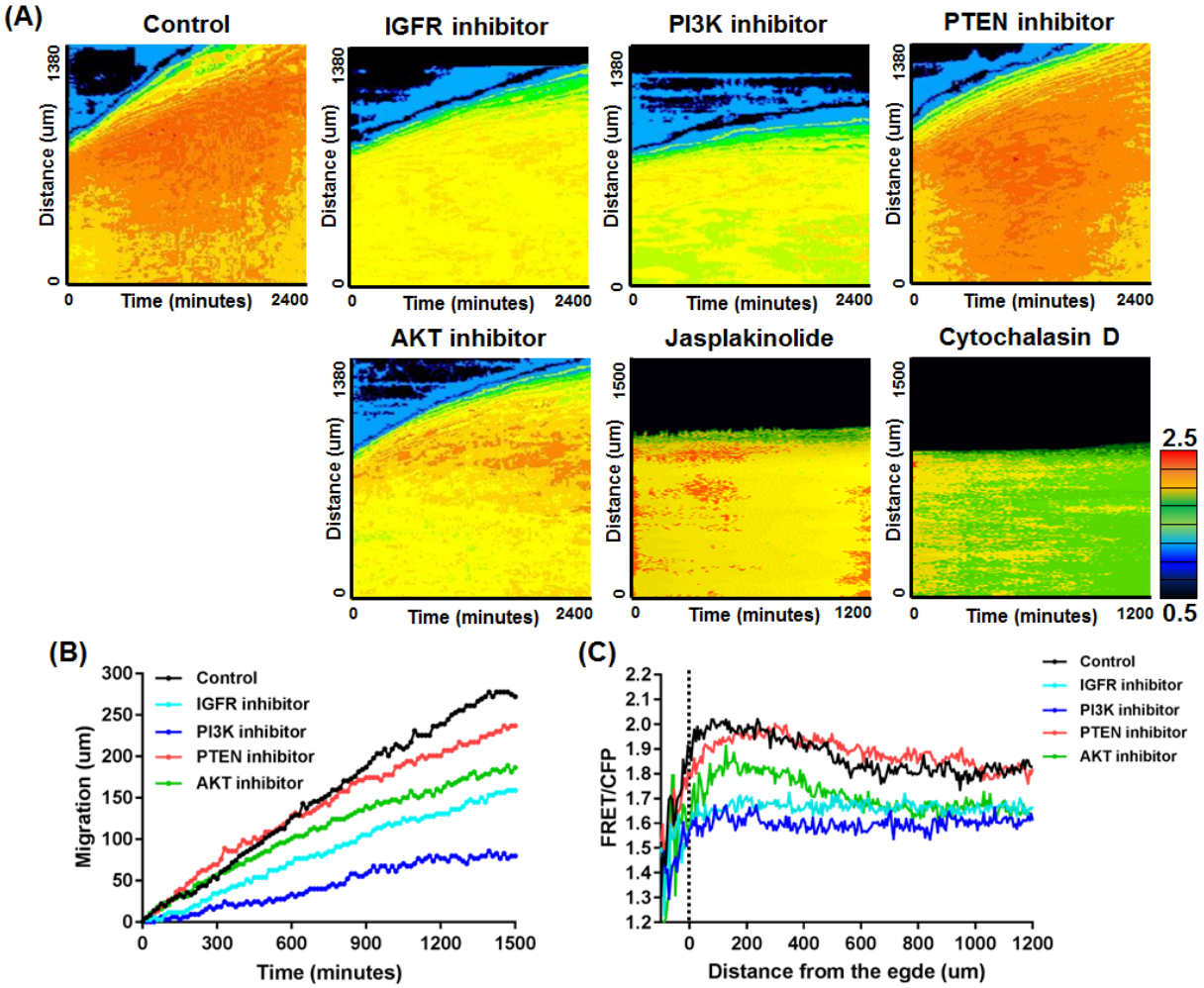


Figure 5-16 Scratch assay of inhbitor-treated MCF-7 cells.
Kymograph of glucose FRET signals in scratch assay. Glucose FRET biosensor expressing MCF-7 cells were incubated with 0.1% DMSO, 5 μM Linsitinib, 5 μM, 1 μM LY294002, 5 μM VO-Ohpic trihydrate, 1 μM MK2206, 0.1 μM CytochalasinD, and 0.1 μM Jasplakinolide. Time-lapse images were acquired for 20-40 hours. The kymographs were generated from three independent scratch assays.

5.3.8 YAP localisation after scratch assay

As I showed in chapter 4.3, cell confluence regulates YAP localisation. The cells in high cell confluence had low YAP N/C ratio. Active YAP in the nucleus can transcribe target genes and promote glucose metabolism. This data suggests that scratch-induced migrating cells might have high YAP N/C ratio and promote glucose metabolism. Therefore, I analysed YAP N/C localisation in migrating and non-migrating cells (Figure 5-17). As I expected, migrating cells at the leading edge have higher YAP nuclear localisation. In addition, I further analysed the effect of actin cytoskeletal remodelling on YAP N/C ratio by supressing RhoA and ROCK expression using siRNA. F-actin formation and YAP N/C ratio was also dramatically reduced by RhoA and ROCK knockdown (Figure 5-17). These

results indicate that cell confluence and migration can regulate YAP activity, and migrating high glucose cells might promote glycolysis through YAP activation.

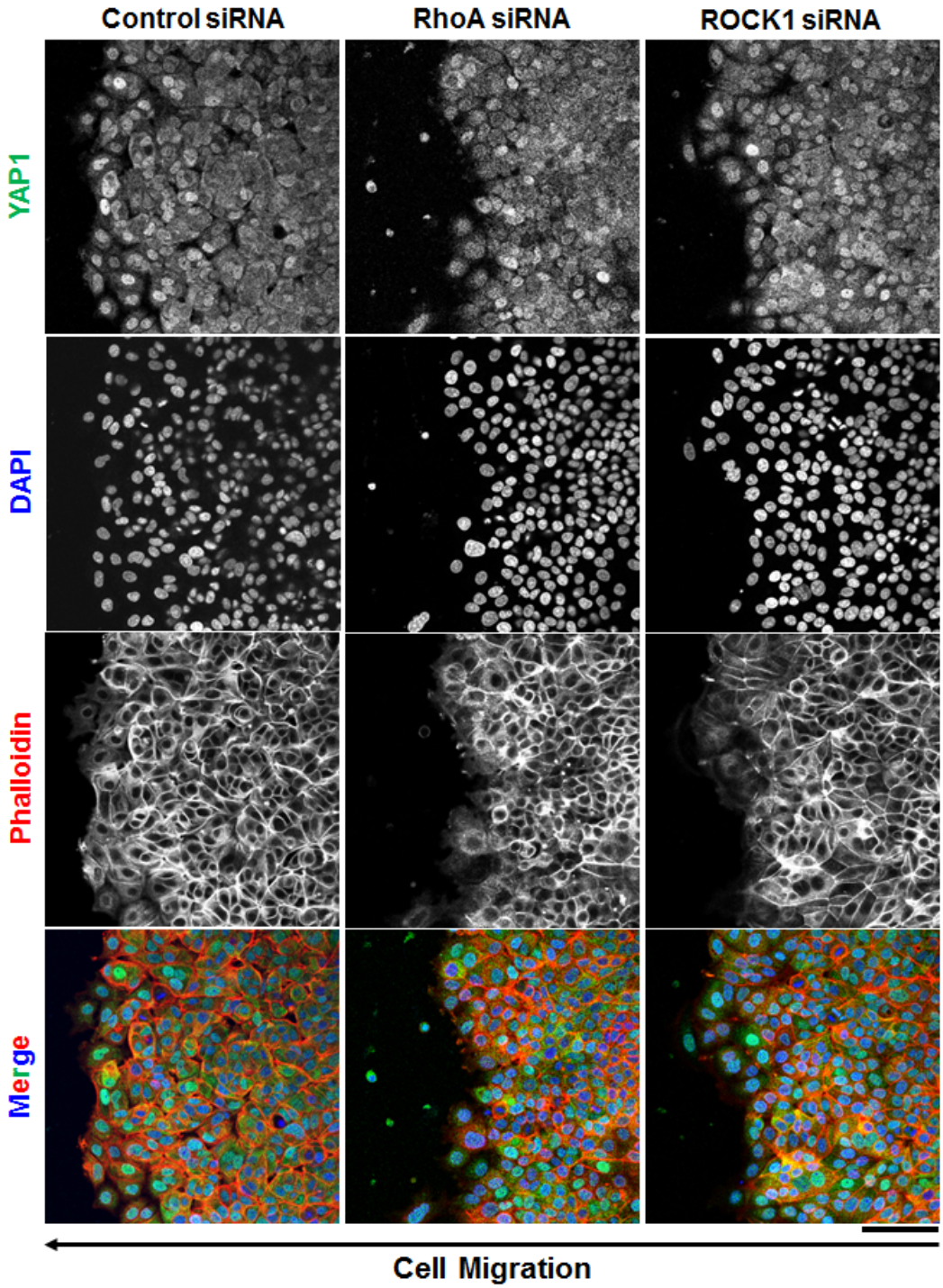


Figure 5-17 YAP localisation in scratch assay.
YAP localisation of MCF-7 cells after scratching the cells. RhoA and ROCK1 expression were supressed using siRNA. The cells were fixed 24 hours after scratch, and YAP was label by YPA antibody. Nuclei and F-actin were stain by DAPI and Phalloidin-Atto 633, respectively. Scale=100 μm.

5.4 Chapter discussion

In this chapter, I found that MCF-7 and MDA-MB-231 tumours have high intracellular glucose levels at the tumour periphery. Because tumours have the patterns of metabolic states, some microenvironmental factors could regulate glucose metabolism *in vivo*. These metabolic patterns are mainly created by cell confluence and cell migratory behaviour. Scratch-induced migrating cells dramatically increased intracellular glucose levels and this population promote glycolysis. In the scratch assay, nutrient accessibility, oxygen level, and extracellular pH should be the same in all individual cells because cells grow in a monolayer. Therefore, cell confluence and cell migration could be the key regulators of metabolic reprogramming. Metabolic reprogramming during cell migration is regulated by PI3K/AKT signalling and actin cytoskeletal dynamics. Cell confluence, cell migration, and PI3K/AKT signalling could establish metabolic patterns of breast cancer *in vivo*. In addition, each nutrient source has a different effect on cell migration. Although both glucose and glutamine are crucial nutrients for cell migration, glutamine has a great impact on migratory behaviour. The cells without glutamine may not be able to produce sufficient amounts of ATP for actin cytoskeletal remodelling.

Chapter 6. Epigenetic regulation of glucose metabolism and combinatorial approaches to therapy

6.1 Chapter summary

In this chapter, I investigate combinatorial inhibitor treatments to effectively supress tumour growth. I found in a previous chapter that a subset of breast cancer cells can promote glycolysis independently from the PI3K signalling pathway. This PI3K inhibitor-resistant cell population might survive and recur after therapeutic treatments. In order to inhibit glucose metabolism of PI3K inhibitor-resistant high glucose cells, I analyse the effect of six different epigenetic inhibitors on glucose metabolism. Among them, HDAC and BET inhibitors dramatically reduce intracellular glucose levels. The BET inhibitor, JQ1, especially has a long-lasting effect to reduce intracellular glucose levels. Combinatorial inhibition of PI3K and BET can reduce intracellular glucose levels including PI3K inhibitor-resistant cells. Combinatorial inhibition can completely supress glycolysis and tumour growth by reducing glucose uptake, ATP production, and increasing ROS stress. In addition, the long-lasting effect of the drugs means that combinatorial inhibition of PI3K and BET provides an opportunity to reduce the drug dosage frequency and relative amount. In scratch assay, combinatorial inhibition can also reduce intracellular glucose increase in migrating cells.

6.2 Epigenetic regulation of glucose metabolism

6.2.1 The effect of epigenetic inhibitors on Intracellular glucose levels.

Glucose metabolism could be regulated by epigenetics because intracellular glucose levels can reversibly fluctuate between high and low glucose states over several days. In order to analyse the epigenetic regulation of cell metabolism, I measured intracellular glucose levels after epigenetic inhibitor treatments (Figure 6-1). The cells were treated with inhibitors targeting DNA methylation, histone methylation, and histone acetylation. The DNA methylation inhibitor, 5-Aza, did not have an effect on intracellular glucose levels. On the other hand, histone modification inhibitors had significant effects on glucose metabolism. The histone methylation inhibitor, EPZ6438, and the histone de-methylation inhibitor, GSK J4, significantly reduced intracellular glucose levels. In addition, the histone acetylation inhibitor, C646, and the histone deacetylation inhibitor, Vorinostat, reduced intracellular glucose levels. Because PI3K-dependent cell metabolism can regulate

histone acetylation levels, there could be a correlation between PI3K activity and epigenetically-regulated cell metabolism. Furthermore, the Bromodomain inhibitor, JQ1, dramatically reduced intracellular glucose levels. Bromodomain is a reader of lysine acetylation and accelerates expression of target genes. Although Vorinostat and JQ1 should have opposite effects, both inhibitors reduced intracellular glucose levels of MCF-7 cells. These results indicate that histone acetylation levels and its reader Bromodomain could be important regulators of heterogeneous glucose metabolism.

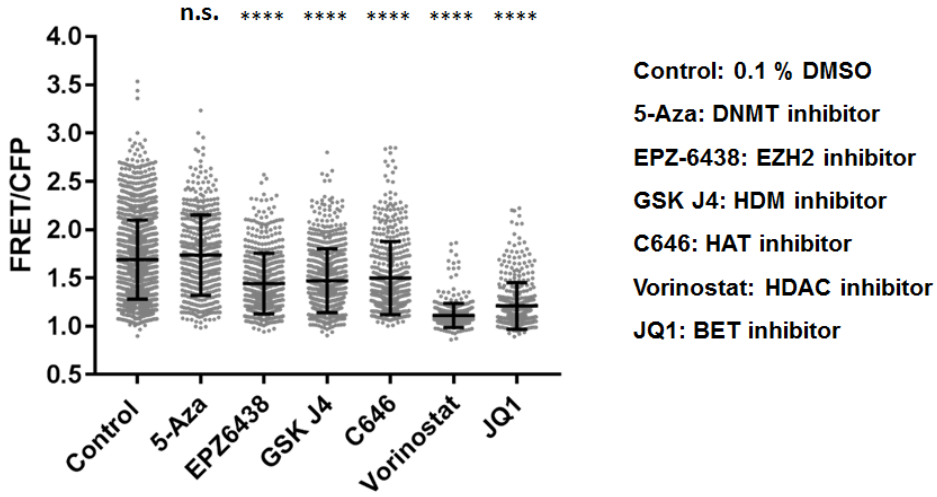


Figure 6-1 Epigenetic regulation of intracellular glucose levels.
FRET distribution of intracellular glucose levels in MCF-7 cells after epigenetic inhibitor treatments for 24 hours. MCF-7 cells were incubated with 10 μM 5-Aza, 1 μM EPZ6438, 1 μM GSK J4, 5 μM C646, 2 μM Vorinostat, and 2 μM JQ1. n > 450 cells for each condition from at least three independent experiments. n.s. $p > 0.05$, ****$p < 0.0001$ Kolmogorov-Smirnov test.

6.2.2 Lasting effect of epigenetic inhibitors

Figure 6-1 showed that epigenetic inhibitors can reduce intracellular glucose levels. The effect of epigenetic inhibitors are expected to have long-lasting effects. In order to analyse the lasting effect of each inhibitor, I measured intracellular glucose levels for three continuous days after washing out the inhibitors (Figure 6-2). Although the effect of HMT, HDM, and HAT inhibitors on intracellular glucose levels was smaller than HDAC and BET inhibitors, these three inhibitors have a long-lasting effect to reduce intracellular glucose levels. On the other hand, the HDAC inhibitor dramatically reduced intracellular glucose levels but metabolic states were rapidly returned to the original states after washing out the inhibitor. Among the five epigenetic inhibitors that I analysed, JQ1 can dramatically reduce intracellular glucose levels and this effect lasted at least 3 days. Therefore, JQ1 could be an ideal epigenetic inhibitor to effectively target high glucose cells with the potential added benefit of reducing drug dosage and frequency.

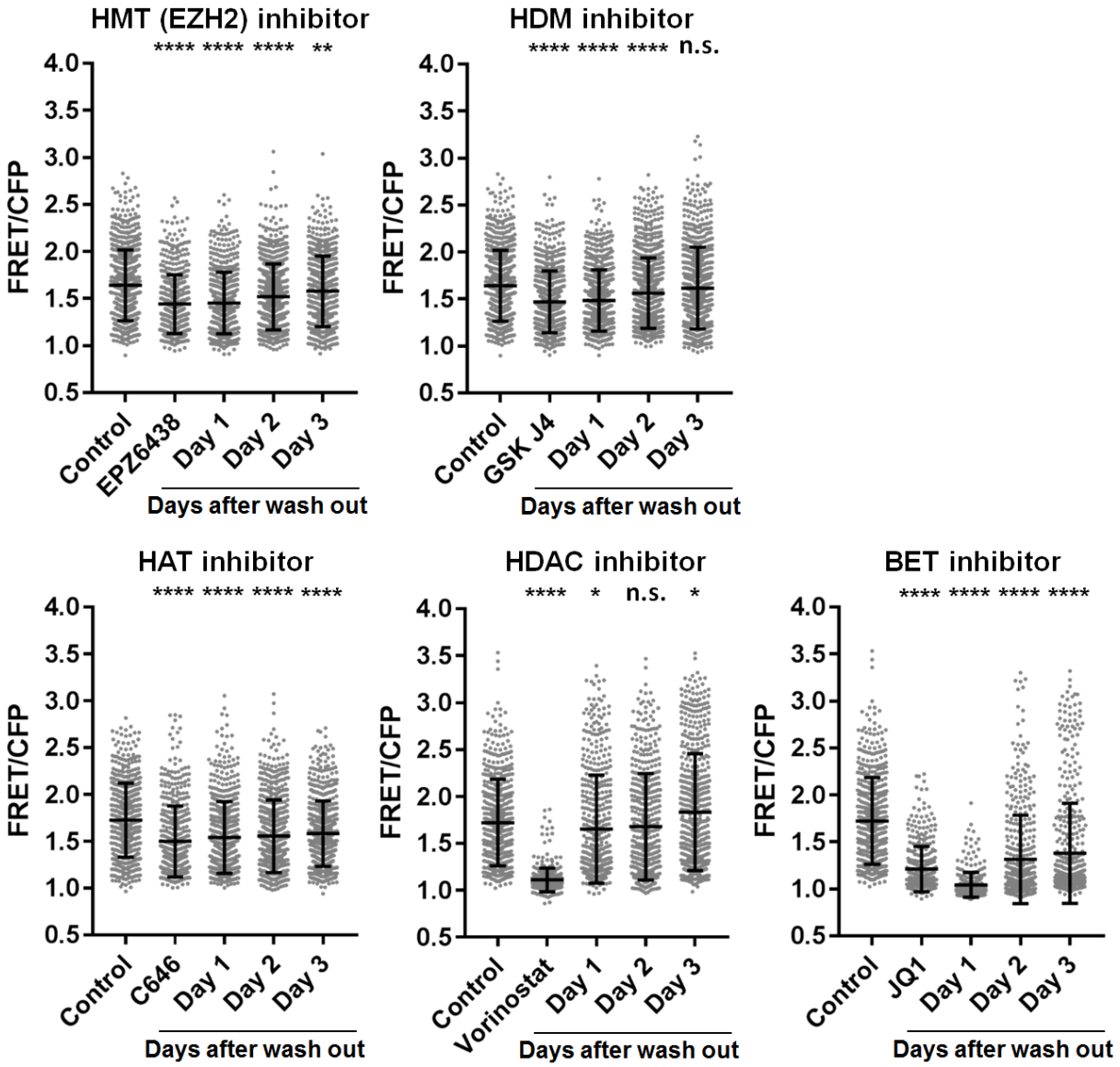


Figure 6-2 Lasting effect of epigenetic inhibitors on intracellular glucose levels.
FRET distribution of intracellular glucose levels in MCF-7 cells after epigenetic inhibitor treatments. Intracellular glucose levels were traced after washing out inhibitors for 3 days. n > 450 cells for each condition from at least three independent experiments. n.s. $p > 0.05$, *$p < 0.05$, **$p < 0.01$, ****$p < 0.0001$ Kolmogorov-Smirnov test.

6.2.3 The effect of epigenetic inhibitors on high and low glucose cells

I found epigenetic inhibitors have different effects on glucose metabolism, and especially JQ1 has a long-lasting effect with dramatic reduction of intracellular glucose levels. However, the effect of epigenetic inhibitors on cell metabolism of high and low glucose cells is unclear. In order to analyse the effect of epigenetic inhibitors on glycolytic high glucose cells and OXPHOS low glucose cells, intracellular glucose levels of FACS-isolated high and low glucose cells were measured after epigenetic inhibitor treatments (Figure 6-

3). As a result, all epigenetic inhibitors reduced intracellular glucose levels of FACS-isolated high glucose cells. This result clarified that epigenetic inhibitors especially change cell metabolism of glycolytic high glucose cells.

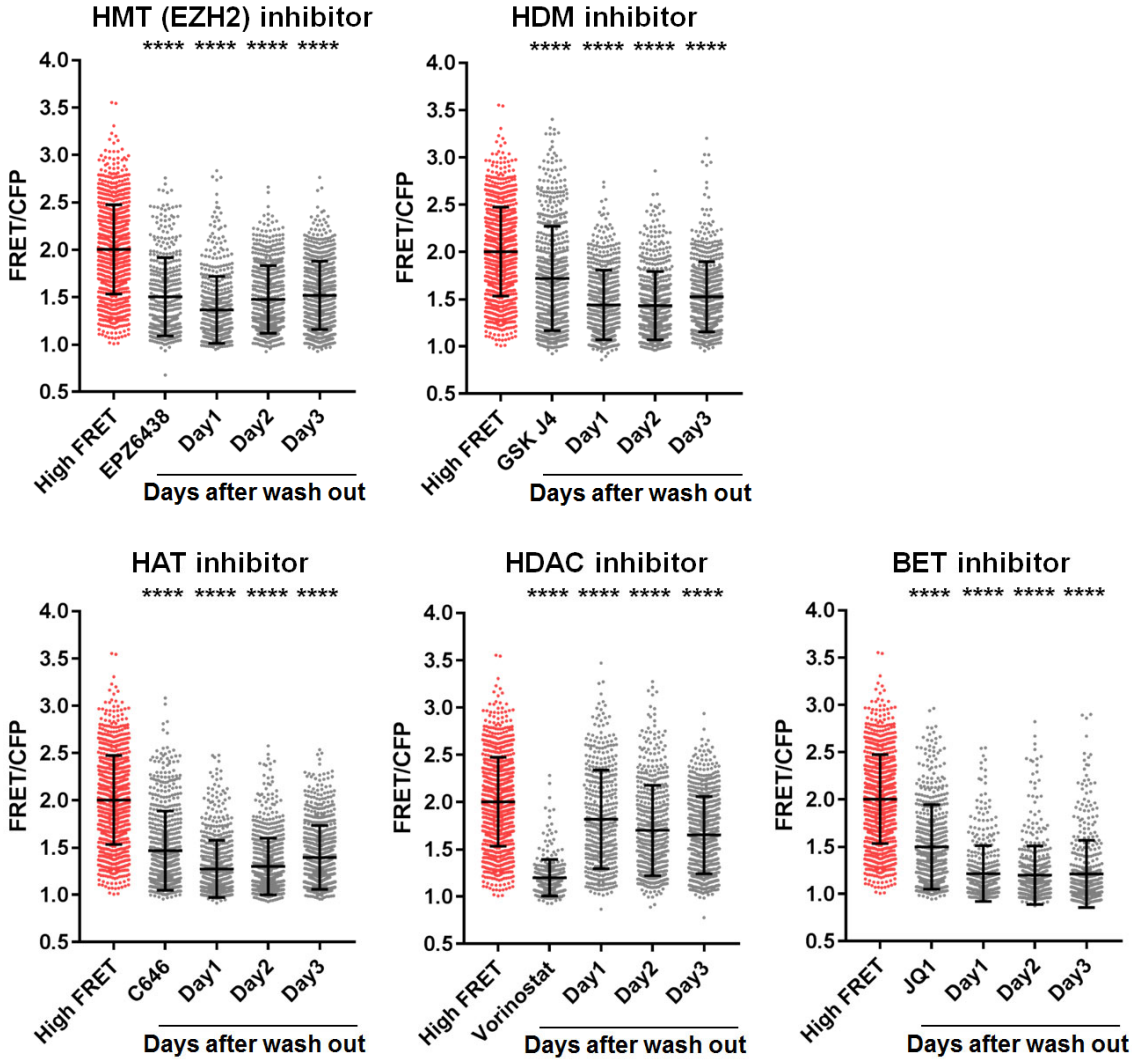


Figure 6-3 The effect of epigenetic inhibitors on FACS-isolated high glucose cells.
FRET distribution of intracellular glucose levels in FACS-isolated high glucose cells after epigenetic inhibitor treatments. Intracellular glucose levels were traced after wash out inhibitors. n > 450 cells for each condition from at least three independent experiments. ****p < 0.0001 Kolmogorov-Smirnov test.

I found that epigenetic inhibitors can supress glucose metabolism of glycolytic high glucose cells. I further analysed the effect of these inhibitors on FACS-isolated low glucose cells (Figure 6-4). The histone methylation inhibitor, EPZ6438, and histone de-methylation inhibitor, GSK J4, did not change intracellular glucose levels of FACS-isolated low glucose cells. This result indicates that histone methylation levels can regulate glucose metabolism of high glucose cells but low glucose cells are independent from the regulation of histone methylation. In contrast, the histone acetylation inhibitor, the histone de-acetylation

inhibitor, and the BET inhibitor significantly reduced intracellular glucose levels of FACS-isolated low glucose cells. As with the effect of the HDAC inhibitor on non-isolated cells, the HDAC inhibitor dramatically reduced intracellular glucose levels but metabolic states rapidly returned to the original low glucose states after washing out the inhibitor. JQ1 treated low glucose cells showed a dramatic reduction of intracellular glucose levels and this inhibitor has a long-lasting effect. Thus, the effect of epigenetic inhibitors on intracellular glucose level was different between high and low glucose cells. These results indicate that histone methylation, acetylation, and Bromodomain have different metabolic regulation. Further, the ability to affect high glucose cells hinted that they may be effective against the high glucose cells that regulate metabolism independently from PI3K signalling.

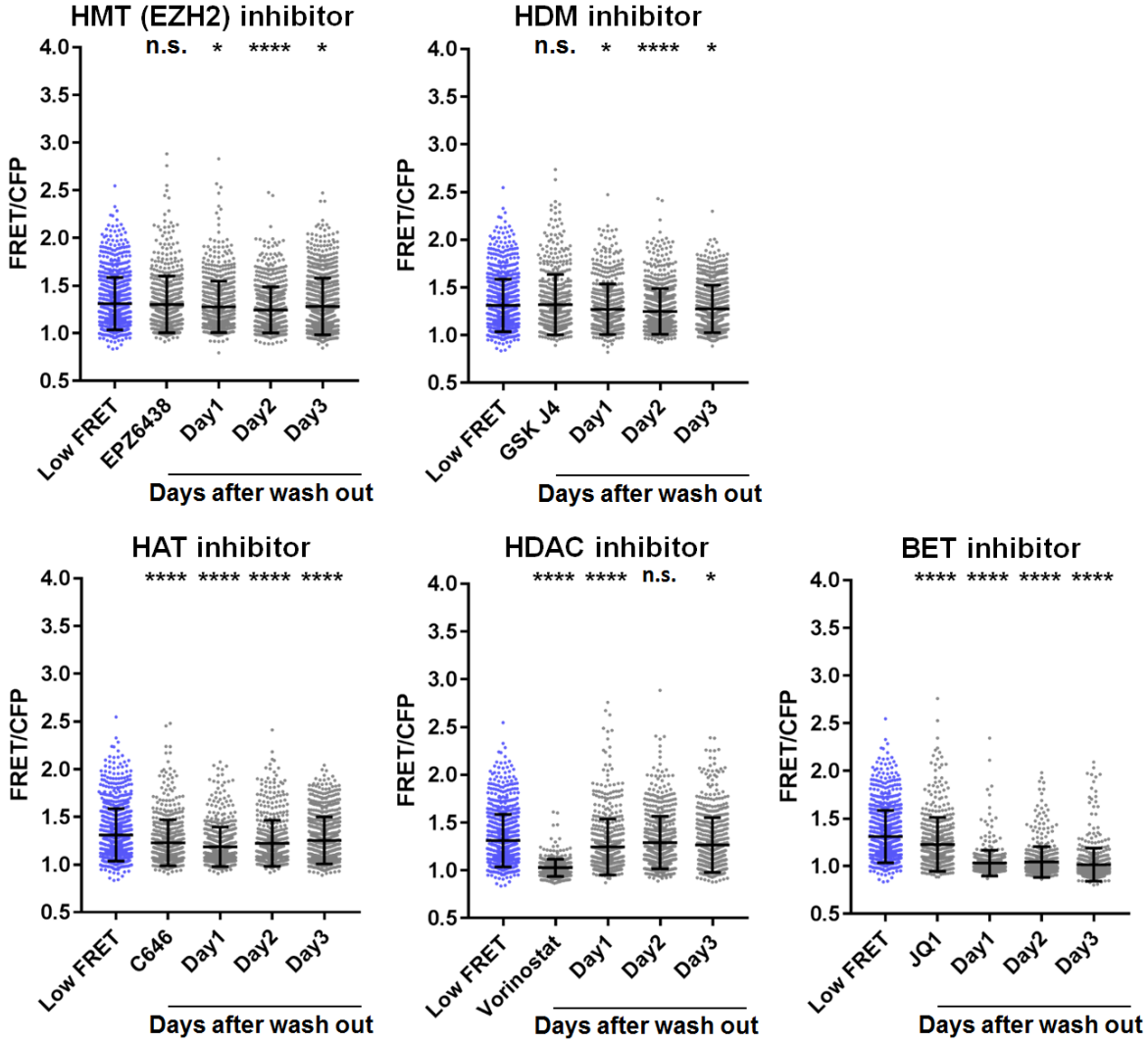


Figure 6-4 The effect of epigenetic inhibitors on FACS-isolated low glucose cells.
FRET distribution of intracellular glucose levels in FACS-isolated low glucose cells after epigenetic inhibitor treatments. Intracellular glucose levels were traced after wash out inhibitors. n > 450 cells for each condition from at least three independent experiments. n.s. $p > 0.05$, *$p < 0.05$, ****$p < 0.0001$ Kolmogorov-Smirnov test.

6.2.4 The effect of Acetyl-CoA on Intracellular glucose levels.

I found histone acetylation levels and Bromodomain regulate glucose metabolism in MCF-7 cells. In addition, I showed in chapter 4.7 that lysine acetylation levels of FACS-isolated low glucose cells are higher than FACS-isolated high glucose cells. Histone acetylation patterns are regulated by HATs and HDACs. HATs transfer acetyl groups of Acetyl-CoA to lysine residues in histones. Therefore, Acetyl-CoA is a key supply source of acetyl groups and its synthesis is an important regulator of histone acetylation. Glucose is a main nutrient source for Acetyl-CoA synthesis. Through glucose metabolism, glucose is converted to pyruvate and then transported into mitochondria. Citrate is exported from mitochondria and Acetyl-CoA is produced from citrate in the cytoplasm (Figure 6-5A). In order to analyse the effect of Acetyl-CoA synthesis on histone acetylation levels and glucose metabolism, intracellular glucose levels of MCF-7 cells were measured after 24 hours incubation with 0.2 mM Acetyl-CoA (Figure 6-5B). The cells cultured with Acetyl-CoA could have high histone acetylation levels, it is possible to analyse the relationship between histone acetylation levels and glucose metabolism by live cell imaging. As a result, intracellular glucose levels of MCF-7 cells were significantly reduced by incubation with Acetyl-CoA. High glucose cells mainly use glucose for glycolysis and low glucose cells use it for the TCA cycle. Therefore, low glucose cells could have high cytoplasmic Acetyl-CoA production and promote histone acetylation.

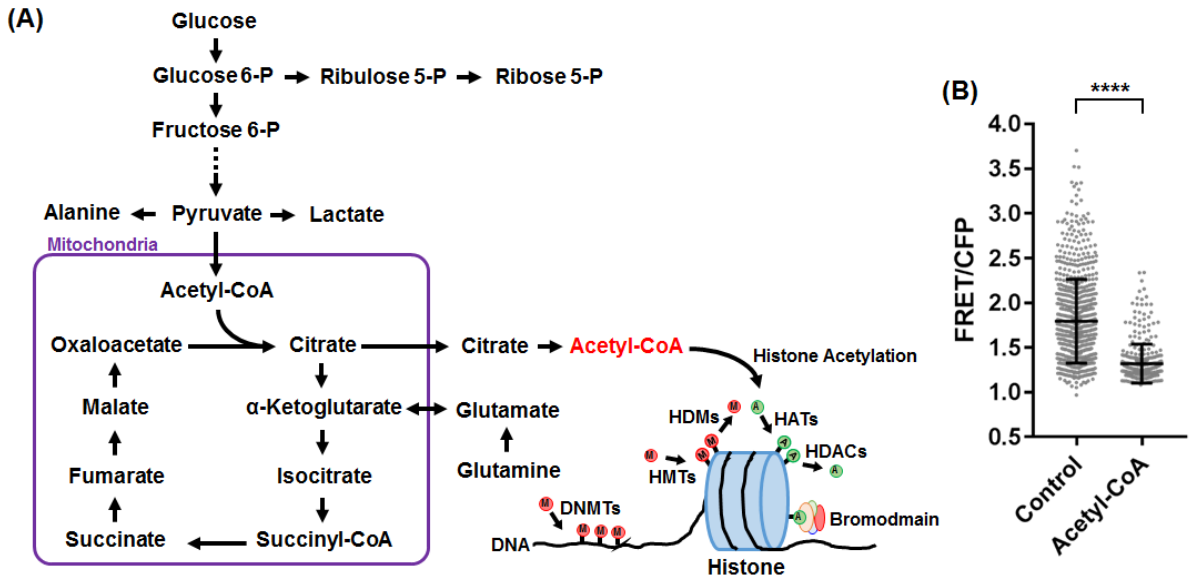


Figure 6-5 The effect of Acetyl-CoA on intracellular glucose level.
(A) Schematic representation of the key metabolic pathways for histone acetylation. (B) FRET distribution of intracellular glucose levels in MCF-7 cells cultured with 0.2 mM Acetyl-CoA. n > 300 cells for each condition from at least three independent experiments. ****p < 0.0001 Kolmogorov-Smirnov test.

6.3 Combinatorial inhibition of PI3K and Bromodomain

6.3.1 Double treatment of PI3K and Bromodomain inhibitors

I found that both PI3K and Bromodomain inhibitors can reduce intracellular glucose levels in MCF-7 cells. Because a subset of glycolytic high glucose cells can regulate glycolysis independently from PI3K signalling, I analysed the effect of double treatment of PI3K and Bromodomain inhibitors on intracellular glucose levels. Single treatment with PI3K or Bromodomain inhibitors can reduce glucose levels but high glucose cells still exist. MCF-7 cells were treated with three types of PI3K inhibitors (Pictilisib, Alpelisib, AZD8186) and two types of Bromodomain inhibitors (JQ1, AZD5153). Among these inhibitors, Alpelisib and AZD5153 are used for clinical trials. In PI3K inhibitor-treated MCF-7 cells, the PI3Kα inhibitor, PI3Kα/δ inhibitor, and PI3Kβ/δ inhibitor can similarly reduce intracellular glucose levels. In Bromodomain inhibitor-treated MCF-7 cells, the BRD2/3/4 inhibitor and the BRD4 inhibitor can also similarly reduce intracellular glucose levels. In addition, double inhibition of PI3K and Bromodomain in all combinations can dramatically reduce glycolytic high glucose cells (Figure 6-6). These results indicate that combinatorial inhibition of PI3K and Bromodomain supress glucose metabolism in whole cell populations.

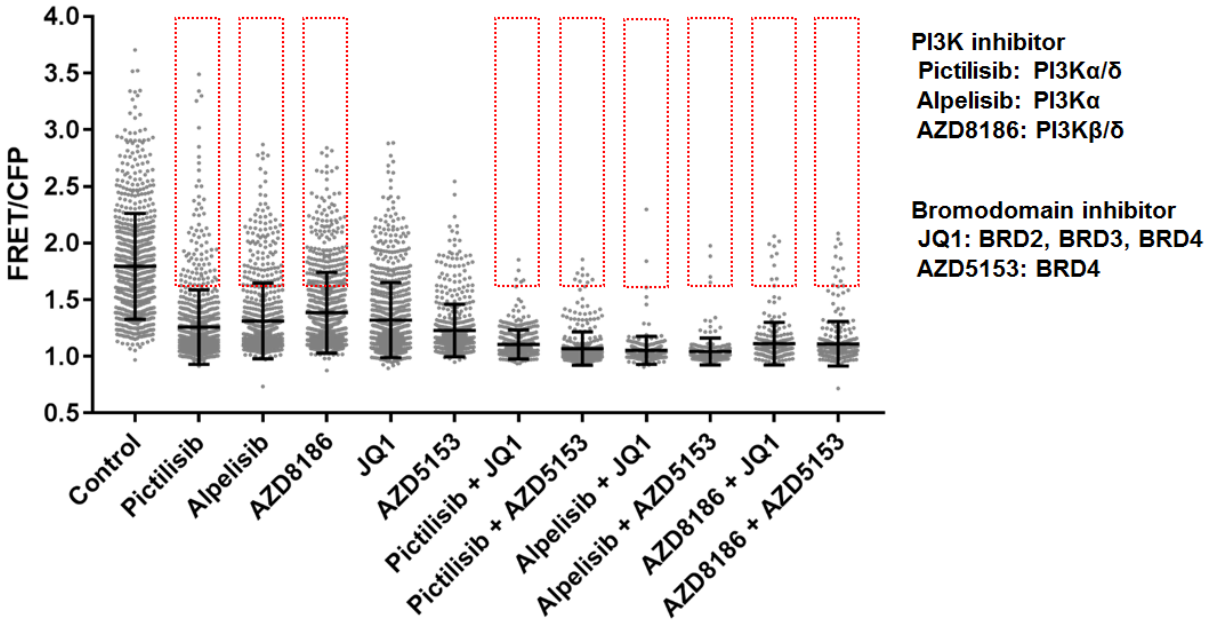


Figure 6-6 Combinatorial inhibition of PI3K and Bromodomain.
FRET distribution of intracellular glucose levels in MCF-7 cells after PI3K and Bromodomain inhibitor treatments. MCF-7 cells were treated with 0.1 μM Pictilisib, 0.5 μM Alpelisib, 0.5 μM AZD8186, 0.5 μM JQ1, and 0.1 μM AZD5153. The cells in the red squares represent inhibitor resistant high glucose cells. n > 300 cells for each condition from at least three independent experiments.

Combinatorial inhibition of PI3K and Bromodomain might change the metabolic stability of MCF-7 cells because double treatment dramatically suppresses glucose metabolism. MCF-7 cells were treated with inhibitors and then time-lapse images were acquired for 10 hours every 5 minutes. As a result of cell segmentation and tracking of intracellular glucose levels, I found that double inhibition of PI3K and Bromodomain significantly reduced metabolic fluctuation (Figure 6-7A, B). This low metabolic fluctuation might be a key mechanism to supress tumour growth. In order to improve the understanding of the impact of double inhibition of PI3K and Bromodomain, the effect of double inhibition on metabolic states, energetic stress, and tumour growth should be analysed *in vitro* and *in vivo*.

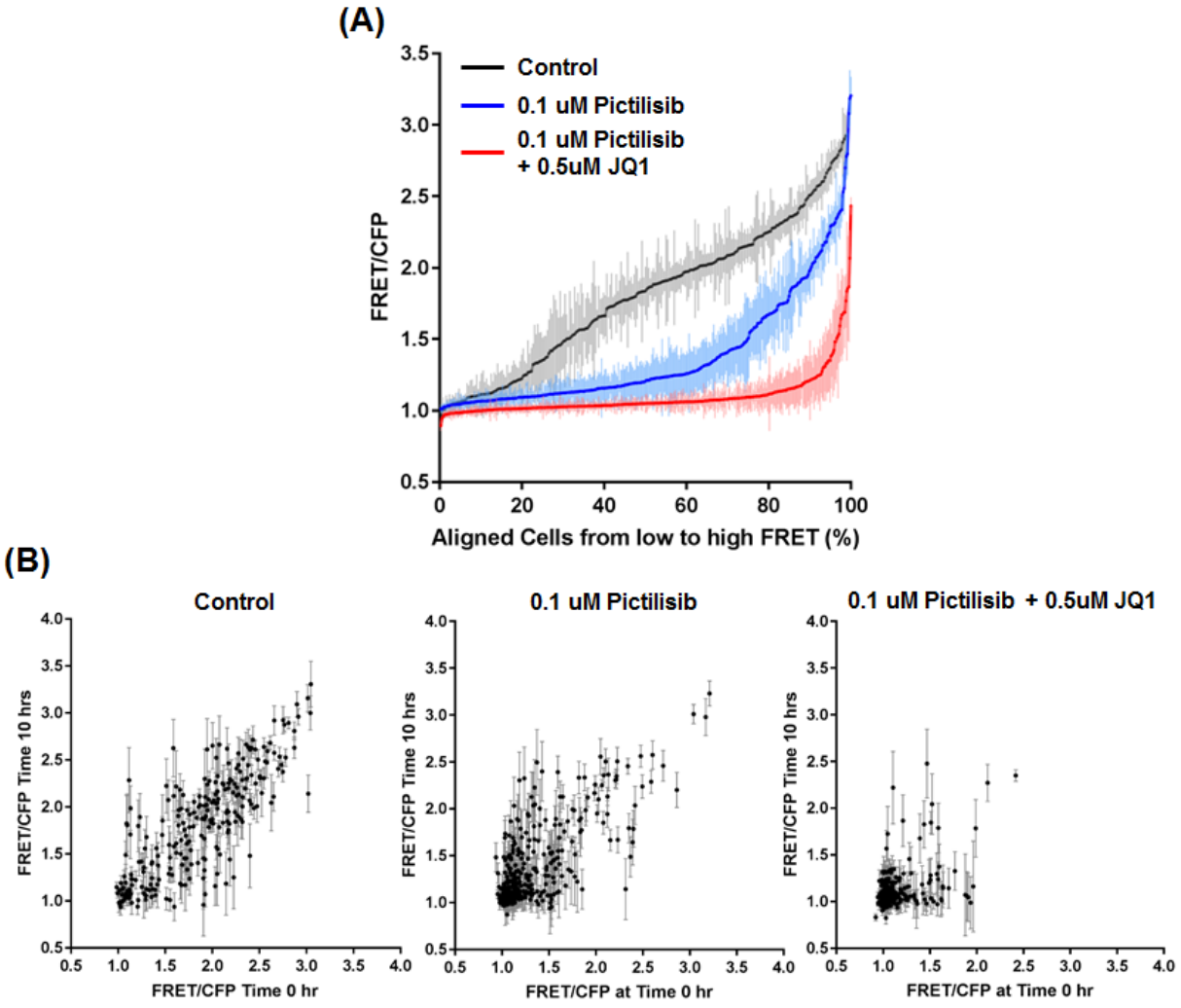


Figure 6-7 The effect of combinatorial inhibition on metabolic stability.
(A) Glucose biosensor-expressing breast cancer cell lines were incubated with 0.1 μM Pictilisib and 0.5 μM JQ1 and then time-lapse images were acquired for 10 hours. (B) Following cell segmentation, the glucose levels were tracked and glucose FRET signal at T=0 against signal at T=10 plotted with the standard deviation over 10 hours. n > 400 cells for each condition from at least three independent experiments.

In addition to the effect of combinatorial inhibition of PI3K and Bromodomain on short term metabolic stability, I also analysed long term metabolic stability. I showed in chapter 4.4 that the effect of the PI3K inhibitor rapidly disappeared after drug wash out. I further found that combinatorial inhibition of PI3K and Bromodomain clearly reduced the population of PI3K-resistant glycolytic-high glucose cells. Because the drug effect of combinatorial inhibition of PI3K and Bromodomain lasted at least 3 days after drug wash out, combinatorial inhibition could be an ideal therapeutic strategy to reduce the frequency of administration (Figure 6-8). Therapeutic treatments of cancer cell metabolism have a risk of damaging normal cells, therefore it is important to reduce the drug dosage amount and frequency.

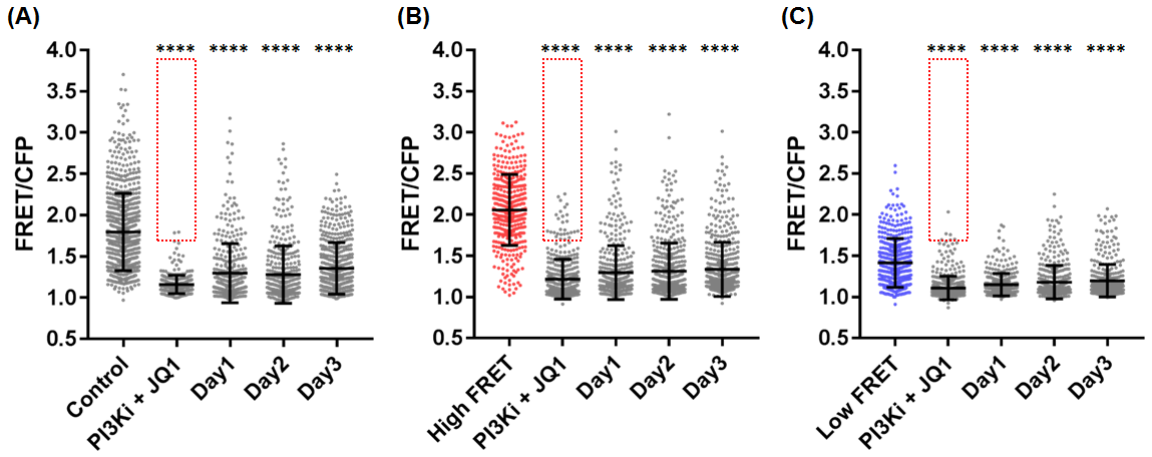


Figure 6-8 The effect of combinatorial inhibitor on high and low glucose cells.
(A) FRET distribution of intracellular glucose levels in MCF-7 cells after 0.1 μM Pictilisib and 0.5 μM JQ1 treatment and its wash out. (B, C) FRET distribution of intracellular glucose levels in FACS-isolated high and low glucose cells after 0.1 μM Pictilisib and 0.5 μM JQ1 treatment and its wash out. n > 300 cells for each condition from at least three independent experiments. ****p < 0.0001 Kolmogorov-Smirnov test.

Combinatorial inhibition of PI3K and Bromodomain significantly reduced intracellular glucose levels and eliminated glycolytic-high glucose cells. PI3K inhibitor-resistant high glucose cells are expected to survive and continue to grow under PI3K inhibition. Therefore, combinatorial inhibition could effectively suppress tumour growth by targeting both PI3K-dependent and independent glycolytic-high glucose cells. In order to evaluate combination therapy for tumour growth, MCF-7 cells were treated with inhibitors for 7 days and then stained by crystal violet (Figure 6-9). As a result, single treatment with PI3K or Bromodomain inhibitors can induce marked tumour regression. Strikingly, combination therapy of PI3K and Bromodomain inhibitors significantly improved tumour regression. Thus, inhibition of glucose metabolism in whole cell populations is a great strategy for effective therapeutic treatment.

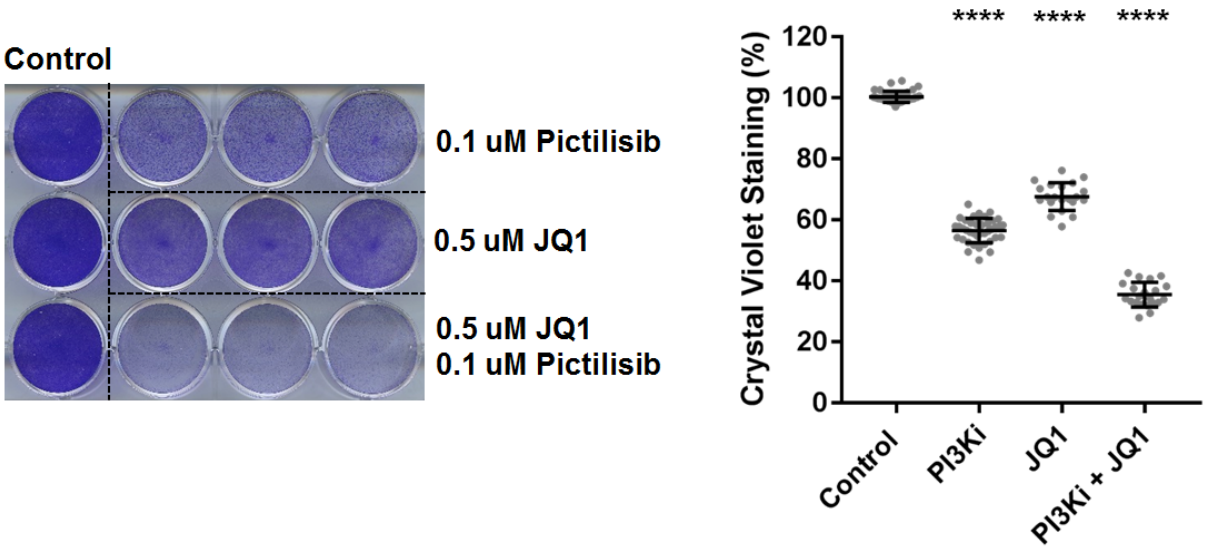


Figure 6-9 Viability analysis of combinatorial inhibition by crystal violet staining.
MCF-7 cells were cultured with 0.1 μM Pictilisib and 0.5 μM JQ1 for 7 days, and the cells were stained with crystal violet. Intensity of crystal violet was measured and quantified using ImageJ software. n > 20 wells for each condition from three independent experiments. ****p < 0.0001 Welch unpaired T test.

In order to analyse the effect of combinatorial inhibition of PI3K and Bromodomain, I further measured the growth rate of inhibitor-treated MCF-7 cells using the IncuCyte S3 Live-Cell Analysis System (Figure 6-10). PI3K and Bromodomain inhibitor-treated cells markedly reduced cell growth but gradually increased cell confluence. In contrast, combinatorial inhibition of PI3K and Bromodomain completely stopped cell proliferation at 50 hours after drug treatment. Although single inhibitor treatment allowed inhibitor-resistant cells to continuously proliferate, combinatorial inhibition supressed tumour growth.

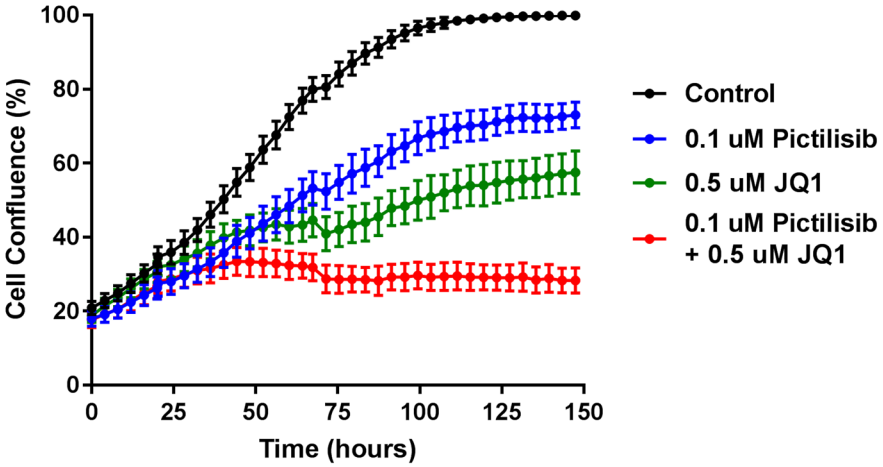


Figure 6-10 Viability analysis of combinatorial inhibition by IncuCyte.
MCF-7 cells were cultured with 0.1 μM Pictilisib and 0.5 μM JQ1 and cell confluence was measured every 3 hours using IncuCyte *S3* Live-Cell Analysis System. n > 10 wells for each condition.

Next, I analysed combination therapy with different strategies to reduce drug dosage and frequency. Both PI3K and Bromodomain inhibitors are targeting cell metabolism, it is very important to reduce the risk of secondary effects. MCF-7 cells were treated with PI3K and Bromodomain inhibitors for 1 day, 2 days, and 3 days intervals and then cell growth was analysed by crystal violet staining (Figure 6-11). PI3K inhibitor treatment effectively suppressed tumour growth especially with all day drug treatment. However, this inhibitor effect was reduced with alternative inhibitor treatments. Therefore, PI3K inhibition requires continuous drug treatment. In contrast, JQ1 treatment inhibited tumour growth also with 1 day, 2 days, and 3 days intervals. As I showed in chapter 6.2.2, JQ1 has a long-lasting effect of inhibiting glucose metabolism. Because intracellular glucose levels were continuously reduced by JQ1 treatment in both high and low glucose cells, a Bromodomain inhibitor might supress glucose metabolism only by single drug dosage. In addition, combinatorial inhibition of PI3K and Bromodomain improved tumour suppression in alternative inhibitor treatments. These results indicate that combinatorial therapy can effectively inhibit tumour growth and it is possible to reduce drug dosage and frequency to reduce the risk of secondary effects.

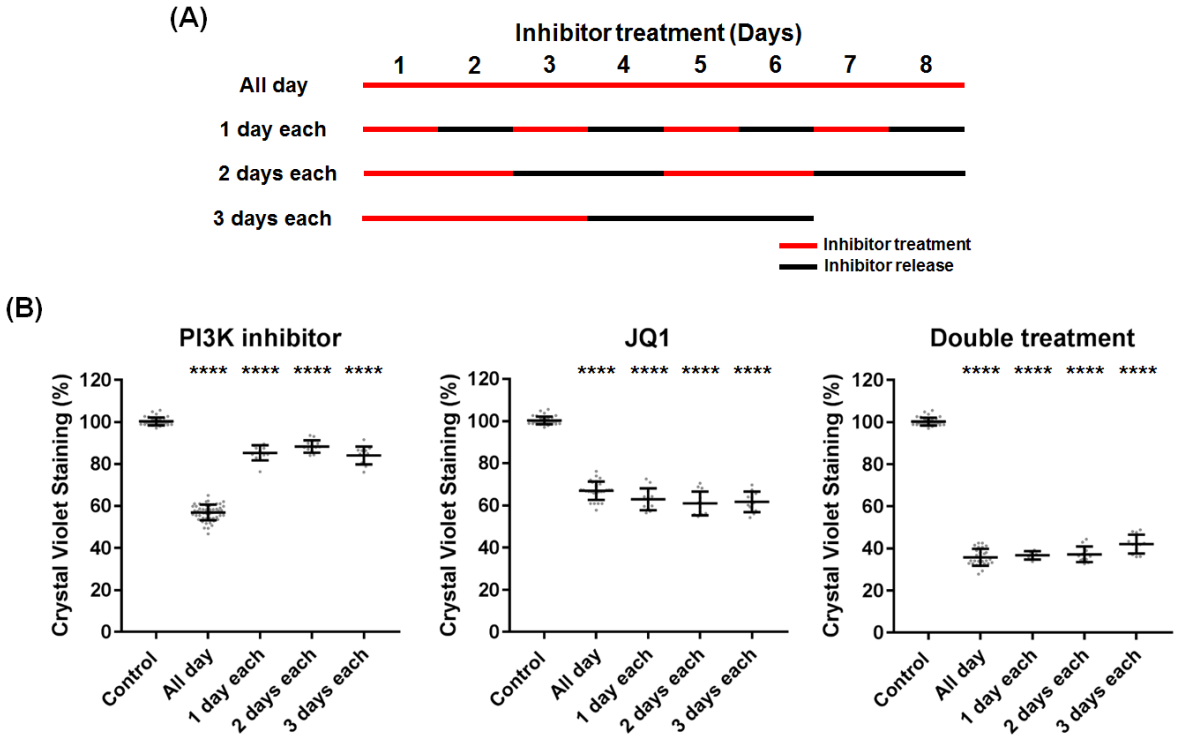


Figure 6-11 Alternative drug treatment of PI3K and Bromodomain inhibitor.
(A) Schematic representation of alternative drug treatment of PI3K and Bromodomain inhibitor. (B) MCF-7 cells were cultured with 0.1 μM Pictilisib and 0.5 μM JQ1 with 1-3 days intervals, and the cells were stained with crystal violet. Intensity of crystal violet was measured and quantified using ImageJ software. n > 10 wells for each condition from three independent experiments. ****p < 0.0001 Welch unpaired T test.

6.3.2 Combinatorial inhibition induced energetic stress

Combinatorial inhibition of PI3K and Bromodomain dramatically reduced intracellular glucose levels and supressed tumour proliferation. Because both glycolysis and OXPHOS could be inhibited by combinatorial inhibitor treatment, I analysed the effect of combinatorial inhibition of PI3K and Bromodomain on energetic stress. MCF-7 cells were treated with inhibitors and then glucose uptake, mitochondrial membrane potential, ROS levels, and ATP levels were measured by fluorescence microscopy (Figure 6-12). As a result, glucose uptake was significantly inhibited by PI3K, Bromodomain, and combinatorial inhibitor treatments. There was no difference in glucose uptake ability by combinatorial inhibition compared with single inhibitor treatments. For mitochondrial membrane potential, PI3K inhibition reduced the mitochondrial membrane potential but Bromodomain inhibition did not change TMRE intensity. Combinatorial inhibition also reduced mitochondrial membrane potential and this effect mainly came from PI3K inhibition. For ROS levels, single treatment with a PI3K inhibitor did not change, and Bromodomain inhibition slightly increased, ROS levels. On the other hand, combinatorial inhibition dramatically increased ROS levels. The very high ROS levels might be able to induce apoptosis. Combinatorial inhibition can also dramatically reduce intracellular ATP levels compared with single treatments. Thus, combinatorial inhibition of PI3K and Bromodomain is an ideal drug combination to supress both glycolysis and OXPHOS.

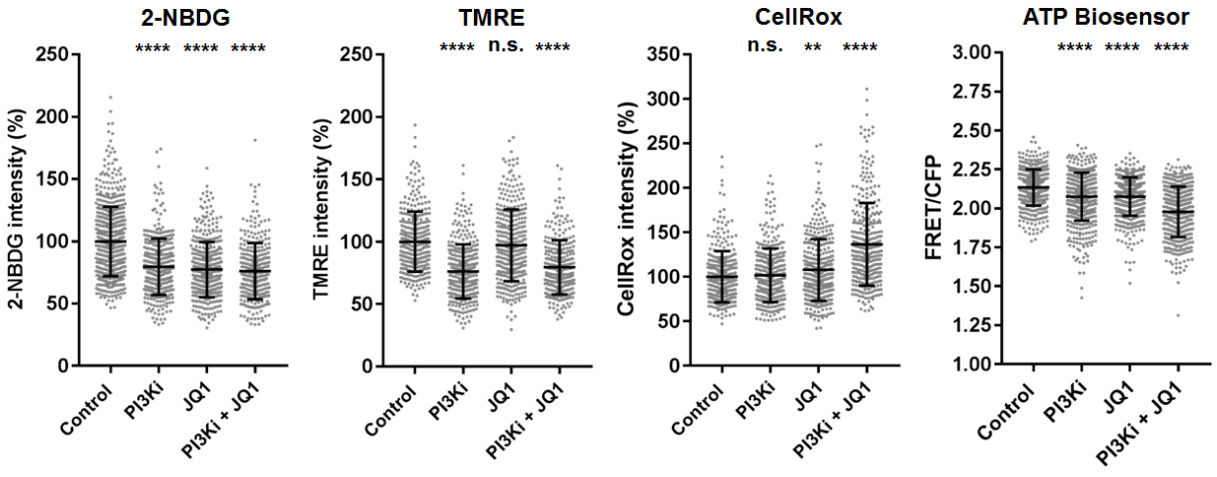


Figure 6-12 The effect of combinatorial inhibition on energetic stress.
Distribution of 2-NBDG intensity, TMRE intensity, CellRox intensity, and ATP FRET signals in inhibitor-treated MCF-7 cells. MCF-7 cells were incubated with 0.1 μM Pictilisib and 0.5 μM JQ1 for 24 hours and then energetic conditions were analysed by imaging metabolic indicators. n > 300 cells for each condition from at least three independent experiments. n.s. $p > 0.05$, **$p < 0.01$, ****$p < 0.0001$ Welch unpaired T test.

6.3.3 The effect of combinatorial inhibition on signalling pathways

Combinatorial inhibition of PI3K and Bromodomain supressed glucose metabolism and induced energetic stress. Bromodomain is known to regulate IGF1 and YAP/TAZ expression. Therefore, combinatorial inhibition is expected to inhibit both PI3K/AKT and YAP/TAZ signalling pathway [165]. In order to analyse the effect of combinatorial inhibition of PI3K and Bromodomain on signal activities, MCF-7 cells were incubated with inhibitors and then phosphorylation and expression levels of AKT, YAP, and Cofilin were measured by Western Blot (Figure 6-13). As a result, both PI3K and Bromodomain inhibitor treatment can supress AKT phosphorylation levels. In addition, combinatorial inhibition reduced AKT phosphorylation levels more than single treatment with a PI3K inhibitor. For YAP phosphorylation levels, the PI3K inhibitor increased, but Bromodomain inhibitor decreased, YAP phosphorylation level. Combinatorial inhibition had very low YAP phosphorylation levels. For Cofilin phosphorylation levels, both single and double inhibitor treatments slightly reduced phosphorylation levels. Comparing single and double inhibitor treatment, the key characteristics of combinatorial inhibition are low AKT and YAP phosphorylation levels. Inactivation of PI3K/AKT signalling and activation of YAP could effectively suppress tumour growth.

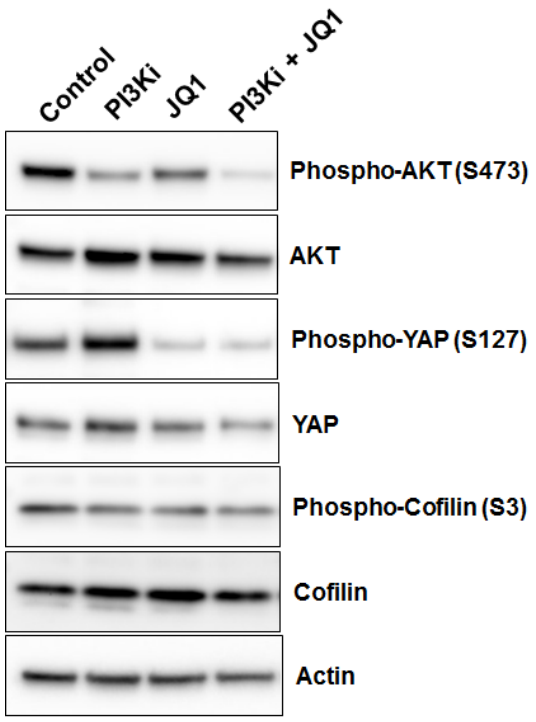


Figure 6-13 The effect of combinatorial inhibition on protein expression.
Western blot of metabolism regulator proteins in PI3K and Bromodomain inhibitor-treated MCF-7 cells. MCF-7 cells were treated with inhibitors for 24 hours, and protein expression and phosphorylation were analysed by western blot.

6.3.4 Combinatorial inhibition in the scratch assay

I found combinatorial inhibition of PI3K and Bromodomain can effectively suppress glucose metabolism and the proliferation of MCF-7 cells. Because scratch-induced migrating high glucose cells could be facilitated by PI3K signalling and actin cytoskeletal remodelling, I analysed the effect of combinatorial inhibition on intracellular glucose increase in migrating cells. Glucose FRET biosensor-expressing MCF-7 cells were treated with inhibitor and then intracellular glucose levels were measured during cell migration (Figure 6-14A, B). Both PI3K and Bromodomain inhibitor-treated cells reduced intracellular glucose levels but scratch-induced migrating cells can slightly increase glucose levels. On the other hand, combinatorial inhibition of PI3K and Bromodomain can completely inhibit intracellular glucose increase at the leading edge.

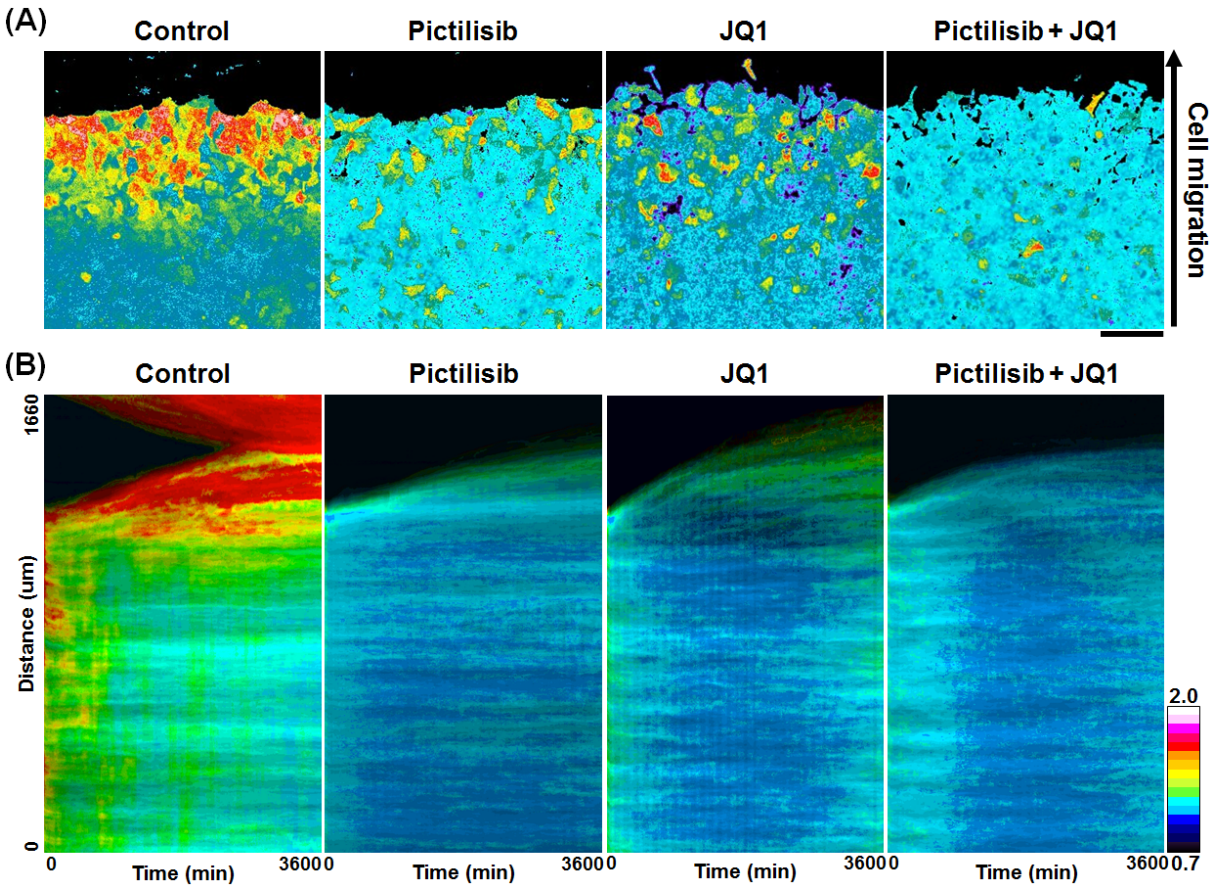


Figure 6-14 The effect of combinatorial inhibition on scratch-induced glucose increase.
(A) Ratiometric FRET images of glucose FRET biosensor in MCF-7 cells were acquired 20 hours after scratching of monolayer. The cells were incubated with 0.1 μM Pictilisib and 0.5 μM JQ1 and then time-lapse images were acquired for 60 hours. Scale=100 μm. (B) Kymograph of glucose FRET signal in scratch assay. The kymographs were generated from three independent scratch assays.

In addition to the measurement of intracellular glucose levels in migrating cells, I measured energetic stress in the scratch assay. I showed in chapter 5.3.3 that scratch-induced migrating cells have low intracellular ATP levels. Because migrating cells require large amounts of ATP for actin cytoskeletal remodelling, scratch-induced migrating cells could rapidly consume energy and had lower intracellular ATP levels. I found migrating cells are glycolytic-high glucose cells, migrating cells could accelerate ATP consumption. In order to analyse the effect of combinatorial inhibition on the energetic stress of migrating and non-migrating cells, ATP FRET biosensor-expressing MCF-7 cells were incubated with inhibitors, scratched, and then time-lapse images were acquired for 45 hours every 5 min (Figure 6-15). In control conditions, migrating cells reduced intracellular ATP levels at the leading edge. In addition, non-migrating cells also gradually reduced ATP levels possibly because of increasing cell confluence. In PI3K and Bromodomain inhibitor-treated cells, ATP levels were reduced and migrating cells could slightly reduce ATP levels compared with non-migrating cells. Combinatorial inhibition of PI3K and Bromodomain further reduced ATP levels and there was no difference of ATP levels between migrating and non-migrating cells. Thus, combinatorial inhibition of PI3K and Bromodomain can induce high energetic stress.

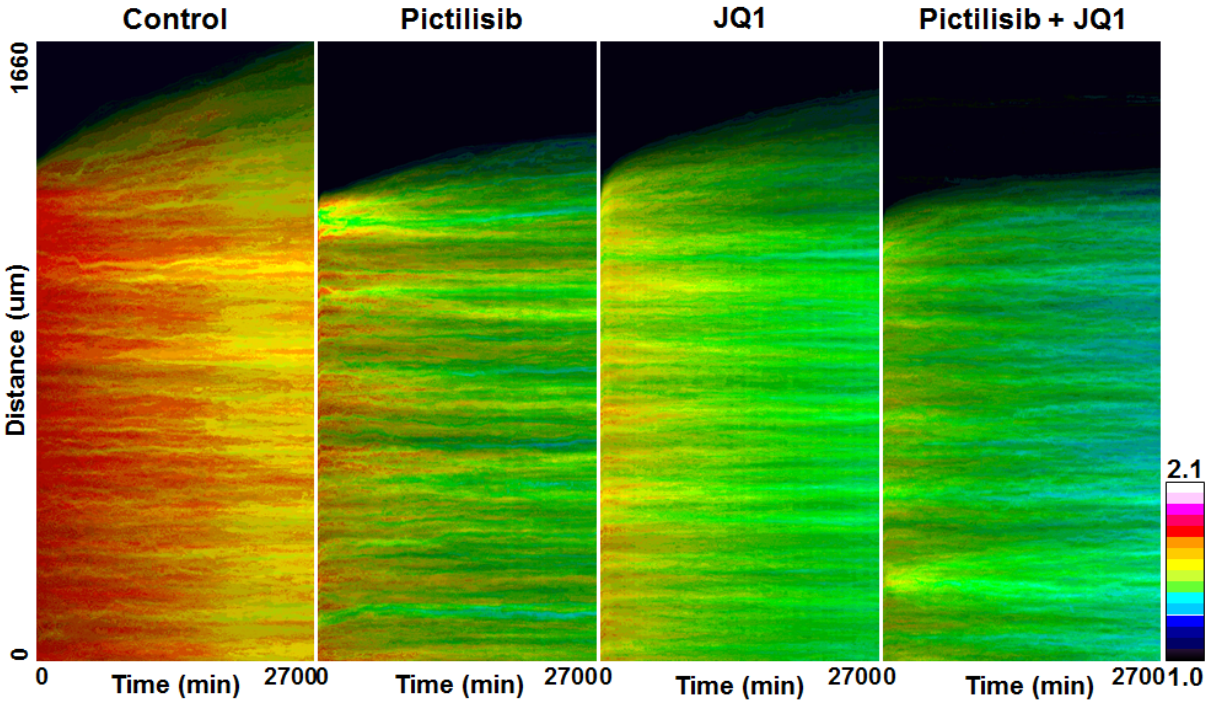


Figure 6-15 The effect of combinatorial inhibition on scratch-induced ATP decrease.
Kymograph of glucose FRET signal in scratch assay. ATP FRET biosensor expressing MCF-7 cells were incubated with 0.1 μM Pictilisib and 0.5 μM JQ1 and then scratched and time-lapse images were acquired for 45 hours. The kymographs were generated from three independent scratch assays.

6.4 Chapter discussion

In this chapter, I found different mechanisms of epigenetic regulation of cell metabolism in breast cancer. Histone methylation levels and patterns could regulate glycolysis because histone methylation and de-methylation inhibitors reduced intracellular glucose levels. However, there was no effect of these two inhibitors on OXPHOS low glucose cells. In contrast, histone acetylation levels had a great impact on glucose metabolism. HDAC and Bromodomain inhibitors dramatically reduced intracellular glucose levels in both high and low glucose cells. This result suggests that histone acetylation is a fundamental regulation mechanism to decide the balance of glycolysis and OXPHOS. In addition, intracellular acetyl-CoA levels can regulate histone acetylation levels. Histone acetylation levels could have positive feedback from glucose metabolism. Combinatorial inhibition of PI3K and Bromodomain has a long-lasting effect and intra-cellular ROS levels were dramatically increased by combinatorial inhibitor treatment. This energetic stress might supress tumour growth and induce apoptosis. This drug combination can also inhibit intracellular glucose increase in migrating cells. The cells at the tumour periphery might be able to migrate towards free space and accelerate proliferation. Targeting therapy to migrating high glucose cells is very important because a subset of high glucose cells are expected to recur after therapeutic treatments. Combinatorial inhibition of PI3K and Bromodomain could effectively supress glucose metabolism and tumour growth of PI3K-dependent and independent breast cancer cells.

Chapter 7. Discussion

7.1 Summary and reflection on the findings

7.1.1 Multiplexed imaging of cancer cell metabolism

Imaging cell metabolism in particular glucose levels clarified that breast cancer cells have metabolic heterogeneity at the single cell scale. Single molecular imaging can measure kinase activity and relative molecular concentration at single cell resolution. However, it is difficult to reveal a correlation between multiple factors. Multiplexed imaging was used to read out several pieces of information from a single cell, the relationship among each factor can be analysed with spatiotemporal resolution. Cancer cells have inter-cellular heterogeneity of signalling pathways and cell metabolism [139, 166-168]. Individual cancer cells have different activities of ERK, PI3K, AKT, as well as glycolytic enzymes, single molecular imaging cannot analyse the relationship of heterogeneous enzyme activities. Therefore, multiplexed imaging is a strong approach to analyse heterogeneous cell metabolism.

For multiplexed imaging of cell metabolism, I developed a new glucose FRET biosensor with mTurquiose2 - sReACh fluorophore combination for FLIM-FRET. Although sReACh does not emit a light, fluorescence lifetime imaging of donor fluorescence protein can read out conformational structural change of a FRET biosensor. The newly-established glucose FRET biosensor and nine other biosensors were optimised in MCF-7 cells for multiplexed imaging. Because these biosensors have different emission wavelengths, multiplexed imaging can read out a maximum of four metabolic parameters from single cells (Figure 7-1).

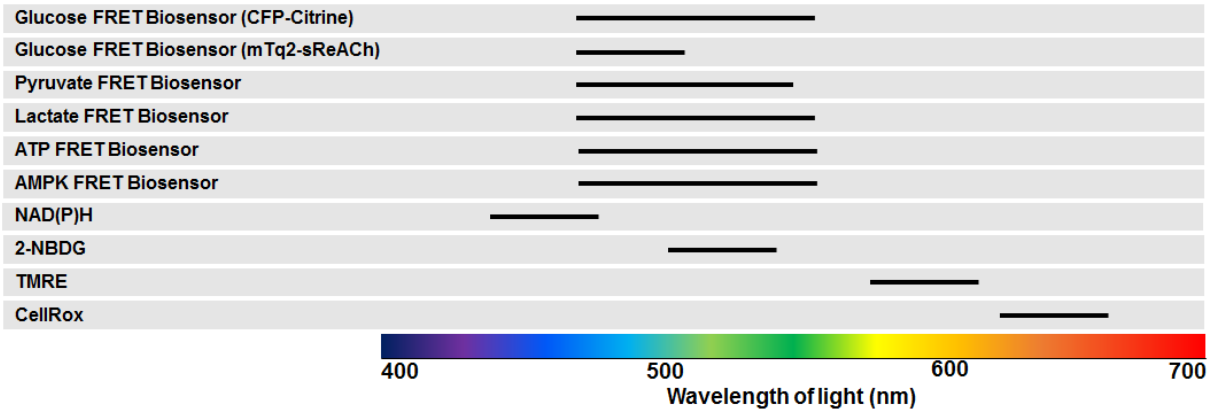


Figure 7-1 Emission ranges of biosensors.
Summary of emission ranges of optimised biosensors. Biosensors without spectrum overlap can be used for the multiplexed imaging.

Among optimised biosensors, the glucose and ATP FRET biosensors have a wide working range to detect metabolic heterogeneity. Furthermore, the fluorescence intensity of 2-NBDG, TMRE, CellRox can measure heterogeneous glucose uptake, mitochondrial membrane potential, and ROS levels. In the current experimental setup, I can measure four different biosensors in the same cells because of their different spectral characteristics (Figure 7-2). Multiplexed imaging of these four biosensors shows that intracellular glucose levels correlate with glycolysis and OXPHOS.

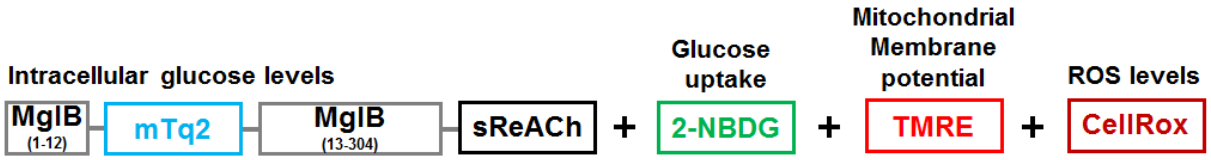


Figure 7-2 Multiplexed imaging of four biosensors.
Summary of multiplexed imaging of four different biosensors in single cells. Glucose FRET biosensor, 2-NBDG, TMRE, and CellRox were used to read out different metabolic information from a single cell.

Recent research has employed multiplexed imaging for the analysis of signalling pathways. In order to measure two different FRET biosensors in the same cells, I needed to change fluorophore combination from a Cyan-Yellow pair to a Green-Red or a Red-Far red pair because most of the FRET biosensors were originally constructed using CFP and YFP. For example, the Caspase FRET biosensor with YFP and DsRed pair was reported in 2005 [169]. The caspase FRET biosensor was further improved by changing fluorophore combination to mAmetrine-tdTomato [170]. In addition, multiplexed imaging of the calcium FRET biosensor Cameleon with eCFP-Venus pair and the FRET biosensor of small Ras GTP-ase with TagRFP-mPlum pair was reported in 2008 [171]. The dual imaging of FRET biosensors clarified a transient rise of calcium level can induce a sustained Ras activation at the plasma membrane. Simultaneous imaging of two different FRET sensors can analyse the correlation of two different proteins. In order to construct a better FRET biosensor, optimisation of fluorophore pairs is one of the most important processes in biosensor development. Fluorophore combinations were analysed and Clover-mCherry pair showed the largest dynamic range (Figure 7-3) [172]. Not only in the new spectral range of FRET biosensor, but the stability of variant fluorescence proteins to temperature and pH is a benefit of Green-Red pair FRET biosensor [87-89]. Therefore, changing fluorophore pairs of FRET biosensors to Clover-mCherry is a next step to improve multiplexed imaging of heterogeneous cell metabolism.

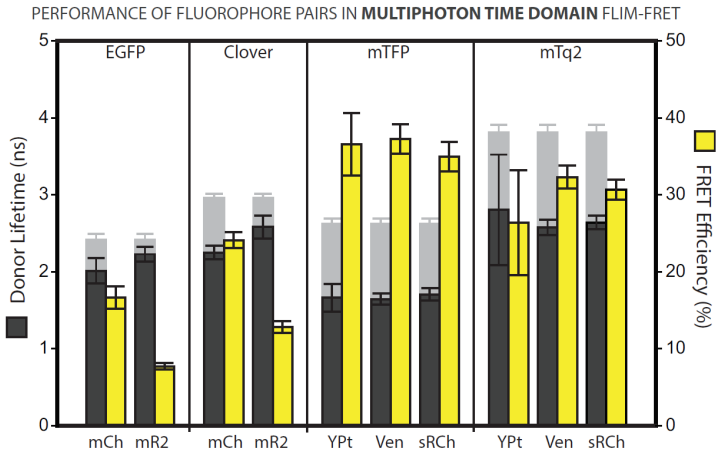


Figure 7-3 Analysis of fluorophore pairs.
Multi-photon time domain measurements of fluorescence lifetimes of FRET donors (dark grey bars) and the respective FRET efficiencies (yellow bars) calculated from the donor-alone lifetimes. The figure is adapted from [172].

7.1.2 Metabolic heterogeneity of breast cancer

Multiplexed imaging indicates that breast cancer cells have heterogeneous metabolism, with high glucose cells having higher glucose uptake and consumption. This high glucose population has low mitochondrial activity and ROS levels. To correlate and extend these findings, I investigated the mechanism to establish metabolic heterogeneity by analysing metabolic stability and heritability of both high and low glucose cells. I found that MDA-MB-231 have low stability and heritability of metabolic states. This different ability to change metabolic states may be common to other subtypes of breast cancer and metastases. FACS-isolated high glucose cells returned to the unsorted glucose levels within 3-4 days, and FACS-isolated low glucose cells returned to the unsorted glucose levels within 1-2 weeks (Figure 7-4A). Thus, oxidative cell metabolism is a more stable and heritable metabolic characteristic in breast cancer cells. These metabolic characteristics are reversibly perturbed, metabolic reprogramming could be epigenetically regulated. Cancer cells remodel cell metabolism in order to adapt the tumour microenvironment for sustainable proliferation. The key microenvironmental factors such as cell confluence, oxygen concentration, ECM stiffness, extracellular pH, and CAFs can remodel cancer cell metabolism. In particular, high cell confluence dramatically reduced intracellular glucose level. High glucose cells have high expression level of glucose transporter, high AKT activity, and low Cofilin phosphorylation level. Cell confluence can regulate cell metabolism through these metabolic regulators. Heterogeneous and variable cancer cell metabolism could be a crucial mechanism for microenvironmental adaptation.

In addition, multiplexed imaging and metabolomic analysis of FACS-isolated high and low glucose cells revealed that high glucose cells mainly utilise glucose for PPP and glycolysis (Figure 7-4B). In contrast, low glucose cells use glucose for the TCA cycle in mitochondria. Heterogeneous glucose metabolism has been observed in tumours using ^{13}C MRI imaging [173]. Therefore, heterogeneous metabolism in cancer cells is expected and key mechanisms to acquire metabolic heterogeneity have been analysed in cancer cells. Especially, pyruvate dehydrogenase (PDH) activity and Lactate dehydrogenase A (LDHA) activities are key regulators of metabolic heterogeneity. PDK1 catalyses the conversion of pyruvate to Acetyl-CoA, and LDHA catalyses the conversion of pyruvate to lactate. Therefore, activities of these two enzymes can regulate the balance of glycolytic and oxidative metabolism. The glycolysis enzymes pyruvate dehydrogenase kinase 1 (PDPK1) and pyruvate kinase isozymes M1/M2 (PKM1/M2) also regulate the balance of glycolytic and oxidative metabolism [174, 175]. These kinase activities can establish heterogeneous cancer cell metabolism.

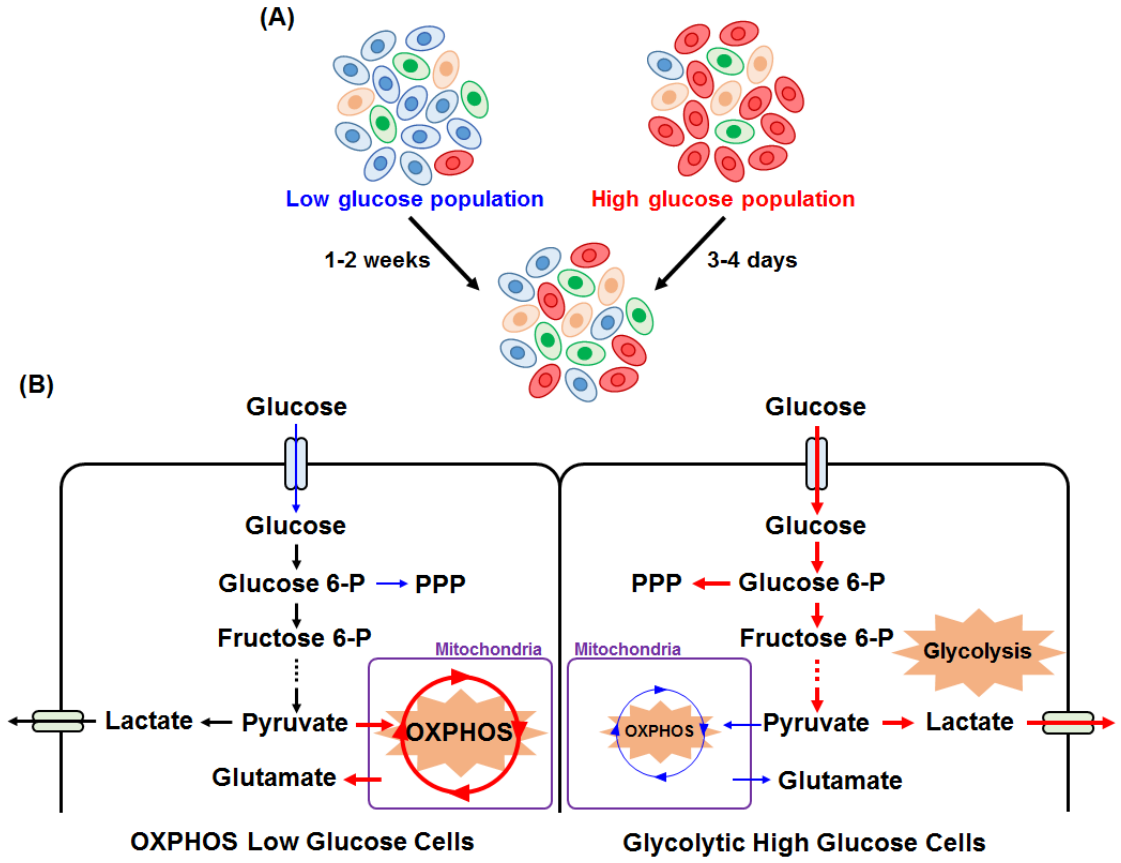


Figure 7-4 Metabolic stability and heterogeneity in breast cancer.
(A) Schematic representation of metabolic stability of FACS-isolated high and low glucose MCF-7 cells.
(B) Summary of metabolic characteristics of high and low glucose cells.

The combination of imaging and metabolomics is an excellent experimental approach to analyse heterogeneous cell metabolism. Although the number of biosensors for imaging is limited, imaging can analyse cell metabolism at the single cell scale *in vitro* and *in vivo*. On the other hand, metabolomic analysis can analyse whole metabolites without spatio-temporal resolution. Mass spectrometry imaging (MSI) is a new experimental technique overcoming these disadvantages. MSI can visualise the spatial distribution of molecules in the tissue sections by mass spectrometry (Figure 7-5). MSI with MALDI has 10 μm spatial resolution and the mass detection range is 0 - 100,000 Da [176]. MSI collects a mass spectrum in the entire sample by scanning and the acquired data set is used for the mapping of target compounds. Thus, MSI can analyse whole cell metabolites and proteins with spatial resolution. I found that MCF-7 and MDA-MB-231 cells have heterogeneous intracellular glucose levels *in vivo*. Especially, cells at the tumour periphery have extremely high intracellular glucose levels. I analysed the GLUT1 expression level and AKT phosphorylation level in MCF-7 tumours. Metabolic profiling of tumours with spatial resolution using MSI should be a next approach to improve the understanding of metabolic heterogeneity *in vivo*.

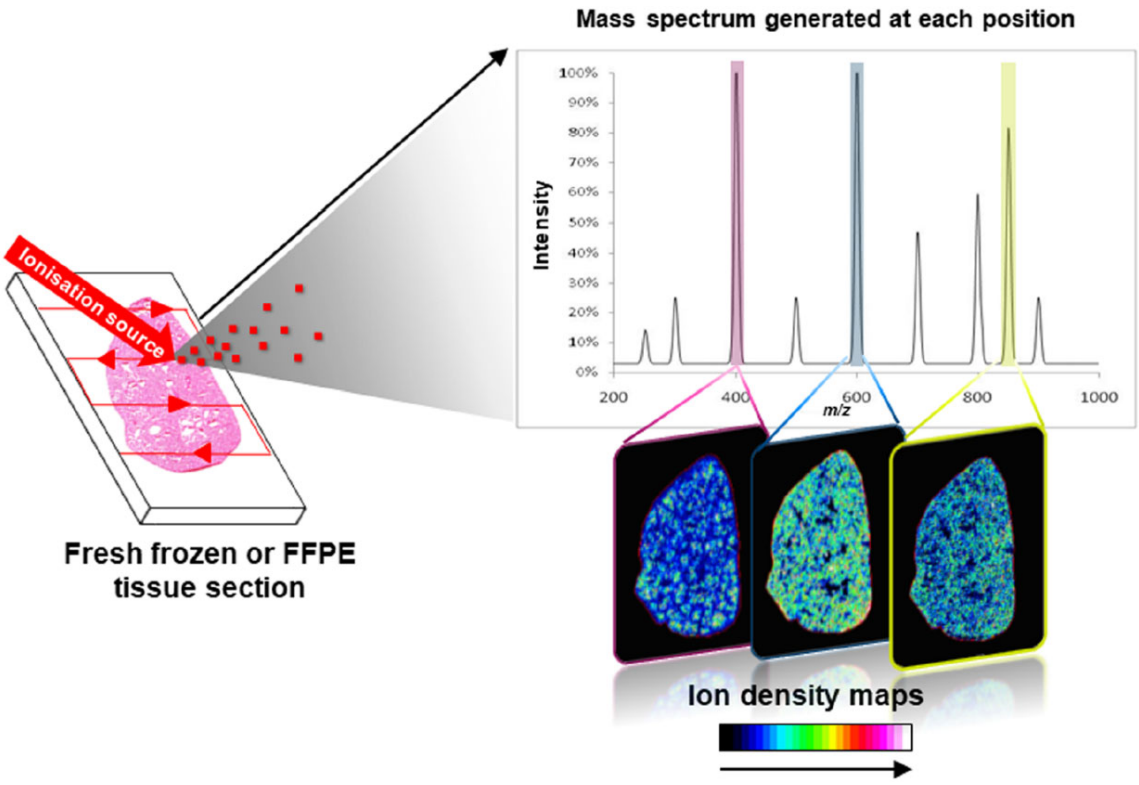


Figure 7-5 Mass spectrometry imaging (MSI) workflow.
Schematic representation of mass spectrometry imaging of frozen or formalin-fixed paraffin-embedded (FFPE) tissue sections. The diagram is adapted from [177].

7.1.3 The mechanism to reprogram glucose metabolism

Imaging intracellular glucose levels with inhibitor treatments and WB analysis of FACS-isolated high and low glucose cells indicate that high and low glucose cells have specific signalling pathways to regulate cell metabolism (Figure 7-6). Glycolytic-high glucose cells have a high expression level of GLUT1 and a high AKT phosphorylation level. In addition, the phosphorylation level of Cofilin is kept low. In contrast, low glucose cells have low activity of PI3K and actin cytoskeletal dynamics. These characteristics of signalling pathways can regulate glucose metabolism. The observation of metabolic states suggest that actin cytoskeletal dynamics may influence glucose metabolism. Recent study supports this observation that F-actin can bind with Aldolase A and inhibit the conversion of Fructose 1,6-bisphosphate (F1,6-BP) to Glyceraldehyde 3-phosphate (GA3P) [36]. Migrating cells can increase intracellular glucose levels possibly because of high actin cytoskeletal dynamics. Taken together, the PI3K signalling pathway and actin cytoskeletal dynamics can establish heterogeneous cell metabolism in breast cancer cells.

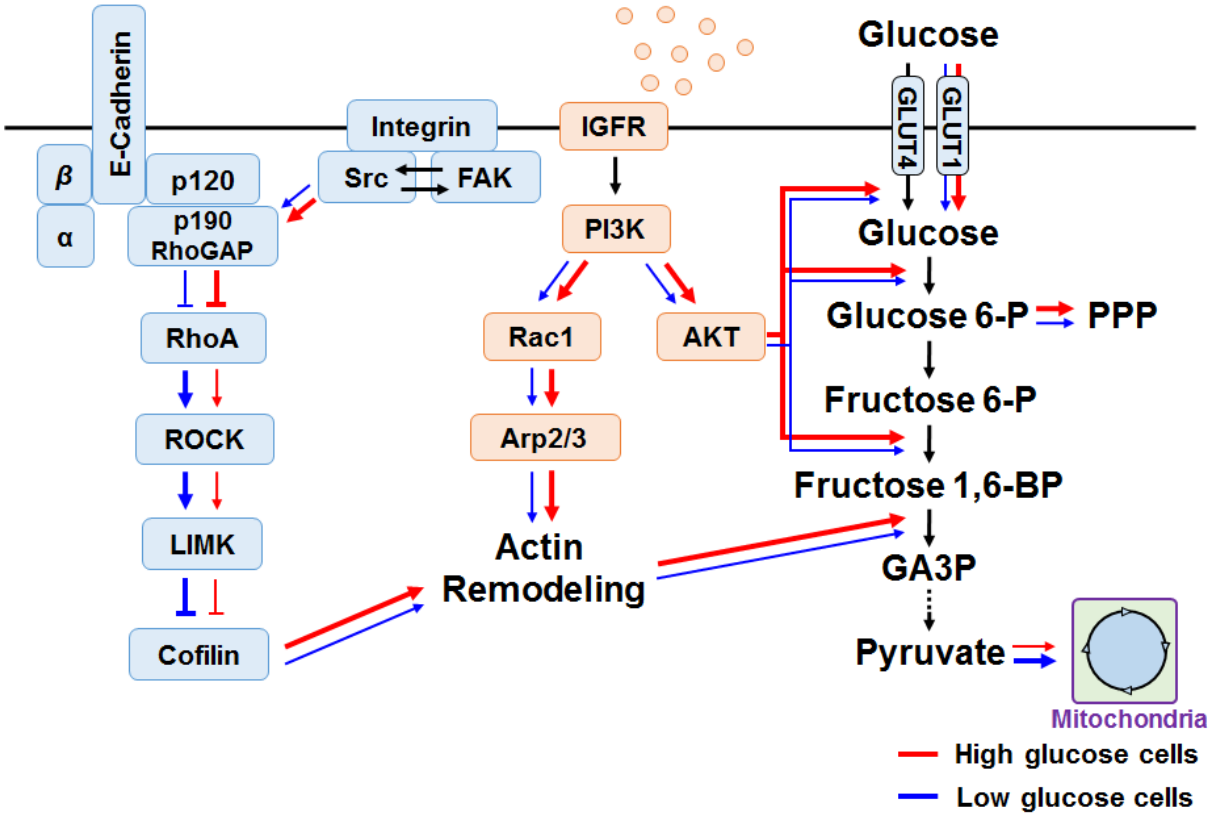


Figure 7-6 Metabolic signalling pathways regulating glucose metabolism.
Schematic representation of expected signalling pathways in high and low glucose cells.

Signalling pathways regulating cell metabolism have been researched and some significant milestones have been achieved. In particular, alterations in the PI3K signalling pathway during tumour progression are key hallmarks of heterogeneous cancer cells (Figure 7-7) [178]. PI3K signalling was analysed in human breast cancer cells and ESR1 levels were negatively correlated with the PI3K activation scores in both proteomic and transcriptional scales [11, 24]. PIK3CA mutated breast cancer cells acquire resistance to PI3K inhibitors by the amplification of c-Myc and Met [14]. The genomic and transcriptional alterations in human cancer were examined across more than 10,000 human cancers and complex PI3K signalling heterogeneity was found in 32 major types of cancer [167, 179, 180]. Inter-tumour heterogeneity of cell metabolism is thus established by heterogeneous activities of signalling.

I found glycolytic-high glucose cells and OXPHOS low glucose cells activate different signalling pathways. However, WB analysis is limited in the measurement of the activity of signalling networks because of the limitations of antibodies. Therefore, the proteome and transcriptome of FACS-isolated high and low glucose cells are necessary for more complete profiling of transcriptional and post-transcriptional characteristics. There are many metabolic regulators whose activities and expression levels are influenced by tumour microenvironments. For example, hypoxia increases the expression of glycolytic enzymes mediated by HIF-1. In addition, oxygen stress can also regulate DNA methylation levels [28, 67]. The overview of proteomic and transcriptional features of glycolytic-high glucose and OXPHOS low glucose cells could reveal the fundamental regulation mechanism of metabolic reprogramming.

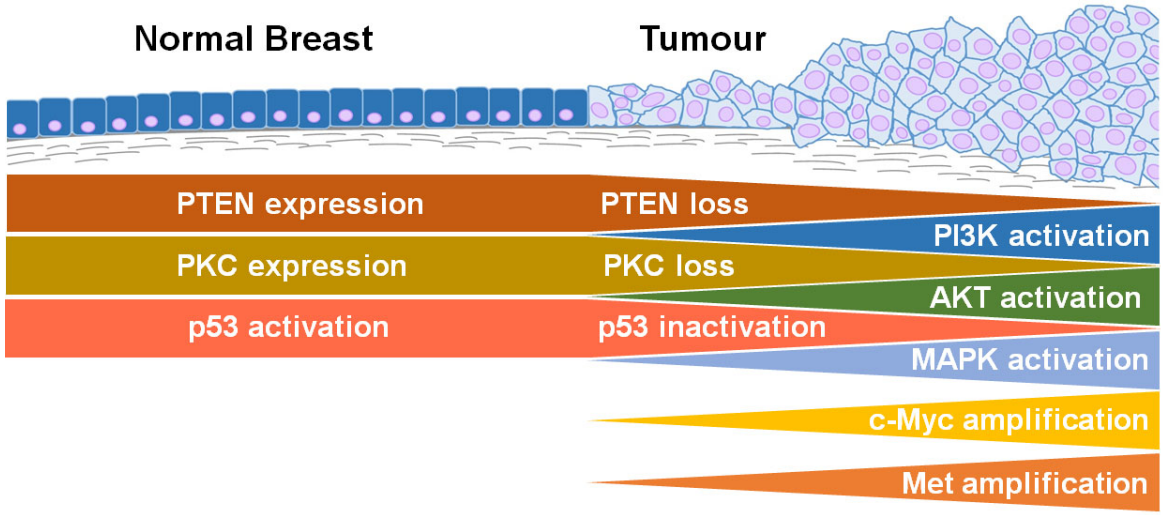
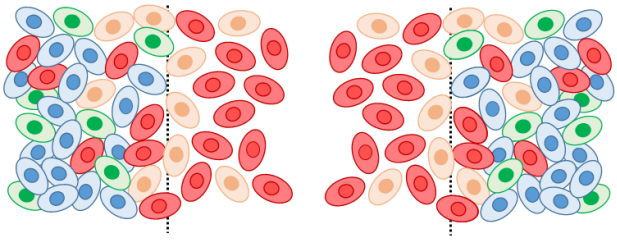


Figure 7-7 Genomic and transcriptional alterations during tumour progression.
Schematic representation of alterations of PI3K, PTEN, PKC, p53, MAPK, c-Myc, and Met as an independent regulators of metabolic heterogeneity.

7.1.4 Cell confluence remodels cell metabolism

Imaging intracellular glucose levels in different cell confluency revealed that cells can remodel cell metabolism from glycolysis to OXPHOS by increasing cell confluence (Figure 7-8). The scratch assay can analyse metabolic reprogramming depending on cell confluence and cell migration. The leading edge of the wound has low cell density because the cells can migrate towards the free space introduced by scratches. Multiplexed imaging showed that the cells at the leading edge have extremely high intracellular glucose levels. Both glucose uptake and consumption in migrating high glucose cells are higher than non-migrating low glucose cells within a glucose wash in/out approach. Although I observed low intracellular ATP levels in migrating cells, migrating cells can accelerate OXPHOS for energy production. Intra-cellular ATP levels of migrating cells are low probably because ATP consumption is higher than production. Migrating cells should have higher energetic stress because migrating high glucose cells have high AMPK activity. In addition, metabolomic analysis identified that scratch-induced high glucose cells utilise high levels of glucose for PPP and glycolysis. In contrast, non-migrating cells use glucose as a fuel for mitochondrial metabolism. Thus, glycolysis and OXPHOS are the metabolic characteristics of migrating high glucose cells at low cell confluence and non-migrating low glucose cells at high cell confluence. PI3K inhibition suppressed the intracellular glucose increase of migrating cells. Combinatorial inhibition of PI3K and Bromodomain can dramatically reduce migrating high glucose cells which regulate glucose metabolism independently from PI3K.

Scratch Assay



Cell confluence	High	Low	High
Cell migration	Low	High	Low
Glucose level	Low	High	Low
Glucose uptake	Low	High	Low
Glucose consumption	Low	High	Low
ATP level	High	Low	High
AMPK activity	Low	High	Low
Glycolysis	Low	High	Low
OXPHOS	High	Low	High

Figure 7-8 Metabolic characteristics during cell migration.
Summary of the metabolic characteristics of migrating high glucose and non-migrating low glucose cells.

7.1.5 Combinatorial inhibition of PI3K and Bromodomain for effective tumour suppression

Heterogeneous glucose metabolism is regulated by epigenetics. In particular, histone acetylation levels and its reader Bromodomain are highly correlated with intracellular glucose levels. I found that high glucose cells have low histone acetylation levels. In addition, HDAC and Bromodomain inhibitors can dramatically reduce intracellular glucose levels. The PI3K signalling pathway increases ACLY-regulated Acetyl-CoA production and promotes glucose metabolism [78]. These results suggest that glucose metabolism and histone acetylation levels have a positive feedback loop. Bromodomain-containing protein 4 (BRD4) can transcribe mRNA from the acetylated H3K27 promoter region. IGF1 and YAP/TAZ are the main transcriptional targets of BRD4, and the glycolytic pathway also has crosstalk with H3K27 acetylation [165, 181]. Thus, PI3K signalling and epigenetic regulation of gene expression establish a reciprocal relationship to promote glucose metabolism (Figure 7-9). BYL719 and BKM120 are the common PI3K inhibitors in clinical trials. However, single treatment with PI3K inhibitors cannot completely eliminate cancer cells. Combinatorial inhibition of PI3K and BRD4 can improve therapeutic effect in breast and lung cancer [165, 182]. Combinatorial inhibition of PI3K and BRD4 in MCF-7 cells completely suppressed tumour growth and scratch-induced intracellular glucose increase in migrating cells. Furthermore, combinatorial inhibition significantly increased ROS levels and reduced ATP levels. Thus, targeted inhibition of PI3K and BRD4 can effectively inhibit glucose metabolism and cell proliferation. Optimisation of drug treatments *in vivo* to minimize dosage amount and frequency is a next step to reduce side effects in clinical trials.

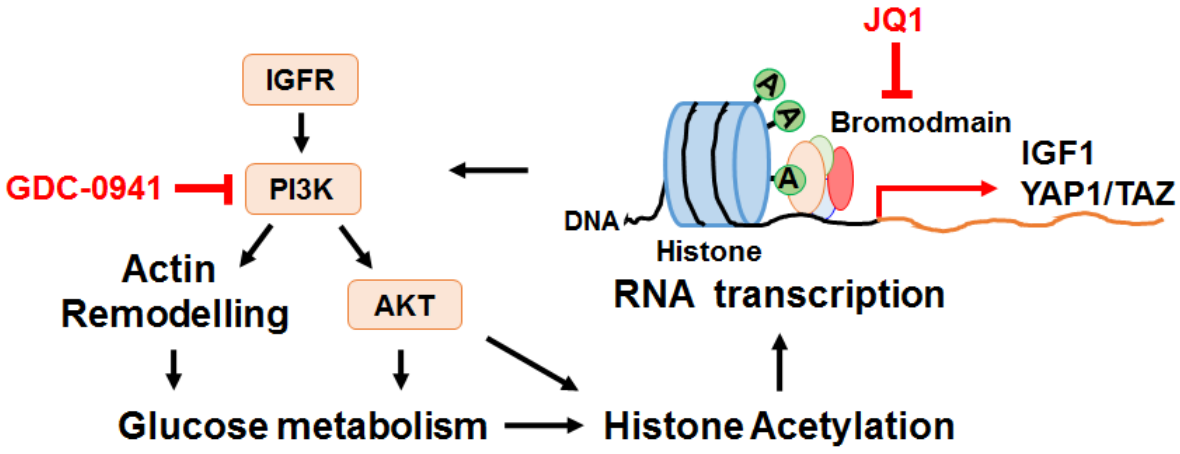


Figure 7-9 Combinatorial inhibition of PI3K and Bromodomain
Schematic representation of signalling pathways and targeting inhibition of PI3K and Bromodomain.

7.2 Future perspective

7.2.1 Non-invasive live cell imaging

The combination of multiplexed imaging and proteome analysis indicates metabolic heterogeneity of breast cancer cells. Heterogeneity has consequences for therapy response, especially therapies that interfere with metabolic regulation. Metabolic profiling of heterogeneous cancer cells is important to characterise clinical samples. Based on metabolic information, the most appropriate drug can be applied for cancer patients. However, conventional FRET imaging techniques cannot be used for the analysis of clinical samples because it is not possible to introduce FRET biosensors into patients. In the clinic, ^{18}F-FDG PET/CT and MRI have been used for the diagnosis of cancer. ^{18}F-FDG PET/CT can detect tumours but has low resolution. MRI has better resolution but does not have metabolic information. Recently, hyper-polarised MRI using ^{13}C-Pyruvate has been used diagnostically, which has better characterisation of tumour metabolism [183].

In order to improve the imaging of heterogeneous cancer metabolism in patient tumours, fluorescence lifetime imaging of NAD(P)H has been developed as a non-invasive method to analyse clinical samples. Metabolically-linked autofluorescence was first observed in 1962 [184] but its fluorescence lifetime has been characterised in recent research [185]. The fluorescence lifetime of the protein-unbound form of NAD(P)H is shorter than the protein-bound form of NAD(P)H. The protein-unbound form of NADH facilitates proton transport in the mitochondrial respiration chain and the protein-bound form of NAD(P)H promotes glycolytic metabolism. These different fluorescence lifetimes of NAD(P)H represent the balance of glycolysis and OXPHOS [96, 175, 186, 187]. Although fluorescence lifetime imaging of NAD(P)H can distinguish glycolysis and OXPHOS, NAD(P)H imaging cannot read out additional metabolic information in current approaches. In cancer therapy, metabolic information about glucose metabolism, glutaminolysis, amino acid metabolism, nucleic acid metabolism, and energetic stress are all important for effective tumour suppression. I can analyse glucose uptake, mitochondrial membrane potential, and intracellular ROS levels using metabolic indicators 2-NBDG, CellRox, and TMRE. Multiplexed imaging of NAD(P)H and these metabolic indicators could improve the understanding of heterogeneous cancer metabolism. In addition, fluorescence lifetime imaging confocal endomicroscopy has been developed for the analysis of tumour drug target engagement *in vivo* [188]. Using confocal endomicroscopy, fluorescence lifetime imaging of NAD(P)H can be used for the non-invasive diagnosis of tumour disease.

7.2.2 Imaging T cell maturation

CD4$^+$ and CD8$^+$ T cells are key players in the tumour microenvironment. The adaptive immune system suppresses tumour progression and immunotherapy has been applied for cancer patients [189]. Naïve T cells are activated, proliferate, and differentiate to effector T cells by encountering antigens. Effector T cells further differentiate into memory T cells for maintaining antigen information and an antigen-specific fast immune response. During these processes of T cell maturation, T cells dramatically reprogram cell metabolism (Figure 7-10). Quiescent naïve T cells have depressed metabolism. On the other hand, effector T cells accelerate glycolysis and memory T cells highly engage both glycolysis and OXPHOS for energy and biomass production [190-192]. This metabolic reprogramming is mainly regulated by GLUT1 expression and activation of the PI3K/AKT/mTOR signalling pathway [193-195]. Although T cell maturation is a very important mechanism to supress tumour progression, single cell scale analysis of metabolic reprogramming is limited. Multiplexed imaging of cell metabolism could be a possible approach to clarify the mechanism of T cell maturation in tumour microenvironments. A transgenic mouse bearing glucose FRET biosensor-expressing CD4$^+$/8$^+$ T cells can be generated using a Cre driver. Imaging the T cell maturation process in tumour microenvironments *in vivo* can analyse the mechanism by which T cells supress heterogeneous cancer cells. Multiplexed imaging of T cell metabolism co-cultured with cancer cells *in vitro* is a simpler system to analyse the T cell maturation process. The T cell maturation process and immune function might be different depending on the interactions with heterogeneous cancer cells with different cell metabolism.

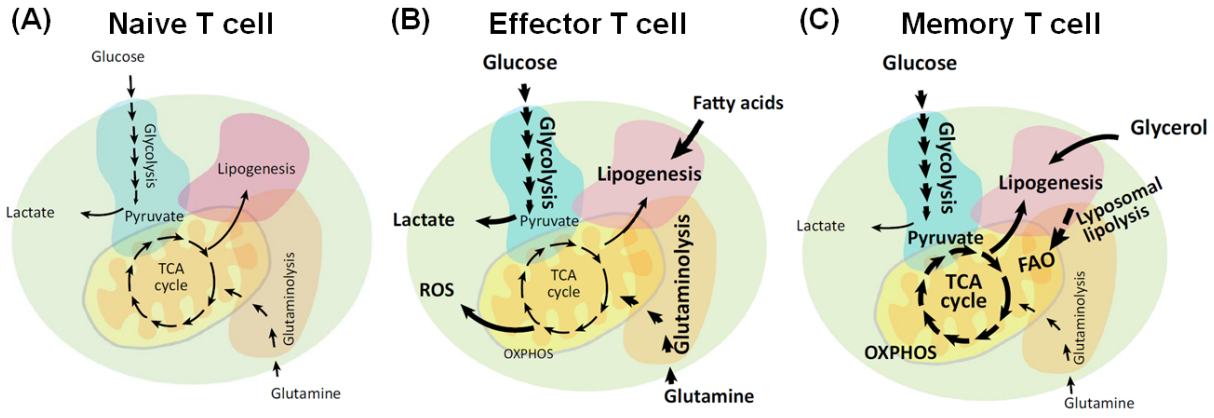


Figure 7-10 Metabolic reprogramming of T cells.
(A) Quiescent metabolism of naïve T cells. Both glycolysis and OXPHOS are kept low. (B) Glycolytic cell metabolism of effector T cells. (C) Energetic cell metabolism of memory T cells. Both glycolysis and OXPHOS are highly utilised for ATP and biomass production. The diagram is adapted from [191].

7.2.3 Imaging metastatic disease

Breast cancer is a highly heterogeneous disease and primary cancer cells can metastasise to other organs such as lung, liver, bone, and brain [196-199]. The majority of breast cancer patients die from metastatic disease. Lung and skin cancers can also metastasise to the brain and the characteristics of brain metastasis formation are different depending on the tumour origin. For example, lung cancer cells highly induce angiogenesis and melanoma cells glow alongside blood vessels. Metastasised cancer cells can grow in the brain microenvironment and metabolic reprogramming could be a key mechanism of tumour microenvironmental adaptation [200, 201]. The brain has high energy requirements and consumes approximately 25% of the human total body glucose consumption [202]. Because only 3 - 5% of cancer cells that reach the brain can form metastasis, metastasized cells could have very specific metabolic characteristics for brain microenvironmental adaptation. In order to analyse the cell metabolism of brain metastasis, multiplexed imaging of individual metastasizing cancer cells in the mouse brain could clarify advantageous metabolic states for brain metastasis (Figure 7-11A). Cancer cells in the brain could remodel cell metabolism because of metabolite exchange with astrocytes and neurons (Figure 7-11B) [203-205]. Because astrocytes mainly utilise glycolytic cell metabolism, cancer cells interacting with astrocytes might promote OXPHOS metabolism [206]. It is hoped that imaging metastatic disease reveals the mechanism of metabolic reprogramming through metastasis.

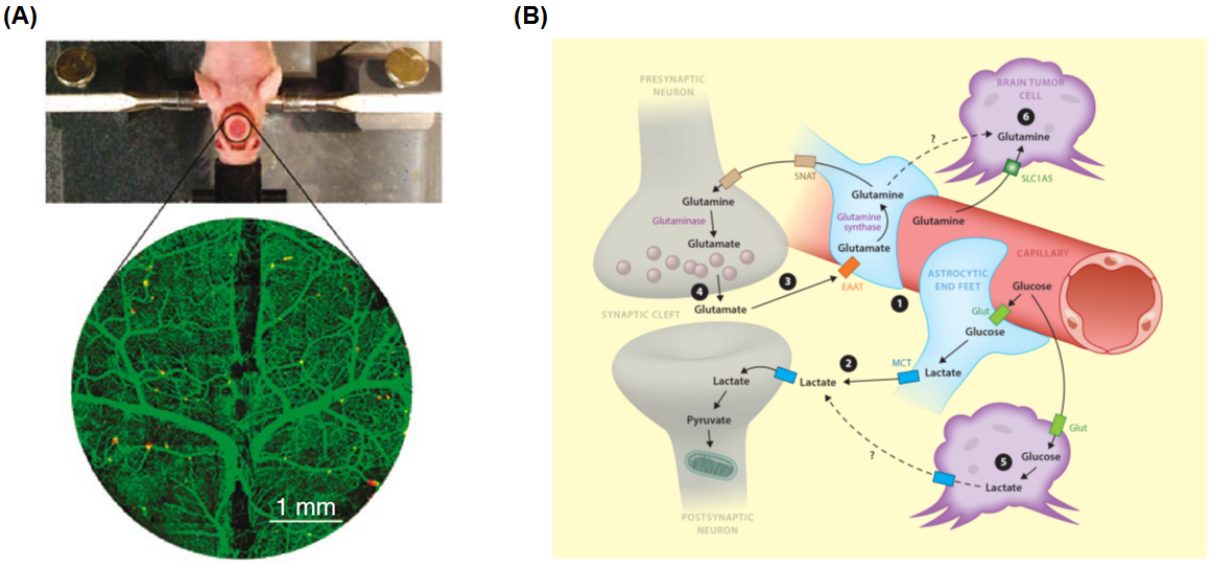


Figure 7-11 Imaging brain metastasis.
(A) Mouse model of imaging brain metastasis. A chronic cranial window with cancer cells stably expressing RFP (red). (B) Schematic representation of gap-junction-mediated cancer cell-astrocyte interaction to support brain metastasis. The diagrams are adapted from [196, 205].

Chapter 8. Appendix

Materials I have used in my research were purchased from the following.

Products	Company	Catalog number
DMEM, high glucose, pyruvate	Thermo Fisher Scientific	41966052
DMEM, high glucose, No Phenol red	Thermo Fisher Scientific	21063-029
DMEM, no glucose, no glutamine, no phenol red	Thermo Fisher Scientific	A1443001
Opti-MEM	Thermo Fisher Scientific	31985047
Insulin-Transferrin-Selenium (ITS -G) (100X)	Thermo Fisher Scientific	41400045
FBS	Sigma-Aldrich	b9433
Dialyzed Fetal Bovine Serum	Sigma-Aldrich	F0392
Penicillin Streptomycin	Thermo Fisher Scientific	15140122
versene solution	Thermo Fisher Scientific	15040033
0.25%trypsin EDTA	Thermo Fisher Scientific	25200056
Lipofectamine 2000	Thermo Fisher Scientific	11668019
X-tremeGENE™ HP	Sigma-Aldrich	6366244001
DharmaFECT 2	Dharmacon	T-2002-03
NEB5 alpha competent bacteria	NEB	c2987H
Gibson Assembly®	NEB	E5510S
GeneArt® Site-Directed Mutagenesis PLUS System	Thermo Fisher Scientific	A14604
QIAprep Miniprep kit	Qiagen	27106
QIAfilter Plasmid Midi kit	Qiagen	12243
QIAfilter Plasmid Maxi kit	Qiagen	12263
protease inhibitor cocktail tablets	Roche	11873580001
phosphatase inh cocktal set II	Calbiochem	524625-1SET
phosphatase inh cocktal set IV	Calbiochem	524628-1SET
4–15% Mini-PROTEAN® TGX™ Precast Protein Gels	Bio-Rad	4561085
Trans-Blot® Turbo™ Mini PVDF membrane	Bio-Rad	1704156
10x Tris/glycine premixed buffer	Bio-Rad	1610732
Immobilon Luminata Crescendo Western HRP substrate	Millipore	WBLUR0100
D-Glucose-13C6	CK isotope	CLM-1396-1
Isoflurane	National Veterinary Services	115095
17β-ESTRADIOL (0.72mg/pellet, 90 day release), 50 pellets	Innovative Research of America	NE-121
Seahorse XFe96 FluxPak mini	Agilent	102601-100
25 Culture-Inserts 2 Well for self-insertion	Ibidi	80209
Collagen I, High Concentration, Rat Tail, 100mg	Corning	354249
Matrigel Matrix	Corning	356235
Cellpath™ OCT Embedding Matrix	Thermo Fisher Scientific	15212776
Acetyl coenzyme A sodium salt	Sigma-Aldrich	A2056
DAPI	Sigma-Aldrich	d9542
Phalloidin–Atto 633	Sigma-Aldrich	68825
Gold nanorods (10 nm diameter, 808 nm absorption)	Sigma-Aldrich	716820
2-NBDG	ThermoFisher	N13195
TMRE	Thermo Fisher	T669
CellROX™ Deep Red Reagent	Thermo Fisher Scientific	C10422
Tetramethylrhodamine isothiocyanate–Dextran	MERCK	T1287
35 mm Dish | No. 1.5 Coverslip | 14 mm Glass Diameter	MatTek Corporation	p35g-1.5-14-c
12-well | No. 1.0 Coverslip | 14 mm Glass Diameter	MatTek Corporation	p12g-1.0-14-f
24-well | No. 1.0 Coverslip | 13 mm Glass Diameter	MatTek Corporation	p24-1.0-13-f

Table 8-1 Materials

Reference List

1. Vargo-Gogola, T. and J.M. Rosen, *Modelling breast cancer: one size does not fit all.* Nat Rev Cancer, 2007. **7**(9): p. 659-72.
2. Perou, C.M., et al., *Molecular portraits of human breast tumours.* NATURE, 2000. **17**(406): p. 747-52.
3. Parker, J.S., et al., *Supervised risk predictor of breast cancer based on intrinsic subtypes.* J Clin Oncol, 2009. **27**(8): p. 1160-7.
4. Monnot, G.C. and P. Romero, *Rationale for immunological approaches to breast cancer therapy.* Breast, 2018. **37**: p. 187-195.
5. Kao, J., et al., *Molecular profiling of breast cancer cell lines defines relevant tumor models and provides a resource for cancer gene discovery.* PLoS One, 2009. **4**(7): p. e6146.
6. Meric-Bernstam, F., et al., *PIK3CA/PTEN mutations and Akt activation as markers of sensitivity to allosteric mTOR inhibitors.* Clin Cancer Res, 2012. **18**(6): p. 1777-89.
7. Razavi, P., et al., *The Genomic Landscape of Endocrine-Resistant Advanced Breast Cancers.* Cancer Cell, 2018. **34**(3): p. 427-438 e6.
8. Ciruelos Gil, E.M., *Targeting the PI3K/AKT/mTOR pathway in estrogen receptor-positive breast cancer.* Cancer Treat Rev, 2014. **40**(7): p. 862-71.
9. Y, S., et al., *High Frequency of Mutations of the PIK3CA Gene in Human Cancers.* Science, 2004. **304**(5670): p. 554.
10. Miller, T.W., et al., *Mutations in the phosphatidylinositol 3-kinase pathway: role in tumor progression and therapeutic implications in breast cancer.* Breast Cancer Research, 2011. **13**(224).
11. Saal, L.H., et al., *Poor prognosis in carcinoma is associated with a gene expression signature of aberrant PTEN tumor suppressor pathway activity.* Proc Natl Acad Sci U S A, 2007. **104**(18): p. 7564-9.
12. Liu, P., et al., *Targeting the phosphoinositide 3-kinase pathway in cancer.* Nat Rev Drug Discov, 2009. **8**(8): p. 627-44.
13. Mukohara, T., *PI3K mutations in breast cancer: prognostic and therapeutic implications.* Breast Cancer (Dove Med Press), 2015. **7**: p. 111-23.
14. Liu, P., et al., *Oncogenic PIK3CA-driven mammary tumors frequently recur via PI3K pathway-dependent and PI3K pathway-independent mechanisms.* Nat Med, 2011. **17**(9): p. 1116-20.
15. Chan, C.H., et al., *The Skp2-SCF E3 ligase regulates Akt ubiquitination, glycolysis, herceptin sensitivity, and tumorigenesis.* Cell, 2012. **149**(5): p. 1098-111.
16. Bader, A.G., S. Kang, and P.K. Vogt, *Cancer-specific mutations in PIK3CA are oncogenic in vivo.* Proc Natl Acad Sci U S A, 2006. **103**(5): p. 1475-9.
17. Burris, H.A., 3rd, *Overcoming acquired resistance to anticancer therapy: focus on the PI3K/AKT/mTOR pathway.* Cancer Chemother Pharmacol, 2013. **71**(4): p. 829-42.
18. Libson, S. and M. Lippman, *A review of clinical aspects of breast cancer.* Int Rev Psychiatry, 2014. **26**(1): p. 4-15.
19. Cuzick, J., et al., *Effect of anastrozole and tamoxifen as adjuvant treatment for early-stage breast cancer: 10-year analysis of the ATAC trial.* The Lancet Oncology, 2010. **11**(12): p. 1135-1141.
20. Blackwell, K.L., et al., *Randomized study of Lapatinib alone or in combination with trastuzumab in women with ErbB2-positive, trastuzumab-refractory metastatic breast cancer.* J Clin Oncol, 2010. **28**(7): p. 1124-30.
21. (EBCTCG), E.B.C.T.C.G., et al., *Relevance of breast cancer hormone receptors and other factors to the efficacy of adjuvant tamoxifen: patient-level meta-analysis of randomised trials.* The Lancet, 2011. **378**(9793): p. 771-784.

22. Simoncini, T., et al., *Interaction of oestrogen receptor with the regulatory subunit of phosphatidylinositol-3-OH kinase.* NATURE, 2000. **407**: p. 538-541.
23. Miller, T.W., J.M. Balko, and C.L. Arteaga, *Phosphatidylinositol 3-kinase and antiestrogen resistance in breast cancer.* J Clin Oncol, 2011. **29**(33): p. 4452-61.
24. Creighton, C.J., et al., *RPerseoartche aortimcle ic and transcriptomic profiling reveals a link between the PI3K pathway and lower estrogen-receptor (ER) levels and activity in ER+ breast cancer.* Breast Cancer Research, 2010. **12**(R40).
25. Kalinsky, K., et al., *PIK3CA mutation associates with improved outcome in breast cancer.* Clin Cancer Res, 2009. **15**(16): p. 5049-59.
26. Heikki Joensuu, M.D., et al., *Adjuvant Docetaxel or Vinorelbine with or without Trastuzumab for Breast Cancer.* The New England Journal of Medicine, 2006. **354**: p. 809-820.
27. T, P., S. S, and B. S, *Cooperation and competition in the evolution of ATP-producing pathways.* Science, 2001. **292**(5516): p. 504-7.
28. MG, V.H., C. LC, and T. CB, *Understanding the Warburg effect: the metabolic requirements of cell proliferation.* Science, 2009. **324**(5930): p. 1029-33.
29. Cairns, R.A., I.S. Harris, and T.W. Mak, *Regulation of cancer cell metabolism.* Nat Rev Cancer, 2011. **11**(2): p. 85-95.
30. Groves, A.M., et al., *Non-[18F]FDG PET in clinical oncology.* The Lancet Oncology, 2007. **8**(9): p. 822-830.
31. A, D.-S. and S. LG, *PET imaging of prostate cancer with 11C-acetate.* Journal of Nuclear Medicine, 2003. **44**(4): p. 556-8.
32. Ben-Haim, S. and P. Ell, *18F-FDG PET and PET/CT in the evaluation of cancer treatment response.* J Nucl Med, 2009. **50**(1): p. 88-99.
33. Kruiswijk, F., C.F. Labuschagne, and K.H. Vousden, *p53 in survival, death and metabolic health: a lifeguard with a licence to kill.* Nat Rev Mol Cell Biol, 2015. **16**(7): p. 393-405.
34. Majewski, N., et al., *Hexokinase-mitochondria interaction mediated by Akt is required to inhibit apoptosis in the presence or absence of Bax and Bak.* Mol Cell, 2004. **16**(5): p. 819-30.
35. Engelman, J.A., *Targeting PI3K signalling in cancer: opportunities, challenges and limitations.* Nat Rev Cancer, 2009. **9**(8): p. 550-62.
36. Hu, H., et al., *Phosphoinositide 3-Kinase Regulates Glycolysis through Mobilization of Aldolase from the Actin Cytoskeleton.* Cell, 2016. **164**(3): p. 433-46.
37. Wullschleger, S., R. Loewith, and M.N. Hall, *TOR signaling in growth and metabolism.* Cell, 2006. **124**(3): p. 471-84.
38. Kim, M.M., et al., *Non-invasive metabolic imaging of brain tumours in the era of precision medicine.* Nat Rev Clin Oncol, 2016. **13**(12): p. 725-739.
39. Sonveaux, P., et al., *Targeting lactate-fueled respiration selectively kills hypoxic tumor cells in mice.* J Clin Invest, 2008. **118**(12): p. 3930-42.
40. Hashim, A.I., et al., *Imaging pH and metastasis.* NMR Biomed, 2011. **24**(6): p. 582-91.
41. Lyssiotis, C.A. and A.C. Kimmelman, *Metabolic Interactions in the Tumor Microenvironment.* Trends Cell Biol, 2017. **27**(11): p. 863-875.
42. Kalluri, R. and M. Zeisberg, *Fibroblasts in cancer.* Nat Rev Cancer, 2006. **6**(5): p. 392-401.
43. Sugimoto, H., et al., *Identification of fibroblast heterogeneity in the tumor microenvironment.* Cancer Biol Ther, 2006. **5**(12): p. 1640-6.
44. Kojima, Y., et al., *Autocrine TGF-beta and stromal cell-derived factor-1 (SDF-1) signaling drives the evolution of tumor-promoting mammary stromal myofibroblasts.* Proc Natl Acad Sci U S A, 2010. **107**(46): p. 20009-14.

45. Jotzu, C., et al., *Adipose tissue-derived stem cells differentiate into carcinoma-associated fibroblast-like cells under the influence of tumor-derived factors.* Anal Cell Pathol (Amst), 2010. **33**(2): p. 61-79.
46. Adams, E.F., et al., *Effects of human breast fibroblasts on growth and 17β-estradiol dehydrogenase activity of MCF-7 cells in culture.* Breast Cancer Research and Treatment, 1988. **11**(2): p. 165-172.
47. Bertero, T., et al., *Tumor-Stroma Mechanics Coordinate Amino Acid Availability to Sustain Tumor Growth and Malignancy.* Cell Metab, 2019. **29**(1): p. 124-140 e10.
48. Orimo, A., et al., *Stromal fibroblasts present in invasive human breast carcinomas promote tumor growth and angiogenesis through elevated SDF-1/CXCL12 secretion.* Cell, 2005. **121**(3): p. 335-48.
49. Loeffler, M., et al., *Targeting tumor-associated fibroblasts improves cancer chemotherapy by increasing intratumoral drug uptake.* J Clin Invest, 2006. **116**(7): p. 1955-62.
50. Sousa, C.M., et al., *Pancreatic stellate cells support tumour metabolism through autophagic alanine secretion.* Nature, 2016. **536**(7617): p. 479-83.
51. Yang, L., et al., *Targeting Stromal Glutamine Synthetase in Tumors Disrupts Tumor Microenvironment-Regulated Cancer Cell Growth.* Cell Metab, 2016. **24**(5): p. 685-700.
52. Zhang, W., et al., *Stromal control of cystine metabolism promotes cancer cell survival in chronic lymphocytic leukaemia.* Nat Cell Biol, 2012. **14**(3): p. 276-86.
53. Achreja, A., et al., *Exo-MFA - A 13C metabolic flux analysis framework to dissect tumor microenvironment-secreted exosome contributions towards cancer cell metabolism.* Metab Eng, 2017. **43**(Pt B): p. 156-172.
54. Zhao, H., et al., *Tumor microenvironment derived exosomes pleiotropically modulate cancer cell metabolism.* Elife, 2016. **5**: p. e10250.
55. Guillaumond, F., et al., *Strengthened glycolysis under hypoxia supports tumor symbiosis and hexosamine biosynthesis in pancreatic adenocarcinoma.* Proc Natl Acad Sci U S A, 2013. **110**(10): p. 3919-24.
56. Salimian Rizi, B., et al., *Nitric oxide mediates metabolic coupling of omentum-derived adipose stroma to ovarian and endometrial cancer cells.* Cancer Res, 2015. **75**(2): p. 456-71.
57. Fiaschi, T., et al., *Reciprocal metabolic reprogramming through lactate shuttle coordinately influences tumor-stroma interplay.* Cancer Res, 2012. **72**(19): p. 5130-40.
58. Wang, W., et al., *Effector T Cells Abrogate Stroma-Mediated Chemoresistance in Ovarian Cancer.* Cell, 2016. **165**(5): p. 1092-1105.
59. Martinez-Outschoorn, U.E., et al., *Anti-estrogen resistance in breast cancer is induced by the tumor microenvironment and can be overcome by inhibiting mitochondrial function in epithelial cancer cells.* Cancer Biol Ther, 2011. **12**(10): p. 924-38.
60. Tessarz, P. and T. Kouzarides, *Histone core modifications regulating nucleosome structure and dynamics.* Nat Rev Mol Cell Biol, 2014. **15**(11): p. 703-8.
61. Jaenisch, R. and A. Bird, *Epigenetic regulation of gene expression: how the genome integrates intrinsic and environmental signals.* Nat Genet, 2003. **33 Suppl**: p. 245-54.
62. Jones, P.A., J.P. Issa, and S. Baylin, *Targeting the cancer epigenome for therapy.* Nat Rev Genet, 2016. **17**(10): p. 630-41.
63. SB, B. and H. JG, *DNA hypermethylation in tumorigenesis: epigenetics joins genetics.* Trends in Genetics, 2000. **16**(4): p. 168-74.
64. SE, G., et al., *Hypomethylation of DNA from benign and malignant human colon neoplasms.* Science, 1985. **228**(4696): p. 187-90.
65. I, R., et al., *DNMT1 and DNMT3b cooperate to silence genes in human cancer cells.* Nature, 2002. **416**(6880): p. 522-6.

66. Baylin, S.B., *DNA methylation and gene silencing in cancer.* Nat Clin Pract Oncol, 2005. **2 Suppl 1**: p. S4-11.
67. O'Hagan, H.M., et al., *Oxidative damage targets complexes containing DNA methyltransferases, SIRT1, and polycomb members to promoter CpG Islands.* Cancer Cell, 2011. **20**(5): p. 606-19.
68. Waterland, R.A., *Assessing the Effects of High Methionine Intake on DNA Methylation.* The Journal of Nutrition, 2006. **136**(6): p. 1706S-1710S.
69. Kaelin, W.G., Jr. and S.L. McKnight, *Influence of metabolism on epigenetics and disease.* Cell, 2013. **153**(1): p. 56-69.
70. Mentch, S.J., et al., *Histone Methylation Dynamics and Gene Regulation Occur through the Sensing of One-Carbon Metabolism.* Cell Metab, 2015. **22**(5): p. 861-73.
71. A, B., et al., *Histone trimethylation at H3K4, H3K9 and H4K20 correlates with patient survival and tumor recurrence in early-stage colon cancer.* BMC Cancer, 2014. **14**(531).
72. Spangle, J.M., et al., *PI3K/AKT Signaling Regulates H3K4 Methylation in Breast Cancer.* Cell Rep, 2016. **15**(12): p. 2692-704.
73. Kaur, M. and M.D. Cole, *MYC acts via the PTEN tumor suppressor to elicit autoregulation and genome-wide gene repression by activation of the Ezh2 methyltransferase.* Cancer Res, 2013. **73**(2): p. 695-705.
74. M, S., et al., *Homozygous deletions of methylthioadenosine phosphorylase (MTAP) are more frequent than p16INK4A (CDKN2) homozygous deletions in primary non-small cell lung cancers (NSCLC).* Oncogeen, 1998. **17**(20): p. 2669-75.
75. Cavuoto, P. and M.F. Fenech, *A review of methionine dependency and the role of methionine restriction in cancer growth control and life-span extension.* Cancer Treat Rev, 2012. **38**(6): p. 726-36.
76. Pan, M., et al., *Regional glutamine deficiency in tumours promotes dedifferentiation through inhibition of histone demethylation.* Nat Cell Biol, 2016. **18**(10): p. 1090-101.
77. Kurdistani, S.K., S. Tavazoie, and M. Grunstein, *Mapping global histone acetylation patterns to gene expression.* Cell, 2004. **117**(6): p. 721-33.
78. Lee, J.V., et al., *Akt-dependent metabolic reprogramming regulates tumor cell histone acetylation.* Cell Metab, 2014. **20**(2): p. 306-319.
79. Schug, Z.T., et al., *Acetyl-CoA synthetase 2 promotes acetate utilization and maintains cancer cell growth under metabolic stress.* Cancer Cell, 2015. **27**(1): p. 57-71.
80. Takahashi, H., et al., *Nucleocytosolic acetyl-coenzyme a synthetase is required for histone acetylation and global transcription.* Mol Cell, 2006. **23**(2): p. 207-17.
81. Ramaswamy, V., et al., *Global control of histone modification by the anaphase-promoting complex.* Mol Cell Biol, 2003. **23**(24): p. 9136-49.
82. Friis, R.M., et al., *A glycolytic burst drives glucose induction of global histone acetylation by picNuA4 and SAGA.* Nucleic Acids Res, 2009. **37**(12): p. 3969-80.
83. Wellen, K.E., et al., *ATP-citrate lyase links cellular metabolism to histone acetylation.* Science, 2009. **324**(5930): p. 1076-80.
84. Donohoe, D.R., et al., *The Warburg effect dictates the mechanism of butyrate-mediated histone acetylation and cell proliferation.* Mol Cell, 2012. **48**(4): p. 612-26.
85. Evertts, A.G., et al., *Quantitative dynamics of the link between cellular metabolism and histone acetylation.* J Biol Chem, 2013. **288**(17): p. 12142-51.
86. A, M., et al., *Fluorescent indicators for Ca2+based on green fluorescent proteins and calmodulin.* Nature, 1997. **338**(6645): p. 882-7.
87. Blatt, E., et al., *Viscosity and temperature dependence of fluorescence lifetimes of anthracene and 9-methylanthracene.* J. Phys. Chem., 1981. **85**(19): p. 2810-2816.
88. Nakabayashi, T., et al., *pH dependence of the fluorescence lifetime of enhanced yellow fluorescent protein in solution and cells.* Journal of Photochemistry and Photobiology A: Chemistry, 2012. **235**: p. 65-71.

89. Koch, K.-W., et al., *Fluorescence Lifetime Readouts of Troponin-C-Based Calcium FRET Sensors: A Quantitative Comparison of CFP and mTFP1 as Donor Fluorophores.* PLoS ONE, 2012. **7**(11): p. e49200.
90. Komatsu, N., et al., *Development of an optimized backbone of FRET biosensors for kinases and GTPases.* Mol Biol Cell, 2011. **22**: p. 4647-56.
91. Hiratsuka, T., et al., *Intercellular propagation of extracellular signal-regulated kinase activation revealed by in vivo imaging of mouse skin.* Elife, 2015. **4**: p. e05178.
92. Aoki, K., et al., *Stochastic ERK activation induced by noise and cell-to-cell propagation regulates cell density-dependent proliferation.* Mol Cell, 2013. **52**(4): p. 529-40.
93. Hirata, E., et al., *Intravital imaging reveals how BRAF inhibition generates drug-tolerant microenvironments with high integrin beta1/FAK signaling.* Cancer Cell, 2015. **27**(4): p. 574-88.
94. Blacker, T.S. and M.R. Duchen, *Investigating mitochondrial redox state using NADH and NADPH autofluorescence.* Free Radical Biology and Medicine, 2016. **100**: p. 53-65.
95. Blacker, T.S., et al., *Separating NADH and NADPH fluorescence in live cells and tissues using FLIM.* Nat Commun, 2014. **5**: p. 3936.
96. Stringari, C., et al., *Metabolic trajectory of cellular differentiation in small intestine by Phasor Fluorescence Lifetime Microscopy of NADH.* Sci Rep, 2012. **2**: p. 568.
97. HW, G., et al., *Correlation of NADH fluorescence lifetime and oxidative phosphorylation metabolism in the osteogenic differentiation of human mesenchymal stem cell.* Journal of Biomedical Optics, 2015. **20**: p. 017004.
98. Skala, M.C., et al., *In vivo multiphoton microscopy of NADH and FAD redox states, fluorescence lifetimes, and cellular morphology in precancerous epithelia.* Proc Natl Acad Sci U S A, 2007. **104**(49): p. 19494-9.
99. Stringari, C., et al., *In vivo single-cell detection of metabolic oscillations in stem cells.* Cell Rep, 2015. **10**(1): p. 1-7.
100. Takanaga, H., B. Chaudhuri, and W.B. Frommer, *GLUT1 and GLUT9 as major contributors to glucose influx in HepG2 cells identified by a high sensitivity intramolecular FRET glucose sensor.* Biochim Biophys Acta, 2008. **1778**(4): p. 1091-9.
101. San Martin, A., et al., *Imaging mitochondrial flux in single cells with a FRET sensor for pyruvate.* PLoS One, 2014. **9**(1): p. e85780.
102. San Martin, A., et al., *A genetically encoded FRET lactate sensor and its use to detect the Warburg effect in single cancer cells.* PLoS One, 2013. **8**(2): p. e57712.
103. Imamura, H., et al., *Visualization of ATP levels inside single living cells with fluorescence resonance energy transfer-based genetically encoded indicators.* Proc Natl Acad Sci U S A, 2009. **106**(37): p. 15651-6.
104. Deuschle, K., et al., *Construction and optimization of a family of genetically encoded metabolite sensors by semirational protein engineering.* Protein Sci, 2005. **14**(9): p. 2304-14.
105. Maioli, V., et al., *Time-lapse 3-D measurements of a glucose biosensor in multicellular spheroids by light sheet fluorescence microscopy in commercial 96-well plates.* Sci Rep, 2016. **6**: p. 37777.
106. Kon, S., et al., *Cell competition with normal epithelial cells promotes apical extrusion of transformed cells through metabolic changes.* Nat Cell Biol, 2017. **19**(5): p. 530-541.
107. Lindenburg, L. and M. Merkx, *Engineering genetically encoded FRET sensors.* Sensors (Basel), 2014. **14**(7): p. 11691-713.
108. Ganesan, S., et al., *A dark yellow fluorescent protein (YFP)-based Resonance Energy-Accepting Chromoprotein (REACh) for Forster resonance energy transfer with GFP.* Proc Natl Acad Sci U S A, 2006. **103**(11): p. 4089-94.

109. Murakoshi, H., et al., *A dark green fluorescent protein as an acceptor for measurement of Forster resonance energy transfer.* Sci Rep, 2015. **5**: p. 15334.
110. Murakoshi, H. and A.C.E. Shibata, *ShadowY: a dark yellow fluorescent protein for FLIM-based FRET measurement.* Sci Rep, 2017. **7**(1): p. 6791.
111. Tsuyama, T., et al., *Mitochondrial dysfunction induces dendritic loss via eIF2alpha phosphorylation.* J Cell Biol, 2017. **216**(3): p. 815-834.
112. Kelley, L.C., et al., *Adaptive F-Actin Polymerization and Localized ATP Production Drive Basement Membrane Invasion in the Absence of MMPs.* Dev Cell, 2019. **48**(3): p. 313-328 e8.
113. Tsou, P., et al., *A fluorescent reporter of AMPK activity and cellular energy stress.* Cell Metab, 2011. **13**(4): p. 476-486.
114. Chennell, G., et al., *Imaging of Metabolic Status in 3D Cultures with an Improved AMPK FRET Biosensor for FLIM.* Sensors (Basel), 2016. **16**(8).
115. Pelosse, M., et al., *Synthetic energy sensor AMPfret deciphers adenylate-dependent AMPK activation mechanism.* Nat Commun, 2019. **10**(1): p. 1038.
116. Konagaya, Y., et al., *A Highly Sensitive FRET Biosensor for AMPK Exhibits Heterogeneous AMPK Responses among Cells and Organs.* Cell Rep, 2017. **21**(9): p. 2628-2638.
117. Bulusu, V., et al., *Spatiotemporal Analysis of a Glycolytic Activity Gradient Linked to Mouse Embryo Mesoderm Development.* Dev Cell, 2017. **40**(4): p. 331-341 e4.
118. Garnett, J.P., et al., *Hyperglycaemia and Pseudomonas aeruginosa acidify cystic fibrosis airway surface liquid by elevating epithelial monocarboxylate transporter 2 dependent lactate-H(+) secretion.* Sci Rep, 2016. **6**: p. 37955.
119. Solis-Maldonado, M., et al., *Altered lactate metabolism in Huntington's disease is dependent on GLUT3 expression.* CNS Neurosci Ther, 2018. **24**(4): p. 343-352.
120. Yin Tang, Z.W., Ziming Li, Jungwoo Kim, Yuliang Deng, Yan Li, James R. Heath, Wei Wei, Shun Lu, and Qihui Shi, *High-throughput screening of rare metabolically active tumor cells in pleural effusion and peripheral blood of lung cancer patients.* Proc Natl Acad Sci U S A, 2017. **114**(14): p. E2983.
121. Madonna, M.C., et al., *Optical Imaging of Glucose Uptake and Mitochondrial Membrane Potential to Characterize Her2 Breast Tumor Metabolic Phenotypes.* Mol Cancer Res, 2019. **17**(7): p. 1545-1555.
122. Zhu, C., et al., *Near-simultaneous intravital microscopy of glucose uptake and mitochondrial membrane potential, key endpoints that reflect major metabolic axes in cancer.* Sci Rep, 2017. **7**(1): p. 13772.
123. Russell C. Scaduto, J., and Lee W. Grotyohann, *Measurement of Mitochondrial Membrane Potential Using Fluorescent Rhodamine Derivatives.* Biophysical Journal, 1999. **76**(1): p. 469-477.
124. Murphy, M.P., *Targeting lipophilic cations to mitochondria.* Biochim Biophys Acta, 2008. **1777**(7-8): p. 1028-31.
125. Turrens, J.F., *Mitochondrial formation of reactive oxygen species.* J Physiol, 2003. **552**(Pt 2): p. 335-44.
126. Korshunov, S.S., V.P. Skulachev, and A.A. Starkov, *High protonic potential actuates a mechanism of production of reactive oxygen species in mitochondria.* FEBS Letters, 1997. **416**(1): p. 15-18.
127. Ju, T.C., et al., *AMPK-alpha1 functions downstream of oxidative stress to mediate neuronal atrophy in Huntington's disease.* Biochim Biophys Acta, 2014. **1842**(9): p. 1668-80.
128. Chan, T.K., et al., *Aeroallergens Induce Reactive Oxygen Species Production and DNA Damage and Dampen Antioxidant Responses in Bronchial Epithelial Cells.* J Immunol, 2017. **199**(1): p. 39-47.
129. Xu, L., et al., *Inhibition of autophagy increased AGE/ROS-mediated apoptosis in mesangial cells.* Cell Death Dis, 2016. **7**(11): p. e2445.

130. L, W., et al., *Effect of glucose and deoxyglucose on the redistribution of calcium in ehrlich ascites tumour and Zajdela hepatoma cells and its consequences for mitochondrial energetics. Further arguments for the role of Ca(2+) in the mechanism of the crabtree effect.* European Journal of Biochemistry, 1999. **263**(2): p. 495-501.
131. Lebiedzinska, M., et al., *Oxidative stress-dependent p66Shc phosphorylation in skin fibroblasts of children with mitochondrial disorders.* Biochim Biophys Acta, 2010. **1797**(6-7): p. 952-60.
132. Franovic, A., et al., *Translational up-regulation of the EGFR by tumor hypoxia provides a nonmutational explanation for its overexpression in human cancer.* Proc Natl Acad Sci U S A, 2007. **104**(32): p. 13092-7.
133. Gallagher, S.M., et al., *Monocarboxylate transporter 4 regulates maturation and trafficking of CD147 to the plasma membrane in the metastatic breast cancer cell line MDA-MB-231.* Cancer Res, 2007. **67**(9): p. 4182-9.
134. Baenke, F., et al., *Functional screening identifies MCT4 as a key regulator of breast cancer cell metabolism and survival.* J Pathol, 2015. **237**(2): p. 152-65.
135. Lin, C. and X. Xu, *YAP1-TEAD1-Glut1 axis dictates the oncogenic phenotypes of breast cancer cells by modulating glycolysis.* Biomed Pharmacother, 2017. **95**: p. 789-794.
136. Nicholls, D.G., *Mitochondrial membrane potential and aging.* Aging Cell, 2004. **3**(1): p. 35-40.
137. Kim, I., S. Rodriguez-Enriquez, and J.J. Lemasters, *Selective degradation of mitochondria by mitophagy.* Arch Biochem Biophys, 2007. **462**(2): p. 245-53.
138. Gambhir, S.S., *Molecular imaging of cancer with positron emission tomography.* Nat Rev Cancer, 2002. **2**(9): p. 683-93.
139. Gentric, G., V. Mieulet, and F. Mechta-Grigoriou, *Heterogeneity in Cancer Metabolism: New Concepts in an Old Field.* Antioxid Redox Signal, 2017. **26**(9): p. 462-485.
140. Dai, X., et al., *Breast Cancer Cell Line Classification and Its Relevance with Breast Tumor Subtyping.* J Cancer, 2017. **8**(16): p. 3131-3141.
141. Hao, X., et al., *Metabolic Imaging Reveals a Unique Preference of Symmetric Cell Division and Homing of Leukemia-Initiating Cells in an Endosteal Niche.* Cell Metab, 2019. **29**(4): p. 950-965 e6.
142. Zhao, Y., et al., *SoNar, a Highly Responsive NAD+/NADH Sensor, Allows High-Throughput Metabolic Screening of Anti-tumor Agents.* Cell Metab, 2015. **21**(5): p. 777-89.
143. Bi, H., et al., *Optimization of harvesting, extraction, and analytical protocols for UPLC-ESI-MS-based metabolomic analysis of adherent mammalian cancer cells.* Anal Bioanal Chem, 2013. **405**(15): p. 5279-89.
144. Wang, L., et al., *Molecular link between glucose and glutamine consumption in cancer cells mediated by CtBP and SIRT4.* Oncogenesis, 2018. **7**(3): p. 26.
145. Buck, M.D., et al., *Metabolic Instruction of Immunity.* Cell, 2017. **169**(4): p. 570-586.
146. Semenza, G.L., *HIF-1: upstream and downstream of cancer metabolism.* Curr Opin Genet Dev, 2010. **20**(1): p. 51-6.
147. Amelio, I. and G. Melino, *The p53 family and the hypoxia-inducible factors (HIFs): determinants of cancer progression.* Trends Biochem Sci, 2015. **40**(8): p. 425-34.
148. Papandreou, I., et al., *HIF-1 mediates adaptation to hypoxia by actively downregulating mitochondrial oxygen consumption.* Cell Metab, 2006. **3**(3): p. 187-97.
149. Kim, J.W., et al., *HIF-1-mediated expression of pyruvate dehydrogenase kinase: a metabolic switch required for cellular adaptation to hypoxia.* Cell Metab, 2006. **3**(3): p. 177-85.
150. T, H., et al., *Fluorescent dye monitoring of mitochondrial changes associated with malignant cell transformation.* Cell Struct Funct., 1987. **12**(6): p. 525-37.

151. G, P., et al., *Transport of pyruvate in mitochondria from different tumor cells.* Cancer Res. , 1983. **43**(11): p. 5068-71.
152. J, B.-H., M. A, and W. P, *Dependence of energy metabolism on the density of cells in culture.* Cell Struct Funct. , 1998. **23**(2): p. 85-93.
153. Panciera, T., et al., *Mechanobiology of YAP and TAZ in physiology and disease.* Nat Rev Mol Cell Biol, 2017. **18**(12): p. 758-770.
154. Y, L., et al., *S100A7 induction is repressed by YAP via the Hippo pathway in A431 cells.* Oncotarget, 2016. **7**(25): p. 38133-38142.
155. Pavel, M., et al., *Contact inhibition controls cell survival and proliferation via YAP/TAZ-autophagy axis.* Nat Commun, 2018. **9**(1): p. 2961.
156. Das, A., et al., *YAP Nuclear Localization in the Absence of Cell-Cell Contact Is Mediated by a Filamentous Actin-dependent, Myosin II- and Phospho-YAP-independent Pathway during Extracellular Matrix Mechanosensing.* J Biol Chem, 2016. **291**(12): p. 6096-110.
157. Zheng, X., et al., *LncRNA wires up Hippo and Hedgehog signaling to reprogramme glucose metabolism.* EMBO J, 2017. **36**(22): p. 3325-3335.
158. Cosset, E., et al., *Glut3 Addiction Is a Druggable Vulnerability for a Molecularly Defined Subpopulation of Glioblastoma.* Cancer Cell, 2017. **32**(6): p. 856-868 e5.
159. Stine, Z.E., et al., *MYC, Metabolism, and Cancer.* Cancer Discov, 2015. **5**(10): p. 1024-39.
160. MR, Z., et al., *Regulation of ATP utilization during metastatic cell migration by collagen architecture.* Mol Biol Cell, 2018. **29**(1): p. 1-9.
161. Vander Heiden, M.G., *Targeting cancer metabolism: a therapeutic window opens.* Nat Rev Drug Discov, 2011. **10**(9): p. 671-84.
162. Asano, S., et al., *Suppression of cell migration by phospholipase C-related catalytically inactive protein-dependent modulation of PI3K signalling.* Sci Rep, 2017. **7**(1): p. 5408.
163. A1, H., et al., *TGF-b promotes PI3K-AKT signaling and prostate cancer cell migration through the TRAF6-mediated ubiquitylation of p85a.* Sci Signal., 2017. **10**(486).
164. Cain, R.J. and A.J. Ridley, *Phosphoinositide 3-kinases in cell migration.* Biol Cell, 2009. **101**(1): p. 13-29.
165. Kitajima, S., et al., *Overcoming Resistance to Dual Innate Immune and MEK Inhibition Downstream of KRAS.* Cancer Cell, 2018. **34**(3): p. 439-452 e6.
166. Kumagai, Y., et al., *Heterogeneity in ERK activity as visualized by in vivo FRET imaging of mammary tumor cells developed in MMTV-Neu mice.* Oncogene, 2015. **34**(8): p. 1051-7.
167. Jacob, T., et al., *Multiplexed imaging reveals heterogeneity of PI3K/MAPK network signaling in breast lesions of known PIK3CA genotype.* Breast Cancer Res Treat, 2016. **159**(3): p. 575-83.
168. Hensley, C.T., et al., *Metabolic Heterogeneity in Human Lung Tumors.* Cell, 2016. **164**(4): p. 681-94.
169. Kawai, H., et al., *Simultaneous real-time detection of initiator- and effector-caspase activation by double fluorescence resonance energy transfer analysis.* J Pharmacol Sci, 2005. **97**(3): p. 361-8.
170. Ai, H.W., et al., *Fluorescent protein FRET pairs for ratiometric imaging of dual biosensors.* Nat Methods, 2008. **5**(5): p. 401-3.
171. Grant, D.M., et al., *Multiplexed FRET to image multiple signaling events in live cells.* Biophys J, 2008. **95**(10): p. L69-71.
172. Martin, K.J., et al., *Accepting from the best donor; analysis of long-lifetime donor fluorescent protein pairings to optimise dynamic FLIM-based FRET experiments.* PLoS One, 2018. **13**(1): p. e0183585.
173. Kishimoto, S., et al., *Imaging of glucose metabolism by 13C-MRI distinguishes pancreatic cancer subtypes in mice.* Elife, 2019. **8**.

174. Morita, M., et al., *PKM1 Confers Metabolic Advantages and Promotes Cell-Autonomous Tumor Cell Growth.* Cancer Cell, 2018. **33**(3): p. 355-367 e7.
175. Pate, K.T., et al., *Wnt signaling directs a metabolic program of glycolysis and angiogenesis in colon cancer.* EMBO J, 2014. **33**(13): p. 1454-73.
176. Bodzon-Kulakowska, A. and P. Suder, *Imaging mass spectrometry: Instrumentation, applications, and combination with other visualization techniques.* Mass Spectrom Rev, 2016. **35**(1): p. 147-69.
177. Porta Siegel, T., et al., *Mass Spectrometry Imaging and Integration with Other Imaging Modalities for Greater Molecular Understanding of Biological Tissues.* Mol Imaging Biol, 2018. **20**(6): p. 888-901.
178. Hsu, A.H., et al., *Crosstalk between PKCalpha and PI3K/AKT Signaling Is Tumor Suppressive in the Endometrium.* Cell Rep, 2018. **24**(3): p. 655-669.
179. Shain, A.H., et al., *Genomic and Transcriptomic Analysis Reveals Incremental Disruption of Key Signaling Pathways during Melanoma Evolution.* Cancer Cell, 2018. **34**(1): p. 45-55 e4.
180. Zhang, Y., et al., *A Pan-Cancer Proteogenomic Atlas of PI3K/AKT/mTOR Pathway Alterations.* Cancer Cell, 2017. **31**(6): p. 820-832 e3.
181. Wu, Q., et al., *A chemical toolbox for the study of bromodomains and epigenetic signaling.* Nat Commun, 2019. **10**(1): p. 1915.
182. Stratikopoulos, E.E., et al., *Kinase and BET Inhibitors Together Clamp Inhibition of PI3K Signaling and Overcome Resistance to Therapy.* Cancer Cell, 2015. **27**(6): p. 837-51.
183. Kurhanewicz, J., et al., *Hyperpolarized (13)C MRI: Path to Clinical Translation in Oncology.* Neoplasia, 2019. **21**(1): p. 1-16.
184. B, C., L. V, and S. B, *Metabolically Linked Changes in Fluorescence Emission Spectra of Cortex of Rat Brain, Kidney and Adrenal Gland.* Nature, 1962. **195**: p. 1073-5.
185. JR1, L., et al., *Fluorescence lifetime imaging of free and protein-bound NADH.* Proc Natl Acad Sci U S A. , 1992. **89**(4): p. 1271-5.
186. C, S., et al., *Phasor approach to fluorescence lifetime microscopy distinguishes different metabolic states of germ cells in a live tissue.* Proc Natl Acad Sci U S A. , 2011. **108**(33): p. 13582-7.
187. Stringari, C., et al., *Phasor fluorescence lifetime microscopy of free and protein-bound NADH reveals neural stem cell differentiation potential.* PLoS One, 2012. **7**(11): p. e48014.
188. Sparks, H., et al., *Heterogeneity in tumor chromatin-doxorubicin binding revealed by in vivo fluorescence lifetime imaging confocal endomicroscopy.* Nat Commun, 2018. **9**(1): p. 2662.
189. Yin, Z., et al., *Targeting T cell metabolism in the tumor microenvironment: an anti-cancer therapeutic strategy.* J Exp Clin Cancer Res, 2019. **38**(1): p. 403.
190. Chi, H., *Regulation and function of mTOR signalling in T cell fate decisions.* Nat Rev Immunol, 2012. **12**(5): p. 325-38.
191. Zhang, L. and P. Romero, *Metabolic Control of CD8(+) T Cell Fate Decisions and Antitumor Immunity.* Trends Mol Med, 2018. **24**(1): p. 30-48.
192. Bantug, G.R., et al., *The spectrum of T cell metabolism in health and disease.* Nat Rev Immunol, 2018. **18**(1): p. 19-34.
193. Macintyre, A.N., et al., *The glucose transporter Glut1 is selectively essential for CD4 T cell activation and effector function.* Cell Metab, 2014. **20**(1): p. 61-72.
194. Nakaya, M., et al., *Inflammatory T cell responses rely on amino acid transporter ASCT2 facilitation of glutamine uptake and mTORC1 kinase activation.* Immunity, 2014. **40**(5): p. 692-705.

195. Macintyre, A.N., et al., *Protein kinase B controls transcriptional programs that direct cytotoxic T cell fate but is dispensable for T cell metabolism.* Immunity, 2011. **34**(2): p. 224-36.
196. Kienast, Y., et al., *Real-time imaging reveals the single steps of brain metastasis formation.* Nat Med, 2010. **16**(1): p. 116-22.
197. Weigelt, B., J.L. Peterse, and L.J. van 't Veer, *Breast cancer metastasis: markers and models.* Nat Rev Cancer, 2005. **5**(8): p. 591-602.
198. Bos, P.D., et al., *Genes that mediate breast cancer metastasis to the brain.* Nature, 2009. **459**(7249): p. 1005-9.
199. Frentzas, S., et al., *Vessel co-option mediates resistance to anti-angiogenic therapy in liver metastases.* Nat Med, 2016. **22**(11): p. 1294-1302.
200. Quail, D.F. and J.A. Joyce, *The Microenvironmental Landscape of Brain Tumors.* Cancer Cell, 2017. **31**(3): p. 326-341.
201. Valiente, M., et al., *The Evolving Landscape of Brain Metastasis.* Trends Cancer, 2018. **4**(3): p. 176-196.
202. Belanger, M., I. Allaman, and P.J. Magistretti, *Brain energy metabolism: focus on astrocyte-neuron metabolic cooperation.* Cell Metab, 2011. **14**(6): p. 724-38.
203. Osswald, M., et al., *Brain tumour cells interconnect to a functional and resistant network.* Nature, 2015. **528**(7580): p. 93-8.
204. Chen, Q., et al., *Carcinoma-astrocyte gap junctions promote brain metastasis by cGAMP transfer.* Nature, 2016. **533**(7604): p. 493-498.
205. Venneti, S. and C.B. Thompson, *Metabolic Reprogramming in Brain Tumors.* Annu Rev Pathol, 2017. **12**: p. 515-545.
206. Vicente-Gutierrez, C., et al., *Astrocytic mitochondrial ROS modulate brain metabolism and mouse behaviour.* Nature Metabolism, 2019. **1**(2): p. 201-211.